

Department of Materials Physics
UNIVERSIDAD DEL PAIS VASCO
THE UNIVERSITY OF THE BASQUE COUNTRY



Universidad Euskal Herriko
del País Vasco Unibertsitatea

Classical and quantum approaches to the interaction of light and matter at the nanoscale

Thesis developed by

MIKOŁAJ KAJETAN SCHMIDT

for the degree of

DOCTOR OF PHILOSOPHY IN PHYSICS

Supervised by

Prof. Javier Aizpurua

Donostia-San Sebastián, Spain, January 2016.

Acknowledgments

First and foremost, I would like to acknowledge my advisor, **Javier Aizpurua**, for inviting me to his group a few years ago and then, over time, draft after draft, and errata after manuscript, patiently and painstakingly molding me into the researcher I aspire to be today.

Luckily, in his efforts Javier has had a great support from **Rubén Esteban**, whom I am privileged to call a friend. Ruben has been for years stretching me, pulling my head all the way into the clouds, while ensuring that I stand firmly on the ground.

Over the last years I have had a great pleasure to work with, and learn from, many wonderful, patient researchers: in Houston, **Peter Nordlander** offered me a tasty, yet tough scientific nut to crack; in Garching, it is only thanks to the guidance and sympathy of **Alejandro Gozález-Tudela** and **Geza Giedke** that I have survived my quantum optics bootcamp in the group of **Ignacio Cirac**; recently **Tomek Antosiewicz** added one more reason for me to feel welcome in Warsaw; to **Sebastian Maćkowski**, for equipping me for the road towards academia; and back at *home*, in Donosti, I got to meet and work with **Juan José Sáenz**, **Pablo Albella** and **Aitzol García-Etxarri**, who helped me, each in a slightly different way, to get a firmer grip on the notion of what *physics* is all about.

I also need to thank my *scientific* family in Donosti, which made the long hours in CFM a bit less overwhelming: my long-time roommates, **Ameen** and **Garikoitz**, short-time roommates, **Tomas**, **Andrea** and **Mattin**, once-in-a-while roommates, **Pavlo** and **Luca**. I had also undergone a throughout internationalization, spending long hours in the canteen, gym and - albeit far less than we were hoping for - climbing, with **Federico**, **Amaia** and **Alvise**. How will I ever switch to half-an-hour lunch breaks?

To the three divas from Gros: **Elizabeth**, **Constance** and **Justina**, for organising the best game-nights, sheltering me and providing the much-needed distraction in the last

Acknowledgments

lap of this race. And to **Marta**, for keeping my health up and keeping my taste bus from the routine of smoked salmon.

Weronice - za narty, za Szwajcarię, Paryż, Barcelonę, Istambuł... za każde wyrwanie z rutyny i oderwanie od tuńczyka, za każdy dzień w Warszawie i Baskonii. I za brykanie.

Rodzicom, Aguli i BP - za cierpliwość, ganiecie mnie do skype'a, i za każdy raz kiedy wracałem do Torunia i czułem się jak piskle w gnieździe. Swoją drogą, myślicie że te kurniki się kiedyś skończą?

Contents

Acknowledgments	iii
Contents	iv
Resumen	ix
Introduction	1
1 Revisiting spectral properties of plasmonic nanoparticles with strong interband contribution	9
1.1 Macroscopic description of metals	11
1.1.1 Surface Plasmon Polaritons	13
1.1.2 Localized Surface Plasmons	16
1.2 Models of polarizability	19
1.2.1 Plasmon as a damped harmonic oscillator	19
1.2.2 Dynamic depolarization	22
1.2.3 Systematic study of gold nanorods	28
1.2.4 Tracing the decay of plasmons in time	30
1.2.5 Phenomenological estimations of the plasmon dynamics	32
1.3 Summary	34
2 Dielectric nanoantennas	35
2.1 Mie theory	36
2.1.1 Optical response of a submicron dielectric sphere	38
2.1.2 Scattering of radiation from a dipolar emitter	38
2.2 Single dielectric-particle nanoantennas	40
2.2.1 Radiating dipoles in the presence of a high-index dielectric particle (Si sphere)	41
2.2.2 Dipole-dipole interaction	45
2.2.3 Conclusion	48
2.3 Optical response of dielectric dimers	48
2.3.1 Hybridization of dipolar modes in a dielectric dimer	49
2.3.2 Experimental realization of scattering of light on dielectric dimers	56
2.3.3 Control of single emitters	65
2.4 Summary	67

3 Helicity and random media	69
3.1 Operators, symmetries and transformations	70
3.1.1 Complete set of commuting operators	71
3.1.2 Operators and symmetries	71
3.1.3 Fields and modes	73
3.2 Helicity preservation in an inhomogeneous medium	77
3.2.1 Macroscopic approach	77
3.2.2 Microscopic approach	79
3.3 Summary	92
4 Quantum plasmonics	95
4.1 Brief introduction to open quantum systems	96
4.1.1 Von Neumann equation	96
4.1.2 Open quantum system	97
4.1.3 Designing the open quantum system - case study	100
4.2 Raman scattering from molecules in plasmonic cavities	103
4.2.1 Quantization of excitations	104
4.2.2 Cavity-vibrations interaction Hamiltonian	108
4.2.3 Master equation	113
4.2.4 Numerical solution	113
4.2.5 Linearized Hamiltonian	115
4.2.6 Breakdown of the linearization	117
4.2.7 Dependence on the laser detuning Δ	118
4.2.8 Correlations of the emitted light	120
4.3 Optomechanical cavities	122
4.4 Summary	125
Final remarks and outlook	127
A Mie theory	129
A.1 Vector spherical harmonics	129
A.2 Scattering of a planewave	132
A.3 Scattering of radiation of a dipolar emitter	134
A.3.1 Electric dipolar emitter	134
A.3.2 Magnetic dipolar emitter	136
B Linearization of the optomechanical Hamiltonian	139
B.1 Analytical treatment of the system	139
B.1.1 Quantum Langevin equations of the original Hamiltonian	140
B.1.2 Analytical solution to the linearized Hamiltonian	140
B.1.3 Steady state of the linearized Hamiltonian	141
B.1.4 Quantum regression theorem	143
B.1.5 Phonon population	145
B.1.6 Quartic dependence of Stokes intensity on the enhancement of the incident field	146

B.2 Threshold for the onset of the phonon-stimulated Raman scattering . . .	146
List of publications	147
List of symbols	149
Bibliography	153

Resumen

La búsqueda y estudio de efectos novedosos relacionados con la interacción entre la luz y la materia, así como el deseo de ofrecer explicaciones más completas sobre diversos fenómenos relacionados con esta interacción son los ejes sobre los que pivota esta tesis doctoral. El desafío de abordar la interacción de la luz no es nuevo, ya que el propio concepto de la luz y la percepción de los colores han atraído la curiosidad del ser humano desde tiempos antiguos a lo largo de la historia. Afortunadamente, y a diferencia de los primeros investigadores, hoy en día disponemos de un conjunto de complejas herramientas matemáticas que suponen el pilar de la ciencia moderna en lo que se ha dado en llamar el *método científico*. Así mismo, se dispone de dispositivos que nos permiten ver objetos muy pequeños para la simple vista, e incluso acceden a objetos aún más pequeños que la longitud de onda de la luz visible que los ilumina.

Sin embargo, a pesar de la sofisticación de los instrumentos a nuestra disposición, continuamos tan fascinados por los colores brillantes de las plumas de los pájaros [1], la iridiscencia de los caparazones de los escarabajos [2], y los colores vivos exhibidos por ciertas especies de monos y de zarigüeyas [3], como lo estuvieron en su día los pioneros de la ciencia. Éstos y muchos otros fenómenos ópticos ocurren porque, mediante un proceso de selección natural, la Naturaleza ha equipado a diversas especies de pájaros, mariposas, escarabajos y, más sorprendentemente, también a ciertos mamíferos, con mecanismos naturales para organizar complejas estructuras fotónicas a partir de partículas de dimensiones menores de la longitud de onda. En un esfuerzo por comprender e imitar las invenciones de la Naturaleza, muchos científicos han estudiado los elementos que forman estos sistemas, y de una manera directa o indirecta, han logrado descubrir las fascinantes propiedades de los nanosistemas metálicos y dieléctricos, como unidades especialmente efectivas para localizar la luz [4–7], manipular su flujo [8–13] y controlar su interacción con otro de los componentes básicos de la naturaleza, las moléculas [14–18]. Los cuatro capítulos de la tesis suponen una continuación de estos esfuerzos, en los que se presentan

cuatro contribuciones que pueden facilitar el camino hacia la comprensión y el control de la luz.

El primer capítulo de esta tesis describe nanosistemas diseñados para concentrar la luz mediante la excitación de Resonancias Plasmónicas de Superficie Localizadas (LSPRs por sus siglas en inglés), un fenómeno según el cual el campo eléctrico de una haz de luz incidente induce oscilaciones coherentes de los electrones de conducción del metal. Estos sistemas se han estudiado ampliamente tanto en trabajos teóricos como experimentales, en los que la capacidad de localización y aumento del campo electromagnético en la nanoescala han dado lugar a muchas aplicaciones tecnológicas, tales como las plataformas sensorías para biología [19, 20], los sistemas que intensifican la señal de espectroscopias ópticas, [5, 21–23], así como para establecer conexiones entre las excitaciones electrónicas y fotónicas [24, 25]. Sin embargo, a pesar de los significativos avances logrados en la comprensión de su dinámica, las nanopartículas metálicas continúan generando resultados desconcertantes.

Un ejemplo de fenómeno difícil de explicar es la aparente inconsistencia en la posición y anchura espectral de los picos de las resonancias plasmónicas al realizar una medida espectroscópica de diferentes magnitudes: la extinción, la dispersión y el campo próximo [26–29] inducidos por las nanopartículas metálicas. Este peculiar efecto se ha estudiado parcialmente mediante modelos que describen los plasmones como osciladores armónicos amortiguados forzados cuyas resonancias son excitadas en el rango espectral del infrarrojo (IR) [30–33]. Sin embargo, paradójicamente, este simple modelo no es capaz de reproducir las posiciones espectrales relativas de los correspondientes picos resonantes en un caso paradigmático de excitación de plasmones localizados: una pequeña partícula de oro de dimensiones inferiores a la longitud de onda, resonante en el espectro visible. En el Capítulo 1 de esta tesis se estudia esta limitación, que se debe a la existencia de una importante contribución de las *transiciones interbanda* del metal en el caso del oro, que impiden una respuesta puramente *plasmónica* de las partículas metálicas.

Para entender y resolver esta discrepancia en los diversos picos plasmónicos, se ha desarrollado un modelo alternativo que puede ser utilizado satisfactoriamente en el caso de partículas metálicas caracterizadas por una función dieléctrica arbitraria, que presente fuertes contribuciones de transiciones interbanda. mediante la aplicación de este modelo, se demuestra y se explica la existencia de corrimientos espectrales en la comparación de los picos de resonancias obtenidos en la sección eficaz de absorción, en la sección eficaz de dispersión, y en la intensidad del campo cercano. La metodología desarrollada en este capítulo permite analizar en detalle y reinterpretar el papel de las transiciones

interbanda en el ensanchamiento y desplazamiento espectral de la respuesta óptica de nanopartículas metálicas resonantes en el espectro visible.

Otro aspecto de interés en torno a la respuesta de nanosistemas metálicos está relacionado con la dinámica de los plasmones localizados. Los modelos más comunes asumen que, una vez excitados, los plasmones deberían exhibir oscilaciones con amortiguamiento exponencial, estableciendo, por tanto, una relación directa entre la tasa de decaimiento del plasmón y la anchura espectral de la resonancia. Sin embargo, un estudio más detallado apunta que el decaimiento del plasmón no se limita en algunos casos a un simple proceso exponencial [34]. Un análisis numérico de la dinámica de las excitaciones plasmónicas permite estudiar este aspecto, en el que, efectivamente, se encuentra que los plasmones inducidos en pequeñas nanopartículas metálicas pueden llegar a exhibir una dinámica no trivial debido a su acoplamiento con las transiciones interbandas. Esta predicción podría ser verificada mediante la utilización de pulsos de laser ultracortos, como los utilizados en estudios recientes de la dinámica de plasmones en escalas de tiempo de femtosegundos.

Tras explorar los efectos de la naturaleza amortiguada de las excitaciones en nanopartículas metálicas, esta tesis aborda el estudio de otros materiales que no sufren tales limitaciones. En concreto, el Capítulo 2 de la tesis estudia sistemas compuestos por resonadores de dimensiones microscópicas fabricados con materiales dieléctricos, que presentan un índice de refracción alto. La utilización de sistemas micrométricos de estos materiales ha sido un elemento fundamental en el desarrollo experimental de la comunidad de óptica cuántica. Las prestaciones de este tipo de configuraciones han sido llevadas al límite submicrométrico recientemente en dos propuestas teóricas recientes de Aitzol García-Etxarri *et al.* [35] y Andrey Evlyukhin *et al.* [36], que indican la posibilidad de utilizar esferas submicrométricas de silicio en un rango de frecuencias del infrarrojo cercano. En estos trabajos se demuestra que dichas nanoantenas puedan dispersar y localizar la luz de una manera muy eficiente mediante la excitación de modos dipolares tanto eléctricos como magnéticos. Las resonancias magnéticas podrían erigirse en una plataforma alternativa respecto a los sistemas plasmónicos, al presentar la ventaja de la ausencia de pérdidas. Además, los sistemas plasmónicos requieren un cuidadoso diseño que permita obtener actividad magnética [37–39], mientras que los sistemas dieléctricos presentan esta actividad de manera natural.

Las aplicaciones a las que dan lugar estos nuevos sistemas sin pérdidas son abordados en el Capítulo 2, donde se estudian nanoantenas dieléctricas como plataformas útiles para aumentar la tasa de emisión espontánea de emisores dipolares eléctricos y magnéticos

localizados en su proximidad. Se demuestra que estos sistemas pueden alcanzar prestaciones similares a las de sus análogos plasmónicos, mediante el acoplo de los emisores con canales de decaimiento puramente radiativos, lo que permite mantener o incluso aumentar su eficiencia cuántica intrínseca. Además de analizar las cotas del rendimiento que se puede alcanzar en las antenas dieléctricas, se propone una descripción simplificada del aumento de la tasa de emisión espontánea, mediante un modelo que describe la interacción entre el emisor dipolar y la excitación dipolar de la partícula dieléctrica. Esto puede hacerse gracias a la gran separación espectral entre los modos dipolares y los de orden superior que presentan las estructuras dieléctricas.

El modelo de interacción dipolo-dipolo puede extenderse para analizar la respuesta de una estructura de tipo dímero formada por dos partículas dieléctricas, caracterizadas por una polarizabilidad eléctrica y magnética arbitrarias. Se analiza en detalle la hibridación de los modos dipolares de las partículas individuales, y cómo esta hibridación da lugar a modos de tipo dímero que pueden ser clasificados de acuerdo a la simetría que presentan. Es especialmente reseñable que la energía de estos modos de tipo dímero no se debe únicamente a la interacción entre pares homogéneos (eléctrico-eléctrico y magnético-magnético) de los modos dipolares de las partículas individuales, sino que es también necesario considerar la interacción electromagnética entre pares heterogéneos de dipolos (eléctrico-magnético). Este estudio analítico se compara con cálculos numéricos, lo que nos permite incorporar las modificaciones espectrales debidas a la forma y la estructura de las nanopartículas. Los resultados teóricos que explican las complejas hibridaciones de los modos dieléctricos se han confirmado experimentalmente gracias a la caracterización óptica de las estructuras de dímeros desarrolladas en colaboración con el *Laser Zentrum Hannover e.V.*

En el último apartado del Capítulo 2 analizamos las prestaciones de los dímeros dieléctricos como antenas que intensifican la emisión de emisores individuales eléctricos o magnéticos situados en la cavidad formada en el centro del dímero. Encontramos que los modos de esta estructura de dímero pueden inducir un considerable aumento de la tasa de emisión espontánea de los emisores dipolares, fundamentalmente debido al acoplo con modos radiativos, manteniendo al mismo tiempo las altas eficiencias cuánticas incluso cuando se incluyen las pérdidas intrínsecas del silicio. Estos resultados permiten concluir que los sistemas dieléctricos de dimensiones sub-micrométricas pueden ser utilizados como elementos viables de una familia alternativa de antenas nanométricas y metamateriales.

Al derivar las expresiones que describen la intensificación de la tasa de decaimiento de

los emisores dipolares acoplados a nanopartículas dieléctricas en el capítulo 2, se utiliza una metodología sencilla: se expande el campo eléctrico originado por un emisor dipolar eléctrico en una serie de armónicos esféricos vectoriales, y éstos son transformados, reemplazando los campos eléctricos por campos magnéticos y, simultáneamente, el emisor eléctrico por un emisor magnético (detalles indicados en el Apéndice A). Esta transformación es un caso específico de la *transformación dual* más general, que mezcla las componentes eléctricas y magnéticas del campo electromagnético a medida que éste se propaga en un medio homogéneo. Sin embargo, tal y como se discute en el Capítulo 3, esta transformación también se puede aplicar a los campos electromagnéticos en un medio inhomogéneo. Podemos diferenciar dos casos en la aplicación de esta transformación. El primero, el caso *macroscópico*, requiere un medio homogéneo a trozos que presente la misma relación entre la permitividad y la permeabilidad en todo el sistema. El caso *microscópico*, en cambio, concierne a configuraciones aleatorias de partículas dispersivas duales, es decir, partículas con idéntica polarizabilidad magnética y eléctrica. En esta tesis, analizamos este segundo caso en detalle, y demostramos la validez de la transformada dual para un campo que se propaga en una distribución de partículas duales de silicio con dimensiones submicrométricas.

La transformación dual puede ser formulada utilizando su generador, el operador de *helicidad*. De manera más específica, si el sistema dual es iluminado con luz de helicidad bien definida (es decir, si el campo incidente puede ser descompuesto en una serie de ondas planas polarizadas circularmente de quiralidad fija), en este caso la luz dispersada preserva su helicidad y, por tanto, también la quiralidad de las ondas planas polarizadas circularmente que constituyen el campo dispersado. Este efecto puede constituir una nueva herramienta para la caracterización de medios aleatorios.

Por último, en el Capítulo 4 se considera el efecto de dispersión Raman no-resonante en moléculas situadas en cavidades plasmónicas. La motivación de este estudio viene dada por una serie de resultados e implementaciones recientes de este tipo de experimentos, que han sido posibles como consecuencia de un mejor diseño de los sustratos y soportes para la realización de medidas de *Dispersión Raman Aumentada por Superficie* (SERS por su acrónimo en inglés). Algunos de los resultados obtenidos con esta técnica de SERS no pueden ser descritos mediante un tratamiento clásico del aumento de los campos electromagnéticos dentro de las cavidades plasmónicas [40–42], y requieren el desarrollo de una descripción cuántica de los campos electromagnéticos .

En este capítulo presentamos un modelo más fundamental de la interacción no lineal entre los cuantos de excitación de la cavidad plasmónica y la estructura vibracional de

la molécula, basada en la mecánica cuántica. Este modelo es capaz de describir efectos que no pueden ser descritos por un tratamiento clásico y que detallamos a continuación: (i) emergencia de dispersión Raman estimulada por fonones debido a una alta población incoherente de los cuantos de vibración de la molécula; (ii) la dispersión anti-Stokes depende de manera sorprendente de la frecuencia de la luz incidente y de la temperatura local. Cabe apuntar que estos efectos se dan para valores realistas de los diferentes parámetros.

Considerando las consecuencias de estos resultados para la interpretación de los estudios experimentales, la predicción de la dispersión Raman estimulada en moléculas individuales situadas en cavidades plasmónicas puede tener una gran importancia, y puede apuntar nuevas vías para intensificar la emisión Stokes y anti-Stokes, que son intrínsecamente débiles. A nuestro entender, este efecto no ha sido demostrado todavía en el laboratorio, pero los resultados presentados en esta tesis indican que algunos de los experimentos actuales se realizan en condiciones muy similares a las expuestas aquí, que permitirían, por tanto, poner de manifiesto estas observaciones.

Desde el punto de vista teórico, nuestro formalismo es exacto y abre nuevas posibilidades para estudiar correlaciones clásicas y cuánticas entre los fotones emitidos por la cavidad. Debido a la equivalencia formal entre el Hamiltoniano analizado en esta tesis para tratar la interacción Raman y el usado en el estudio de sistemas optomecánicos cuánticos, el esquema que presentamos en el último capítulo de la tesis permite extender el estudio de estos sistemas cuánticos a un nuevo régimen de valores de los parámetros optomecánicos. En un sistema optomecánico Raman se pueden alcanzar fuerzas de acoplamiento relativamente elevadas, observadas con anterioridad solamente para átomos fríos, y se pueden encontrar de manera natural poblaciones térmicas muy pequeñas.

En resumen, los siguientes capítulos de esta tesis presentan una serie de fenómenos ópticos que rigen la respuesta y eficiencia de nanoantenas plasmónicas y dieléctricas. Investigamos estos sistemas como posibles plataformas para estructurar y manipular el flujo de la luz en la nanoescala, así como para aumentar su interacción con moléculas. Los nuevos efectos que se predicen, tales como el decaimiento no exponencial de los plasmones, la formación de modos heterogéneos en dímeros dieléctricos, la conservación de la helicidad de la luz dispersada en un medio dual, o la emergencia de dispersión Raman estimulada por fonones, puede encontrar aplicaciones directas en diversos sistemas nanofotónicos, y abrir nuevos caminos para un mejor control de la luz en escalas inferiores a la longitud de onda.

Introduction

At the very heart of this thesis, lies an effort to propose new effects related to the interaction of light with matter and to provide better explanations to a variety of reported phenomena. The challenge we undertake is not a new one, as one could hardly imagine a time in history where the very notion of light or the perception of colors, would not trouble curious minds. Luckily, unlike the first discoverers, we are equipped with an advanced mathematical framework, the cornerstone of modern science, the *scientific method*, as well as with devices that allow us to see not only objects too small to be observed with the sharpest sight, but even smaller than the wavelength of visible light.

And yet, despite all the sophistication of the available tools, we are still, just like the pioneers of science, awed by the great show of bright coloring of the feathers of birds [1], the *iridescence* of beetles' shells [2] and vivid colors demonstrated by some species of monkeys and opossums [3] (see Fig. 1). All these, and many other optical phenomena occur because, through evolution, Nature has equipped birds, butterflies, beetles and, somewhat surprisingly, certain mammals, with mechanisms to assemble subwavelength particles into complex, photonics structures.

Therefore, in an effort to understand and mimic Nature's inventions, scientists have been studying building blocks of such systems, and uncovered the fascinating properties of metallic and dielectric nanosystems that allow them to localize light [4–7], mold its flow [8–13] and tune its interaction with another toy of Nature, molecules [14–18]. Following their efforts, in the four chapters of this thesis we present four stepping stones, set up to facilitate our progress towards an understanding and control over light.

The first chapter of this thesis describes nanosystems designed to focus light through the excitations of *localized surface plasmon resonances* (LSPRs), a phenomenon in which the electric component of incident illumination induces coherent oscillations of conduction

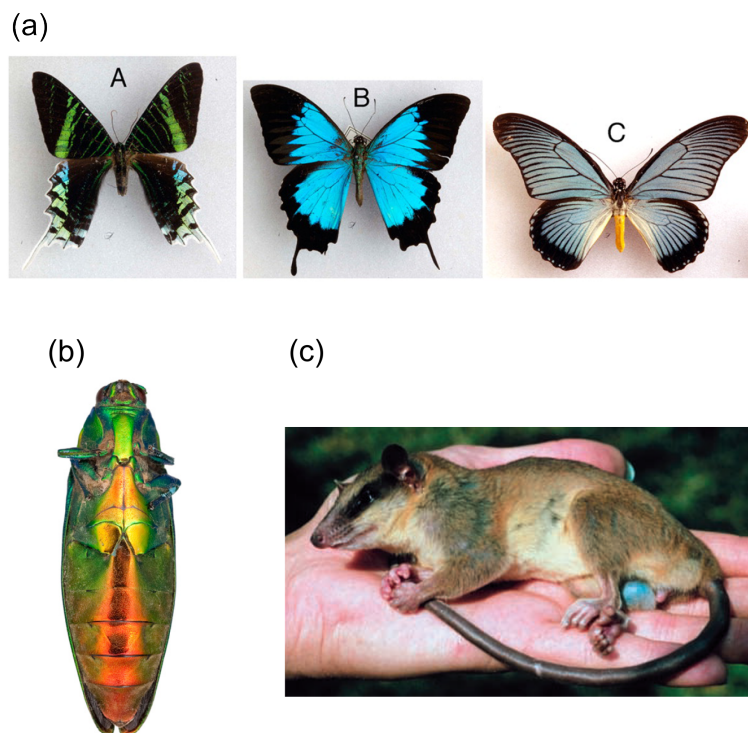


FIGURE 1: Structural coloration in the animal kingdom. (a) Photographs of butterfly species (adapted from Ref. [1]). (b) Abdominal plane of the body of a female Japanese jewel beetle *Chrysochroa fulgidissima* (adapted from Ref. [2]). (c) Male mouse opossum (*Marmosa robinsoni*) with blue scrotum (adapted from Ref. [3]). The bright colors and iridescence demonstrated by these animals is a result of a coherent scattering in photonic structures, rather than pigmentation.

electrons in the metal. Such systems have been extensively studied both through experimental and theoretical efforts, and found many applications as platforms for biosensing [19, 20], enhanced spectroscopies [5, 21–23], as well as opened avenues to interfacing electronic and photonic excitations [24, 25]. However, despite the significant progress in the understanding of their dynamics, metallic nanoparticles continue to deliver baffling results.

One example of such curious effects is the apparent inconsistency in the spectral positions and widths of resonant features found in measurements of the extinction, scattering and near-field spectra [26–29] of metallic nanoparticles. This peculiar effect has been partially addressed by modeling localized plasmons, resonant in the infra-red (IR) spectral regime as damped, driven harmonic oscillators [30–33]. However, this model unexpectedly fails to reproduce the shifts between the spectral characteristics of the flagship of localized plasmons, a small, subwavelength-sized gold nanoparticle resonant in the visible spectral range. As we discuss in Chapter 1 of this thesis, this shortcoming is caused by the onset

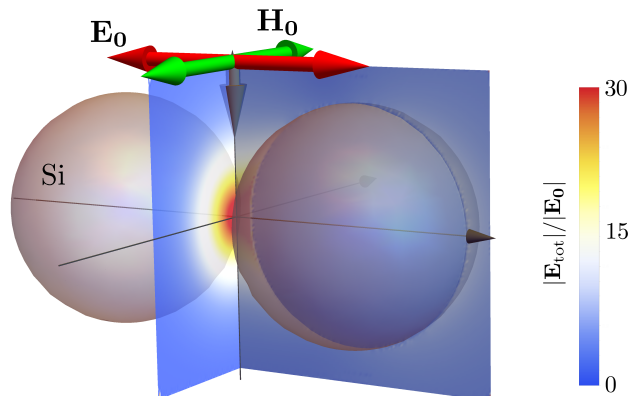


FIGURE 2: Localization and enhancement of the electric field, \mathbf{E}_0 , of an incident plane wave by a dimer of silver spheres of 35 nm radii.

of *interband transitions* in the metal, which hinder the purely *plasmonic* nature of gold particles.

We therefore construct an alternative model which can be successfully applied to metallic particles characterized by an arbitrary dielectric function, and develop it to demonstrate and explain the spectral shifts between resonances observed in the absorption and scattering cross sections, and in the spectra of the near-field intensity. This approach allows us to dissect and understand the role of interband transitions in the broadening and shifting of the optical response of metallic nanoparticles resonant in the visible spectral range.

Another interesting aspect of the optical response of metallic nanosystems is related to the dynamics of localized plasmons. Current models assume that, once excited, plasmons should exhibit exponentially decaying oscillations, with the rate of the decay related to the spectral width of the resonance. However, a more detailed study suggests that the decay of the plasmon might not be a simple exponential process [34]. We explore this possibility by analyzing numerically the dynamics of plasmon excitations and indeed find that the plasmons induced in small metallic nanoparticles exhibit a non-trivial dynamics due to their coupling to interband transitions. This prediction could be verified through experiments, as ultrashort laser pulses have been recently employed to investigate the dynamics of plasmons at femtosecond timescales.

Having explored the effects imposed by the lossy nature of the excitations in metallic nanoparticles, we look towards other materials which would not suffer from such limitations. As it turns out, systems comprising microscale resonators made up of high

refractive index dielectrics have been a centerpiece of experimental setups in the community of researchers realizing quantum-optical microsystems. This type of design has been recently proposed in the submicron regime by two publications from Aitzol García-Etxarri *et al.* [35] and Andrey Evlyukhin *et al.* [36], who hinted on the possibility of using submicron silicon spheres as antennas operating in the near-infrared regime. They found that such nanoantennas can efficiently scatter and localize light through the excitation of both electric and, somewhat surprisingly, magnetic dipolar modes (see Fig. 3). This last feature would stand out as a tremendous advantage of these lossless systems over the plasmonic ones, which require careful structuring to exhibit any magnetic activity [37–39].

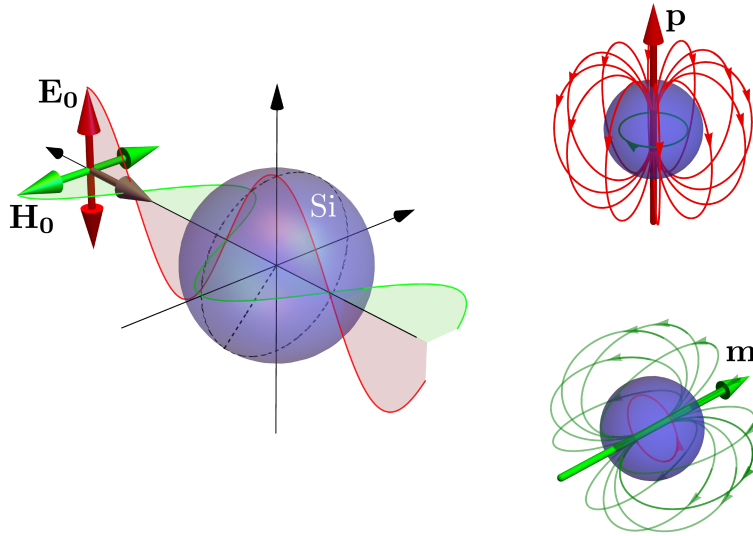


FIGURE 3: Scattering of light by a submicron silicon sphere. The electric (\mathbf{E}_0) and magnetic (\mathbf{H}_0) components of the incident planewave induce orthogonal electric (\mathbf{p}) and magnetic (\mathbf{m}) dipoles.

To explore the applications enabled by these new lossless systems, in Chapter 2 we employ dielectric nanoantennas as platforms for enhancing rates of spontaneous emission from electric and magnetic dipolar emitters. We show that such systems can match the performance of their plasmonic counterparts, efficiently coupling the emitters to purely radiative decay channels, thus retaining or even boosting their intrinsic quantum efficiency. Furthermore, taking advantage of the large spectral separation between the

dipolar and higher-order modes of the dielectric antennas, we propose a simplified description of the enhancement of the spontaneous emission rate by means of a model of interaction between the dipolar emitter and the dipolar excitation in the particle.

An extension of this dipole-dipole interaction model can be further applied to understand the response of a dielectric dimer structure, comprising two dielectric particles described as scatterers with arbitrary dipolar electric and magnetic polarizabilities. We discuss in detail how the dipolar modes of single spheres can hybridize, forming dimer modes which are then classified through symmetry considerations. Interestingly, the energies of these dimer modes are not governed exclusively by the interaction between homogeneous pairs of single-particle dipolar modes (electric-electric and magnetic-magnetic), but also by the interaction between heterogeneous pairs of dipoles (electric-magnetic). This analytical work is compared with numerical calculations which allowed us to account for the distortions of the shape and composition of the nanoparticles, and corroborated by the experiments on dimer structures performed at the *Laser Zentrum Hannover e.V.*

In the last section of Chapter 2 we analyze the performance of dielectric dimers as antennas for enhancing the emission from single dipolar electric and magnetic emitters placed in the gap of the dimer. We find that the modes of the dimer structure discussed above can provide a significant enhancement of the rate of spontaneous emission of dipolar emitters primarily through the coupling to radiation, while retaining high quantum efficiencies even in the presence of intrinsic losses in silicon. We therefore conclude that dielectric submicron systems can serve as viable and robust building blocks for alternative types of nanoscale antennas and metamaterials.

When deriving the expressions of the decay rate enhancement of dipolar emitters coupled to dielectric nanoparticles in Chapter 2, we apply a simple trick: we expand the electric field originated by an electric dipolar emitter into a series of vector spherical harmonics, and transform it, replacing the electric fields with magnetic fields and, simultaneously, the electric emitter with a magnetic emitter (see Appendix A for details). Such transformation is a special case of the general *duality transformation* which mixes the electric and magnetic components of the electromagnetic field propagating in a homogeneous medium. However, as we discuss in Chapter 3, this transformation can be also applied to electromagnetic fields in inhomogeneous media in two cases. The first, *macroscopic* case, requires the piecewise-homogeneous medium to exhibit an identical ratio of permittivity and permeability throughout the entire system. The second, *microscopic* case, applies to a random solution of *dual scatterers*, objects with identical electric and magnetic polarizabilities. We analyze the microscopic case in detail, and

demonstrate the validity of the duality transformation applied to a field propagating in a distribution of dual submicron silicon particles.

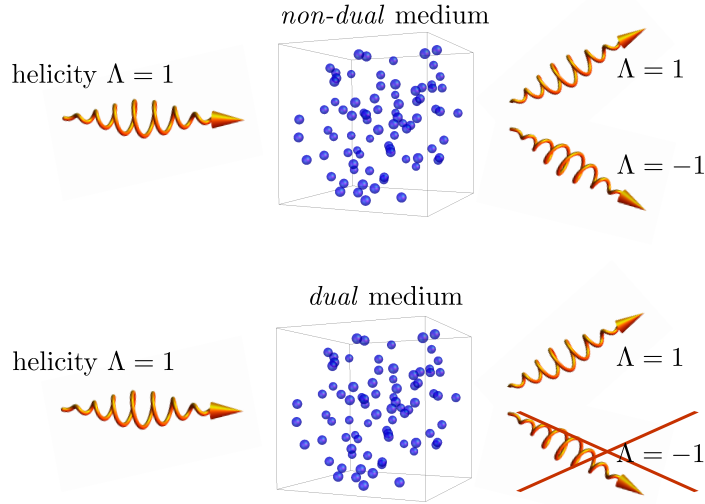


FIGURE 4: Helicity in scattering on random media. If the medium is *dual*, (i.e. a solution of *dual* nanoparticles with identical electric and magnetic polarizabilities), the helicity is conserved in the single- and multiple scattering.

We also note that the duality transformation can be formulated through its generator, an operator of *helicity*. Therefore, if a dual system is illuminated with light with a well-defined helicity (i.e. the incident field can be decomposed into a set of circularly polarized planewaves with identical handedness), then the scattered light will preserve its helicity and, consequently, the handedness of the circularly polarized planewaves making up the scattered field (see Fig. 4). This effect can be used as an additional tool for characterizing random media.

Finally, in Chapter 4 we consider the effect of an off-resonant Raman scattering from molecules placed in plasmonic cavities. This research is motivated by a recent surge of novel results and implementations of such experiments, enabled by a better understanding of the interaction between light and Raman-active molecules and the engineering of efficient substrates for *Surface Enhanced Raman Scattering* (SERS). Among the variety of reported results, some appear to escape the standard description based on the classical treatment of the electromagnetic enhancement of fields inside the cavity [40–42].

We present a more fundamental, quantum-mechanical model of the non-linear interaction between the quantized excitations of the plasmonic cavity, and the vibrational structure of the molecule (see Fig. 5). This approach readily describes effects which are not encompassed by the classical framework: (i) we observe the onset of a *phonon-stimulated*

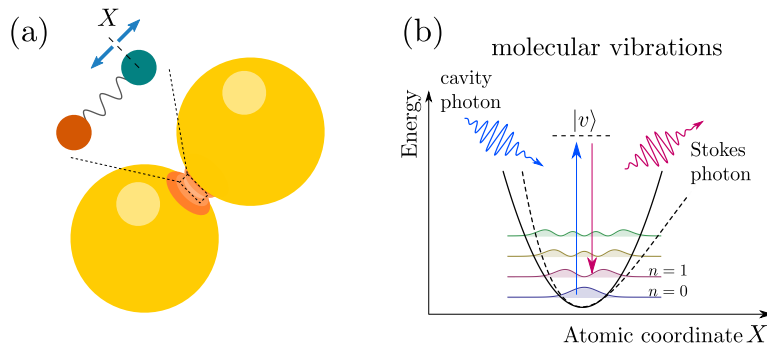


FIGURE 5: (a) Schematic of a plasmonic cavity formed by a dimer of gold nanoparticles, coupled to a molecule placed in the gap. (b) Schematic of the two-photon non-resonant Stokes scattering between two vibrational states of a molecule ($n = 0 \rightarrow 1$) mediated by a virtual state $|v\rangle$ (dotted line). In a one-dimensional model discussed here, molecule vibrates along an atomic coordinate X .

Raman scattering enabled by the large, incoherent populations of the quantized vibrations of the molecule; (ii) we find an unexpected dependence of the anti-Stokes scattering on the frequency of the incident laser and the local temperature.

From the experimental perspective, our prediction of the stimulated Raman scattering from single molecules in plasmonic cavities should be of vital importance, as it opens a new pathway to enhancing the intrinsically weak Stokes and anti-Stokes emission. While this effect, to our best knowledge, has not been clearly demonstrated, our results indicate that the experimental setups should be reaching the regime where such observations would be possible.

On the theoretical side, our exact formalism opens avenues to studying classical and quantum correlations of the photons emitted from the cavities. Furthermore, thanks to the formal equivalence of our interaction Hamiltonian to that used for treating quantum optomechanical systems, the theoretical scheme proposed takes the studies of such systems to a novel parameter regime of relatively strong couplings, observed previously only for cold atoms, and low thermal populations.

In summary, the following chapters of this thesis outline a set of optical phenomena which govern the response and efficiencies of plasmonic and dielectric nanoantennas. We investigate these systems as possible platforms for structuring and molding the flow of light on the nanoscale, as well as for enhancing its interactions with molecules. Predicted novel effects, such as the non-exponential decay of plasmons, formation of heterogeneous modes in dielectric dimers, conservation of the helicity of light scattered in dual media, or the onset of phonon-stimulated Raman scattering, should find applications in various

Introduction

nanophotonic systems, and open avenues to the enhanced control over light on the subwavelength scale.

Chapter 1

Revisiting spectral properties of plasmonic nanoparticles with strong interband contribution

“The horse was willing and allowed the man to place bridle and saddle upon him. The man mounted hunted down the wolf and killed him. The horse joyful and relieved thanked the man and said ‘Now that our enemy is dead, remove the bridle and saddle and restore my freedom.’ Whereupon the man laughed loudly and replied ‘The hell you say giddy-up Dobbin’ and applied the spurs with a will.”

– Isaac Asimov, *Foundation*

A magnifying glass could easily be considered as one of the most fascinating devices human kind has even invented. In the hands of a curious child it visibly *increases* the sizes of investigated objects, making beetles grow tremendously, or *shrinks* them, instantaneously moving insects beyond the hand’s reach. It can also darken paper, burn skin on a sunny day or redirect light at a command. It appears that with just the right magnifying glass, one could concentrate all the incoming light in an infinitely small spot.

And yet, as we learn in school, that dream can never be realized, no matter how big the lens, or the *aperture* of our magnifying glass is. This daunting result, formally known as the *diffraction limit*, forbids us from focusing light on scales smaller than its wavelength λ or, by reciprocity, discerning features smaller than λ .

Over the years and through some ingenuitive approaches, scientists have developed a vast arsenal of tools that would help us to beat this limit, or at least to circumvent it. Probably the most representative and timely examples of the latter approach are Stimulated Emission Depletion (STED) [43] and Photoactivated Localization Microscopy (PALM) [44].

Another path, that can be interpreted as an actual conquering of the diffraction limit, stems from the remarkable ability of an object smaller than the wavelength of incident light to act like an antenna, and transfer the energy and the information between the propagating radiation and its immediate surroundings. Systems based on this principle of operation are limited by the size of the *nanoantennas*, rather than the wavelength of light, and can achieve resolutions which beat the diffraction limit in a spectacular manner [45].

A particularly interesting implementation of this idea is found in metallic nanoparticles, in which the electric component of the incident illumination can induce coherent oscillations of the free electron gas at the surface of the particles. Such excitations, dubbed as *localized plasmons*, have been recognized as a versatile and tunable tool for engineering of scattering and localization of light [4, 45, 46], enhancing its interaction with matter [16, 47, 48], and opening avenues to new field-enhanced spectroscopies [33, 42, 49, 50]. However, despite an extensive theoretical effort, the exact *dynamics* of the decay of localized plasmons, which determines their lifetimes and their spectral linewidths, remains unclear.

In this chapter we attempt to contribute to the discussion of these fundamental properties of plasmons. In order to avoid framing it exclusively in phenomenological terms, we derive an analytical model of the optical response of a metallic nanoparticle, and analyze its consequences in detail. To do this, we first briefly review the material properties of metals and formally introduce the concept of *plasmon resonance*. We then proceed to derive and analyze our model of the polarizability of a non-spherical nanoparticle and discuss its predictions.

1.1 Macroscopic description of metals

In a first approximation, academic text-books [51–53] on solid state physics characterize *metal* as a material with the optical, electrical and thermal properties determined by the high density of conduction electrons¹, which form the so-called *free-electron gas*. To the community of optical physicists, the crucial elements of this picture are encapsulated by the *Drude-Sommerfeld model*, which states that the dielectric function of the metal ε_D is characterized by the density of conduction electrons n , their charge e and effective mass m_e through a simple relationship

$$\varepsilon_D(\omega) = 1 - \frac{\omega_p^2}{\omega^2 + i\gamma_p\omega}, \quad (1.1)$$

where γ_p describes the damping term proportional to the rate of electron collisions. In SI units, used throughout this thesis, the *plasma frequency* ω_p is given by

$$\omega_p = \sqrt{\frac{ne^2}{m_e\varepsilon_0}}, \quad (1.2)$$

where ε_0 is the permittivity of vacuum. The real and imaginary parts of the dielectric function can be separated by rewriting ε_D as

$$\varepsilon_D(\omega) = 1 - \frac{\omega_p^2}{\omega^2 + \gamma_p^2} + i\frac{\gamma_p\omega_p^2}{\omega(\omega^2 + \gamma_p^2)}. \quad (1.3)$$

We can thus expect that for the small collision rate, $\gamma_p \ll \omega$, the material behaves as a good metal with predominantly real and negative $\varepsilon_D(\omega)$ for $\omega < \omega_p$. Before we analyze the two typical choices for *plasmonic* systems, we briefly discuss two major corrections to the Drude-Sommerfeld model.

Interband transitions

Let us step away for a moment from the classical model of free electrons oscillating in the harmonic field of the incident light, and consider the effect of the excitation of a bound electron to the conduction band due to the absorption of an incident photon. Naturally, this process is only triggered if the photon carries sufficient energy. This phenomenon can be analyzed by considering a damped, driven oscillations of an electron in a harmonic

¹That is not true for astronomers who inexplicably define as metal any element different from hydrogen or helium.

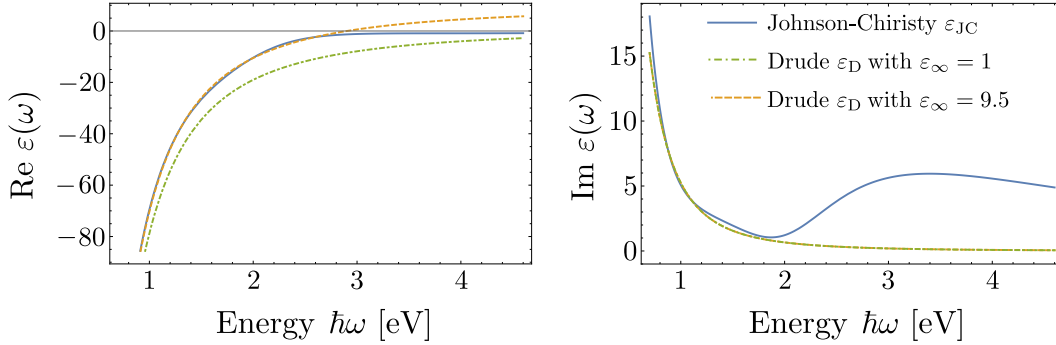


FIGURE 1.1: Real (left panel) and imaginary (right panel) part of the dielectric functions of gold obtained by fitting the experimental tabulated data, ε_{sca} , from Johnson and Christy [54, 55] (blue solid line), by considering a perfect Drude-Sommerfeld model, ε_D , with $\varepsilon_\infty = 1$ (dot-dashed green lines) and assuming a realistic Drude-Sommerfeld model ε_D with $\varepsilon_\infty = 9.5$ (dashed red lines).

potential [56], allowing us to introduce interband transitions (ITs) as corrections to the Drude-Sommerfeld dielectric function in the form of narrow Lorentzian profiles.

Background permittivity

If we consider a metal in which ITs occur at frequencies much higher than the region of interest, they will simply yield an almost-constant, real and positive contribution to the dielectric function. We can therefore expect that in the spectral regimes far from any interband transitions, the dielectric function ε will be given by the Drude-Sommerfeld model with a real offset, which we will be referring to as the *background permittivity* ε_∞ :

$$\varepsilon_D(\omega; \varepsilon_\infty) = \varepsilon_\infty - \frac{\omega_p^2}{\omega^2 + i\gamma_p\omega}, \quad (1.4)$$

Naturally, for the *ideal* Drude material, we have $\varepsilon_\infty = 1$.

In this chapter we will be focusing our attention on one of the most commonly used plasmonic materials - gold - and we will attempt to identify the optical properties of gold nanoparticles which arise due to the deviation of this material from the free-electron gas model. In Fig. 1.1 we compare the response of a free electron gas characterized by a plasma frequency $\omega_p = 2.15 \times 10^{15}$ Hz (using the reduced Planck constant \hbar we can write $\hbar\omega_p = 8.89$ eV) and collision rate $\gamma_p = 16 \times 10^{12}$ Hz ($\hbar\gamma_p = 0.066$ eV), with the experimental data for gold provided by Johnson and Christy [54] (ε_{sca} , solid blue line) and fitted to a series of analytical functions by Hao *et al.* [55]. Within the Drude-Sommerfeld model of the dielectric permittivity ε_D we consider two values of the background permittivity: $\varepsilon_\infty = 1$ (dot-dashed green lines), and $\varepsilon_\infty = 9.5$ (dashed red

lines). The latter parameter is fitted to provide the best match of the Drude-Sommerfeld model to the experimental data. While this approach yields very good fit for energies below 2 eV, it also allows us to dissect the contribution from the interband transitions which dominate the dielectric function for energies above approximately 2 eV.

1.1.1 Surface Plasmon Polaritons

Our motivation for paying so much attention to the Drude-Sommerfeld model of the dielectric function and the deviations from it in the case of gold, is that the conduction electrons in metal are one of the building blocks of a central concept in nano-optics, *surface plasmons polaritons* (SPPs) [57–61]. As the name suggests, SPPs are collective oscillations of the surface charge density coupled to electromagnetic waves.

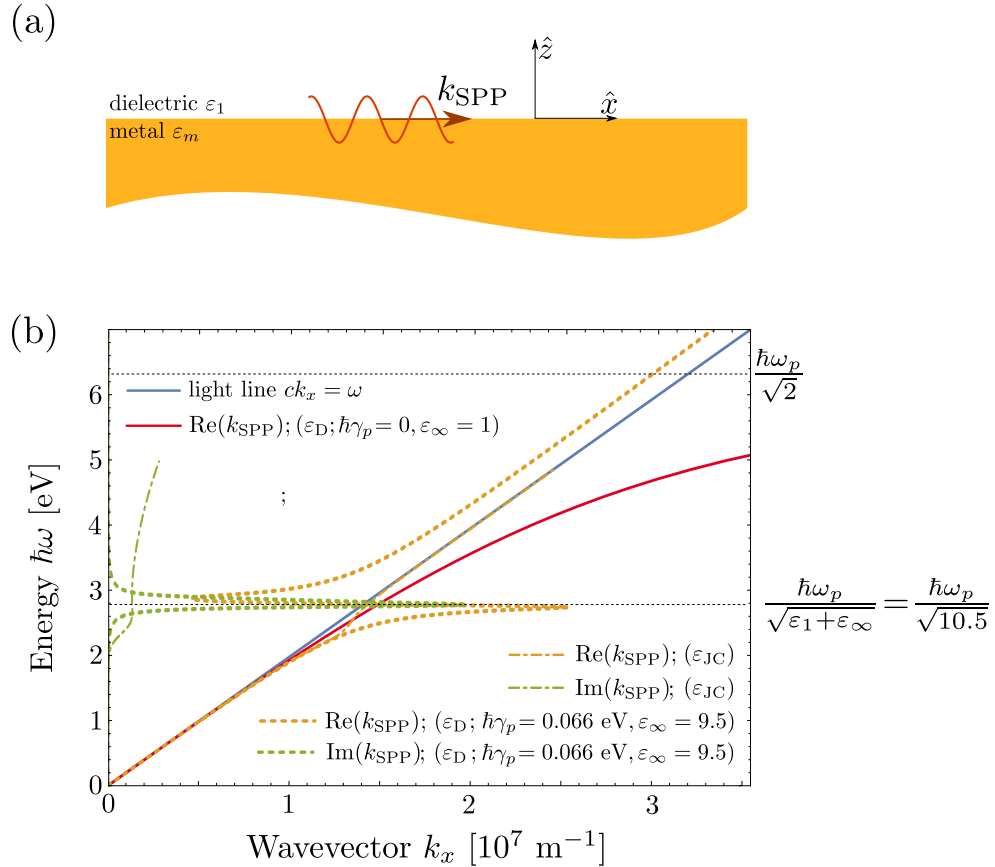


FIGURE 1.2: (a) Schematic for the analysis of dispersion relation of SPPs. (b) Dispersion relations of the SPPs propagating along the air-gold interface calculated with various dielectric functions derived with the Drude-Sommerfeld model (ϵ_D with parameters given in the legend) and with the literature data (ϵ_{sca} , Ref. [54]). $\text{Re}(k_{\text{SPP}})$ and $\text{Im}(k_{\text{SPP}})$ denote the real and imaginary components of the SPP wavevector.

More formally, SPPs are solutions of the Maxwell's equations derived in the absence of external excitation, and confined to the metal-dielectric interface. To get a firm, mathematical grasp on the properties of SPPs, let us consider the *Fresnel reflection coefficients* for an electromagnetic monochromatic planewave propagating in a dielectric (characterized by a dielectric function ε_1), impinging on the surface of a metal (ε_m) spanning the $\hat{x}\hat{y}$ plane, as shown schematically in Fig. 1.2(a). Let us assume that both the wavevector of this planewave $\mathbf{k}^{(1)}$ and the polarization of the electric field lie in the $\hat{x}\hat{z}$ plane. The Fresnel reflection coefficient of the p-polarized planewave, r_p , can be then derived as

$$r_p = \frac{\varepsilon_m k_z^{(1)} - \varepsilon_1 k_z^{(2)}}{\varepsilon_m k_z^{(1)} + \varepsilon_1 k_z^{(2)}}, \quad (1.5)$$

where $k_z^{(i)}$ is the z component of the wavevector (perpendicular to the interface) in the dielectric ($i = 1$) or metal ($i = 2$). Subscript p denotes the p (or TM) polarization of the incident field. Using the dispersion relation of the wavevector

$$\left(k_x^{(i)}\right)^2 + \left(k_z^{(i)}\right)^2 = \left(\frac{\omega}{c}\right)^2 \varepsilon_i, \quad (1.6)$$

where c is the speed of light in vacuum and ω is the frequency of the monochromatic incident light, we can find that the reflection coefficient has a pole defined by the in-plane component of the wavevector

$$k_x^{(1)} = k_x^{(2)} \equiv k_{\text{SPP}} = \frac{\omega}{c} \sqrt{\frac{\varepsilon_1 \varepsilon_m}{\varepsilon_1 + \varepsilon_m}}. \quad (1.7)$$

For future reference, we can also write down the expressions for the normal (z) components of the wavevectors:

$$k_z^{(1)} = \frac{\omega}{c} \sqrt{\frac{\varepsilon_1^2}{\varepsilon_1 + \varepsilon_m}}, \quad k_z^{(2)} = \frac{\omega}{c} \sqrt{\frac{\varepsilon_m^2}{\varepsilon_1 + \varepsilon_m}}. \quad (1.8)$$

Let us for a moment assume that the dielectric function of the metal is purely real. Then, for the k_{SPP} to describe the non-decaying electromagnetic modes propagating along the surface, k_{SPP} has to be real, imposing the following conditions:

$$\varepsilon_1 \varepsilon_m < 0, \quad \varepsilon_1 + \varepsilon_m < 0, \quad (1.9a)$$

or

$$\varepsilon_1 \varepsilon_m > 0, \quad \varepsilon_1 + \varepsilon_m > 0. \quad (1.9b)$$

We can winnow through these two cases by imposing yet another condition for the SPPs:

they should be confined to the interface. In mathematical terms, this requirement calls for a non-zero imaginary component of wavevectors $k_z^{(1)}$ and $k_z^{(2)}$ defined in Eq. (1.8), a condition only fulfilled if the sum of the dielectric functions is negative. We thus discard the case presented in Eq. (1.9b) and consider the inequalities in Eq. (1.9a) as the conditions for the presence of SPP modes.

It can be further shown that in the presence of weak losses in the metal (that is, the dielectric function $\varepsilon_m = \varepsilon'_m + i\varepsilon''_m$ follows $|\varepsilon''_m| \ll |\varepsilon'_m|$) the complex wavevector k_{SPP} is approximately given by

$$k_{\text{SPP}} = \frac{\omega}{c} \sqrt{\frac{\varepsilon_1 \varepsilon_m}{\varepsilon_1 + \varepsilon_m}} \approx \frac{\omega}{c} \sqrt{\frac{\varepsilon_1 \varepsilon'_m}{\varepsilon_1 + \varepsilon'_m}} \left(1 + i \frac{\varepsilon_1 \varepsilon''_m}{2\varepsilon'_m (\varepsilon_1 + \varepsilon'_m)} \right). \quad (1.10)$$

For a metal described by the Drude-Sommerfeld model introduced earlier and characterized by small intrinsic losses, the pole of k_{SPP} can thus be found at the *surface plasma frequency*

$$\omega_{\text{SPP}} \approx \frac{\omega_p}{\sqrt{\varepsilon_1 + \varepsilon_\infty}}. \quad (1.11)$$

This feature is illustrated in Fig. 1.2(b), where we plot the dispersion relation of the SPPs (Eq. (1.7)) induced at the interface between air ($\varepsilon_1 = 1$) and gold, calculated using different models of the dielectric function of gold. The simplest dispersion, marked with the solid red line, can be found for the lossless Drude-Sommerfeld model ε_D , with background permittivity $\varepsilon_\infty = 1$ and plasma frequency $\omega_p = 2.15 \times 10^{15}$ Hz. In the small k_x wavevector limit the dispersion asymptotically converges to the *light line* (blue line), which describes the dispersion relation of light propagating in air, with the wavevector parallel to the interface. On the other hand, for large wavevectors, the SPPs asymptotically converge to ω_{SPP} ($\hbar\omega_{\text{SPP}} = \hbar\omega_p/\sqrt{2} \approx 6.3$ eV in this model). The fact that the dispersion of SPPs does not cross with the light line (and lies outside of the light cone defined as $ck_x < \omega$) implies that the SPPs cannot couple to free radiation in air, that is, neither do they radiatively decay, nor can they be excited by the incident planewave illumination. Various techniques have been proposed to circumvent this limitation, for example relying on breaking the translational invariance of the interface by introducing local scatterers or gratings on the surface [62, 63].

The dashed lines in Fig. 1.2(b) correspond to the more realistic Drude-Sommerfeld model for gold with $\gamma_p = 16 \times 10^{12}$ Hz (or $\hbar\gamma_p = 0.066$ eV) and $\varepsilon_\infty = 9.5$. Both the real and imaginary components of k_{SPP} (depicted with orange and green dashed lines, respectively) exhibit the resonant behavior for the frequency ω_{SPP} defined in Eq. (1.11)

($\hbar\omega_{\text{SPP}} = \hbar\omega_p/\sqrt{10.5} \approx 2.8$ eV in this model). Interestingly, the dispersion depicted with the orange dashed line appears to have two branches, one laying outside of the light cone, denoting the SPPs and bounded in energy by the surface plasmon frequency, and a high-energy one, found inside the light cone. The latter branch describes the bulk plasmons (although we should keep in mind that, as can be easily shown from Eq. (1.1) and the following discussion, for $\omega > \omega_p/\sqrt{\varepsilon_\infty}$ the dielectric function becomes predominantly real and positive and the plasmonic nature of the excitations is lost).

Finally, with the dot-dashed lines we denote the SPP dispersion calculated with the use of the dielectric function from the literature [54] which accounts for interband transitions and thus yields a significantly broader spectrum of the imaginary part of k_{SPP} ($\text{Im}(k_{\text{SPP}})$). This difference between the Drude-Sommerfeld model and the realistic dielectric function, which for gold becomes striking in the most interesting spectral region near the surface plasmon frequency, will be the focus of this chapter.

1.1.2 Localized Surface Plasmons

The coupling between the electromagnetic field and the collective oscillations of the electron gas can be of course induced also in finite systems, which do not exhibit translational invariance. The first example of such *localized surface plasmon resonances* (LSPRs), is provided by considering the scattering of light by a small metallic sphere of radius a and the dielectric function ε_m , embedded in a homogeneous dielectric medium (ε_1) and illuminated by a monochromatic planewave with frequency ω and wavenumber $k = \omega/c\sqrt{\varepsilon_1}$. Similarly as in the previous section, we will indirectly investigate the onset of LSPRs by identifying resonant features in the mathematical formulas governing their scattering and absorption properties. In this case, we consider the respective cross-sections of the sphere which, in the *quasi-static limit* (denoted by superscript qs), $ka \ll 1$, are given by

$$\sigma_{\text{sca}}^{\text{qs}}(\omega) = \frac{k^4}{6\pi} |\alpha^{\text{qs}}(\omega)|^2, \quad (1.12a)$$

$$\sigma_{\text{abs}}^{\text{qs}}(\omega) = k \text{Im}[\alpha^{\text{qs}}(\omega)]. \quad (1.12b)$$

The *dipolar polarizability* of the sphere α^{qs} is defined as

$$\alpha^{\text{qs}}(\omega) = 4\pi a^3 \frac{\varepsilon_m(\omega) - \varepsilon_1}{\varepsilon_m(\omega) + 2\varepsilon_1}. \quad (1.13)$$

The usual definition of the LSPR frequency is based on the *Rayleigh condition* for the pole of α^{qs}

$$\text{Re}[\varepsilon_m(\omega)] + 2\varepsilon_1 = 0, \quad (1.14)$$

In the most elementary case of the Drude-Sommerfeld sphere with low losses and $\varepsilon_\infty = 1$, in air, we arrive at the trivial solution for the dipolar resonance frequency

$$\omega_{\text{LSPR}} = \frac{\omega_p}{\sqrt{3}}. \quad (1.15)$$

As we increase the background permittivity or the permittivity of the medium, this frequency will red-shift according to

$$\omega_{\text{LSPR}} = \frac{\omega_p}{\sqrt{2\varepsilon_1 + \varepsilon_\infty}}. \quad (1.16)$$

The polarizability of the sphere governs the amplitude and the phase of the oscillating dipole \mathbf{p} of the polarized particle, induced by the electric field of the incident illumination \mathbf{E}_0 ,

$$\mathbf{p} = \varepsilon_0 \varepsilon_1 \alpha^{\text{qs}} \mathbf{E}_0. \quad (1.17)$$

This dipole, associated with the oscillations of the electrons inside the entire volume of the metal, can thus trigger an oscillating concentration of electrons at the boundaries of the particle, and induce a significant enhancement of the electric field near its surface.

Examples of metallic nanostructures, such as a sphere, a dimer and an ellipsoid are shown in Fig. 1.3, with their corresponding scattering and absorption spectra, calculated using Lumerical FDTD software [83], and the distributions of electric fields at resonance wavelengths. The three selected systems are a typical choice for plasmonic nanoantennas, with numerous applications spanning from enhancing the incident field for field-enhanced spectroscopies [21, 64], through sensing of changes in the dielectric response of the medium, [65–67] to optical trapping and manipulation of other nanoscale objects [68, 69]. However, despite the extensive effort devoted to the study of these structures, only for the first of the listed shapes an analytical model which would describe exactly the optical response, has been proposed by Gustav Mie [70] (see Appendix A for a discussion of the *Mie theory*). In the following section of this chapter, we discuss an approximated model developed to describe the response of ellipsoidal particles. Furthermore, in Chapter 2 we discuss the dipole-dipole approach for the analysis of dielectric dimer structures.

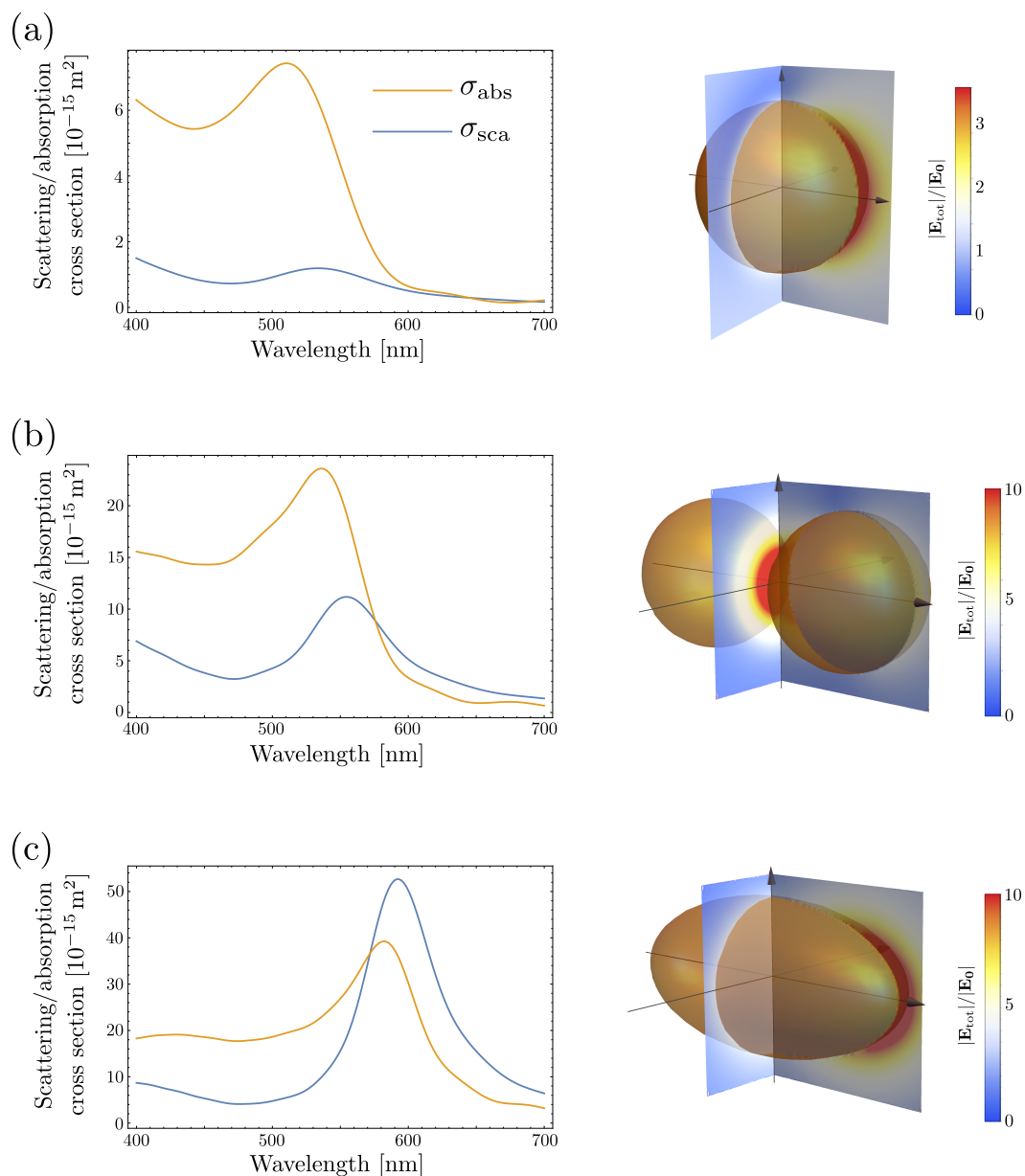


FIGURE 1.3: Scattering and absorption spectra (left) and distributions of the electric fields (right) at the resonant wavelengths calculated for three plasmonic gold nanosystems in vacuum: (a) a single sphere, (b) a dimer, (c) an ellipsoid. Radius of the spheres, as well as the minor radius of the ellipsoid, is set to 35 nm, and the major radius of the ellipsoid is 70 nm. The systems are illuminated with light polarized parallel to their long symmetry axis. Calculations were performed using the *Finite Difference Time Domain* (FDTD) method implemented in the Lumerical FDTD software [83], using literature data on dielectric function of gold [54].

1.2 Models of polarizability

As we have mentioned above, we attempt to find a model for the dipolar polarizability of a non-spherical plasmonic scatterer, which considers all the aspects of the complex interband structure in the radiative and nonradiative optical response. We will begin by introducing the model in which plasmonic excitation in an arbitrarily shaped, small metallic nanoparticle is described as a damped, driven harmonic oscillator, and discuss its limitations. Afterwards, we will turn our attention to another approach, which also describes the polarizability of ellipsoidal nanoparticles but, unlike the previous model, does not require an extensive fitting of the parameters of the model.

1.2.1 Plasmon as a damped harmonic oscillator

In the contributions by Chen *et al.* [30] and Zuloaga *et al.* [31], the authors consider localized plasmons as driven damped harmonic oscillators (HOs) and relate the amplitude of their oscillations to the frequency-dependent polarizability of a particle. The harmonic oscillator, a workhorse of classical and, as we will discuss later, quantum physics, has been successfully applied to model the hybridization in plasmonic nanosystems [71, 72], exciton-plasmon coupling [73, 74] and numerous other effects related to plasmonic excitations [32, 75, 76]. On the other hand, descriptions based on HO formalism often serve merely as toy-models, since they require extensive *a posteriori* fitting of parameters to describe experimental situations, and are therefore rarely seen as a proper tool to make quantitative predictions. Below we derive a model based on HO which demonstrates both of these characteristics.

Let us first follow the concept coined in Refs. [30, 31] and consider a driven, one-dimensional, damped harmonic oscillator whose dynamics is governed by the simple equation for the displacement $x(t)$

$$m \frac{d^2}{dt^2} x(t) = -kx(t) - m\Gamma_{NR} \frac{d}{dt} x(t) + F_0 e^{i\omega t}. \quad (1.18)$$

The HO is characterized by its mass m , *spring constant* $k = \omega_0^2 m$ related to the *natural frequency* of the oscillator ω_0 , an abstract *damping parameter* Γ_{NR} and the external harmonic force $F_0 e^{i\omega t}$ oscillating at generic frequency ω . We should note that in this

simplest model both the damping parameter and the spring constant are frequency-independent. The usual ansatz

$$x(t) = D(\omega)e^{i\omega t}, \quad (1.19)$$

leads to the explicit expression for the response function $D(\omega)$

$$D(\omega) = \frac{F_0}{m} \frac{1}{\omega^2 - \omega_0^2 + i\Gamma_{NR}\omega}. \quad (1.20)$$

It can be easily shown that the amplitude of the oscillations given by $|D(\omega)|^2$ peaks at a frequency lower, ω_{amp} , than ω_0

$$\omega_{\text{amp}} = \sqrt{\omega_0^2 - \frac{\Gamma_{NR}^2}{2}}, \quad (1.21)$$

which converges to ω_0 for the vanishing damping parameter Γ_{NR} . In fact, in the regime of very narrow resonances ($\Gamma_{NR} \ll \omega_0$), we can approximate the response function $D(\omega)$ around the resonance ω_0 by a Lorentzian profile, $D_{\text{Lor}}(\omega)$, as

$$D(\omega) \approx D_{\text{Lor}}(\omega) = \frac{F_0}{2m\omega_0} \frac{1}{\omega - \omega_0 + i\Gamma_{NR}/2}. \quad (1.22)$$

The time-averaged power absorbed by the oscillator, $P(\omega)$, can be calculated as the real part of the product of the first time derivative of the oscillator's displacement and the complex conjugate of the applied force, leading to

$$P(\omega) = m\Gamma_{NR}\omega^2 |D(\omega)|^2. \quad (1.23)$$

The *friction* term proportional to $\Gamma_{NR}dx/dt$, which we have introduced in the dynamics equation of the harmonic oscillator (Eq. (1.18)), was meant to describe the *internal damping* (Kats *et al.* [32]), *intrinsic and radiative damping* (Zuloaga *et al.* [31]) or simply *damping* (Chen *et al.* [30]). We propose a more accurate description of this term in the later part of this chapter, and for the purposes of this section, simply refer to it, and to the dissipation introduced by it as *non-radiative damping* or *absorption*. To reflect this interpretation, from here on we replace coefficient Γ_{NR} with Γ_A .

1.2.1.1 Radiation reaction

While for small and lossy metallic particles the absorption is the dominant channel of energy dissipation, the optical response of larger particles is partially determined by the radiative dissipation channel. We can include this effect into the presented HO model by adding an *Abraham-Lorentz* term [77, 78] as the force F_R

$$F_R(t) = \frac{q^2}{6\pi\epsilon_1\epsilon_0c^3} \frac{d^3}{dt^3}x(t) = \Gamma_R \frac{d^3}{dt^3}x(t) \quad (1.24)$$

to the right-hand side of Eq. (1.18). Note that here we have introduced the charge q , since we need to specify that the energy loss is related to the oscillations of q . Following the prescription used earlier, we can solve the new dynamical equation and arrive at the modified response function

$$D(\omega) = \frac{F_0}{m} \frac{1}{\omega^2 - \omega_0^2 + i(\Gamma_A\omega + \Gamma_R\omega^3)}. \quad (1.25)$$

If we now return to the physical picture of the dipole $p(\omega) = qx(\omega)$ induced in a small metallic particle illuminated by the electric component E_0 of the incident light (so that $F_0 = qE_0$), we obtain from Eqs. (1.19) and (1.25)

$$p(\omega) = \frac{q^2}{m} \frac{1}{\omega^2 - \omega_0^2 + i(\Gamma_A\omega + \Gamma_R\omega^3)} E_0 = \epsilon_0\epsilon_1\alpha^{\text{HO}}(\omega)E_0, \quad (1.26)$$

where we have introduced the *polarizability* of the particle α^{HO} . We can thus interpret the amplitude function $|D(\omega)|^2$ as the *strength* of the dipole, which is a real function governing the intensity of the electric near-field of the dipolar mode of the particle.

The approximated spectral position of the peak of this new amplitude $|D|^2$, which we label as $\omega_\alpha^{\text{HO}}$, in the limit of narrow profile (where $\Gamma_R\omega^3 \approx \Gamma_R\omega\omega_0^2$), is given as

$$\omega_\alpha^{\text{HO}} \approx \omega_0 \sqrt{1 - \frac{(\Gamma_A + \omega_0^2\Gamma_R)^2}{2\omega_0^2}}. \quad (1.27)$$

Having differentiated between the absorption and scattering decay channels, we can write the expression for the power dissipation, split into the absorption, P_A , and scattering, P_R powers

$$P_A(\omega) = m\Gamma_A\omega^2|D(\omega)|^2, \quad (1.28a)$$

$$P_R(\omega) = m\Gamma_R\omega^4|D(\omega)|^2, \quad (1.28b)$$

and derive simple approximations to the spectral positions of the peaks of these functions:

$$\omega_A \approx \omega_0, \quad \omega_R \approx \omega_0 \sqrt{\frac{1}{1 - \frac{(\Gamma_A + \omega_0^2 \Gamma_R)^2}{2\omega_0^2}}} \approx \omega_0 \left[1 + \left(\frac{\Gamma_A + \omega_0^2 \Gamma_R}{2\omega_0} \right)^2 \right]. \quad (1.29)$$

We can therefore predict, using relationships listed in Eqs. (1.27) and (1.29) that if the optical response of a plasmonic particle can be described by the HO model with a friction term as in Eq. (1.18), and the radiation correction expressed through the Lorentz-Abraham force (Eq. (1.24)), then the frequencies of the spectral peaks of the amplitude function $|D|^2$ ($\omega_\alpha^{\text{HO}}$), the absorbed power P_A (ω_A) and the scattered power P_R (ω_R) follow the inequalities

$$\omega_\alpha^{\text{HO}} < \omega_A < \omega_R. \quad (1.30)$$

In previously mentioned references, Kats *et al.* [32], Zuloaga *et al.* [31] and Chen *et al.* [30] listed a number of antennas which follow Eq. (1.30). An experimental illustration of these properties was also provided by Alonso-Gonzalez *et al.* [33]. We should however note that the last three reports only considered the shift between the extinction and the amplitude peaks. Consequently, Ref. [32] is possibly the clearest theoretical demonstration of the inequality given in Eq. (1.30), illustrated by the calculations of the optical response of gold nanowires resonant in the IR regime (4 – 10 μm). Importantly, the authors also point out that this model should break down in the visible range. We will pick up this issue later in this chapter to unveil the influence of the band structure on the spectral response of nanoparticles.

1.2.2 Dynamic depolarization

We can wonder whether one could easily improve this simple HO model. The most striking shortcoming of this description is the fact that so many of the parameters: ω_0 , Γ_A and Γ_R (or q) need to be fitted, or otherwise estimated. Luckily, we can find a less ambiguous description proposed in a seminal contribution by Meier and Wokaun [79]. For a detailed summary of this work and the following contributions, we direct the reader to the report by Moroz [80].

Meier and Wokaun in a very short, but tremendously insightful paper, “*Enhanced fields on large metal particles: dynamic depolarization*”, introduced the concept of the *depolarizing field*, \mathbf{E}_{dep} , which, together with the electric field \mathbf{E}_0 of incident light, induces a polarization in the metallic particle

$$\mathbf{P} = \varepsilon_0(\varepsilon - 1)(\mathbf{E}_0 + \mathbf{E}_{\text{dep}}). \quad (1.31)$$

The depolarizing field $\mathbf{E}_{\text{dep}}(\mathbf{r})$ at position \mathbf{r} is calculated by assigning a dipolar moment $d\mathbf{p}(\mathbf{r}')$ to each volume element dV , and integrating the electric field produced by dipoles $d\mathbf{p}(\mathbf{r}')$ at position \mathbf{r} , expressed through the Green’s function $\overset{\leftrightarrow}{\mathbf{G}}_E(\mathbf{r}' - \mathbf{r})$ (see Eq. (2.12) for a definition and the discussion of the Green’s functions) [78]. A similar idea lies at the center of the discrete dipole approximation (DDA) [77, 81]. However, unlike in the DDA, we avoid the cumbersome self-consistent calculations of the dipolar moments $d\mathbf{p}(\mathbf{r})$ by assuming that the polarization \mathbf{P} is homogeneous throughout the volume V of the particle (arriving at $d\mathbf{p}(\mathbf{r}) = \mathbf{P}dV(\mathbf{r})$), and we calculate the depolarization field induced by the polarization \mathbf{P} only at the geometric center of the particle. For the incident harmonic illumination polarized along the \hat{z} axis we use the definition of the zz component of the Green’s function in spherical coordinates,

$$\left[\overset{\leftrightarrow}{\mathbf{G}}_E(\mathbf{r}' - \mathbf{r})\right]_{zz} = \frac{e^{ikr}}{4\pi r} \left[\left(1 + \frac{ikr - 1}{k^2 r^2}\right) + \frac{3 - 3ikr - k^2 r^2}{k^2 r^2} \cos^2 \theta \right] \quad (1.32)$$

with the coordinate origin at the center of the particle, and θ and r denoting the azimuthal and radial coordinates, respectively [56]. By expanding the exponential e^{ikr} up to the k^3 order, we arrive at the following expression for the z component of the depolarizing field, $E_{\text{dep},z}$, at the center of the sphere, related to the z component of the integrated polarization $P_z dV(\mathbf{r})$

$$E_{\text{dep},z}(\mathbf{r}) = \frac{1}{4\pi\varepsilon_0} \int_V \left[\frac{1}{r^3}(3\cos^2\theta - 1) + \frac{k^2}{2r}(\cos^2\theta + 1) + i\frac{2}{3}k^3 \right] P_z dV(\mathbf{r}). \quad (1.33)$$

This expression was first derived by Meier and Wokaun in Ref. [79], and the resulting model was later dubbed as Meier-Wokaun Long Wavelength Approximation (MWLWA) [80].

In Eq. (1.33) we can thus clearly identify the contributions from the near-, intermediate- and far-field components of the Green’s functions, which will give rise to:

- *Geometric static depolarization factor L .*

- *Geometric dynamics depolarization factor* D .
- Radiation reaction term proportional to the total induced dipole.

These three terms can be conveyed as:

$$E_{\text{dep},z} = -4\pi \left(L - \frac{k^2 V}{4\pi} D + i \frac{k^3 V}{6\pi} \right) \frac{P_z}{\varepsilon_0}. \quad (1.34)$$

Let us for example consider a sphere of radius a . In the spherical coordinates the integral $\int_V dV$ is transformed into $2\pi \int_0^a \int_0^\pi r^2 \sin \theta \, dr \, d\theta$, and the integration of the second and the third terms in Eq. (1.33) is straightforward. However, certain care needs to be taken when calculating the static depolarization factor [80]. With that in mind, we arrive at

$$L_{\text{sphere}} = \frac{1}{3}, \quad D_{\text{sphere}} = 1. \quad (1.35)$$

We can consider now the sphere as a special case of a prolate (or oblate) ellipsoid with the major and minor radii: $a_>$ and $a_<$, respectively, for incident light polarized along the major axis of the particle. In this case the depolarization coefficients can be expressed through the *ellipticity* parameter $e = (a_>^2 - a_<^2)/a_>^2$ as

$$L = \frac{1 - e^2}{e^2} [-e + \text{arctanh}(e)], \quad D = \frac{3}{4} \left(\frac{1 + e^2}{1 - e^2} L + 1 \right). \quad (1.36)$$

We can now plug Eq. (1.34) back into Eq. (1.31) and, after some elementary algebra, arrive at the expression for the *microscopic polarizability* $\tilde{\alpha}$, $P_z = \varepsilon_0 \tilde{\alpha} E_{0,z}$, induced by the z component of the incident electric field $E_{0,z}$:

$$\tilde{\alpha}(\omega) = -\xi \left\{ \left[\omega^2 - \xi \left(L - \text{Re} \frac{1}{\varepsilon(\omega) - 1} \right) \right] + i\xi \left[-\text{Im} \frac{1}{\varepsilon(\omega) - 1} + \frac{k^3 V}{6\pi} \right] \right\}^{-1} \quad (1.37)$$

where $\xi = 4\pi a_> c^2 / (DV)$. Applying again the assumption that the polarization is homogeneous within the volume of the particle, we can relate $\tilde{\alpha}$ to a more familiar polarizability of the particle $\alpha = V\tilde{\alpha}$. In the following paragraphs we interpret the terms appearing in this formula, and justify the somewhat artificial division of the term proportional to $(\varepsilon - 1)^{-1}$ introduced above.

Restoring force and the Lamb shift

In the first square brackets of Eq. (1.37) we find the following term:

$$-\xi \left(L - \operatorname{Re} \frac{1}{\varepsilon(\omega) - 1} \right), \quad (1.38)$$

which quantifies the restoring force (which in the simplest harmonic oscillator model we considered as a constant ω_0) given by the sum of the static depolarization factor L and the dispersive correction, which we identify as the Lamb-shift. We plot this contribution in Fig. 1.4 with a solid blue line, considering the experimental dielectric function [54], ε_{sca} , fitted with a series of Lorentzian profiles [55]. The other blue lines in Fig. 1.4 correspond to the Lamb shift calculated within the Drude model of permittivity $\varepsilon_D(\omega)$ given by Eq. (1.4) with background permittivities of $\varepsilon_\infty = 9.5$ (dashed blue line) and $\varepsilon_\infty = 1$ (dotted blue line).

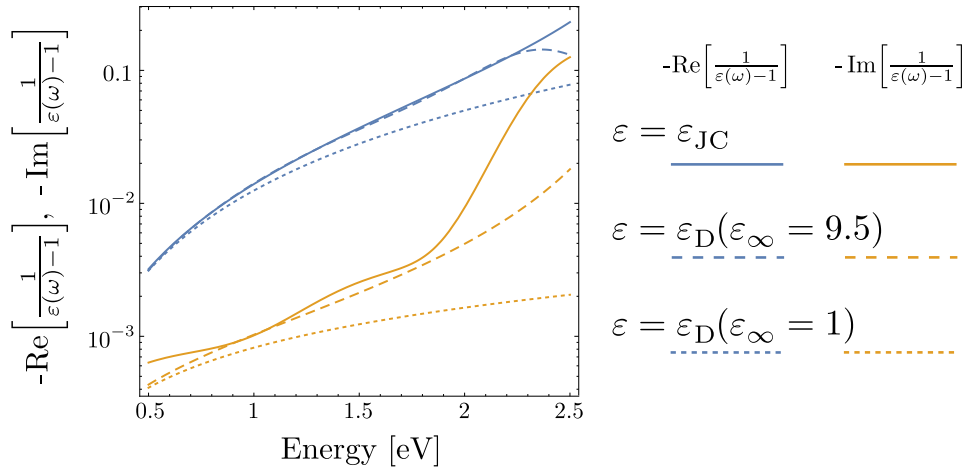


FIGURE 1.4: Lamb-shift ($\operatorname{Re}\{[\varepsilon(\omega) - 1]^{-1}\}$, blue lines) and loss function ($-\operatorname{Im}\{[\varepsilon(\omega) - 1]^{-1}\}$, orange lines) calculated using three prescriptions for the dielectric permittivity ε : Johnson-Christy [54] (ε_{sca} , solid lines), Drude with $\varepsilon_\infty = 9.5$ ($\varepsilon_D(\varepsilon_\infty = 9.5)$, dashed lines) and Drude with $\varepsilon_\infty = 1$ ($\varepsilon_D(\varepsilon_\infty = 1)$, dotted lines).

Radiative and non-radiative broadening

The second square bracket in Eq. (1.37),

$$\xi \left[-\operatorname{Im} \frac{1}{\varepsilon(\omega) - 1} + \frac{k^3 V}{6\pi} \right], \quad (1.39)$$

contains the previously recognized Abraham-Lorentz term which describes the radiation reaction, and the non-radiative contribution. Let us consider on the former, less familiar

term. Within the three models of dielectric function discussed above, we can calculate the *loss function* $-\text{Im}\{[\varepsilon(\omega) - 1]^{-1}\}$, and plot it in Fig. 1.4 for the three models of permittivity: ε_{sca} (solid orange line), $\varepsilon_D(\varepsilon_\infty = 9.5)$ (dashed orange line) and $\varepsilon_D(\varepsilon_\infty = 1)$ (dotted orange line).

In the simplest case of the free-electron gas model ($\varepsilon_\infty = 1$), the Lamb shift and the loss functions are given by

$$-\frac{1}{\varepsilon(\omega) - 1} = \left(\frac{\omega}{\omega_p}\right)^2 + i\frac{\omega\gamma_p}{\omega_p^2}. \quad (1.40)$$

This case was recently analyzed in detail by Zorić *et al.* [82], and led to simple expressions for the frequency and width of the resonance. If we further simplify this model by including the small Lamb shift into the natural frequency ω_0 , we will arrive at yet another model of polarizability α_D :

$$\alpha_D(\omega)^{-1} \propto \omega^2 - \omega_0^2 + i\xi \left(\frac{\omega\gamma_p}{\omega_p^2} + \frac{k^3 V}{6\pi} \right). \quad (1.41)$$

This form of polarizability is reminiscent of the expression for the amplitude of a damped harmonic oscillator, $D(\omega)$, introduced in Eq. (1.25), derived originally by considering the non-radiative friction-like damping term proportional to γ_p (Γ_A in the HO model corresponds to $\xi\gamma_p/\omega_p^2$) and the radiation reaction term (with Γ_R given by $\xi V/(6\pi c^3)$). In Fig. 1.4 we show that, while the approximation of ε by the free electron gas yields a good description of the polarizability for energies below 1 eV in the case of gold, for lower frequencies, it dramatically underestimates both the Lamb shift and the loss function, yielding narrower, blue-shifted resonances. The inclusion of the background permittivity further allows to dissect the contribution from interband transitions in gold above 2 eV.

1.2.2.1 Scattering and absorption cross sections

To further examine the effect of the different contributions to the permittivity in the optical response of plasmonic scatterers, we define the scattering σ_{sca} and absorption σ_{abs} cross-sections as

$$\sigma_{sca} = \frac{k^4}{6\pi} |\alpha(\omega)|^2, \quad (1.42a)$$

$$\sigma_{abs} = -\frac{k}{V} \text{Im} \frac{1}{\varepsilon(\omega) - 1} |\alpha(\omega)|^2. \quad (1.42b)$$

These definitions can be found by comparing the powers dissipated into absorption and scattering with the intensity of the incident illumination. We note that if the metal

is described solely by the free-electron gas, the above definitions of σ_{sca} and σ_{abs} yield expression proportional to the powers scattered (P_R , Eq. (1.28b)) and absorbed in the nanoparticle (P_A , Eq. (1.28a)), obtained from the HO model (Eq. (1.26)).

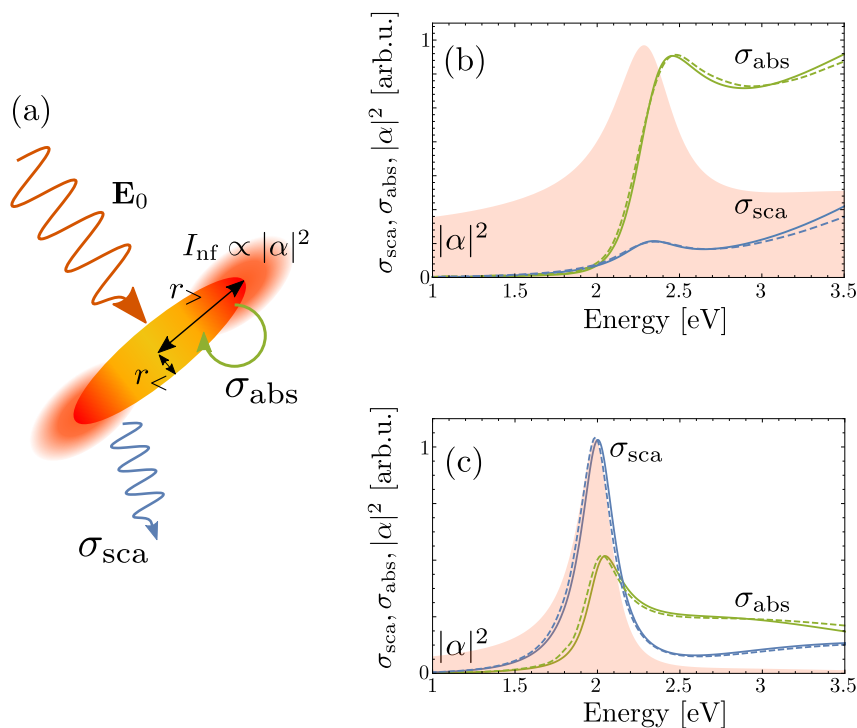


FIGURE 1.5: (a) Scheme of plasmon excitation and decay channels in a generic metallic scatterer. Light incident at the metallic nanoparticle, \mathbf{E}_0 , excites a dipolar charge distribution within the metal \mathbf{p} . The induced dipole then scatters its energy into radiative channels (σ_{sca}), or interacts with itself in a two-fold manner, yielding two non-radiative effects: depolarization leading to the Lamb shift of the plasmon energy, and Ohmic losses (σ_{abs}). The intensity of the electric field in the *near-field* region I_{nf} is proportional to the amplitude function $|\alpha|^2$. (b,c) Scattering (blue lines) and absorption (green lines) cross sections of a gold ellipsoid (radii (b) $(a_<, a_>) = (35, 35)$ nm, (c) $(a_<, a_>) = (35, 80)$ nm) illuminated with light polarized along the major axis. The cross sections were calculated using FDTD method [83] (solid lines) and the *Maier-Wokaun long wavelength approximation* (MWLWA) model [79] (dashed lines) with the use of literature dielectric function ε_{sca} . The red-shaded area depicts the profile of the amplitude of the oscillations of the plasmon $|\alpha|^2$ derived from the MWLWA.

We illustrate the applicability of the model based on the MWLWA in Fig. 1.5, where we plot the scattering (σ_{sca} , solid blue line) and absorption (σ_{abs} , solid green lines) cross sections of gold ellipsoids with minor radii $a_< = 35$ nm and aspect ratios of (b) 1 and (c) 2 calculated using FDTD Lumerical software [83] with the Johnson-Christy dielectric function of gold. The dashed lines represent the profiles predicted by the analytical model described above. The red-shaded profiles denote the amplitude function $|\alpha|^2$.

Interestingly, for both antennas analyzed in Fig. 1.5, the absorption peaks at a higher energy than the scattering, in direct violation of the second inequality in Eq. (1.30). By considering the elementary examples of gold nanoantennas, we will show below that this is a general phenomenon characteristic of nanoantennas operating in the visible regime (denoted by superscript *vis*), and that Eq. (1.30) should be replaced by a partially reversed relationship:

$$\omega_{\alpha}^{\text{vis}} < \omega_R^{\text{vis}} < \omega_A^{\text{vis}}. \quad (1.43)$$

1.2.3 Systematic study of gold nanorods

The results shown in Fig. 1.4, as well as the analysis of the Lamb shift and loss function given by Eq. (1.40) suggest that the reversal of the inequality between the peak frequencies of the scattering and the absorption is related to the deviation of the dielectric function of the metal from the free electron gas model. To analyze this process in a systematic manner, in Fig. 1.6 we plot with solid lines the spectral positions of the peaks of the polarizability $|\alpha(\omega)|^2$ (red lines), scattering (solid blue lines) and absorption (solid green lines) cross sections for gold ellipsoidal nanoparticles with minor radii of $a_{<} = 35$ nm and major radii from $a_{>} = 35$ nm to $a_{>} = 140$ nm. The profiles were obtained with the analytical model presented earlier, for three dielectric functions: (a) the experimental $\varepsilon_{\text{scat}}$, (b) the Drude-Sommerfeld model with background permittivity $\varepsilon_D(\varepsilon_{\infty} = 9.5)$ and (c) the ideal free electron gas model described by Drude-Sommerfeld model with background permittivity $\varepsilon_{\infty} = 1$.

The results shown in Fig. 1.6(a) identify an *anomalous* blue-shift of the absorption peak with respect to the scattering maximum in gold nanoparticles resonant in the blue part of the visible range. In the left inset of Fig. 1.6(a) we zoom in on the region of parameters where a *crossing* between the scattering and absorption peak frequencies occurs. Surprisingly, this effect is identified at around 1.7 eV, far below that of the dominant interband transition (2.5 eV), suggesting that the resonant contribution from this IT is not the only factor that promotes the blue-shifting of the absorption cross-sections. In fact, as we show in Fig. 1.6(b), the same anomalous, albeit significantly weaker, shift occurs for gold described by the Drude model with $\varepsilon_{\infty} = 9.5$ (see the left inset in Fig. 1.6(b)). For metal described with an ideal Drude model (with $\varepsilon_{\infty} = 1$), we retrieve the results reported previously for nanoantennas operating in the near-IR regime, which follow Eq. (1.30).

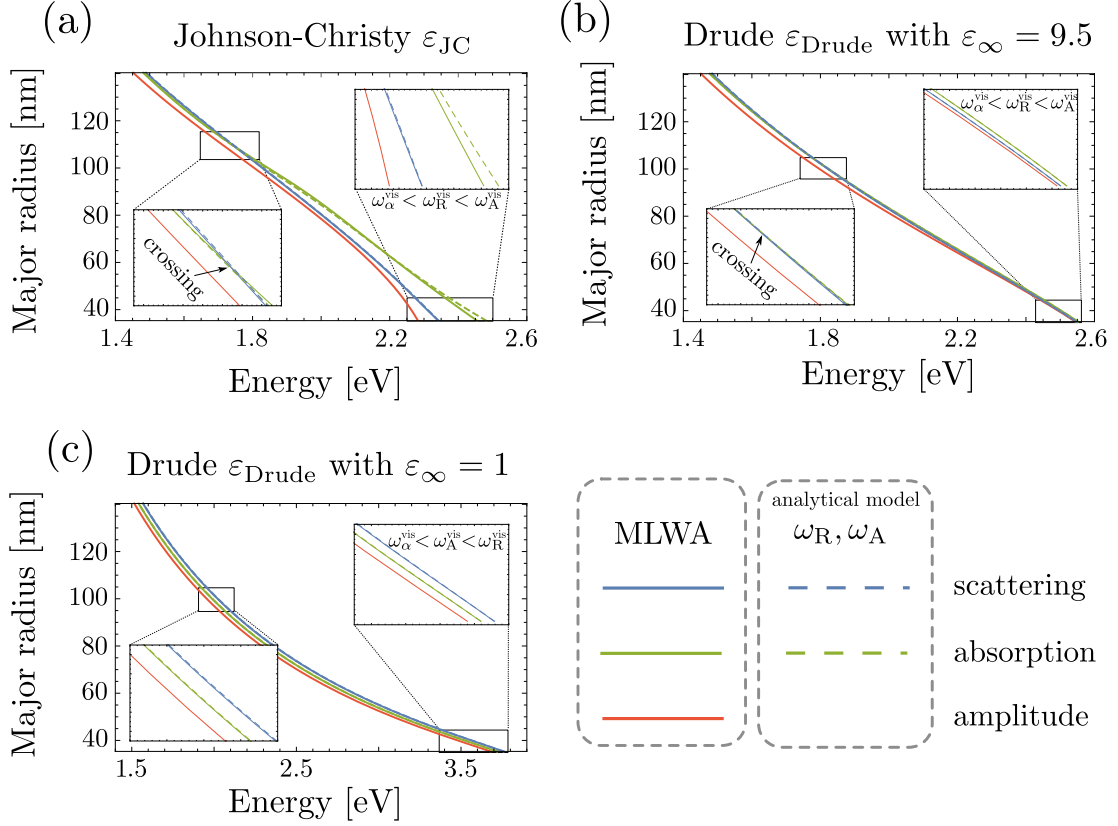


FIGURE 1.6: Spectral positions of the maxima of the amplitude function ($|\alpha|^2$, red lines), scattering (σ_{sca} , blue lines) and absorption cross sections (σ_{abs} , green lines), for gold ellipsoids with minor radii of 35 nm and major radii from 35 to 120 nm. The solid and dashed lines of scattering and absorption peaks correspond to the results of the MWLWA model and the values of ω_R , ω_A predicted by the simple analytical formulas given in Eqs. (1.48b) and (1.48a), respectively. The three panels correspond to various dielectric functions of gold used for calculations: (a) the experimentally measured permittivity ϵ_{sca} [54, 55], (b) Drude model with background permittivity $\epsilon_D(\epsilon_\infty = 9.5)$, (c) Drude model of a pure free electron gas $\epsilon_D(\epsilon_\infty = 1)$.

1.2.3.1 Spectral shifts - analytical model

To estimate the spectral shifts between the spectral positions of the amplitude, scattering and absorption peaks, we first consider the Taylor expansion of the amplitude $|\alpha|^2$ around its resonance frequency ω_α defined as

$$\left(\frac{d}{d\omega} |\alpha(\omega)|^2 \right)_{\omega=\omega_\alpha} = 0, \quad (1.44)$$

arriving at

$$|\alpha(\omega)|^2 \approx |\alpha(\omega_\alpha)|^2 - \frac{\chi}{2} (\omega - \omega_\alpha)^2, \quad (1.45)$$

where $\chi = -\left(\frac{d^2}{d\omega^2}|\alpha(\omega)|^2\right)_{\omega=\omega_\alpha}$. We can also expand the prefactors found in the expressions for the absorption (Eq. (1.42b)) and scattering (Eq. (1.42a)) cross sections, f_{abs} and f_{sca} , respectively, as

$$f_{\text{abs}}(\omega) = -\frac{k}{V}\text{Im}\frac{1}{\varepsilon(\omega)-1} \approx f_{\text{abs}}(\omega_\alpha) + (\omega - \omega_\alpha)\beta_{\text{abs}}, \quad (1.46a)$$

$$f_{\text{sca}}(\omega) = \frac{k^4}{6\pi} \approx f_{\text{sca}}(\omega_\alpha) + (\omega - \omega_\alpha)\beta_{\text{sca}}. \quad (1.46b)$$

Then, by writing the conditions for the peak of either cross section as

$$|\alpha(\omega)|^2 f_{\text{abs}}(\omega_A) = 0, \quad |\alpha(\omega)|^2 f_{\text{sca}}(\omega_R) = 0, \quad (1.47)$$

inserting the expansions listed above and dropping the quadratic term $\propto (\omega - \omega_\alpha)^2$, we can find the approximated solutions

$$\omega_A \approx \omega_\alpha + \frac{\beta_{\text{abs}}|\alpha(\omega_\alpha)|^2}{\chi f_{\text{abs}}(\omega_\alpha)}, \quad (1.48a)$$

$$\omega_R \approx \omega_\alpha + \frac{\beta_{\text{sca}}|\alpha(\omega_\alpha)|^2}{\chi f_{\text{sca}}(\omega_\alpha)}. \quad (1.48b)$$

The peak energies calculated with the equations above are depicted in Fig. 1.6 with dashed lines, and reveal a remarkable agreement with the predictions of the analytical model of polarizability. Interestingly, if the shifts were dependent on the prefactors f_{abs} and f_{sca} solely through their derivatives (β_{abs} and β_{sca} , respectively) and not their values ($f_{\text{abs}}(\omega_\alpha)$ and $f_{\text{sca}}(\omega_\alpha)$, respectively), as was suggested in earlier reports, the crossing point between blue and green lines in Fig. 1.6(a) would be found for higher energies, around 2 eV.

1.2.4 Tracing the decay of plasmons in time

Let us now consider the time-dynamics of the plasmon excitation. In the simplest picture, plasmons are assumed to decay in an exponential manner, with the decay rate related to the *full width at half maximum* (FWHM) of the amplitude profiles $|\alpha|^2$ [84]. This framework has been widely accepted and applied in the analysis of the attosecond streaking spectroscopy [85–87] and recently explored in experiments with femtosecond pulses [88]. In this subsection we attempt to question this assumption by accessing the dynamics of the plasmon by Fourier transformation of the polarizability α . As a side

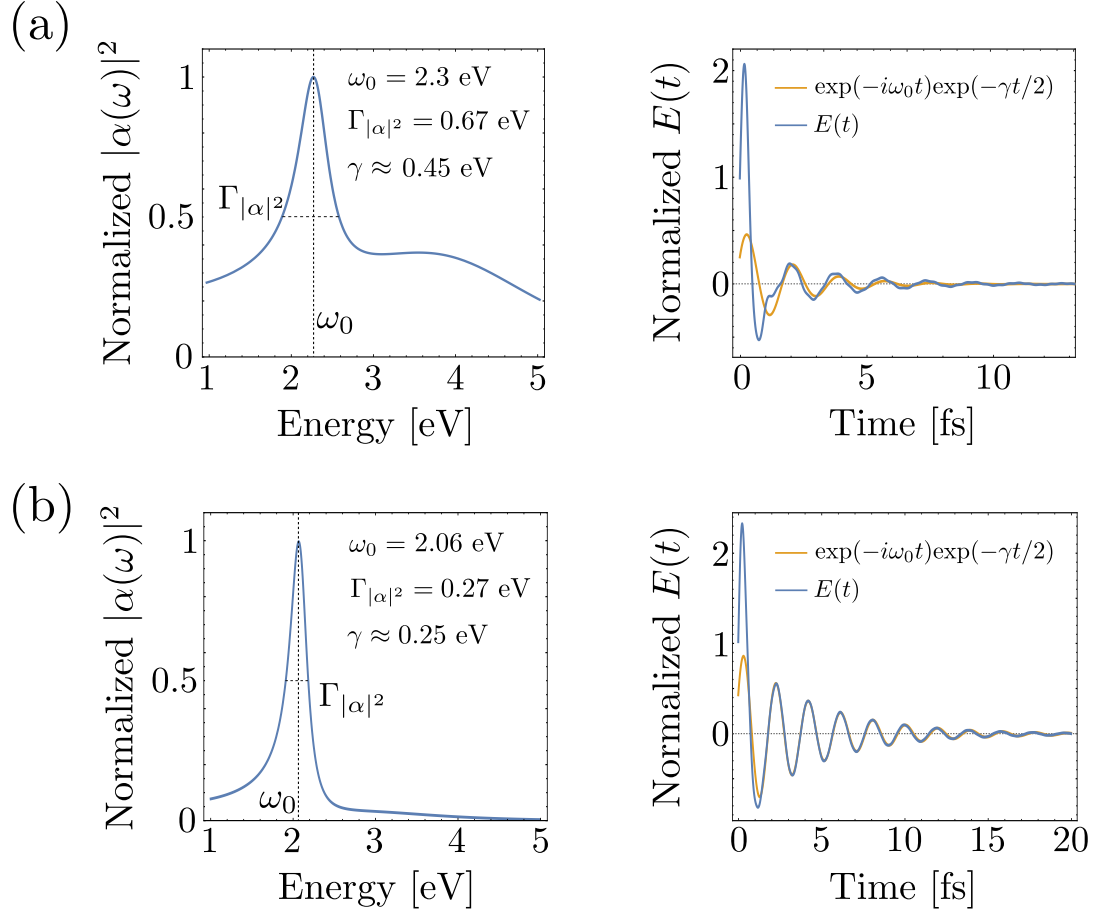


FIGURE 1.7: Polarizability profiles of gold ellipsoids ($|\alpha|^2$, left panels) and the evolution of electric fields of the plasmons $E(t)$ (blue line in right panels) obtained by Fourier transformation of the spectral profiles. The minor radii of the ellipsoids is 35 nm and the aspect ratios are (a) 1 and (b) 2. Orange lines in right panels represent the function $\exp(-i\omega_0 t)\exp(-\gamma t/2)$, with the parameters: frequency ω_0 and decay rate γ (listed in the left panels), determined by a fit to $E(t)$ in the region where it exhibits exponentially decaying oscillations. Parameters $\Gamma_{|\alpha|^2}$ listed in left panels denote the FWHM of the polarizability profiles $|\alpha|^2$.

note, we should point out that without an analytical model for α , the theoretical analysis would require accessing the response function by cumbersome numerical calculations of the dipolar polarizability of the particle. While in practice difficult, this approach is definitely feasible, and in fact we apply a related method in Chapter 2 of this thesis to investigate the hybridization scheme in dielectric scatterers.

For the polarizability given by a Lorentzian profile $\alpha_{\text{Lor}}^{-1} \propto (\omega - \omega_0 + i\gamma)$, with arbitrary width FWHM of $|\alpha_{\text{Lor}}|^2$: $\Gamma_{|\alpha_{\text{Lor}}|^2} = \gamma$, the dynamics of the electric field intensity can be

described as an exponentially decaying function

$$|E(t)|^2 \propto \exp(-\gamma t). \quad (1.49)$$

However, the expression for the polarizability α given in Eq. (1.37) suggests a deviation of the general response from the simple Lorentzian profiles. Indeed, plots of the polarizabilities $|\alpha|^2$ of gold ellipsoids shown in the left panels of Fig. 1.7(a) (sphere with $a_{<} = a_{>} = 35$ nm) and (b) ($(a_{<}, a_{>}) = (35$ nm, 70 nm)) are strongly asymmetric. In the right panels, we plot with blue lines the time dependence of the electric field, calculated by the Fourier transformation of the polarizabilities $\alpha(\omega)$ derived from MWLWA (using $\alpha(-\omega) = [\alpha(\omega)]^*$). In both cases, the dynamics of the electric field over the first oscillation period exhibits a very fast decay, and then settles as damped oscillations $E(t) \propto \exp[-(i\omega_0 + \gamma/2)t]$, plotted with orange lines. The resonant frequencies ω_0 , FWHM of $|\alpha|^2$ profiles $\Gamma_{|\alpha|^2}$, and the phenomenological decay rates γ obtained from fitting of $E(t)$ to the exponentially decaying oscillations, are given in the left panels. Interestingly, and unlike in the case of Lorentzian resonances, the latter two quantities are dramatically different for the shorter ellipsoid (a), reflecting the breakdown of the association between the width of a resonance line and the decay rate of the plasmon excitation.

1.2.5 Phenomenological estimations of the plasmon dynamics

In Fig. 1.8 we compare the decay rates γ (orange line) obtained from the fitting of the respective Fourier-transformed polarizabilities, with the FWHMs of polarizability $\Gamma_{|\alpha|^2}$, scattering Γ_{sca} and absorption Γ_{abs} cross sections for ellipsoids with varying major radius. The FWHM of absorption cannot always be determined since the relevant cross section does not exhibit a clear resonant profile (see for example green line in Fig. 1.5(b)). However, for aspect ratios around 4, Γ_{abs} becomes consistent with the remaining estimations of the plasmon decay. In this regime the resonance becomes very narrow, and the absorption and scattering profiles differ only in intensity.

In the more interesting regime of low aspect ratios, the FWHMs of the polarizability and scattering, as well as the decay rates obtained from the time dependencies of the field of the plasmon γ , remain in rather good agreement. Interestingly however, the matching between Γ_{sca} and $\Gamma_{|\alpha|^2}$ appears to be a rather accidental effect, since neither one of the respective profiles exhibits a narrow Lorentzian profile (see Fig. 1.5(c)). The deviation from the exponential decay of the plasmon in the regime denoted by an orange

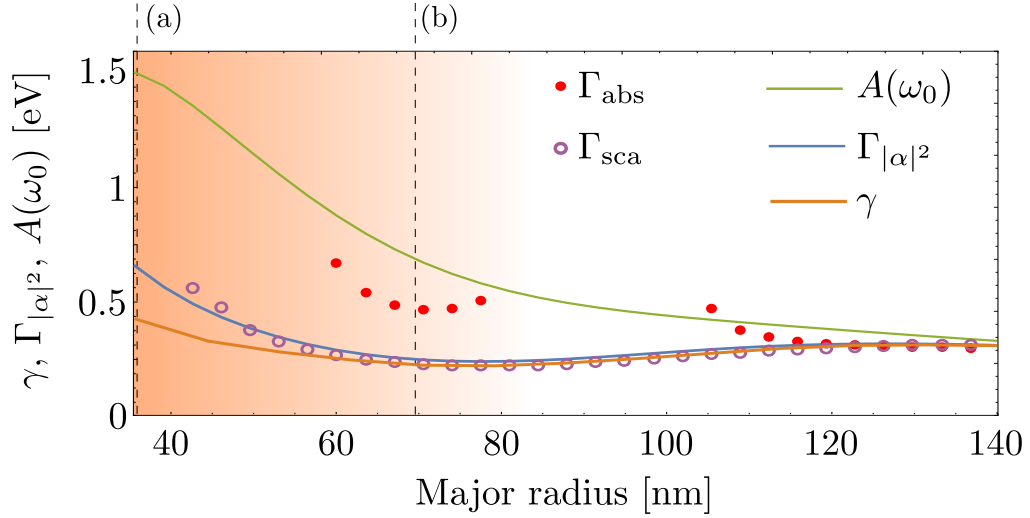


FIGURE 1.8: Comparison of different phenomenological estimations of the decay rate of the localized plasmon in ellipsoids with increasing major radius $a_>$ and fixed minor radius $a_< = 35$ nm: $A(\omega) = \text{Im}[\alpha(\omega_0)^{-1}]/\omega_0$ (green line), the FWHMs of the amplitude function $|\alpha|^2$ ($\Gamma_{|\alpha|^2}$, blue line), absorption (Γ_{abs} , red filled dots) and scattering cross sections (Γ_{sca} , violet empty dots) with the decay rate γ extracted from the time dependence of the induced field $E(t) \propto \exp[-(i\omega_0 + \gamma/2)t]$. Orange area denotes the range of parameters in which the decay becomes strongly non-exponential and dashed vertical lines marked as (a) and (b) indicate the major radii of ellipsoids analyzed in Fig. 1.7(a) and (b), respectively.

background, originates from the onset of the IT in the metal in a two-fold manner: first the large losses broaden the resonance, and then the strongly dispersive loss function $-\text{Im}\{[\varepsilon - 1]^{-1}\}$ distorts the shape of the polarizability, enabling the non-exponential evolution of the plasmon. Interestingly, this effect occurs also when the IT in the metal is partially addressed with the use of the Drude model with background permittivity $\varepsilon_\infty = 9.5$.

Finally, the green line in Fig. 1.8 depicts yet another estimation of the decay rate, given by the imaginary part of the denominator in the definition of α :

$$A(\omega_0) = \frac{\xi}{\omega_0} \left[-\text{Im} \frac{1}{\varepsilon(\omega_0) - 1} + k^3 \frac{V}{6\pi} \right]. \quad (1.50)$$

This estimation, while relevant for the resonances with large quality factor $Q = \omega_0/A(\omega_0)$, for which $A(\omega)$ is almost constant throughout the width of the profile, yields a significantly overestimated decay for shorter ellipsoids, and a rather good estimation for high-aspect ratio scatterers.

1.3 Summary

In conclusion, building on a well-established theory of MWLWA, we have designed a simple model of dipolar plasmon resonances which accurately predicts the position and the relative shifts of the scattering and absorption spectra of metallic nanoparticles. Our model addresses the most appealing, yet difficult regime where the interband transitions break down the description based on the simple Drude model, and additionally predicts the onset of non-exponential dynamics of the plasmon excitations in particles resonant in the visible range. The detailed studies of the time dependence of the decay of the plasmon excitation is particularly interesting in light of the recent experiments on generation and coherent manipulation of plasmons with few-femtosecond pulses [88, 89]. We explore this effect to identify the transition to the exponential decay regime and investigate the relationship between the plasmon decay rate and the widths of different spectral profiles.

Chapter 2

Dielectric nanoantennas

Over the last two decades a vigorous debate, conducted in the community of optical physicists, on novel designs of devices for the manipulation of light on the nanoscale, has been predominantly focused on utilizing the collective oscillations of the free electron gas in noble metals. With silver, gold and, recently, aluminium nanoparticles occupying the center of attention of numerous works, less attention has been given to the dielectric counterparts of such scatterers.

At the same time, in a neighboring, but slightly detached scientific community of quantum-optical physicists, dielectric micro-cavities are considered the quintessential photonic resonators that can be efficiently populated [90, 91], coupled to nearby atoms [92], or even coupled to their own vibrations [93]. These applications are possible thanks to the intrinsic properties of dielectric materials, which exhibit low intrinsic losses in the spectral ranges of interest, and the suppression of radiation by utilizing high-order whispering gallery modes (WGMs) [94]. Between those two effects, the dielectric micro-cavities improve on two of the most appealing properties of plasmonic scatterers: (i) the WGMs localize light in a very small region near the edge of the dielectric cavity and (ii) the linewidths of these resonances are very small, implying that the photons released into the cavity mode remain in it for a significant time.

Unfortunately, the straightforward transfer of the properties of dielectric micro-structures from the few-THz regime to the near-IR or visible region of the spectrum calls for a controllable method of manufacturing dielectric sub-micron particles with very few defects - a serious challenge which has not been fully addressed to this day.

With the benefit of hindsight, one could ask the following questions: can we trade away some of the radiation suppression offered by the WGMs and focus on lower order modes of attainable sub-micron nanoparticles? How would such scatterers perform as antennas for redirecting, absorbing or localizing incident light? Finally, how would they couple with nearby emitters?

These questions were prompted a few years ago in two independent studies reported by Aitzol García-Etxarri *et al.* [35] and Andrey B. Evlyukhin *et al.* [36]. Their calculations of the near-IR light scattering by sub-micron silicon spheres showed that dielectric nanoparticles of high refractive index can efficiently scatter light through *dipolar geometric resonances* and, even more surprisingly, scatter it also through strong magnetic excitations. This discovery led to a number of fascinating studies and designs which make use of both the magnetic activity of dielectric scatterers [8, 10, 15, 95, 96] and their low-loss properties [7, 97].

In this chapter, we discuss in details two of such concepts investigated during the course of this doctoral study: the use of dielectric spherical nanoantennas as platforms for enhancing the spontaneous decay rate of electric and magnetic dipolar emitters and the hybridization of dipolar modes in pairs of such dielectric nanoparticles.

2.1 Mie theory

The process of light scattering on nanoparticles lies at the very center of *classical nanooptics*. Its importance has assured a considerable attention in the last century, which in turn provided numerous analytical, and - thanks to the rapid development of computational techniques - numerical tools to address this problem. One of the most fundamental, and possibly the most elegant analytical methods for describing the light scattering process was proposed by Gustav Mie [70]. In Appendix A we outline the derivation and some of the results obtained within the *Mie theory* of scattering of light by spherical particles.

The elementary result of the Mie theory is the formulation of the closed, analytical formulas for the scattering σ_{sca} and extinction σ_{ext} cross sections of a homogeneous sphere of radius a and dielectric permittivity ϵ_2 , immersed in a homogeneous lossless medium with dielectric permittivity ϵ_1 , as shown schematically in Fig. 2.1(a). If the particle is illuminated by a planewave with frequency ω and wavevector $\mathbf{k}_0 = -k\hat{z} = -\omega/c\sqrt{\epsilon_1(\omega)}\hat{z}$, its cross sections are given by a weighted sum of the so-called *Mie coefficients* a_n and b_n ,

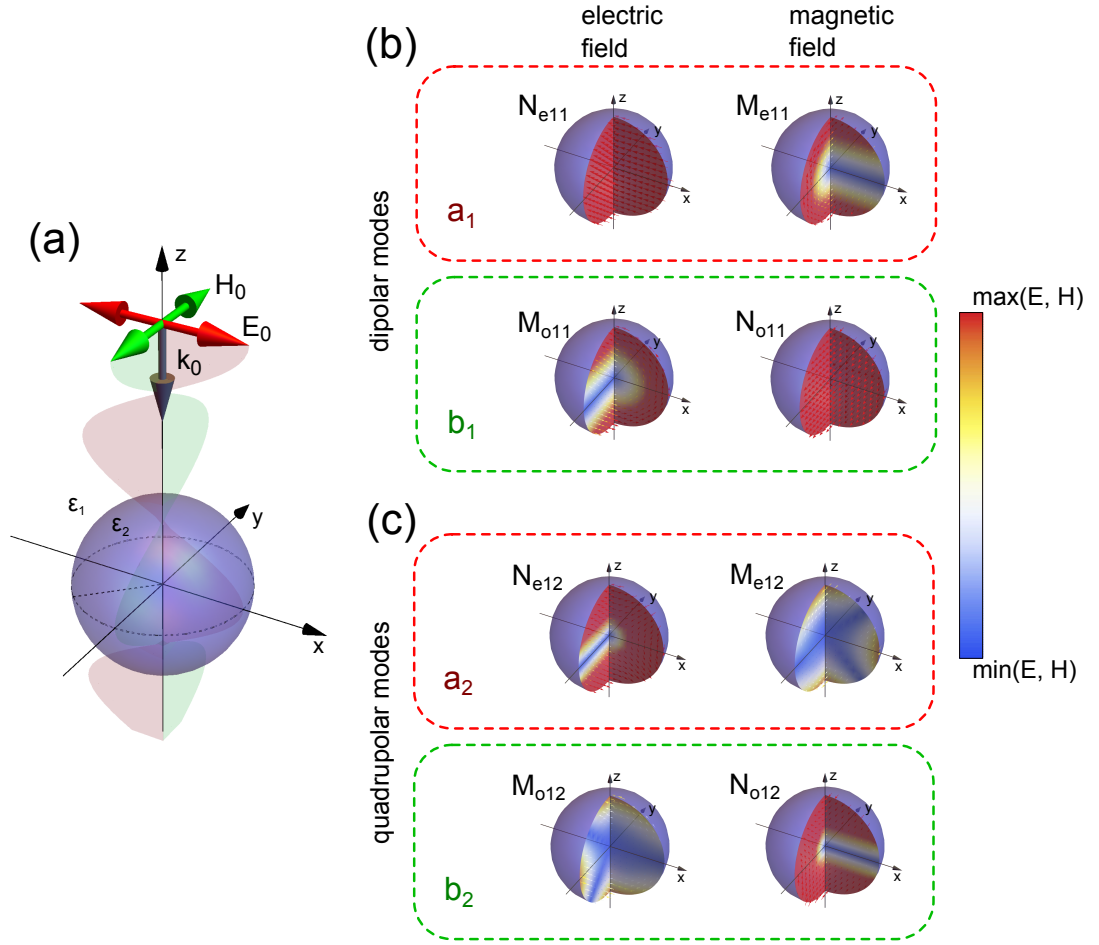


FIGURE 2.1: (a) Schematics of the canonical geometry for introducing Mie theory. A homogeneous sphere of dielectric permittivity ϵ_2 and radius a is immersed in a lossless medium with dielectric function ϵ_1 and illuminated by a linearly polarized monochromatic plane wave incident along the \hat{z} axis. (b, c) Electric (left plots) and magnetic (right plots) field distributions in the cross-sections of the sphere corresponding to the (b) dipolar electric (a_1 , upper panel) and dipolar magnetic mode (b_1 , lower panel) and (c) quadrupolar electric (a_2 , upper panel) and quadrupolar magnetic mode (b_2 , lower panel). The labels denoting the spherical harmonics, $M_{(e/o)mn}$ and $N_{(e/o)mn}$, shown in the plots, are defined in Appendix A.

which describe the contributions from the dipolar ($n = 1$), quadrupolar ($n = 2$), etc., *vector spherical harmonics* of electric (a_n) and magnetic (b_n) nature (see schematics in Fig. 2.1(b,c) and the derivations in Appendix A):

$$\sigma_{\text{sca}} = \frac{2\pi}{k^2} \sum_{n=1}^{\infty} (2n+1)(|a_n|^2 + |b_n|^2), \quad \sigma_{\text{ext}} = \frac{2\pi}{k^2} \sum_{n=1}^{\infty} (2n+1)\text{Re}(a_n + b_n). \quad (2.1)$$

2.1.1 Optical response of a submicron dielectric sphere

With this elementary knowledge of Mie theory presented above, we can reproduce the results reported by Aitzol García-Etxarri *et al.* [35], who found the strong and spectrally separated electric and magnetic dipolar resonances in the near-infrared scattering cross sections of a high-permittivity sub-micron sphere. For convenience, instead of the relevant cross sections, we analyze the *scattering* and *extinction efficiencies*, defined as the respective cross sections normalized to the geometrical cross section of the scatterer. For spherical particles we get:

$$C_{\text{sca}} = \frac{\sigma_{\text{sca}}}{\pi a^2}, \quad C_{\text{ext}} = \frac{\sigma_{\text{ext}}}{\pi a^2}. \quad (2.2)$$

In Fig. 2.2 we plot the planewave scattering efficiency spectrum (blue line) of a silicon sphere of radius $a = 230$ nm, in air (relative refractive index $M = \sqrt{\varepsilon_2/\varepsilon_1} = 3.5$). By separating the contributions to the scattering efficiency, according to Eq. (2.1), we can extract the scattering due to the electric dipolar (red area, $C_{\text{sca}}(a_1)$) and magnetic dipolar (green area, $C_{\text{sca}}(b_1)$) Mie modes. The spectral feature resonant at $\lambda = 1160$ nm represents the scattering by the quadrupolar magnetic b_2 mode.

Note that for lossless materials, the scattering and extinction efficiencies are identical, since for real M the Mie coefficients fulfill $|a_n|^2 = \text{Re}(a_n)$ and $|b_n|^2 = \text{Re}(b_n)$. In this section we assume that for the IR energies of the incoming photons below 1 eV this descriptions applies to silicon.

2.1.2 Scattering of radiation from a dipolar emitter

Mie theory offers more interesting results than those captured by the simple equations for the scattering and extinction cross sections. Specifically, it provides tools to calculate the scattered and absorbed powers for any *physical* illumination (described by the electromagnetic fields which fulfill the vector wave equation in the homogeneous,

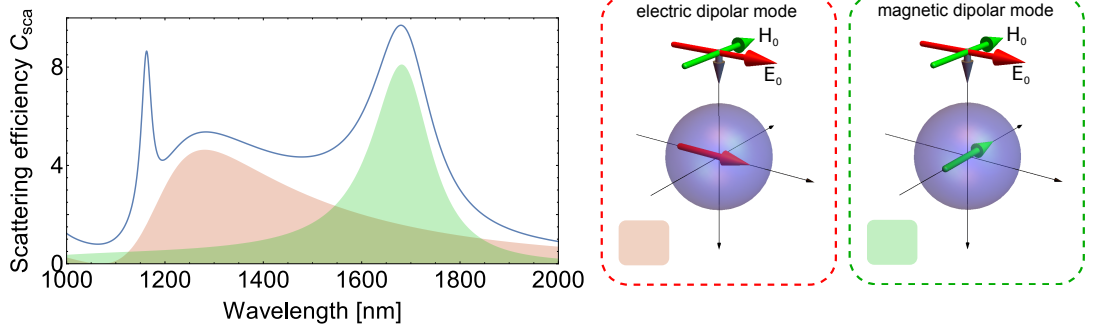


FIGURE 2.2: Scattering efficiency of a 230 nm radius Si nanosphere in air ($M = 3.5$) illuminated by a plane wave. The schematics of the illumination setup and the induced electric and magnetic dipolar modes are shown in the boxes on the right. The scattering efficiency C_{sca} is separated into contributions from the electric dipolar (red area, a_1) and magnetic dipolar modes (green area, b_1).

lossless medium). One of such illuminations that is of particular interest is the radiation from a dipolar emitter placed in the vicinity of the scatterer. This case is discussed in Appendix A, and the explicit expressions for the power of the outgoing radiation (P_{sca}) and the power absorbed by the scatterer (P_{abs}), originated by the classical electric (e) or magnetic (m) dipolar emitters are also derived. Comparing these powers to the power P_0 emitted by the dipole in the absence of the scatterer, we can draw a parallel to the process of enhancing the rate of spontaneous emission Γ_0 from a quantum dipolar emitter [56], and formulate the *radiative* and *total decay rate enhancement* factors of an emitter as

$$\frac{\Gamma_{\text{sca}}}{\Gamma_0} = \frac{P_{\text{sca}}}{P_0}, \quad \frac{\Gamma_{\text{tot}}}{\Gamma_0} = \frac{P_{\text{sca}} + P_{\text{abs}}}{P_0}, \quad (2.3)$$

respectively. For the spherical homogeneous particle characterized by the Mie coefficients a_n and b_n and an electric (e) dipolar emitter positioned at a distance z from the center of the sphere ($z > a$), oriented either radially (\perp) or parallelly (\parallel) to the surface of the particle, the expressions for the decay rate enhancements for each case are:

$$\frac{\Gamma_{\text{sca}}^{\perp,e}}{\Gamma_0} = \frac{3}{2} \sum_{n=1}^{\infty} (2n+1)n(n+1) \left| \frac{j_n(kz) - a_n h_n^{(1)}(kz)}{kz} \right|^2, \quad (2.4a)$$

$$\frac{\Gamma_{\text{sca}}^{\parallel,e}}{\Gamma_0} = \frac{3}{4} \sum_{n=1}^{\infty} (2n+1) \left[|j_n(kz) - b_n h_n^{(1)}(kz)|^2 + \left| \frac{\psi'_n(kz) - a_n \zeta'_n(kz)}{kz} \right|^2 \right], \quad (2.4b)$$

$$\frac{\Gamma_{\text{tot}}^{\perp,e}}{\Gamma_0} = 1 - \frac{3}{2} \text{Re} \sum_{n=1}^{\infty} (2n+1)n(n+1) a_n \left[\frac{h_n^{(1)}(kz)}{kz} \right]^2, \quad (2.4c)$$

$$\frac{\Gamma_{\text{tot}}^{\parallel,e}}{\Gamma_0} = 1 - \frac{3}{4} \sum_{n=1}^{\infty} (2n+1) \text{Re} \left\{ a_n \left[\frac{\zeta'_n(kz)}{kz} \right]^2 + b_n [h_n^{(1)}(kz)]^2 \right\}, \quad (2.4d)$$

while for the magnetic (m) dipolar emitter

$$\frac{\Gamma_{\text{sca}}^{\perp,m}}{\Gamma_0} = \frac{3}{2} \sum_{n=1}^{\infty} (2n+1)n(n+1) \left| \frac{j_n(kz) - b_n h_n^{(1)}(kz)}{kz} \right|^2, \quad (2.5a)$$

$$\frac{\Gamma_{\text{sca}}^{\parallel,m}}{\Gamma_0} = \frac{3}{4} \sum_{n=1}^{\infty} (2n+1) \left[|j_n(kz) - a_n h_n^{(1)}(kz)|^2 + \left| \frac{\psi'_n(kz) - b_n \zeta'_n(kz)}{kz} \right|^2 \right], \quad (2.5b)$$

$$\frac{\Gamma_{\text{tot}}^{\perp,m}}{\Gamma_0} = 1 - \frac{3}{2} \text{Re} \sum_{n=1}^{\infty} (2n+1)n(n+1) b_n \left[\frac{h_n^{(1)}(kz)}{kz} \right]^2, \quad (2.5c)$$

$$\frac{\Gamma_{\text{tot}}^{\parallel,m}}{\Gamma_0} = 1 - \frac{3}{4} \sum_{n=1}^{\infty} (2n+1) \text{Re} \left\{ b_n \left[\frac{\zeta'_n(kz)}{kz} \right]^2 + a_n [h_n^{(1)}(kz)]^2 \right\}, \quad (2.5d)$$

where we have made use of the spherical Bessel j_n and Hankel $h_n^{(1)}$ functions and a Riccati-Bessel functions $\zeta_n(\rho) = \rho h_n^{(1)}(\rho)$ and $\psi_n(\rho) = \rho j_n(\rho)$.

2.2 Single dielectric-particle nanoantennas

Having introduced the mathematical framework for the description of light scattering on spherical particles in the previous section, let us now proceed to exploring the concept of coupling dielectric submicron antennas with electric and magnetic dipolar emitters [15]. To this end, we develop the description now presented in subsection A.3 of Appendix A, and presented in the above Eqs. (2.4a-2.5d). Within this framework, we perform a detailed study of the dependence of the decay rate enhancement of dipolar emitters on their distance z to the surface of the spherical antenna, and its polarization.

To place these results in the context of the current research, we note a recent surge in the interest of the scientific community in controlling magnetic transitions in lanthanide ions embedded in nanocrystals. We should especially mention the experimental contributions by S. Karaveli and R. Zia [98], who have shown that the rate of spontaneous emission from trivalent europium (Eu^{3+}) exhibiting a magnetic dipolar transition can be modified by carefully placing it near a flat gold mirror. Their work can be acknowledged as a successful realization of the simpler experiments reported almost 35 years earlier by K. Drexhage [99], and later by R.E. Kunz and W. Lukosz [100], who studied the rates of primarily electric transitions of europium ions placed on dielectric mirrors.

In the following subsections, we first analyze the decay rate enhancements for dipolar emitters placed near a submicron silicon antenna with spectrally well-separated electric and magnetic dipolar resonances [35] (see Fig. 2.2). Later, we present a simple dipole-dipole interaction model which accurately describes the interaction between the dipolar emitters and the lowest-order Mie modes of dielectric nanoparticles.

2.2.1 Radiating dipoles in the presence of a high-index dielectric particle (Si sphere)

In Fig. 2.3 we show the spectra of the enhancement of the decay rates for the electric (red lines) and magnetic (green lines) emitters positioned at a distance of 50 nm from the surface of a 230 nm radius silicon sphere. The enhancement factors are shown for the two orientations of both types of emitters - perpendicular (a) and parallel (b) to the closest surface of the nanoparticle. The calculations were performed using the appropriate formulas listed in Eqs. (2.4a-2.5d).

For the dipole oriented radially (Fig. 2.3(a), Eqs. (2.4a,2.4c,2.5a,2.5c)), it is possible to dissect the contributions originating from each of the Mie modes in the sphere to the decay rates. We illustrate this in Fig. 2.3(a) by marking with red and green areas the contribution from the dipolar electric modes to the electric dipolar emission (a_1 , red area) and magnetic dipolar mode to the magnetic dipolar emission (b_1 , red area).

We observe in Fig. 2.3 that both the orientation of the emitter as well as its electric or magnetic nature determine which modes of the sphere are excited. An electric emitter oriented parallelly (Fig. 2.3(b), red line) excites the magnetic dipolar b_1 (at $\lambda = 1680$ nm), quadrupolar b_2 (at $\lambda = 1160$ nm) and - although very weakly - the electric dipolar a_1 (at $\lambda = 1350$ nm) resonance, while the same emitter aligned perpendicularly (Fig. 2.3(a), red line) couples exclusively to the broad electric dipolar a_1 mode, peaking at $\lambda = 1350$ nm. The complementary behavior is observed for the magnetic emitter: for perpendicular orientation (Fig. 2.3(a), green line), only the magnetic b_1 , b_2 modes are excited, while in the parallel orientation (Fig. 2.3(b), green line) the emitter couples to both the magnetic and electric modes. In principle, this effect can be used to discriminate between the two types of emitters.

To further investigate the selectivity of the emission, we plot in Fig. 2.4 the enhancements of the decay rates of the electric (\mathbf{p}_{emi}) and magnetic (\mathbf{m}_{emi}) dipolar emitters as a function of the emission wavelength of the emitter λ and the radius a of the dielectric

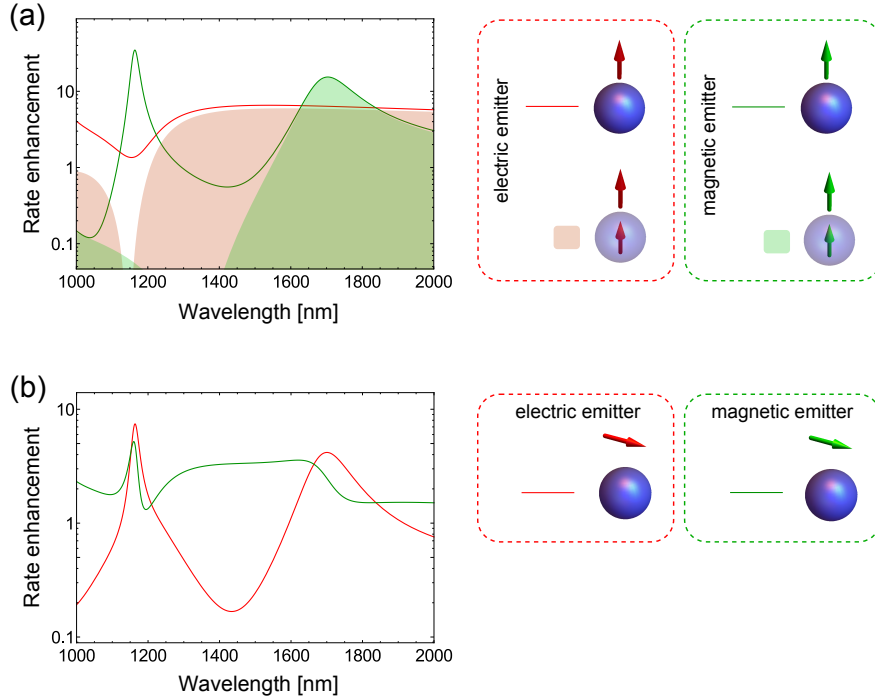


FIGURE 2.3: Decay rate enhancements of an electric (red lines) or magnetic (green lines) emitters positioned in the vicinity of the particle. The emitter is oriented either perpendicularly (a) or parallelly (b) with respect to the closest surface of the sphere. Spectra of the radiative rate enhancements shown are calculated using Eqs. (2.4a-2.5d). Contributions to the decay rates from the electric (a_1) and magnetic (b_1) dipolar modes of the sphere can be isolated for the perpendicular orientation of the dipole, and are denoted in (a) red and green areas, respectively. The refractive index of the silicon nanosphere is 3.5, while the distance from the emitter to the surface of the sphere is set to 50 nm.

nanosphere. Since Eqs. (2.4a-2.5d) depend on the parameter $ka \propto \lambda^{-1}a$ through the Mie coefficients, the spectral positions of the Mie resonances follow straight lines as marked in the decay rate maps of Fig. 2.4 by dashed lines defined by $a \propto \lambda$. The dependence of Eqs. (2.4a-2.5d) on the distance from the dipole to the center of the sphere z does not affect significantly the spectral features of the enhancements, but governs the relative strength of the resonances. Furthermore, for the largest sphere, many high-order resonances appear clearly in the high-energy region of spectra, as these modes can be efficiently activated for small values of $(z - a)/a$.

Similarly to Fig. 2.3(a), for the perpendicular orientation, the electric emitter (Fig. 2.4(a)) couples only to the electric modes (marked as a_n), and excites mostly magnetic contribution when oriented parallelly (Fig. 2.4(b)). In the latter case however, an electric contribution is also present, which is mostly visible for the high order modes. Similarly, the perpendicular magnetic emitter excites magnetic modes exclusively (Fig. 2.4(c)),

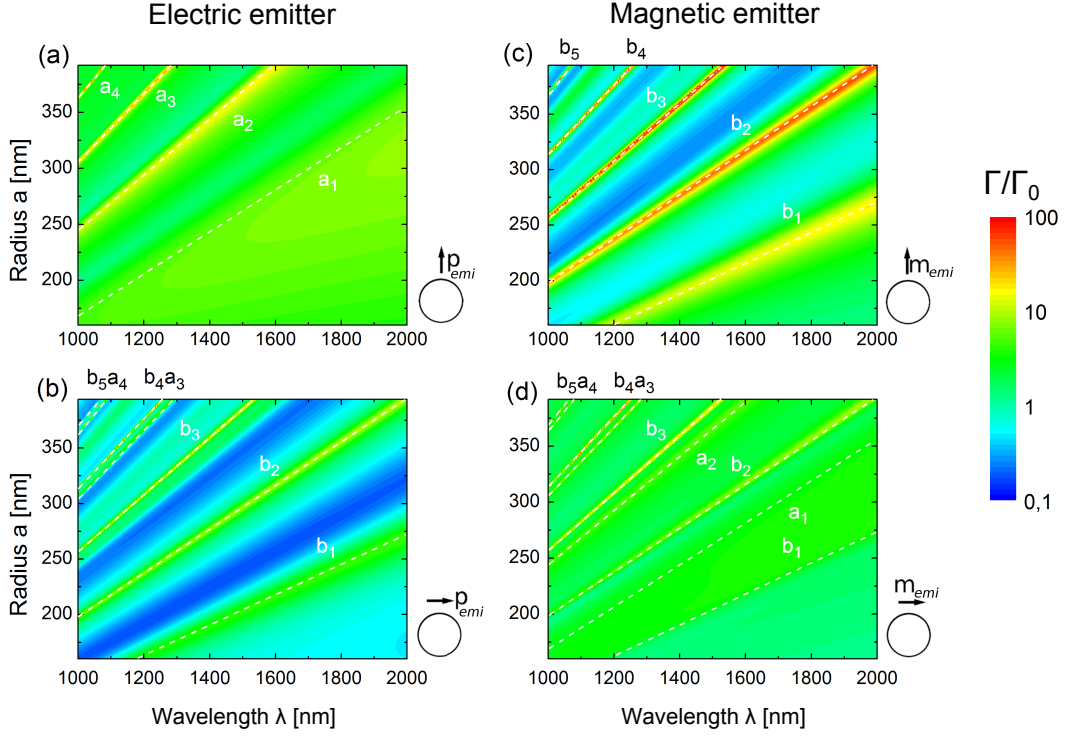


FIGURE 2.4: Spectra of the decay rate enhancements Γ/Γ_0 of electric (\mathbf{p}_{emi} , (a,b)) or magnetic (\mathbf{m}_{emi} , (c,d)) nature near the silicon sphere of varying radius a in vacuum. Dipoles are oriented either perpendicularly (a,c) or parallelly (b,d) to the surface of the antenna, positioned at fixed distance of 50 nm from its surface. Dashed lines correspond to the Mie resonances a_n and b_n , as displayed in each of the plots. Geometries of the setups are shown in the schematics.

whereas in parallel orientation it couples to the electric and to the magnetic modes (Fig. 2.4(d)). Thus, the orientation and the nature of the emitters allows for a selective excitation of the modes of the dielectric sphere.

This modal selectivity can be understood by tracing the presence of Mie coefficients in Eqs. (2.4a-2.5d) for each case. For the emitter perpendicular to the surface of the antenna (Eqs. (2.4a,2.4c,2.5a,2.5c)), only one type of Mie coefficient is present: electric a_n terms for the electric emitter and magnetic b_n terms for the magnetic emitter. On the other hand, since the equations for the emitter oriented parallelly (Eqs. (2.4b,2.4d,2.5b,2.5d)) include both electric and magnetic coefficients, both types of resonances are excited.

We can further confirm the identification of the contributions from the electric and magnetic modes to the enhancement of the decay rates (Fig. 2.3) by plotting the distributions of the fields induced in the system. In Fig. 2.5 the induced electric (a,c,e,g) and magnetic field (b,d,f,h) distributions are shown for two resonances of the Si sphere:

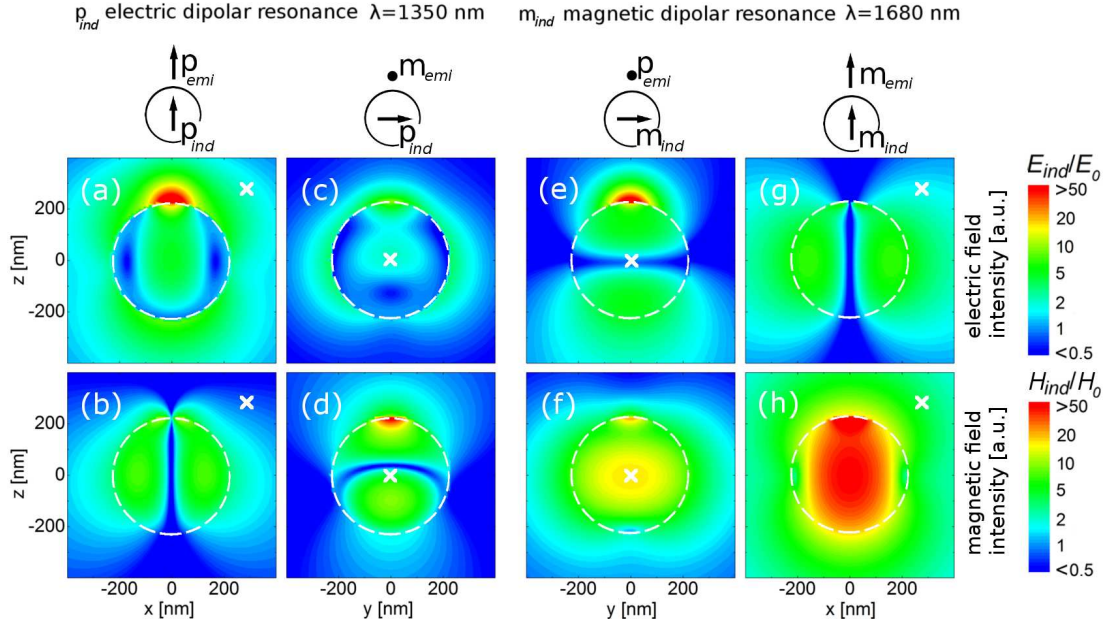


FIGURE 2.5: Distribution of the electric (upper row) and magnetic (lower row) induced field amplitude enhancements by an electric (\mathbf{p}_{emi}) and magnetic (\mathbf{m}_{emi}) dipole at a distance of the 50 nm from the surface of a 230 nm radius silicon sphere. Shown cross-sections contain the dipole and the center of the sphere. Plots (a-d) correspond to the dipolar electric mode induced at $\lambda = 1350$ nm, with the induced dipole denoted as \mathbf{p}_{ind} , excited by the perpendicular electric (a,b) or parallel magnetic (c,d) emitter. (e-h) illustrate the field distributions at the dipolar magnetic mode $\lambda = 1680$ nm (\mathbf{m}_{ind}), induced by the parallel electric (e,f) or perpendicular magnetic (g,h) emitter. Schematics of the exciting and induced dipoles are shown at the top of the figures. Intensities of the induced fields E_{ind} and H_{ind} are normalized to the values of the fields E_0 and H_0 produced by the dipolar emitter in the absence of the particle and evaluated at distance of 280 nm from the emitter in the direction perpendicular to its axis. The position of the normalization point is marked by a white cross in each case.

electric a_1 ((a-d), denoted in the schematics as the induced electric \mathbf{p}_{ind}) and magnetic b_1 ((e-h), induced magnetic \mathbf{m}_{ind}) dipolar modes. These excitations are induced by the emitter of the electric (\mathbf{p}_{emi}) or magnetic (\mathbf{m}_{emi}) nature, oriented as shown in the top schematic of each panel in Fig. 2.5. The fields have been obtained from a vector harmonic decomposition (see Appendix A for details). Dipolar electric resonances at $\lambda = 1350$ nm are excited by the perpendicularly oriented electric emitter (Fig. 2.5(a,b)) or parallelly oriented magnetic emitter (Fig. 2.5(c,d)). The dipolar magnetic resonance at $\lambda = 1680$ nm is induced both by the electric emitter oriented parallelly (Fig. 2.5(e,f)) and by the magnetic emitter oriented perpendicularly (Fig. 2.5(g,h)) to the surface of the sphere. The distributions of the fields shown in Fig. 2.5 clearly indicate the dipolar nature of the induced resonances and qualitatively agree with the field distributions of the resonances obtained with excitation of the Si sphere by a plane wave [35].

In Ref. [15] we provided a detailed comparison of the decay rate enhancement factors with the case of a dipolar emitter coupled to a silver nanoparticle. We concluded that the performance of silicon nano-antennas coupled to electric emitters matched that of the plasmonic systems, and showed some improvements over their metallic counterparts when applied to controlling the emission from magnetic emitters.

2.2.2 Dipole-dipole interaction

The electromagnetic coupling in the previous examples was often dominated by the dipolar modes induced in the sphere. By limiting the sum in Eqs. (2.4c, 2.4d, 2.5c, 2.5d) to the $n = 1$ terms and taking the explicit form of the spherical Hankel function $h_1^{(1)}$, we obtain the following expressions for the enhancement of the decay rates within the dipole-dipole approximation:

$$\left. \frac{\Gamma_{\text{tot}}^{\perp,e}}{\Gamma_0} \right|_{\text{dip}} = 1 - \frac{3}{2\pi k z^4} \text{Im} \left[\alpha_E e^{2ikz} \left(1 + \frac{2i}{kz} - \frac{1}{(kz)^2} \right) \right], \quad (2.6a)$$

$$\begin{aligned} \left. \frac{\Gamma_{\text{tot}}^{\parallel,e}}{\Gamma_0} \right|_{\text{dip}} &= 1 + \frac{3k}{8\pi z^2} \text{Im} \left[\alpha_E e^{2ikz} \left(1 + \frac{2i}{kz} - \frac{3}{(kz)^2} - \frac{2i}{(kz)^3} + \frac{1}{(kz)^4} \right) \right] \\ &\quad + \frac{3k}{8\pi z^2} \text{Im} \left[\alpha_M e^{2ikz} \left(-1 - \frac{2i}{kz} + \frac{1}{(kz)^2} \right) \right], \end{aligned} \quad (2.6b)$$

$$\left. \frac{\Gamma_{\text{tot}}^{\perp,m}}{\Gamma_0} \right|_{\text{dip}} = 1 - \frac{3}{2\pi k z^4} \text{Im} \left[\alpha_M e^{2ikz} \left(1 + \frac{2i}{kz} - \frac{1}{(kz)^2} \right) \right], \quad (2.6c)$$

$$\begin{aligned} \left. \frac{\Gamma_{\text{tot}}^{\parallel,m}}{\Gamma_0} \right|_{\text{dip}} &= 1 + \frac{3k}{8\pi z^2} \text{Im} \left[\alpha_M e^{2ikz} \left(1 + \frac{2i}{kz} - \frac{3}{(kz)^2} - \frac{2i}{(kz)^3} + \frac{1}{(kz)^4} \right) \right] \\ &\quad + \frac{3k}{8\pi z^2} \text{Im} \left[\alpha_E e^{2ikz} \left(-1 - \frac{2i}{kz} + \frac{1}{(kz)^2} \right) \right], \end{aligned} \quad (2.6d)$$

where the electric α_E and the magnetic α_M dipolar polarizabilities are associated with the first order Mie coefficients according to

$$\alpha_E = i \frac{6\pi}{k^3} a_1, \quad \alpha_M = i \frac{6\pi}{k^3} b_1, \quad (2.7)$$

respectively.

Out of the four equations above, only Eqs. (2.6b) and (2.6d) depend on both magnetic (α_M) and electric (α_E) contributions. The perpendicular electric (magnetic) emitter couples only with the electric (magnetic) dipolar mode. In the cases when a single dipolar mode of the sphere, either electric or magnetic, dominates the response at a given wavelength, it is possible to describe the coupling at that wavelength as a simple dipole-dipole interaction.

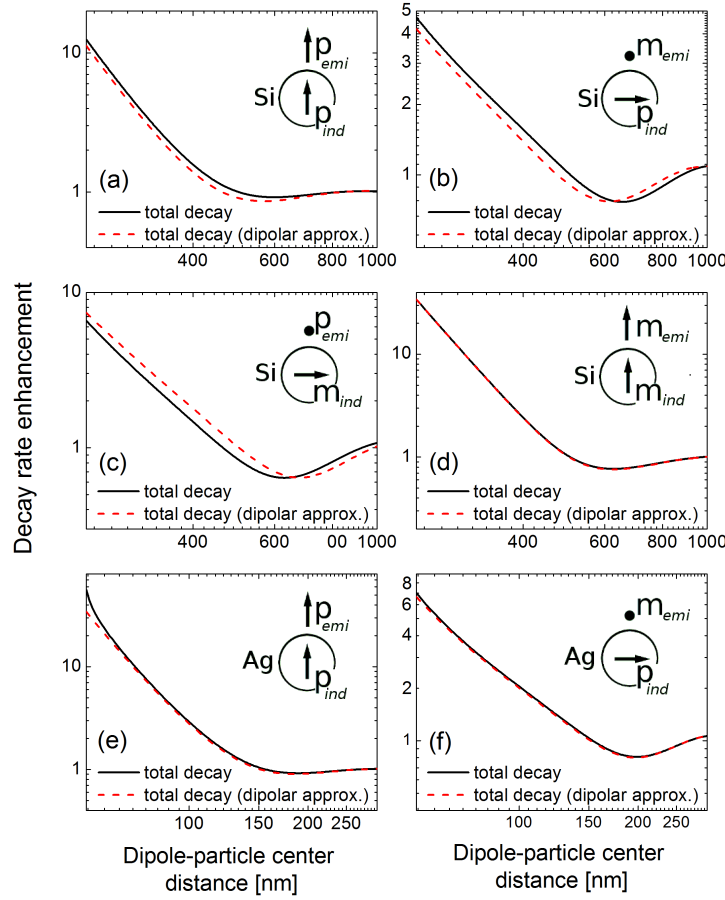


FIGURE 2.6: Distance dependence of the decay rate enhancements calculated using the exact formulas (solid lines) and the dipolar interaction approach (dashed lines). In plots (a-d), the emitter is positioned near a 230 nm radius silicon sphere and for (e-f) - near a 50 nm radius silver sphere. The wavelength of radiation matches the dipolar modes of the silicon particle: (a-b) electric at 1350 nm and (c-d) magnetic at 1680 nm, and the electric dipolar mode of the silver sphere at 420 nm (e-f). In each case, only the dominant induced dipole is considered for the dipolar approximation, while the mode of the complementary nature (magnetic or electric) is neglected. The insets show the orientation and the electric or magnetic nature of both the emitter (\mathbf{p}_{emi} or \mathbf{m}_{emi}) and the induced dipolar mode (\mathbf{p}_{ind} or \mathbf{m}_{ind}) in the antenna. The distance is measured between the dipolar emitter and the center of the antenna.

To illustrate this property, we show in Fig. 2.6 the enhancement of the decay rate as a

function of the distance between the dipole and the center of the nanoparticle. Results were obtained with the use of the exact formulas given by Eqs. (2.4c-2.4d) (solid black lines) as well as with the dipolar-interaction approximation (dashed red lines). We consider a 230 nm radius silicon particle and, for the sake of comparison with a common plasmonic systems, a 50 nm silver sphere described by a dielectric function from the literature [101]. To extract the dominant contributions, we choose the wavelengths corresponding to the dipolar electric a_1 and dipolar magnetic b_1 resonances, and set the polarizabilities of the complementary nature to 0 in Eqs. (2.4c-2.4d). Namely, in the case of the Si sphere, α_E is neglected for $\lambda = 1680$ nm (corresponding to b_1 resonance) and α_M is ignored for $\lambda = 1350$ nm (a_1). For the Ag sphere, we put the magnetic dipolar polarizability $\alpha_M = 0$ for $\lambda = 420$ nm (coinciding with the electric dipolar resonance a_1).

The dipole-dipole interaction model very accurately reproduces the exact results in all the considered dielectric antennas. In Fig. 2.6(a), we plot the decay rate enhancements of an electric emitter, perpendicular to the surface of the silicon sphere, radiating at $\lambda = 1350$ nm (dipolar electric antenna resonance). The disagreement between the curves can be attributed to the influence of the quadrupolar electric mode, not considered in the dipole-dipole approximation. In the analogous situation of an identically oriented magnetic emitter at the magnetic dipolar resonance ($\lambda = 1680$ nm, Fig. 2.6(d)), the agreement with the analytical solution is almost perfect, as no higher-order magnetic modes contribute in this spectral range. Small differences due to the neglected dipolar polarizabilities can be seen for emitters oriented parallelly to the surface of the sphere: the magnetic emitter coupled to the silicon antenna at its electric dipolar resonance ($\lambda = 1350$ nm, Fig. 2.6(b)) and the electric emitter at the magnetic dipolar resonance ($\lambda = 1680$ nm, Fig. 2.6(c)).

For the silver antenna (Fig. 2.6(e-f)), we show the distance dependence of the total decay rate enhancement for the radiation wavelength of 420 nm, which corresponds to the excitation of the dominant dipolar electric mode of the Ag particle. Almost perfect agreement between the exact solution and the results of the dipole-dipole interaction model is obtained both for the electric (Fig. 2.6(e)) and the magnetic emitter (Fig. 2.6(f)) oriented perpendicularly or parallelly to the surface of the antenna, respectively. The slight deviations are mostly due to high order non-radiative contributions that become more significant for very short separation distances. However, we emphasize that the agreement between the simple model and the complete analytical solution is very good in all the considered cases.

2.2.3 Conclusion

We have presented a detailed analysis of the radiative and non-radiative decay rates of both dipolar electric and magnetic emitters positioned in the vicinity of a high-refractive index spherical dielectric particle. Thanks to their strong magnetic dipolar resonances in the near infrared, such antennas provide a canonical example of dielectric antennas that can be used to selectively enhance magnetic dipolar emission. Interestingly, the resonant coupling between a dipolar (electric or magnetic) emitter and the dipolar Mie resonances in a particle is well described by the dipole-dipole interaction approach at certain wavelengths even when the emitter is in close proximity to the sphere surface.

Near the magnetic resonance, we found a strong enhancement of the decay rate of magnetic emitters which resembles the enhancement of electric dipole emission near a resonant plasmonic particle. However, while the total decay rate in plasmonic nanoantennas is often dominated by non-radiative channels, the total emission rate in lossless silicon antennas is purely radiative. These results show that nanosphere dielectric antennas are excellent platforms to enhance and manipulate magnetic dipolar emission with important possible applications as elements of infrared and telecommunication devices.

2.3 Optical response of dielectric dimers

Considering the content of the previous section, it might be natural to wonder what the optical response of the system discussed above would be, if we replaced the dipolar emitter by another dielectric nanoparticle. Could one design an appropriate dipole-dipole interaction model that would accurately describe the optics of a dielectric dimer? How good of an approximation would it be in the regimes where the spheres exhibit contributions from the higher modes?

In this section we attempt to answer these questions by presenting a detailed derivation of an analytical model of hybridization in dimers of electric and magnetic dipolar scatterers, and illustrating this concept by considering the optical response of a dimer of dielectric spheres. Afterwards we discuss the optical response of dielectric dimers obtained from experiments, and interpret them by means of numerical analysis, relating them to the predictions of the analytical model. Finally, we attempt to answer the question whether dimer structures can provide a more effective platform for enhancing the emission from dipolar emitters compared to the single spheres.

For other interesting aspects of silicon dimer structures, such as their ability to enhance the electric and magnetic fields, as well as the comparison between the performance of dielectric and metallic nanoantennas, we direct the reader to Ref. [7].

2.3.1 Hybridization of dipolar modes in a dielectric dimer

Let us consider a dielectric dimer antenna shown schematically in Fig. 2.7. Spherical nanoparticles of radii a are separated by the *dimer gap* d , and are centered on the \hat{y} axis, equally spaced from the coordinate origin. The two panels of Fig. 2.7 depict the (a) *transverse electric* TE and (b) *transverse magnetic* TM polarizations of the planewave incident along axis \hat{z} , with wavevector \mathbf{k}_0 , and incident electric \mathbf{E}_0 and magnetic \mathbf{H}_0 fields.

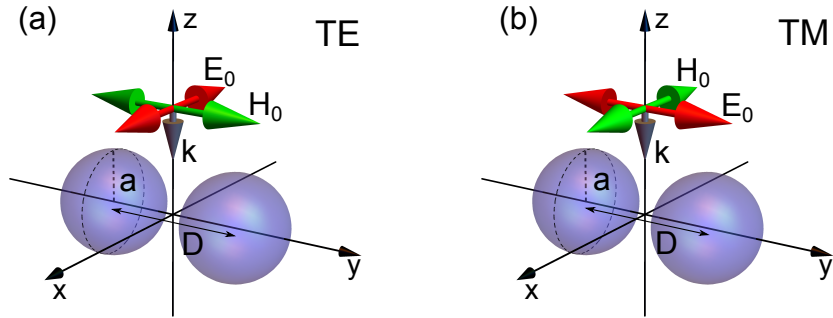


FIGURE 2.7: Schematic representation of a particle dimer showing the orientation of the incoming radiation with electric field \mathbf{E}_0 polarized (a) perpendicular and (b) parallel to the dimer axis in TE and TM configurations, respectively.

Since each of the constituent nanoparticles exhibits both electric and magnetic resonances, we expect that the response of strongly coupled dimer structures will be governed by *hybridized* modes, composed of the *homogeneous* pairing of electric dipoles similar to those observed in plasmonic dimers [71, 72], the less explored pairs of magnetic dipoles [37, 102], and also novel *heterogeneous* pairs comprising one electric and one magnetic dipole.

To study the formation of these modes in detail, we develop a simple model in which the spheres (numbered as 1 and 2, and centered at \mathbf{r}_1 and \mathbf{r}_2 , with the center-to-center separation $D = d + 2a = |\mathbf{r}_1 - \mathbf{r}_2|$), immersed in environment with relative permittivity ϵ_1 and permeability μ_1 , are represented as point-polarizable dipolar scatterers with the

electric (α_e) and magnetic (α_m) polarizabilities given by the first (dipolar) Mie coefficients as in Eq. (2.7). In general, this model can be identified as a realization of the *coupled electric and magnetic dipole method* [103–105].

The induced electric \mathbf{p}_j and magnetic \mathbf{m}_j dipoles in the j th sphere are proportional to the total fields at the position of the point scatterer, $\mathbf{E}_{\text{tot}}(\mathbf{r}_j)$ and $\mathbf{H}_{\text{tot}}(\mathbf{r}_j)$:

$$\mathbf{p}_j = \varepsilon_0 \varepsilon_1 \alpha_e \mathbf{E}_{\text{tot}}(\mathbf{r}_j), \quad \mathbf{m}_j = \alpha_m \mathbf{H}_{\text{tot}}(\mathbf{r}_j). \quad (2.8)$$

The total electric and magnetic fields at any point \mathbf{r} are given by the sum of the incident fields: \mathbf{E}_0 and \mathbf{H}_0 and the electric and magnetic field scattered by the two particles, \mathbf{E}_{sca} and \mathbf{H}_{sca} respectively. For the plane wave illumination, the former are given by:

$$\text{(TE)} \quad \mathbf{E}_0(\mathbf{r}) = E_0 e^{ikz} \hat{\mathbf{x}}, \quad \mathbf{H}_0(\mathbf{r}) = \frac{E_0}{Z} e^{ikz} \hat{\mathbf{y}} \equiv H_0 e^{ikz} \hat{\mathbf{y}}, \quad (2.9a)$$

$$\text{(TM)} \quad \mathbf{E}_0(\mathbf{r}) = E_0 e^{ikz} \hat{\mathbf{y}}, \quad \mathbf{H}_0(\mathbf{r}) = -\frac{E_0}{Z} e^{ikz} \hat{\mathbf{x}} \equiv -H_0 e^{ikz} \hat{\mathbf{x}}, \quad (2.9b)$$

where $Z = \sqrt{\mu_0 \mu_1 / (\varepsilon_0 \varepsilon_1)}$ is the impedance of the medium. $\hat{\mathbf{x}}$ and $\hat{\mathbf{y}}$ are the unit vectors along the \hat{x} and \hat{y} axes, respectively.

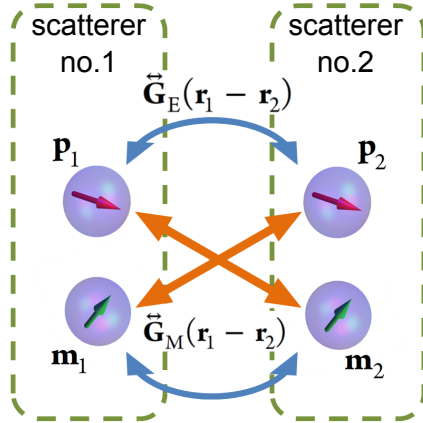


FIGURE 2.8: Schematics of the interaction between the electric (red arrows, \mathbf{p}_1 , \mathbf{p}_2) and magnetic (green arrows, \mathbf{m}_1 , \mathbf{m}_2) dipoles induced in the particles positioned at \mathbf{r}_1 and \mathbf{r}_2 , mediated by the electric ($\overset{\leftrightarrow}{\mathbf{G}}_E$, orange arrows) and magnetic ($\overset{\leftrightarrow}{\mathbf{G}}_M$, blue arrows) Green's functions.

The scattered fields at any position \mathbf{r} are given by

$$\mathbf{E}_{\text{sca}}(\mathbf{r}) = \sum_{j=1,2} \left[\frac{k^2}{\varepsilon_0 \varepsilon_1} \overset{\leftrightarrow}{\mathbf{G}}_E(\mathbf{r} - \mathbf{r}_j) \cdot \mathbf{p}_j + iZk^2 \overset{\leftrightarrow}{\mathbf{G}}_M(\mathbf{r} - \mathbf{r}_j) \cdot \mathbf{m}_j \right], \quad (2.10)$$

$$\mathbf{H}_{\text{sca}}(\mathbf{r}) = \sum_{j=1,2} \left[-\frac{i}{Z} \frac{k^2}{\varepsilon_0 \varepsilon_1} \overset{\leftrightarrow}{\mathbf{G}}_M(\mathbf{r} - \mathbf{r}_j) \cdot \mathbf{p}_j + k^2 \overset{\leftrightarrow}{\mathbf{G}}_E(\mathbf{r} - \mathbf{r}_j) \cdot \mathbf{m}_j \right], \quad (2.11)$$

where $\overset{\leftrightarrow}{\mathbf{G}}_E(\mathbf{r})$ and $\overset{\leftrightarrow}{\mathbf{G}}_M(\mathbf{r})$ denoted the free-space Green's functions which, acting on an arbitrary vector \mathbf{v} give [56, 106]:

$$\overset{\leftrightarrow}{\mathbf{G}}_E(\mathbf{r}) \cdot \mathbf{v} = \left[\left(1 + \frac{i}{kr} - \frac{1}{k^2 r^2} \right) \mathbf{v} + \left(-1 - \frac{3i}{kr} + \frac{3}{k^2 r^2} \right) (\hat{\mathbf{r}} \cdot \mathbf{v}) \hat{\mathbf{r}} \right] g(r), \quad (2.12)$$

$$\overset{\leftrightarrow}{\mathbf{G}}_M(\mathbf{r}) \cdot \mathbf{v} = (\hat{\mathbf{r}} \times \mathbf{v}) \left(i - \frac{1}{kr} \right) g(r). \quad (2.13)$$

$\hat{\mathbf{r}}$ is the unit vector along $\mathbf{r} = \hat{\mathbf{r}}r$ and $g(r) = e^{ikr}/(4\pi r)$ the scalar Green's function. The two Green's functions are related to each other by

$$\overset{\leftrightarrow}{\mathbf{G}}_M \equiv \frac{1}{k} \nabla \times \overset{\leftrightarrow}{\mathbf{G}}_E. \quad (2.14)$$

In the following chapter, we will attribute a physical interpretation to the operator $k^{-1} \nabla \times$.

We can thus write down the self-consistent equations for the coupled dipoles:

$$\begin{pmatrix} \mathbf{p}_1 \\ \mathbf{m}_1 \\ \mathbf{p}_2 \\ \mathbf{m}_2 \end{pmatrix} = \begin{pmatrix} \varepsilon_0 \varepsilon_1 \alpha_e \mathbf{E}_0(\mathbf{r}_1) \\ \alpha_m \mathbf{H}_0(\mathbf{r}_1) \\ \varepsilon_0 \varepsilon_1 \alpha_e \mathbf{E}_0(\mathbf{r}_2) \\ \alpha_m \mathbf{H}_0(\mathbf{r}_2) \end{pmatrix} + \begin{pmatrix} 0 & 0 & \alpha_e \overset{\leftrightarrow}{\mathbf{G}}_E^{(12)} & i\varepsilon_0 \varepsilon_1 \alpha_e Z \overset{\leftrightarrow}{\mathbf{G}}_M^{(12)} \\ 0 & 0 & -\frac{i\alpha_m}{Z\varepsilon_0 \varepsilon_1} \overset{\leftrightarrow}{\mathbf{G}}_M^{(12)} & \alpha_m \overset{\leftrightarrow}{\mathbf{G}}_E^{(12)} \\ \alpha_e \overset{\leftrightarrow}{\mathbf{G}}_E^{(21)} & -i\varepsilon_0 \varepsilon_1 \alpha_e Z \overset{\leftrightarrow}{\mathbf{G}}_M^{(21)} & 0 & 0 \\ -\frac{i\alpha_m}{Z\varepsilon_0 \varepsilon_1} \overset{\leftrightarrow}{\mathbf{G}}_M^{(21)} & \alpha_m \overset{\leftrightarrow}{\mathbf{G}}_E^{(21)} & 0 & 0 \end{pmatrix} \begin{pmatrix} \mathbf{p}_1 \\ \mathbf{m}_1 \\ \mathbf{p}_2 \\ \mathbf{m}_2 \end{pmatrix}, \quad (2.15)$$

where

$$\overset{\leftrightarrow}{\mathbf{G}}_E^{(12)} \equiv \overset{\leftrightarrow}{\mathbf{G}}_E(\mathbf{r}_1 - \mathbf{r}_2), \quad \overset{\leftrightarrow}{\mathbf{G}}_M^{(12)} \equiv \overset{\leftrightarrow}{\mathbf{G}}_M(\mathbf{r}_1 - \mathbf{r}_2), \quad (2.16a)$$

and

$$\overset{\leftrightarrow}{\mathbf{G}}_E^{(21)} \equiv \overset{\leftrightarrow}{\mathbf{G}}_E(\mathbf{r}_2 - \mathbf{r}_1), \quad \overset{\leftrightarrow}{\mathbf{G}}_M^{(21)} \equiv \overset{\leftrightarrow}{\mathbf{G}}_M(\mathbf{r}_2 - \mathbf{r}_1). \quad (2.16b)$$

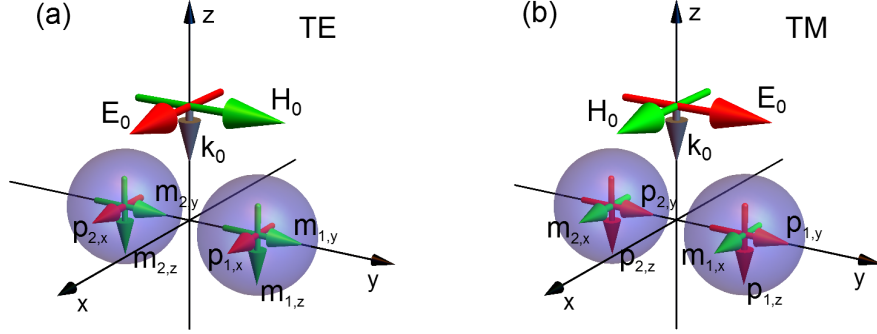


FIGURE 2.9: Schematic representation of the dipolar system used to model the electromagnetic response of the silicon sphere dimer. Red (green) arrows on the spheres correspond to the induced electric (magnetic) dipoles. For the TE polarization in (a) (TM in (b)) the magnetic (electric) dipoles along the z -axis are the secondary dipoles induced by the field of the primary electric (magnetic) dipoles p_x (m_x), and are not directly excited by the incoming plane wave.

2.3.1.1 Transverse-magnetic illumination

The general equation shown above can be solved without any incident illumination, offering the description of the eigenmodes of the system. Such approach has been recently used to find the fundamental modes of strongly coupled trimers [107, 108] and quadrumers [109] of dielectric scatterers. Here however, we will arbitrarily assume a TM illumination scheme, shown schematically in Fig. 2.9(b), to simplify the calculations and learn about the polarization-selectivity of the system. In such setup, the only non-vanishing components of the induced dipoles are shown in Fig. 2.9(b) with red (p_y , p_z) and green (m_x) arrows. Equation (2.15) can be then rewritten using the properties of the Green's functions:

$$\overset{\leftrightarrow}{\mathbf{G}}_E(\mathbf{r}_1 - \mathbf{r}_2) \cdot \hat{\mathbf{x}} = \left(1 + \frac{i}{kD} - \frac{1}{k^2 D^2}\right) g(D) \hat{\mathbf{x}} \equiv -g_{xx} \hat{\mathbf{x}}, \quad (2.17)$$

$$\overset{\leftrightarrow}{\mathbf{G}}_M(\mathbf{r}_1 - \mathbf{r}_2) \cdot \hat{\mathbf{x}} = -\left(i - \frac{1}{kD}\right) g(D) \hat{\mathbf{z}} \equiv g_{zx} \hat{\mathbf{z}}, \quad (2.18)$$

$$\overset{\leftrightarrow}{\mathbf{G}}_E(\mathbf{r}_1 - \mathbf{r}_2) \cdot \hat{\mathbf{z}} = \left(1 + \frac{i}{kD} - \frac{1}{k^2 D^2}\right) g(D) \hat{\mathbf{z}} \equiv -g_{zz} \hat{\mathbf{z}}, \quad (2.19)$$

$$\overset{\leftrightarrow}{\mathbf{G}}_M(\mathbf{r}_1 - \mathbf{r}_2) \cdot \hat{\mathbf{z}} = \left(i - \frac{1}{kD}\right) g(D) \hat{\mathbf{x}} \equiv -g_{zx} \hat{\mathbf{x}}, \quad (2.20)$$

$$\overset{\leftrightarrow}{\mathbf{G}}_E(\mathbf{r}_1 - \mathbf{r}_2) \cdot \hat{\mathbf{y}} = \left(-\frac{2i}{kD} + \frac{2}{k^2 D^2}\right) g(D) \hat{\mathbf{y}} \equiv g_{yy} \hat{\mathbf{y}}, \quad (2.21)$$

$$\overset{\leftrightarrow}{\mathbf{G}}_M(\mathbf{r}_1 - \mathbf{r}_2) \cdot \hat{\mathbf{y}} = 0, \quad (2.22)$$

yielding the following equations

$$p_{1y} = \varepsilon_0 \varepsilon_1 \alpha_e E_0 + \alpha_e k^2 g_{yy} p_{2y}, \quad (2.23)$$

$$p_{2y} = \varepsilon_0 \varepsilon_1 \alpha_e E_0 + \alpha_e k^2 g_{yy} p_{1y}, \quad (2.24)$$

$$p_{1z} = -\alpha_e k^2 g_{xx} p_{2z} + i \varepsilon_0 \varepsilon_1 \alpha_e Z k^2 g_{zx} m_{2x}, \quad (2.25)$$

$$p_{2z} = -\alpha_e k^2 g_{xx} p_{1z} - i \varepsilon_0 \varepsilon_1 \alpha_e Z k^2 g_{zx} m_{1x}, \quad (2.26)$$

$$m_{1x} = -\frac{\alpha_m}{Z} E_0 + i \frac{\alpha_m}{Z} \frac{k^2}{\varepsilon_0 \varepsilon_1} g_{zx} p_{2z} - \alpha_m k^2 g_{xx} m_{2x}, \quad (2.27)$$

$$m_{2x} = -\frac{\alpha_m}{Z} E_0 - i \frac{\alpha_m}{Z} \frac{k^2}{\varepsilon_0 \varepsilon_1} g_{zx} p_{1z} - \alpha_m k^2 g_{xx} m_{1x}. \quad (2.28)$$

We have marked the terms of particular interest, which describe the *heterogeneous* electric-magnetic interactions between the p_{jz} and $m_{j'x}$ dipoles ($j \neq j'$). Note that these modes are enabled by the coupling of the incident light to the $m_{j'x}$ dipoles, which in turn (through the magnetic Green's function $\overset{\leftrightarrow}{\mathbf{G}}_M$) excite the secondary p_{jz} dipoles. Furthermore, the terms proportional to g_{xx} and g_{zz} describe the interaction between parallel dipoles of homogeneous nature and, finally, the terms proportional to E_0 correspond to the single-particle excitations induced directly by the incident light.

The solution to the above set of equations can be elegantly expressed by introducing *dressed polarizabilities* $\tilde{\alpha}$, defined as

$$\tilde{\alpha}_{ey} \equiv \frac{\alpha_e}{1 - \alpha_e k^2 g_{yy}}, \quad \tilde{\alpha}_{ez} \equiv \frac{\alpha_e}{1 - \alpha_e k^2 g_{xx}}, \quad \tilde{\alpha}_{mx} \equiv \frac{\alpha_m}{1 + \alpha_m k^2 g_{xx}} \quad (2.29)$$

$$\tilde{\alpha}_{e-m, TM} \equiv \frac{\tilde{\alpha}_{mx} \tilde{\alpha}_{ez} k^2 g_{zx}}{1 - \tilde{\alpha}_{mx} \tilde{\alpha}_{ez} k^4 g_{zx}^2}, \quad (2.30)$$

and relating

$$p_{1y} = p_{2y} = \varepsilon_0 \varepsilon_1 \tilde{\alpha}_{ey} E_0, \quad (2.31)$$

$$p_{1z} = -p_{2z} = -i \varepsilon_0 \varepsilon_1 \tilde{\alpha}_{e-m, TM} E_0, \quad (2.32)$$

$$m_{1x} = m_{2x} = \left[-\frac{\tilde{\alpha}_{mx}}{Z} - (\tilde{\alpha}_{e-m, TM} k^2 g_{zx}) \frac{\tilde{\alpha}_{mx}}{Z} \right] E_0. \quad (2.33)$$

The respective dressed polarizabilities $\tilde{\alpha}_{ex}$, $\tilde{\alpha}_{my}$, and $\tilde{\alpha}_{e-m, TE}$ can be found for the case of TE polarization of the incident light and the induced components of the dipoles p_x , m_y and m_z (see Fig. 2.9(a)).

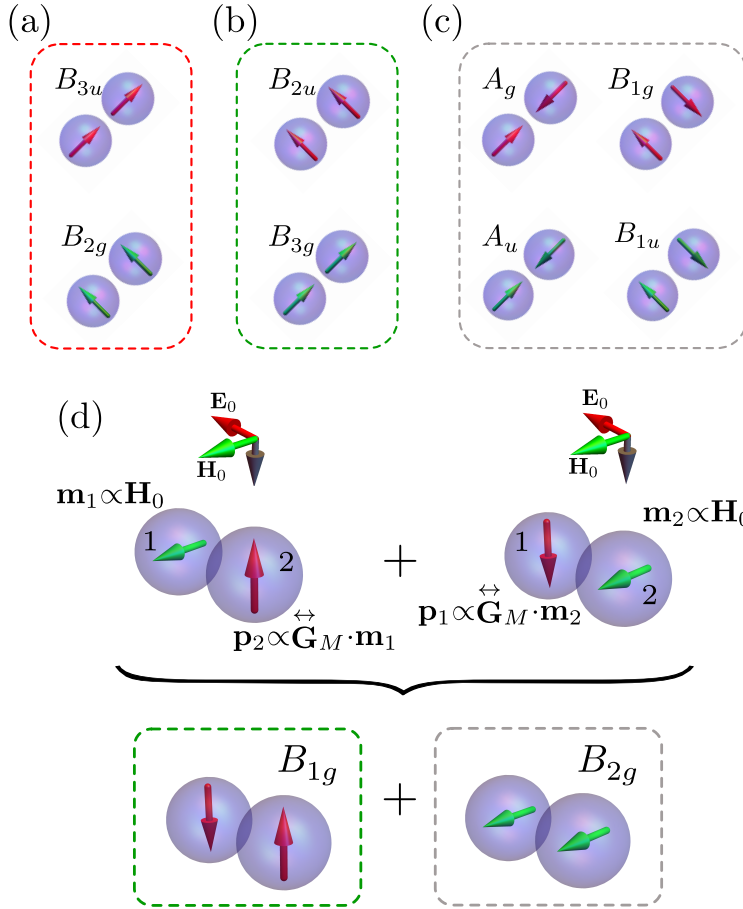
2.3.1.2 Dimer symmetry group D_{2h} 

FIGURE 2.10: Schematic representation of the irreducible representations of the D_{2h} dimer symmetry group and their coupling to the incident planewave. (a) Modes B_{3u} and B_{2g} are directly excited by the incident TM-polarized light as they exhibit non-vanishing total dipoles parallel to the respective components of the incident light. (b) Similarly, modes B_{2u} and B_{3g} couple to the incident TE-polarized light. While the remaining homogeneous modes shown in (c) do not directly couple to light in any of those polarizations, the B_{1g} and B_{1u} can be excited indirectly due to the coupling between the scatterers. (d) Schematic of the coherent homogeneous modes in which the magnetic dipoles are induced in the "1" (left) or "2" (right) sphere by the incident magnetic field \mathbf{H}_0 . The magnetic Green's function \mathbf{G}_M then couples this dipole to the perpendicular, electric dipole in the other sphere. The coherent sum of these two modes can be rewritten as the coherent sum of two modes B_{1g} and B_{2g} .

In a slightly more pictorial manner, we can consider the modes of the dimer as irreducible representations of the dimer symmetry group D_{2h} . While this approach allows for a detailed analysis of the symmetries of the modes, we will use it predominantly to simplify the description presented above. For an interesting example of a more elaborate analysis, we note the recent contributions in Refs. [107,109]. We have gathered these

representations in Fig. 2.10. and grouped them by their ability to couple directly to the normally incident (a) TM- or (b) TE-polarized planewave.

The remaining modes, depicted in (c), cannot couple directly to normally incident, linearly-polarized light. However, as we discuss below, two of them - B_{1g} and B_{1u} - will contribute to the extinction cross-section of the dimer through the mechanics shown schematically in Fig. 2.10(d) for the former case of mode B_{1g} : in the scheme on the left, the incident magnetic field of TM polarization induces a magnetic dipole in one of the spheres (\mathbf{m}_1) which in turn, through the Green's function $\overset{\leftrightarrow}{\mathbf{G}}_M$, induces the electric excitation in the other sphere (\mathbf{p}_2). Similarly, the magnetic mode \mathbf{m}_2 in the second sphere can induce the electric excitation \mathbf{p}_1 in the first sphere. As a result, the two coherently excited dimer modes can be decomposed into a sum of B_{1g} and B_{2g} , as depicted in the bottom schematics of Fig. 2.10(d).

In a similar manner, under TE polarization, the coherent sum of heterogeneous modes leads to the excitation of complementary modes B_{2u} and B_{1u} .

The expressions for the extinction cross-sections of such dimers have been derived in Ref. [7] from the optical theorem by considering the scattering amplitude in the forward direction by the induced dipoles in the $\hat{x}\hat{y}$ plane (dipoles p_{jz} and m_{jz} do not radiate along the z axis):

$$\text{(TE)} \quad \sigma_{ext} = 2k\text{Im} \left[\tilde{\alpha}_{my} + \tilde{\alpha}_{px} + \left(\tilde{\alpha}_{e-m,TE} k^2 g_{zx} \right) \tilde{\alpha}_{px} \right] \quad (2.34a)$$

$$\text{(TM)} \quad \sigma_{ext} = 2k\text{Im} \left[\tilde{\alpha}_{ey} + \tilde{\alpha}_{mx} + \left(\tilde{\alpha}_{e-m,TM} k^2 g_{zx} \right) \tilde{\alpha}_{mx} \right]. \quad (2.34b)$$

In Fig. 2.11 we plot the extinction cross sections of a dimer of dielectric spheres with 150 nm radii, calculated with Eq. (2.34b) (solid blue lines) and using the exact FDTD method [83] (dashed blue lines) for two dimer gaps of 10 nm and 50 nm, respectively and normally incident TM polarization. The two methods yield very similar results for both separation distances, except for the presence of the quadrupolar peak around a wavelength of 800 nm. Within the analytical model, the contributions to the extinction can be separated, displaying the extinction due to the homogeneous electric B_{3u} (dashed red lines) and magnetic B_{2g} (dashed green lines) homogeneous modes. The significant contribution from the heterogeneous modes is marked with black lines which is particularly relevant in the case of the small gap (Fig. 2.11(b)), exhibiting a double-peak structure. This

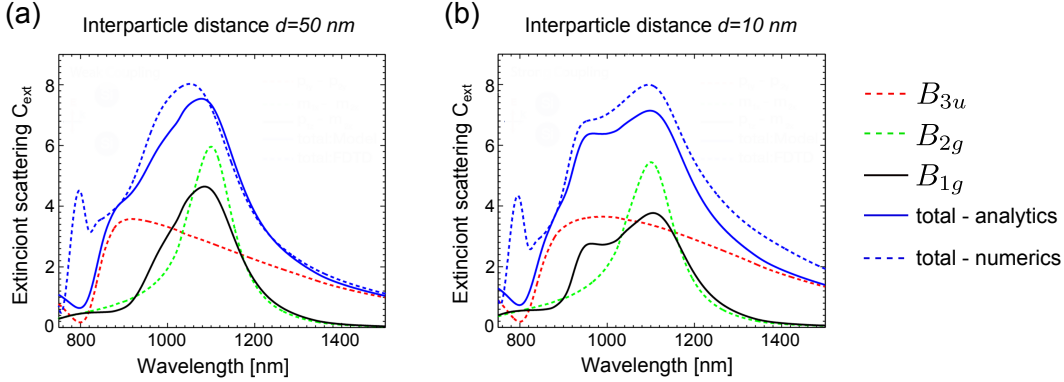


FIGURE 2.11: Extinction spectra of a dimer of silicon particles of 150 nm radii under TM polarization (see Fig. 2.9(b) for schematics) with the gap separations of (a) 10 nm and (b) 50 nm, calculated using the dipole-dipole model (solid blue line) and compared with numerical results obtained from FDTD calculations [83] (dashed blue line). Our model (Eq. (2.34b)) allows us to dissect the contributions from the B_{3u} (red dashed line), B_{2g} (green dashed line) and B_{1g} (black solid line) modes, displayed in Fig. 2.10.

shape stems from the fact that, as we have noted above, the coherent excitation of heterogeneous modes leads to the simultaneous excitation of both B_{2g} and B_{1g} .

We have thus developed a simple dipole-dipole interaction model to address the optical far-field response of a dimer of dielectric particles. Within this model, we have predicted the onset of the heterogeneous electric-magnetic modes, induced indirectly by an incident planewave, and quantified their contribution to the extinction spectra of the dimer structure. Considerations based on the theory of symmetry groups can help to design and guide the engineering of magnetic models in high-refractive index photonics materials.

2.3.2 Experimental realization of scattering of light on dielectric dimers

The experimental confirmation of the theoretical predictions described in the previous section of this thesis has been, until recently, hampered by the shortage of methods for generation and positioning of spherical Si nanoparticles. One of the few methods which addresses these problems was developed in the group of Prof. Boris Chichkov in *Laser Zentrum* in Hannover (LZH), who proposed to apply the laser printing technique, used previously for generating metallic nanoparticles, to dielectric systems [110]. This technology relies on femtosecond laser printing of Si nanoparticles onto a glass receiver substrate using silicon-on-insulator (SOI) wafers as laser targets.

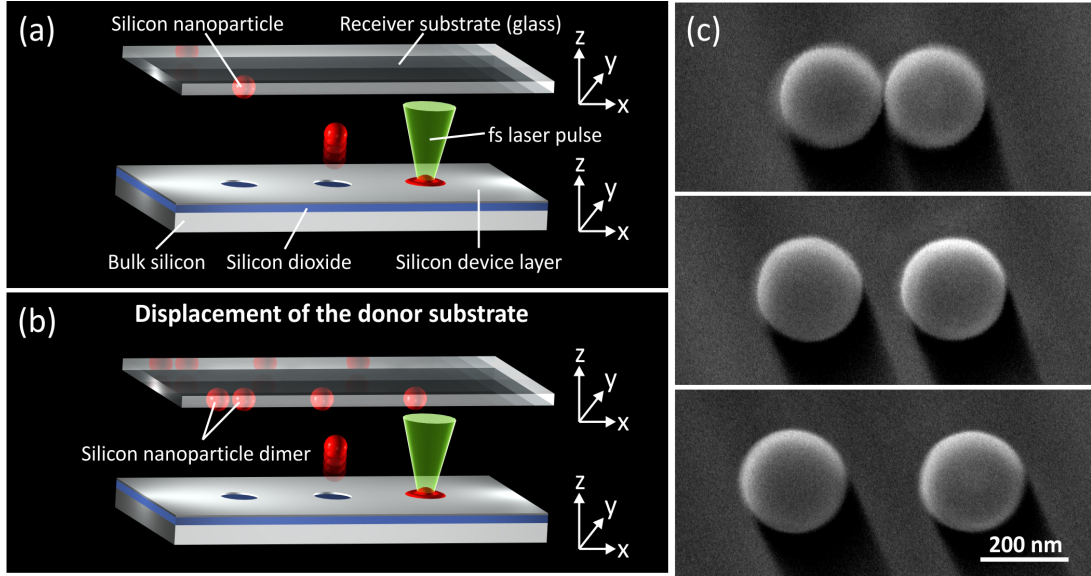


FIGURE 2.12: (a) Schematic illustration of femtosecond laser printing of nanoparticles. A silicon-on-insulator (SOI) wafer was used as a target to transfer spherical Si nanoparticles from a 50 nm crystalline Si layer onto the transparent glass receiver substrate. (b) To print Si nanoparticle dimer structures, one can displace either the target material or the receiver substrate. (c) SEM-images of the Si nanoparticle dimer structures obtained on a glass substrate. Experimental implementation at the Laser Zentrum in Hannover.

2.3.2.1 Experimental details

A schematic illustration of the generation of nanoparticles and nanoparticle dimer structures in LZH is shown in Fig. 2.12. First, silicon nanoparticles are transferred by single femtosecond laser pulse irradiation of an SOI substrate toward a glass receiver substrate (Fig. 2.12(a)). Subsequently, the SOI substrate is shifted relative to the receiver substrate. By repeating the printing process, silicon nanoparticle dimer structures with varying interparticle distances are realized (Fig. 2.12(b)). Initially, these structures are in the amorphous phase (a-Si). By additional single-pulse laser irradiation, the amorphous nanoparticles can be controllably transformed into crystalline particles (c-Si). The resulting silicon nanoparticle dimer structures consist of two identical nanoparticles, as shown in the SEMS images of Fig. 2.12(c).

In Fig. 2.13 we show the polarization-resolved dark-field scattering spectra of the dimer structures with a gap separation of 375 nm (a,b) and 5 nm (c,d), illuminated by light polarized perpendicularly (a,c) or parallelly (b,d) to the long axis of the dimer. These two setups correspond to the TE and TM polarization schemes, respectively, discussed in

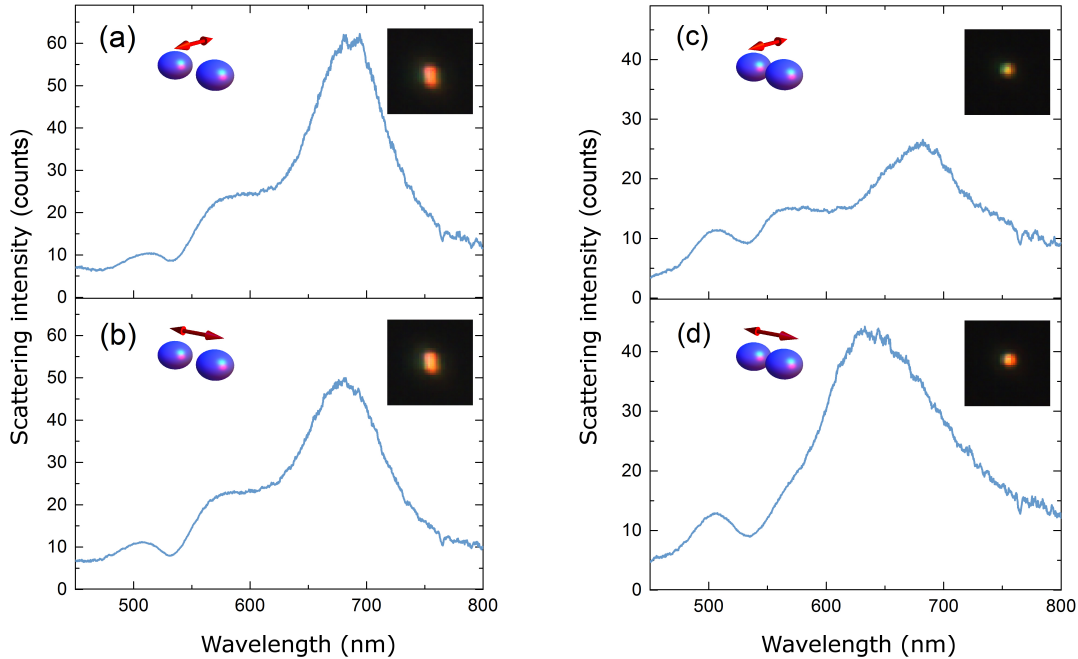


FIGURE 2.13: Scattering spectra of crystalline silicon nanoparticle dimer structures for incident light polarized perpendicular (a,c) and parallel (b,d) to the axis of the dimer structure, as displayed in the insets. The distance between the nanoparticle surfaces is 375 nm (a,b) and 5 nm (c,d) and was measured using SEM image analysis software with a standard deviation of 0.8 nm. Insets show the dark scattering images of the corresponding dimer structures. Measurements were carried out at the Laser Zentrum in Hannover.

the previous section. Measurements of the Si nanoparticle dimer structure with an interparticle distance of about 375 nm reveal no significant difference in the spectral position of the scattering peaks for different polarizations (see Fig. 2.13(a) and (b)) indicating a weak electromagnetic interaction between the nanoparticles in well-separated dimers. In contrast, scattering measurements for the case of a small interparticle distance (5 nm) demonstrate a significant difference between the two types of polarization (see Fig. 2.13(c) and (d)). For light polarized parallel to the major dimer axis a single broad scattering peak emerges (Fig. 2.13(d)) between the two resonant features observed for perpendicular polarization (Fig. 2.13(c)).

The exact shape and geometries of the nanoparticles cannot be read out from the SEM images exclusively, as the nanoparticles suffer deformation during the impact against the SOI wafer. Furthermore, as pointed out in Refs. [111] and [8], the outer layer of silicon oxidizes, forming a SiO_2 coating. To address these effects, below we present a detailed discussion of how the flattening and oxidation of Si nanospheres influence the position of

the electric and magnetic dipolar resonances, deriving a protocol to determine the most suitable parameters to describe the morphology of the experimentally obtained sample.

2.3.2.2 Numerical analysis of single nanoparticle scattering

The optical response of a single c-Si scatterer can be influenced by many different factors such as the presence of the substrate, the oxidation of the outer layer of the particle or its departure from the spherical shape. Therefore, before we attempt to unravel the optical response of the dimer structures shown in Fig. 2.13, let us consider a single c-Si nanoparticle. To this goal, in Fig. 2.14 and in the following paragraphs we present a careful numerical analysis of the effects listed above. The dielectric function of crystalline silicon was taken from the literature [112].

Presence of the substrate

The black solid line in Fig. 2.14(a) denotes the scattering cross section of a c-Si nanoparticle of 97 nm radius in air, with two dominant contributions: electric and magnetic dipolar modes marked with the green and red lines, respectively. As previously reported [111], the spectral positions of the lowest-order Mie resonances in dielectric spheres are rather insensitive to the presence of a substrate (dashed line). This is mostly due to the localization of the displacement currents inside the dielectric material. We observe this effect in Fig. 2.14(a), where both the dipolar electric and magnetic resonances of a 97 nm radius c-Si nanosphere peak at 600 nm and 750 nm independently of the presence of the silica substrate.

Oxidation of the particle

Silicon nanoparticles undergo oxidation of their outer layers, a process that leads to the formation of a core-shell nanoparticle with a shrunken c-Si core and a silica shell. Since the refractive index of silica is significantly lower than that of the c-Si, the optical response of the nanoparticle is primarily determined by the c-Si core. In Fig. 2.14(b) we show how the optical features blue-shift with the shell thickness h increasing from 0 nm (black line) to 8 nm (blue line), and simultaneously decreasing the core radius from 97 nm to 89 nm.

Distorting the shape of nanoparticle

Silicon nanoparticles formed in the printing process are not ideally spherical, but rather

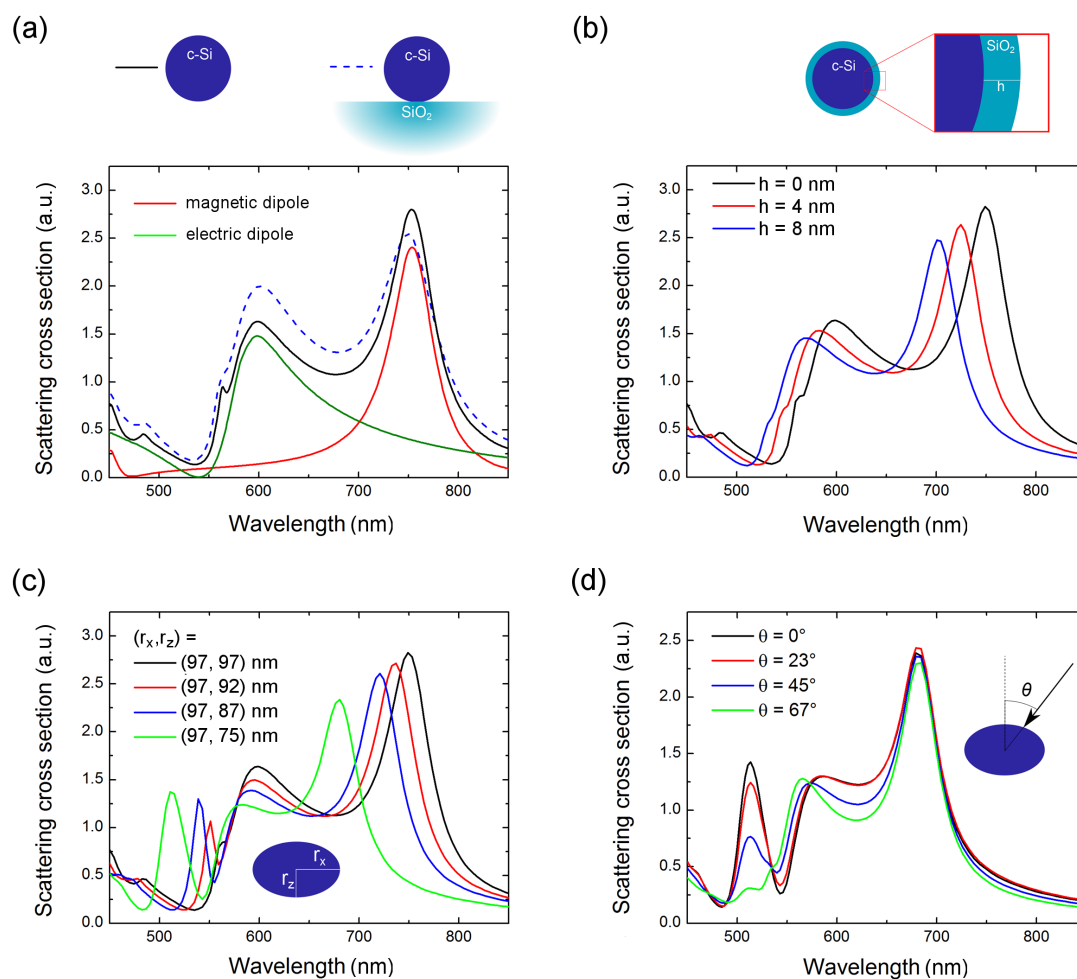


FIGURE 2.14: Calculated scattering cross sections of single dielectric scatterers. (a) Scattering by a c-Si nanosphere of 97 nm radius (black solid line) dominated by the electric dipolar (green line) and magnetic dipolar (red line) contributions. Spectral positions of these resonances are largely insensitive to the presence of the silica substrate (dashed line). (b) Oxidation of the outer layer of the nanoparticle of thickness h significantly blue-shifts all of the spectral features. (c) Contraction of the c-Si scatterer along the \hat{z} axis selectively blue-shifts magnetic resonances. See definitions of r_x and r_z in the inset. (d) By modifying the illumination angle, it is possible to selectively tune the strength of higher order resonances. Here, calculations for the oblate spheroid described by $(r_x, r_z) = (97, 75)$ nm are shown.

take on a form of oblate spheroids. As shown in Fig. 2.14(c), such lowering of the symmetry of the scatterers influences the electric and magnetic dipolar modes slightly differently. Specifically, contracting the nanoparticle along the illumination direction (changing r_z) shifts the low-energy magnetic and high-energy electric modes by 70 nm and 20 nm, respectively. This is clearly a very different behavior with respect to the homogeneous shift induced by the formation of the oxide layer. A similar analysis of the geometrical parameters of nanodisks and their effect on the optical response can be found in Ref. [95].

Angled incidence

To model the dark-field scattering microscopy scheme, we present the spectra obtained for varying illumination angles. As observed in Fig. 2.14(d), changing the angle of illumination modifies the relative intensity of the resonances. For instance, it is possible to eliminate the scattering from the 525 nm mode (quadrupolar magnetic) for grazing incidence.

Considering all the effects reported above, we have estimated the optimal parameters that correctly describe the spectral features of the optics of the single scatterers prepared by laser printing. This will set up the morphology of the system to further study the interaction in the dimer structure. We will hence describe the nanoparticles as ellipsoidal core(c-Si)-shell(SiO_2) structures with major and minor core radii of 95 and 78 nm, respectively, and a 4 nm oxide layer.

2.3.2.3 Numerical analysis of the dimer scattering

Let us now proceed to analyze the optical response of dimer structures and its dependence on the separation between the scatterers and on the polarization of the incident light. In Figs. 2.15(b) and 2.16(b) we present the experimental (black lines) and calculated (solid red lines) scattering intensities of dimer structures with varying dimer separations d ranging from 320 nm (tops) to 5 nm (bottom plots), illuminated by the normally incident light with TM (Fig. 2.15) and TE (Fig. 2.16) polarizations. For each spectrum we have also calculated numerically the strengths of the dipoles induced in each of the nanoparticles (\mathbf{p}_i , \mathbf{m}_i for $i = 1, 2$) by integrating the polarization \mathbf{P} ($\mathbf{p}_i = \int_{V_i} \mathbf{P} dV$) and polarization currents \mathbf{J} ($\mathbf{m}_i = \frac{1}{2} \int_{V_i} \mathbf{r} \times \mathbf{J} dV$) inside the volume of

the i -th particle V_i . Having obtained these quantities, we have calculated the contribution to the scattering intensity from the different dimer modes, which were introduced in the discussion of the analytical model, in Section 2.3.1.1.

For example, for the TM polarization (Fig. 2.15) the scattering from the bonding mode of the electric dipoles B_{3u} (dashed green line) is dominant for all the dimer separations d , and it red-shifts with decreasing d , similarly to the electric bonding modes of plasmonic dimer antennas. Simultaneously, the magnetic mode B_{2g} , denoted with a dashed orange line, blue-shifts and decreases significantly in intensity. We should note here that this shift is not monotonous and might point to a more complex near-field interaction not described within this model. Finally, we can consider the B_{1g} mode which, as shown earlier, can couple to light (blue dashed line) through the excitations of the heterogeneous modes, each comprising one electric and one magnetic dipole. Similarly as in the analytical spectra shown in Fig. 2.11, this last mode exhibits a double-peak structure.

The resulting hybridization scheme shown in Fig. 2.15(a), which - unlike the corresponding schemes drawn for electric-only excitations in plasmonic nanoparticles - contains the homogeneous magnetic mode B_{2g} and the heterogeneous modes which give rise to the B_{1g} mode.

The numerical calculations reveal a remarkable agreement with the experimental results (see comparison in Fig. 2.15(b)). Importantly, this close correspondence allows us to identify the small contribution in the experimental results around 570 nm, for a small $d = 5$ nm separation, as due to the effects of the excitation of the heterogeneous modes. The slight deviation in the intensities of the features most likely stems from the particular situation of the setup of the dark-field microscope, i.e., the finite aperture and the non-normal incidence of light.

A similar analysis can be conducted for the TE polarization of the incident light (electric field normal to the dimer axis). The hybridization scheme shown in Fig. 2.16 reveals the emergence of two homogeneous modes: electric B_{2u} and bonding magnetic B_{3g} , both induced directly by the incident light, as well as the pair of heterogeneous modes which give rise to the excitation of the magnetic B_{1u} mode. The decomposition of the scattering intensity in Fig. 2.16(b) reveals the evolutions of the modes as indicated by the hybridization scheme (Fig. 2.16(a)), with the red-shifting B_{1u} (dashed blue) and B_{3g} (dashed orange) and blue-shifting B_{2u} (dashed green) modes. As in the previous case, the agreement between the experimental and numerical results is very good, including

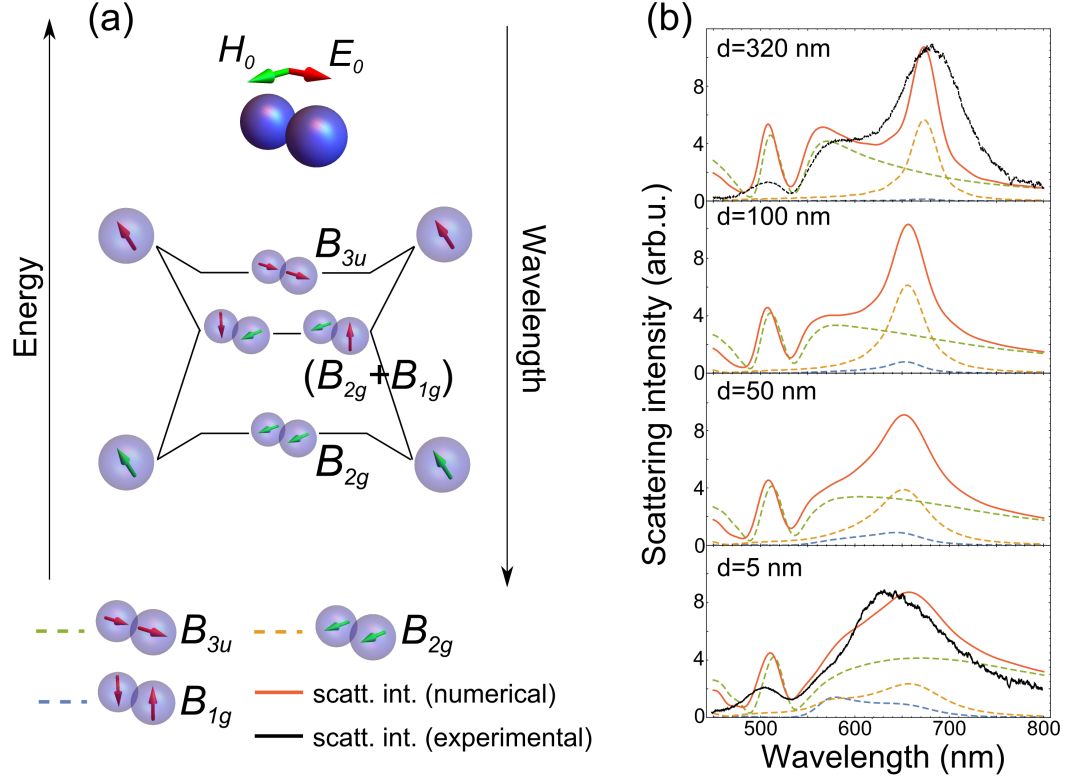


FIGURE 2.15: Scattering of normally incident light with electric field along the axis of a dimer of silicon scatterers. (a) Energy-level diagram describing the hybridization of electric (red arrows) and magnetic (green arrows) dipolar resonances of single scatterers with the representations of the D_{2h} symmetry group: B_{3u} , B_{1g} and B_{2g} . (b) Calculated scattering intensities of dimer structures (solid red line) for separations of $d = 320$, 100, 50 and 5 nm (top to bottom) compared to the experimental results (black line). The spectra are decomposed according to the hybridization scheme of electric and magnetic modes: B_{3u} (green dashed line), B_{1g} (blue dashed line) and B_{2g} (orange dashed line). Each single scatterer is an oblate ellipsoidal core(c-Si)-shell(SiO_2) structure with major and minor external radii of 95 and 78 nm, respectively, and a 4 nm oxide layer.

an emergence of the heterogeneous mode at around 710 nm for the smallest separation (blue dashed line contribution in the bottom spectrum).

The additional resonant feature at a wavelength of 510 nm (see Figs. 2.15 and 2.16) is weakly dependent on the separation of the dimers for both polarizations of light, pointing to the multipolar character of this excitation.

2.3.2.4 Conclusion

As a summary, we have investigated dimers of sub-micrometer crystalline silicon nanoparticles with different interparticle distances, ranging from 5 nm to 375 nm. The dimers

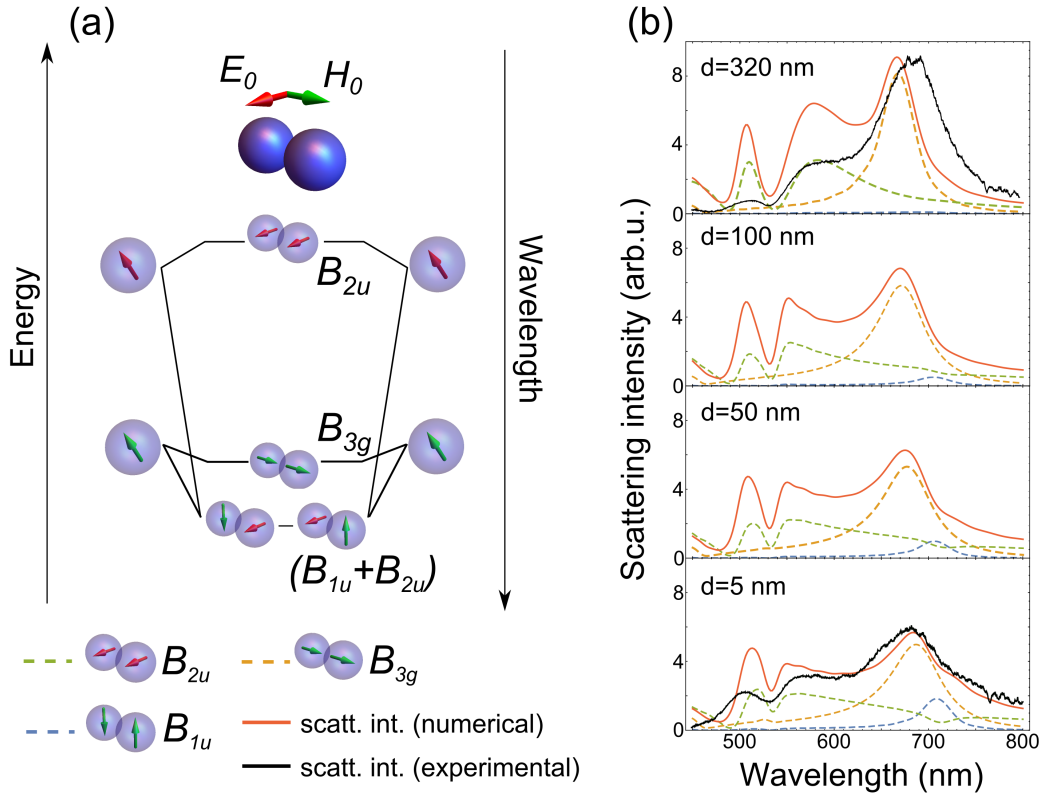


FIGURE 2.16: Scattering of normally incident light with electric field perpendicular to the axis of a dimer of silicon scatterers. (a) Energy-level diagram describing the hybridization of electric (red arrows) and magnetic (green arrows) dipolar resonances of single scatterers with the representations of the D_{2h} symmetry group: B_{2u} , B_{3g} and B_{1u} . (b) Calculated scattering intensities of dimer structures (solid red line) for separations of $d = 320, 100, 50,$ and 5 nm (top to bottom) compared to the experimental results (black line). The spectra are decomposed according to the hybridization scheme of electric and magnetic modes: B_{2u} (green dashed line), B_{1u} (blue dashed line) and B_{3g} (orange dashed line). Scatterers are identical to those used in Fig. 2.15.

have been fabricated on a glass substrate by a laser printing method which has been recently developed for Si nanoparticles with resonant optical responses.

For small interparticle distances the electric and magnetic dipolar modes of single scatterers hybridize and form homogeneous electric-electric, magnetic-magnetic, and more complex heterogeneous electro-magnetic modes, following the hybridization scheme discussed herein. These findings are reproduced very accurately by numerical simulations, which further allowed us to access information about the exact shape and composition of the scatterers. We conclude that tunable and strongly interacting dielectric dimers are a versatile tool for studying the coupling of light in dielectric nanostructures.

2.3.3 Control of single emitters

As we have shown in the Section 2.2, single dielectric nanoparticles can serve as efficient platforms to enhance the electric and magnetic emission from dipolar emitters. Below we briefly describe how such systems can be improved by adding a second nanoparticle, thus effectively placing the emitter in the gap of a dielectric dimer. We should note that these results include the description of non-radiative processes, which we have neglected when considering lossless single particle nanoantennas. To account for this effect, the real constant refractive index of silicon was replaced with the dispersive function from Palik [112].

In Fig. 2.17 we show the spectra of the radiative decay rate enhancement $\Gamma_{\text{sca}}/\Gamma_0$ and the quantum efficiency Q defined as

$$Q = \frac{\Gamma_{\text{sca}}}{\Gamma_{\text{tot}}} \quad (2.35)$$

for (a) electric and (b) magnetic dipolar emitters, placed at the center of 10 nm (red lines), 50 nm (green lines) and 200 nm (blue lines) gaps between two silicon spheres of 150 nm radii each. The emitters are oriented either along (left panels) or perpendicularly (right panels) to the symmetry axis, as shown in the corresponding insets.

Spectra of the radiative enhancement rates of the electric dipolar emitter shown in Fig. 2.17(a) exhibit selective coupling to the modes of the dimer structure, which we have described earlier. For an orientation of the electric dipolar emitter along the symmetry axis (left panel in Fig. 2.17(a)) the spectrally broad and strong enhancement is due to coupling with the bonding B_{3u} mode of the dimer (see schematics in Fig. 2.10). For perpendicular orientation (right panel in Fig. 2.17(a)) the enhancement is given predominantly by the magnetic mode B_{1u} , although we can expect from the symmetry considerations a contribution from the electric B_{2u} resonance. For the smallest gap widths (red lines), at resonance wavelengths, the radiative decay rate is enhanced by up to 300 (left panel in Fig. 2.17(a), $\lambda = 1300$ nm) and 12 (right panel in Fig. 2.17(a), $\lambda = 800$ nm), depending on the emitter's orientation, while retaining quantum efficiencies over 0.1.

For the magnetic emitter oriented along the symmetry axis of the dielectric dimer antenna (left panel in Fig. 2.17(b)), we obtain the strongest enhancement of the radiation rate (up to 250 for 10 nm separation) due to coupling to the quadrupolar magnetic mode at a wavelength of 810 nm, and a large enhancement (up to 100, around a wavelength

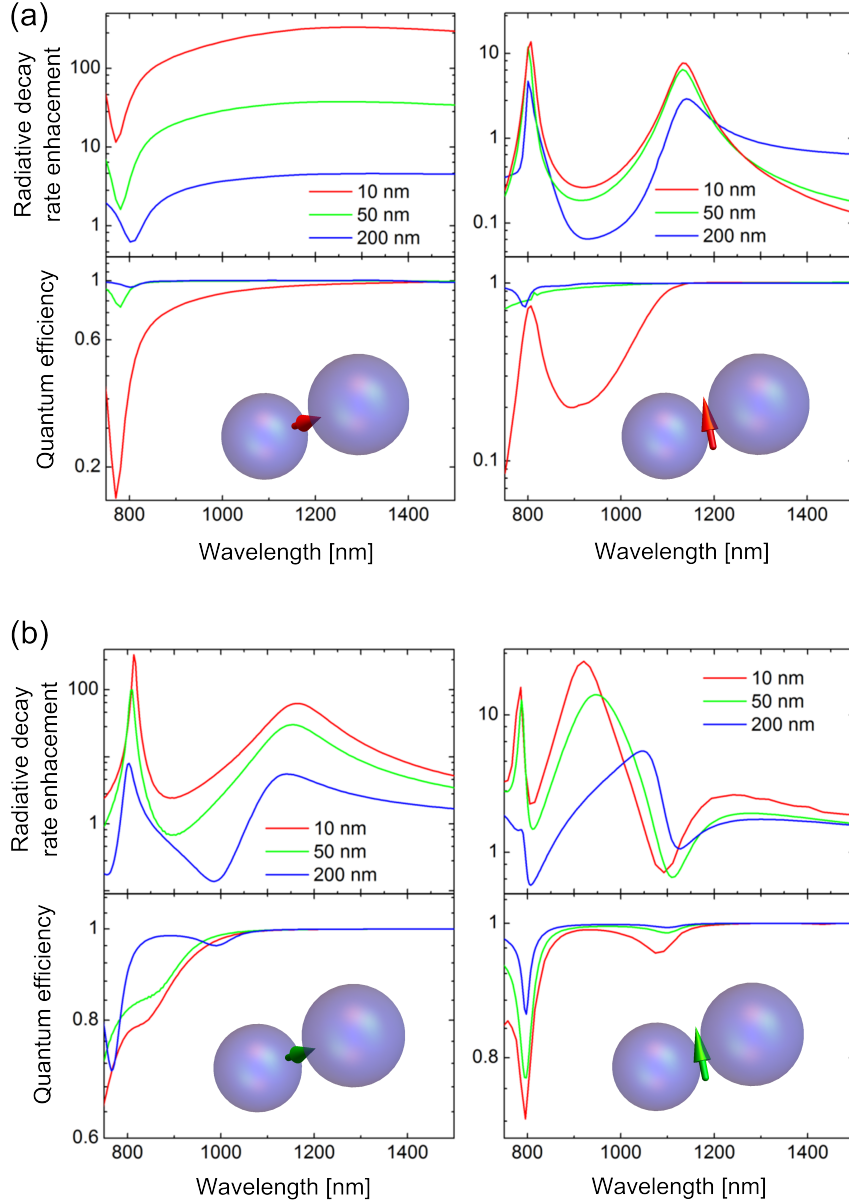


FIGURE 2.17: Enhancement of the radiative decay rate and quantum efficiency of an (a) electric and (b) magnetic dipolar emitter positioned at the center of a gap of a silicon dimer formed by two spheres of 150 nm radius. For the electric emitter, the enhancement is given predominantly by the coupling to the electric B_{3u} mode for the orientation of the emitter along the axis (left panel in (a)) or the interplay of the dominant magnetic mode B_{1u} and a weak electric B_{2u} for the perpendicular dipole (right panel in (a)). Similarly, the magnetic emitter couples to the B_{3g} mode when oriented along the axis (left panel in (b)) and both B_{1g} and B_{2g} modes. Orientations of the emitters are shown in the schematics. Gap widths are given in the legends.

of 1150 nm) from the B_{3g} mode of the dimer. Significantly weaker enhancements (up to 25) are obtained for the emitter oriented perpendicularly to the dimer axis (right

panel in Fig. 2.17(b)), as a result of the interplay of the electric B_{1g} and magnetic B_{2g} excitations.

The quantum efficiency of the emitter is primarily governed by the extinction coefficient of silicon, which grows steadily for energies above around 1 eV. Furthermore, significant dips in the quantum efficiency can be qualitatively assigned to the dips in the radiative rate enhancement.

It is worth to mention that, in some frequency ranges, the emission rates, for both electric (Fig. 2.17(a)) and magnetic (Fig. 2.17(b)) emitters, are strongly reduced. For very small gap widths, this suppression of radiative decays coincides with a low quantum efficiency. However, inhibition of spontaneous emission does not necessarily correlate with quantum efficiency as it can be seen from our results for large gap widths. Notice that emission rates are constrained by specific sum rules derived from the Kramers-Kronig relationship [113, 114]. In particular, any reduction in spontaneous emission rate over some range of wavelengths must necessarily be compensated by an increase over some other range of frequencies. Dips in the emission rates observed in all the cases considered in Fig. 2.17 could also be found even for a single lossless sphere, where quantum efficiency is 1, as discussed in Ref. [15] and Section 2.2. While such effects can be found in the radiative decay rate enhancement near plasmonic nanoparticles, they are often masked by the enhancement of the non-radiative decay rates. These effects can be avoided by embedding the emitters into photonics crystals with the bandgap matched to the emission energy of the emitters [115, 116]. Our significantly simpler systems can be thus seen as an intriguing alternative to these complex setups.

2.4 Summary

In this chapter we have analyzed the optical response of two elementary systems comprising dielectric dipolar nanoantennas: a single spherical nanoparticle, serving as a platform for enhancing the emission from electric or magnetic dipolar emitters, and a dimer of subwavelength particles, either illuminated by an incident planewave or coupled to a dipolar emitter. In order to provide a physical interpretation to the spectral characteristics of these structures, we have designed simple analytical models which explain the observed spectral features in terms of the dipolar modes induced in the dielectric scatterers. We have thus observed an interaction between homogeneous pairs of two electric dipoles, commonly discussed in the literature, as well as the more exotic pairs of

magnetic dipoles and, finally, the heterogeneous pairs comprising electric and magnetic dipoles.

These models can be further developed by removing their dependence on the external illumination, thus obtaining the description of the eigenmodes of the system, or by including additional, dipolar scatterers and forming trimer or quadrumer structures. In another interesting extension of this study, one could introduce a rigorous analysis of the coupling between the bright and dark modes which would go beyond the quasi-static limit already studied for the coupling in plasmonic nanosystems.

Chapter 3

Helicity and random media

“It’s a poor sort of memory that only works backwards,’ says the White Queen to Alice.”

– Lewis Carroll, *Through the Looking-Glass*

Classical electrodynamics is endowed, as any elegant theory, with numerous intrinsic symmetries and associated conservation laws which, if used properly, can greatly simplify derivations and provide novel results with just a bit of ingenuity. However, the revelation about the symmetries underlying certain physical phenomena often comes from hindsight.

In this chapter, we present two complementary paths to finding a new physical effect: the conservation of helicity in light scattering processes. The first approach, perhaps the more elegant one, is based on arguments of conservation principles and symmetries of Maxwell’s equations. It provides the necessary and sufficient macroscopic conditions to preserve helicity when light propagates through a piecewise-homogeneous medium. The second approach is more phenomenological, and is based on the description of the multiple scattering of helical light in a solution of dipolar scatterers. Before we report on these findings, let us first introduce the formalism that will sustain our results.

3.1 Operators, symmetries and transformations

For future reference, let us write down Maxwell's equations in a linear, non-dispersive, source-free and homogeneous medium for monochromatic harmonic fields in the frequency domain:

$$\nabla \cdot \mathbf{E} = 0, \quad (3.1a)$$

$$\nabla \cdot \mathbf{H} = 0, \quad (3.1b)$$

$$\nabla \times \mathbf{E} = i\omega\mu_0\mu\mathbf{H}, \quad (3.1c)$$

$$\nabla \times \mathbf{H} = -i\omega\varepsilon_0\varepsilon\mathbf{E}, \quad (3.1d)$$

where ε_0 (μ_0) and ε (μ) are the vacuum and relative permittivities (permeabilities) of the medium and ω is the frequency of the harmonic fields \mathbf{E} and \mathbf{H} .

In Appendix A we discuss how, by considering the intrinsic symmetries of a system, one can find a convenient basis to solve Maxwell's equations. Specifically, for the derivation of light scattering on spherical particles [70], the choice was particularly simple. The basis for the components of the electromagnetic fields was spanned by the *vector spherical harmonics* defined as

$$\mathbf{M}(\mathbf{r}) = \nabla \times [\mathbf{r}\Psi(\mathbf{r})], \quad \mathbf{N}(\mathbf{r}) = \frac{\nabla \times \mathbf{M}(\mathbf{r})}{k}, \quad (3.2)$$

where \mathbf{r} is the position vector and Ψ a solution of the scalar wave equation. We note that, while this choice of basis allows for a particularly simple description of scattering on a system with spherical symmetry, it is rather inconvenient for the expansion of a planewave or dipolar illumination.

A more sensible choice of the basis, that would yield a simple description of the planewave illumination, is provided by functions

$$\mathbf{M}^{\text{TE}}(\mathbf{r}) = \nabla \times [\hat{\mathbf{a}}\Psi(\mathbf{r})], \quad \mathbf{M}^{\text{TM}}(\mathbf{r}) = \frac{\nabla \times \mathbf{M}^{\text{TE}}(\mathbf{r})}{k}, \quad (3.3)$$

where $\hat{\mathbf{a}}$ is a constant unitary vector dubbed as the *guiding* or *pilot vector* [117]. With the choice of

$$\Psi(\mathbf{r}) = \exp(i\mathbf{k} \cdot \mathbf{r}), \quad (3.4)$$

functions \mathbf{M}^{TE} and \mathbf{M}^{TM} themselves represent planewaves with wavevectors \mathbf{k} , and orthogonal polarizations.

We can now pose the following question: *Is it possible* and, if it is, *how* to construct a basis of functions that would exhibit an arbitrary set of symmetries, e.g. a symmetry with respect to the spatial translation along \hat{z} axis, rotation around \hat{z} and temporal translation? Before we answer these questions, we need to formalize our considerations a bit further.

3.1.1 Complete set of commuting operators

Let us consider two properties (or *observables*) of the electromagnetic field represented by operators \mathcal{F} and \mathcal{G} . If the operators commute, that is

$$[\mathcal{F}, \mathcal{G}] = 0, \quad (3.5)$$

then one can find an *eigenbasis* formed by the electromagnetic fields denoted as $\bar{\Phi} \equiv \{\Phi_i = (\mathbf{E}_i, \mathbf{H}_i)\}_{i=1, \dots, n}$ (the eigenbase does not have to be finite), which fulfill Maxwell's equations, and are simultaneously eigenfunctions of both operators:

$$\mathcal{F}\Phi_i = \phi_i^{\mathcal{F}}\Phi_i, \quad (3.6a)$$

$$\mathcal{G}\Phi_i = \phi_i^{\mathcal{G}}\Phi_i. \quad (3.6b)$$

This property can be then extended to a larger set of operators $\bar{\mathcal{F}} \equiv \{\mathcal{F}_k\}_{k=1, \dots, N}$, until they fully characterize the field (so that no two modes Φ_i and Φ_j have identical eigenvalues of all the operators $\bar{\mathcal{F}}$). $\bar{\mathcal{F}}$ is then called the *complete set of commuting operators*.

3.1.2 Operators and symmetries

Let us consider a set of operators which are the generators of symmetries of interest. Below we present the short list, assembled by Xavier Zambrana-Puyalto [118], of the operators which we will be making use of later:

1. *Linear momentum operator* defined as

$$\mathbf{P} = -i\nabla, \quad (3.7)$$

in the Cartesian coordinates has three commuting components: $P_x = -i\partial_x$, $P_y = -i\partial_y$, $P_z = -i\partial_z$, and is a generator of the spatial translation $T_{\delta\mathbf{r}} = \exp(-i\mathbf{P} \cdot \delta\mathbf{r})$.

2. *Hamiltonian* defined as

$$H = -i \frac{\partial}{\partial t}, \quad (3.8)$$

is a generator of the time evolution $T_{\delta t} = \exp(-iH\delta t)$, and commutes with \mathbf{P} .

3. *Angular momentum operator* defined as

$$\mathbf{J} = \mathbf{L} + \mathbf{S}, \quad (3.9a)$$

where \mathbf{L} is the *orbital angular momentum* OAM

$$\mathbf{L} = \mathbf{r} \times \mathbf{P}, \quad (3.9b)$$

and \mathbf{S} - the *spin angular momentum* SAM, expressed in Cartesian coordinates as

$$\mathbf{S} = -i(\hat{\mathbf{x}}\epsilon_{1jk} + \hat{\mathbf{y}}\epsilon_{2jk} + \hat{\mathbf{z}}\epsilon_{3jk}), \quad (3.9c)$$

with the Levi-Civita symbol ϵ_{ijk} :

$$\epsilon_{ijk} = \begin{cases} 1 & \text{if } (i, j, k) \text{ is } (1, 2, 3), (2, 3, 1), (3, 1, 2) \\ -1 & \text{if } (i, j, k) \text{ is } (3, 2, 1), (1, 3, 2), (2, 1, 3) \\ 0 & \text{if } i = j \text{ or } j = k \text{ or } i = k. \end{cases} \quad (3.9d)$$

\mathbf{J} is the generator of rotation around vector $\hat{\mathbf{n}}$: $R_{\hat{\mathbf{n}}}(\phi) = \exp(-i\mathbf{J} \cdot \hat{\mathbf{n}})$. Therefore, unlike in the linear momentum case, the components of \mathbf{J} do not commute

$$[J_i, J_j] = i\epsilon_{ijk}J_k. \quad (3.9e)$$

Interestingly, neither one of the two operators constituting \mathbf{J} : OAM nor SAM is a generator of proper rotations. Furthermore, if we apply those operators to the fields fulfilling Eqs. (3.1), the resulting fields do not fulfill Maxwell's equations.

4. *Casimir operator*

$$J^2 = J_x^2 + J_y^2 + J_z^2, \quad (3.10)$$

commutes with all the components of \mathbf{J} ,

5. *Helicity operator*

$$\Lambda = \frac{\mathbf{J} \cdot \mathbf{P}}{|\mathbf{P}|} = \frac{\mathbf{S} \cdot \mathbf{P}}{|\mathbf{P}|}, \quad (3.11)$$

is the generator of the *duality transformation* defined as

$$D_\phi \begin{pmatrix} \mathbf{E} \\ \mathbf{B} \end{pmatrix} = \begin{pmatrix} \mathbf{E} \cos \phi - c\mathbf{B} \sin \phi \\ \mathbf{E} \sin \phi + c\mathbf{B} \cos \phi \end{pmatrix}, \quad (3.12)$$

where $\mathbf{B} = \mu_0\mu\mathbf{H}$. For monochromatic fields ($|\mathbf{P}| = k$), we can rewrite it as

$$\mathbf{A} = \frac{\nabla \times}{k}. \quad (3.13)$$

Almost all of the above operators commute with the rest, with the following exceptions:

- $[P_i, J_j] = i\epsilon_{ijk}P_k$,
- $[J_i, J_j] = i\epsilon_{ijk}J_k$.

With this last remark, we are ready to answer the first part of the question posed earlier: *yes*, it is possible to find an eigenbasis of the set of commuting operators:

$$\{P_{\hat{\mathbf{n}}}, J_{\hat{\mathbf{n}}}, H\}. \quad (3.14)$$

By definition, such eigenbasis will be invariant with respect to the spatial translation along $\hat{\mathbf{n}}$ ($T_{\delta\hat{\mathbf{n}}}$), rotation around $\hat{\mathbf{n}}$ ($R_{\hat{\mathbf{n}}}$) and temporal translation ($T_{\delta t}$).

In the following section we try to answer the natural follow-up question: how to derive such a basis.

3.1.3 Fields and modes

Let us analyze the modes which we have introduced earlier: \mathbf{M}^{TE} and \mathbf{M}^{TM} . For the sake of simplicity, we assume that these modes were defined with the pilot vector $\hat{\mathbf{a}} = \hat{\mathbf{z}}$ - a unit vector along axis $\hat{\mathbf{z}}$, yielding

$$\mathbf{M}^{\text{TE}}(\mathbf{r}) = \xi^s(\mathbf{r})\Psi(\mathbf{r}), \quad \mathbf{M}^{\text{TM}}(\mathbf{r}) = \xi^p(\mathbf{r})\Psi(\mathbf{r}), \quad (3.15)$$

with the two orthogonal vector fields

$$\xi^s(\mathbf{r}) = \frac{i}{k_\rho}(k_y\hat{\mathbf{x}} - k_x\hat{\mathbf{y}}), \quad (3.16a)$$

$$\xi^p(\mathbf{r}) = \frac{1}{kk_\rho}[-k_z(k_x\hat{\mathbf{x}} + k_y\hat{\mathbf{y}}) + k_\rho^2\hat{\mathbf{z}}], \quad (3.16b)$$

where $\mathbf{k} = (k_x, k_y, k_z)$ and $k_\rho = \sqrt{k^2 - k_z^2}$ was introduced into the definitions of ξ^s and ξ^p to properly normalize the fields. Both planewaves are eigenvectors of the Hamiltonian H and the linear momentum operator \mathbf{P} .

The helicity operator acting on these modes gives

$$\mathbf{\Lambda}[\xi^s(\mathbf{r}) \exp(i\mathbf{k} \cdot \mathbf{r})] = \xi^p(\mathbf{r}) \exp(i\mathbf{k} \cdot \mathbf{r}), \quad (3.17a)$$

$$\mathbf{\Lambda}[\xi^p(\mathbf{r}) \exp(i\mathbf{k} \cdot \mathbf{r})] = \xi^s(\mathbf{r}) \exp(i\mathbf{k} \cdot \mathbf{r}). \quad (3.17b)$$

Thus, in a manner reminiscent of the construction of the *Jones vectors for circular polarizations*, we can introduce two new modes with well-defined helicities

$$\epsilon_+ = \frac{1}{\sqrt{2}}(\xi^s + \xi^p) \exp(i\mathbf{k} \cdot \mathbf{r}), \quad \text{with } \mathbf{\Lambda}\epsilon_+ = \epsilon_+, \quad (3.18a)$$

$$\epsilon_- = \frac{1}{\sqrt{2}}(\xi^s - \xi^p) \exp(i\mathbf{k} \cdot \mathbf{r}), \quad \text{with } \mathbf{\Lambda}\epsilon_- = -\epsilon_-, \quad (3.18b)$$

We can also express these modes through the circular polarization vectors of a planewave propagating along \hat{z} : $\hat{\sigma}_\pm = \frac{1}{\sqrt{2}}(\hat{\mathbf{x}} \pm i\hat{\mathbf{y}})$ as

$$\epsilon_\pm = \frac{1}{2} \left[\left(1 \mp \frac{k_z}{k} \right) e^{i\phi_k} \hat{\sigma}_- - \left(1 \pm \frac{k_z}{k} \right) e^{-i\phi_k} \hat{\sigma}_+ \pm \frac{\sqrt{2}k_\rho}{k} \hat{\mathbf{z}} \right] \exp(i\mathbf{k} \cdot \mathbf{r}), \quad (3.19)$$

where ϕ_k is the azimuthal component of wavevector \mathbf{k} . The resulting modes are eigenfunctions of the linear momentum \mathbf{P} , helicity $\mathbf{\Lambda}$ and the Hamiltonian H operators.

3.1.3.1 Bessel beams

Let us now consider another class of electromagnetic fields characterized by

1. symmetry under temporal translations (eigenfunctions of H),
2. well-defined helicity (eigenfunctions of $\mathbf{\Lambda}$),
3. symmetry under spatial translations along $\hat{\mathbf{a}}$ (eigenfunctions of $P_{\hat{\mathbf{a}}}$),
4. symmetry under rotations around $\hat{\mathbf{a}}$ (eigenfunctions of $J_{\hat{\mathbf{a}}}$),

Without the loss of generality, we again assume $\hat{\mathbf{a}} \equiv \hat{\mathbf{z}}$ and consider beams composed of modes

1. with identical $|\mathbf{k}|$ (monochromatic),
2. with identical and well-defined helicities, either ϵ_+ or ϵ_- ,
3. with identical \hat{z} component of linear momentum P_z .

To address these constraints, we write the sought-after beam as a superposition of ϵ_+ (ϵ_-) modes with \mathbf{k} vectors distributed on a cone with aperture θ_k around the axis $\hat{\mathbf{z}}$, such that $k_z = k \cos \theta_k$ (denoted by superscripts $+, \hat{\mathbf{z}}$ and $-, \hat{\mathbf{z}}$). The aperture angle and the distribution function of the wavevectors on the cone $f(\phi_k)$, where ϕ_k is the azimuthal angle, are denoted in the subscript:

$$\mathbf{B}_{f, \theta_k}^{\pm, \hat{\mathbf{z}}} = \int_0^{2\pi} d\phi_k f(\phi_k) \epsilon_{\pm} \exp(i\mathbf{k} \cdot \mathbf{r}). \quad (3.20)$$

The function $f(\phi_k)$ needs to be selected to ensure that the resulting field $\mathbf{B}_{f, \theta_k}^{\pm, \hat{\mathbf{z}}}$ is an eigenstate of J_z . Choosing $f(\phi_k) = \exp(i\phi_k m)$ yields the field with the required properties:

$$P_z \mathbf{B}_{m, \theta_k}^{\pm, \hat{\mathbf{z}}} = k_z \mathbf{B}_{m, \theta_k}^{\pm, \hat{\mathbf{z}}}, \quad (3.21a)$$

$$J_z \mathbf{B}_{m, \theta_k}^{\pm, \hat{\mathbf{z}}} = m \mathbf{B}_{m, \theta_k}^{\pm, \hat{\mathbf{z}}}, \quad (3.21b)$$

$$\Lambda \mathbf{B}_{m, \theta_k}^{\pm} = \pm \mathbf{B}_{m, \theta_k}^{\pm, \hat{\mathbf{z}}}, \quad (3.21c)$$

where we have replaced the subindex f with the eigenvalue of operator J_z : m . Expanding the integrals and the definitions of modes $\hat{\epsilon}_{\pm}$ we can write

$$\begin{aligned} \mathbf{B}_{m, \theta_k}^{\pm, \hat{\mathbf{z}}} = & \sqrt{\frac{k_{\rho}}{2\pi}} i^m e^{ik_z z} \left[\frac{i}{\sqrt{2}} \left(1 \mp \frac{k_z}{k} \right) J_{m+1}(k_{\rho} \rho) e^{i(m+1)\phi} \hat{\sigma}_- + \right. \\ & \left. + \frac{i}{\sqrt{2}} \left(1 \pm \frac{k_z}{k} \right) J_{m-1}(k_{\rho} \rho) e^{i(m-1)\phi} \hat{\sigma}_+ \pm \frac{k_{\rho}}{k} J_m(k_{\rho} \rho) e^{im\phi} \hat{\mathbf{z}} \right]. \end{aligned} \quad (3.22)$$

Functions J_m used in this definition are the Bessel function of the first kind, and they originate from the expansion of the transversal components of the momentum in $\exp(i\mathbf{k} \cdot \mathbf{r})$. Therefore, we will be referring to this class of beams as *Bessel beams*.

3.1.3.2 Circularly-polarized light

We should note that for vanishing aperture angle $\theta_k \rightarrow 0$ (and $k_z \rightarrow k$) we obtain

$$\mathbf{B}_{m, \theta_k \rightarrow 0}^{\pm, \hat{\mathbf{z}}} \propto i^{m+1} e^{ik_z z} J_{m\mp 1}(0) e^{i(m\mp 1)\phi} \hat{\sigma}_{\pm}. \quad (3.23)$$

In this limit the normalization scheme needs to be changed, since the coefficient $\sqrt{\frac{k_\rho}{2}} \rightarrow 0$. With the Bessel function J_n non-vanishing at $k_\rho = 0$ only for the Bessel function of the 0th order, the only meaningful \mathbf{B} functions are

$$\mathbf{B}_{m=\pm 1, \theta_k \rightarrow 0}^{\pm, \hat{\mathbf{z}}} \propto e^{ik_z z} \hat{\sigma}_\pm, \quad (3.24)$$

and describe the *circularly polarized* (CP) light. The argument for choosing a certain sign (+ or -) of σ to denote the *right-hand* circularly polarized (RCP) or *left-hand* circularly polarized (RCP) light depends on whether we observe the beam from behind the source, or heading towards us. In the former case the real component of the electric field described by the vector field $\mathbf{B}_{m=+1, \theta_k \rightarrow 0}^{+, \hat{\mathbf{z}}} \propto \sigma_+$ is performing a counter-clockwise rotation, identifying it as the LCP light. Accordingly, vector field $\mathbf{B}_{m=-1, \theta_k \rightarrow 0}^{-, \hat{\mathbf{z}}} \propto \sigma_-$ describes clockwise rotation of the electric field, and the RCP light:

$$(\text{observer behind the source}), \quad \text{LCP: } \sigma_+, \quad \text{RCP: } \sigma_-. \quad (3.25)$$

Conversely, if the observer is facing the incoming light, $\mathbf{B}_{m=+1, \theta_k \rightarrow 0}^{+, \hat{\mathbf{z}}}$ and $\mathbf{B}_{m=-1, \theta_k \rightarrow 0}^{-, \hat{\mathbf{z}}}$ appear to be describing the clockwise (RCP) and counter-clockwise rotation (LCP), respectively.

$$(\text{observer facing the source}), \quad \text{LCP: } \sigma_-, \quad \text{RCP: } \sigma_+. \quad (3.26)$$

The first convention is typically used in the community of quantum physics, while the second one in that of optics. Throughout the rest of the chapter we will follow the latter.

We can also generalize this result to any helical field and interpret the field with positive helicity $\Lambda = +1$ as that which can be decomposed into right-hand circularly polarized planewaves, and the field with negative helicity $\Lambda = -1$ as that which can be decomposed into left-hand circularly polarized planewaves.

3.1.3.3 Constructing the electric and magnetic fields

The abstract derivation provided above deserves some clarification regarding the construction of the electric \mathbf{E} and magnetic \mathbf{H} fields of a beam with a well-defined helicity (helical beam). The two fields are related to each other through the Faraday's equation (Eq. (3.1c)), which can be rewritten using the definition of the helicity operator (Eq. (3.13)) as an eigenvalue equation

$$\mathbf{H} = -\frac{i}{\mu_0 c} \Lambda \mathbf{E} = -\frac{i}{\mu_0 c} \Lambda \mathbf{E}. \quad (3.27)$$

Therefore, by choosing the electric field as a superposition of the $\mathbf{B}_{m,\theta_k}^{\pm,\hat{\mathbf{n}}}$ modes with various orders m and aperture angles θ_k around an arbitrary axis $\hat{\mathbf{n}}$, we automatically define the corresponding magnetic field \mathbf{H} as a superposition of all those beams with the appropriate sign determined by their helicity.

3.2 Helicity preservation in an inhomogeneous medium

In this section we discuss two complementary results published recently, both of which report the conservation of helicity of the electromagnetic field in an inhomogeneous medium, but treat the problem with very different tools.

The first report deals with the scattering of helical electromagnetic fields on arbitrarily-shaped, homogeneous scatterers, described solely by their permittivities and permeabilities. This result allows us to formulate the conditions under which the light propagating in a piecewise-homogeneous medium retains its helicity [119].

The second result describes the preservation of helicity in the scattering on a solution of dipolar, resonant scatterers which behave like point electric and magnetic dipoles with equal polarizabilities [120]. In this approach the induced dipoles can be seen as the microscopic building blocks of a macroscopic medium with equal permittivity and permeability.

3.2.1 Macroscopic approach

Let us consider a homogeneous medium characterized by permittivity ε_1 and permeability μ_1 , and a distribution of electric \mathbf{E}_1 and magnetic \mathbf{H}_1 fields which fulfill Maxwell's equations (Eq. (3.1)). If this medium is unbound, then in the absence of charges and currents, Maxwell's equations are invariant in the entire system with respect to the duality transformation D_ϕ , that is, the fields transformed according to Eq. (3.12) will fulfill the Maxwell's equations. This description can be extended to include sources, as we demonstrate in Appendix A when deriving the electromagnetic fields generated by a magnetic dipole.

We can now complicate the system, by dividing it into two regions (Ω_1 and Ω_2) characterized by the material properties (ε_1, μ_1) and (ε_2, μ_2) , respectively. The electric and magnetic fields $\{\mathbf{E}_i, \mathbf{H}_i\}_{i=1,2}$ fulfill (i) the Maxwell conditions inside the homogeneous

media, and (ii) the boundary conditions on the interface between Ω_1 and Ω_2 :

$$\hat{\mathbf{n}} \times (\mathbf{E}_1 - \mathbf{E}_2) = \hat{\mathbf{n}} \times (\mathbf{H}_1 - \mathbf{H}_2) = 0, \quad (3.28a)$$

$$\hat{\mathbf{n}} \cdot (\varepsilon_1 \mathbf{E}_1 - \varepsilon_2 \mathbf{E}_2) = \hat{\mathbf{n}} \cdot (\mu_1 \mathbf{H}_1 - \mu_2 \mathbf{H}_2) = 0, \quad (3.28b)$$

where $\hat{\mathbf{n}}$ is a unitary vector normal to the boundary between two media. If we apply the duality transformation to both sets of fields in the two media

$$\begin{pmatrix} \tilde{\mathbf{E}}_i^\phi \\ \tilde{\mathbf{H}}_i^\phi \end{pmatrix} = D_\phi \begin{pmatrix} \mathbf{E}_i \\ \mathbf{H}_i \end{pmatrix}, \quad (3.29)$$

we arrive at the obvious question whether these fields fulfill both Maxwell's equations and the boundary conditions.

In their work, Fernandez-Corbaton *et al.* [119] prove that these conditions are fulfilled if and only if the ratios of the permittivities and permeabilities of each material are identical:

$$\frac{\varepsilon_1}{\mu_1} = \frac{\varepsilon_2}{\mu_2}. \quad (3.30)$$

Importantly, this result, trivially expanded to a system comprising more homogeneous media, holds independently of the geometric properties of the homogeneous domains Ω_i .

An important implication of this conclusion is that in the piecewise-homogeneous medium fulfilling the generalized condition formulated in Eq. (3.30), the response of the system (or, equivalently, Maxwell's equations and the boundary conditions describing the system) is invariant with respect to the dual transformation D_ϕ . Furthermore, since this helicity is the generator of the dual transformation, the system preserves the helicity of the field with which it interacts.

A convenient illustration of this effect is given in Fig. 3.1, where we plot the value of scalar function introduced in Ref. [119] to locally measure the helicity of the electromagnetic field

$$\tilde{\Lambda}_\pm = |\mathbf{E} \pm ic\mu_0 \mathbf{H}|^2. \quad (3.31)$$

For a helical field $\{\mathbf{E}, \mathbf{H}\}$ which follows the helicity eigenvalue equation (Eq. (3.27)) we get

$$\tilde{\Lambda}_\pm = |\mathbf{E}|^2 |1 \pm 1|^2. \quad (3.32)$$

The system Ω , shown in Fig. 3.1(c), comprises a two-dimensional homogeneous scatterer Ω_1 with material properties: $\varepsilon_1 = 2.25$ and μ_1 , immersed in vacuum Ω_2 ($\varepsilon_2 = \mu_2 = 1$).

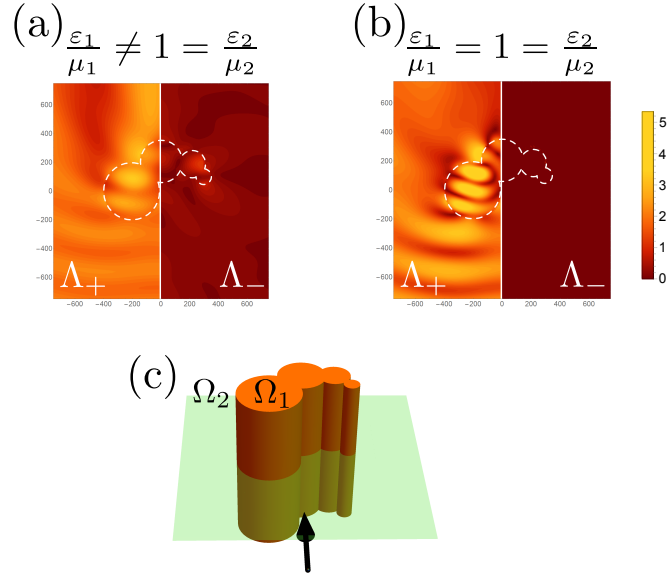


FIGURE 3.1: Helicity of the field scattered on a pan flute-like object composed of infinite cylinders, immersed in air ($\epsilon_2 = \mu_2 = 1$) and illuminated by a circularly polarized light. Functions Λ_{\pm} are calculated in the plane denoted in green in (c), and the permeability of the scatterer (Ω_1) was chosen either not to fulfill (a) or to fulfill (b) the condition for helicity preservation given in Eq. (3.30). Illustrations inspired by Ref. [119]

The incident helical field is a monochromatic, left-hand circularly polarized planewave (LCP) incident along the black arrow. In (a) we plot the $\tilde{\Lambda}_+$ and $\tilde{\Lambda}_-$ functions, calculated for $\mu_1 = 1 \neq \epsilon_1$, in the plane schematically depicted with light green color in (c). Neither of those functions vanish, indicating that the system Ω does not preserve helicity of the incident LCP. On the other hand, function $\tilde{\Lambda}_-$ shown in (b), where $\mu_1 = 2.25 = \epsilon_1$, vanishes in the whole system Ω , demonstrating that the helicity of the scattered field is identical to that of the incident LCP ($\Lambda = -1$). The calculations were performed using the FDTD software [83], and the shape of the scatterer, although not the illumination, was chosen to mimic the structure investigated in Ref. [119].

3.2.2 Microscopic approach

In this section we analyze the scattering of helical beams on a random medium comprising identical particles with strong electric and magnetic activity. These particles can be similar to those studied in Chapter 2, made of high-refractive index dielectric material. In parallel to the study of macroscopic structures discussed earlier, we formulate a clear criterion for the scattering process to conserve the helicity of the electromagnetic fields.

3.2.2.1 Random media and polarization

Although the study of the statistical properties of complex, irregular distribution of electromagnetic fields known as *speckle patterns* [121, 122] has been a topic of high interest during the last decades, the statistics of the *polarization* of electromagnetic vector waves is still not well understood. The depolarization of light in a random medium is the basis of an increasingly broad range of applications from remote sensing [123], enhanced backscattering phenomena [124–127], to biomedical imaging and diagnostics [128–130]. Even for static samples, the polarization of the scattered field is far from being isotropic [123] and the polarization of the speckle pattern may exhibit rapid changes from one speckle grain to another [131] with a nontrivial statistical distribution of polarization singularities [132, 133]. It is generally assumed that multiple scattering of light from inhomogeneities in optically dense media randomizes the state of polarization of light. A wave propagating in such a medium becomes rapidly depolarized in a characteristic length scale that depends on the properties of both the scattering medium and the illuminating light [134–136].

Therefore, if we could show that a solution of particles (which can be readily obtained) exhibits an isotropic conservation of the polarization state of the incident illumination, we could add an important contribution to the research of scattering of light in random media. To this end we first analyze the scattering of helical light by particles in the dipolar approximation, with identical electric and magnetic polarizabilities (so-called *dual particles*). This case is then expanded to treat multiple scattering processes in systems comprising dimers and random ensembles of such *dual* nanoparticles.

3.2.2.2 Degree of helical polarization

Figure 3.2 depicts the process of the scattering of helical light on a single nanoparticle. For illustrative purposes, throughout this section we use a special form of the helical beam $\mathbf{B}_{m=1, \theta_k=\pi/4}^{\pm, \hat{z}}$ with the axial symmetry around the propagation direction \hat{z} defined in Eq. (3.22). We should stress that all of the results discussed in this section are general and hold true for any given helical incident beam, for instance for Bessel beams of order $m \neq 1$, or circularly polarized planewaves. In fact, the only property of the incident fields $\{\mathbf{E}, \mathbf{H}\}$ which we will make use of is that they are the eigenfunctions of the helicity operator (see Eq. (3.27)).

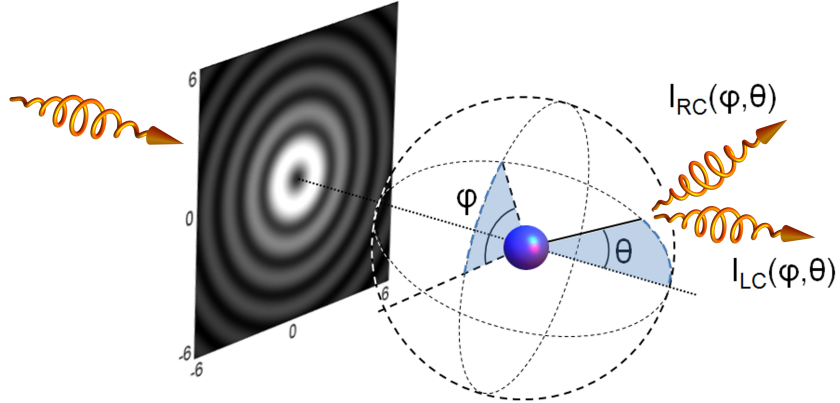


FIGURE 3.2: Schematic of the scattering process of helical light on a dielectric nanoparticle. The incident helical light is a Bessel beam of $m = 1$ order with aperture $\theta_k = \pi/4$ and helicity $\Lambda = -1$, given by Eq. (3.22). The panel shows the cross section of the intensity of the beam with characteristic Bessel function-like radial oscillations. The scattered light contains right- and left-handed circularly polarized components measured by the differential scattering cross sections I_{RC} and I_{LC} , respectively.

The measurements of the scattered light are always performed in the far-field regime, and can therefore only access the components of scattered fields carried by a very narrow distribution of wavevectors. In the limit of vanishing detector aperture, this distribution becomes singular and thus, as we have shown before, the helical beam simplifies to a circularly-polarized planewave. Consequently, the two functions I_{RC} and I_{LC} which describe the *intensity of the right- and left-hand circularly polarized scattered light*, respectively (see Fig. 3.2), can be used to define a *degree of helical polarization* $\eta \in [-1, 1]$:

$$\eta(\varphi, \theta) = \frac{I_{RC}(\varphi, \theta) - I_{LC}(\varphi, \theta)}{I_{RC}(\varphi, \theta) + I_{LC}(\varphi, \theta)}. \quad (3.33)$$

Integrating η over the polar and azimuthal angles, we define the *total degree of helical polarization*

$$\eta_{\text{tot}} = \frac{1}{4\pi} \int_{-\pi/2}^{\pi/2} \int_0^{2\pi} \sin(\theta) \eta(\varphi, \theta) d\theta d\varphi \in [-1, 1]. \quad (3.34)$$

As an example of dipolar scatterers with strong electric and magnetic polarizabilities we choose submicron silicon spherical nanoparticle, such as the ones analyzed in detail in the previous chapter. We should note that some unusual scattering properties of such particles associated with their overlapping electric and magnetic polarizabilities (e.g. the strongly asymmetric angular distributions of scattered intensity), have been recently reported in the literature [8, 10, 137–139].

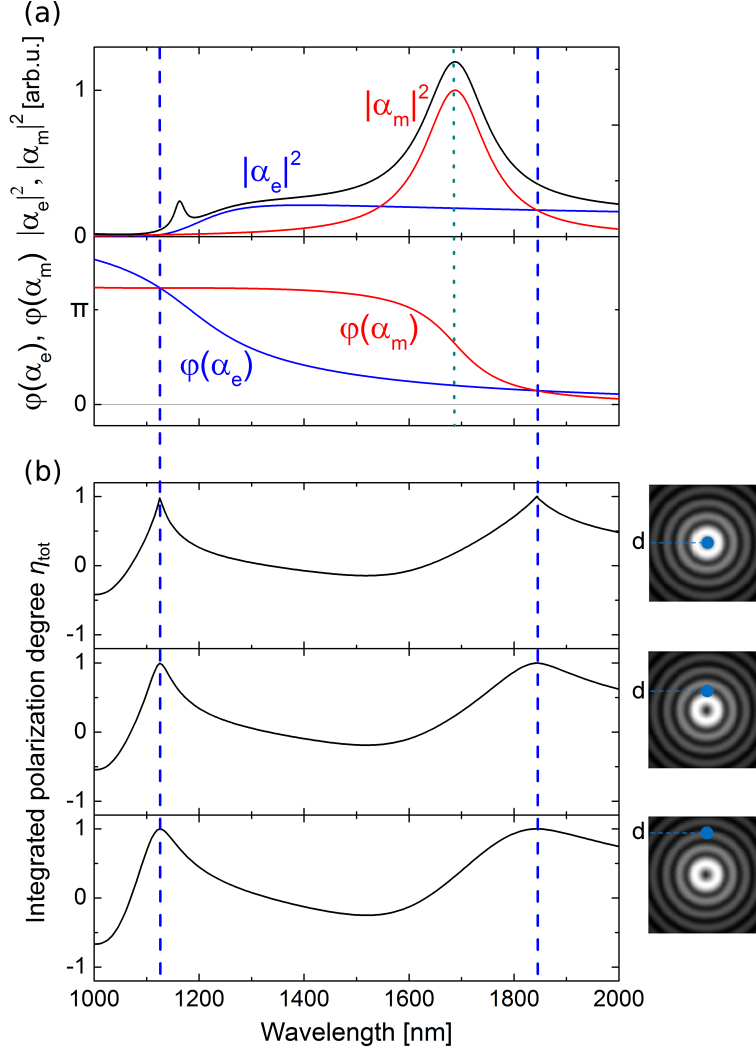


FIGURE 3.3: (a) Square moduli (top panel) and phases (bottom panel) of the electric (α_e , blue line) and magnetic (α_m , red line) polarizabilities of a 230 nm radius silicon sphere in the near-IR. Scattering cross section ($\sigma_{\text{scatt}} k^{-4}$ shown with a black line) is dominated by the contributions from these dipolar terms. Dashed vertical lines indicate wavelengths at which the polarizabilities are equal both in magnitude and phase. (b) Integrated circular polarization factors η_{tot} for the sphere positioned on the axis of a helical beam as the introduced in Fig. 3.2 (top panel), displaced by 2 μm from the beam axis (middle panel) and 4 μm (bottom panel) from the axis, as shown in the insets with a blue dot denoting the particle.

In Fig. 3.3(a) we plot the electric α_e and magnetic α_m polarizabilities of a 230 nm radius silicon ($n = 3.5$) sphere in air. The two polarizabilities are identical for wavelengths of $\lambda = 1844$ nm and 1160 nm, which we have marked with vertical dashed blue lines. Note that for the latter case, the scattering spectrum is dominated by higher-order modes, and we cannot consider the spheres as dipolar scatterers. Furthermore, the spectra of $|\alpha_e|^2$ and $|\alpha_m|^2$ cross also at $\lambda = 1520$ nm, but for this wavelength the phases of the polarizabilities are different (i.e. $\text{Re}\{\alpha_e\} = -\text{Re}\{\alpha_m\}$, which corresponds to the almost-zero-forward condition [10, 137, 138]). The polarizabilities and the scattering cross section plotted in Fig. 3.3(a) have been calculated with Mie theory.

It should be noted that these scatterers are not *dual* in terms of the ratio of their permittivity and permeability being equal to that of the surrounding medium (the *macroscopic* case we discussed in Section 3.2.1). Instead, as we prove below, the duality arises when the electric and magnetic polarizabilities are identical [140].

3.2.2.3 Scattering on a single nanoparticle

In the spectral range where the scattered fields can be described by dipolar electric and magnetic responses, the previously introduced polarization-resolved intensities of the scattered light are given by the following analytical form [78]

$$I_\epsilon(\hat{\mathbf{n}}) \propto |\boldsymbol{\epsilon}^* \cdot \mathbf{p} + (\hat{\mathbf{n}} \times \boldsymbol{\epsilon}^*) \cdot \mathbf{m}/c|^2, \quad (3.35)$$

with subindex ϵ and vectors $\boldsymbol{\epsilon}$ corresponding to the left- (LC, $\epsilon = \epsilon_-$) and right-hand (RC, $\epsilon = \epsilon_+$) circular polarization of the scattered light (see the definition of ϵ_\pm in Eq. (3.18) and the discussion of circular polarizability in Section 3.1.3.2), and \mathbf{p} and \mathbf{m} denoting the electric and magnetic dipolar momenta induced in the particle, respectively. Unit vector $\hat{\mathbf{n}}$ describes the direction of scattering, and was previously determined by the polar and azimuthal angles θ and ϕ . This expression can be obtained by considering the far-field components of the electric field originating from \mathbf{p} and \mathbf{m} . These electric and magnetic dipolar momenta are induced by the incident fields $\{\mathbf{E}, \mathbf{H}\}$:

$$\mathbf{p} = \varepsilon_0 \alpha_e \mathbf{E}, \quad \mathbf{m} = \alpha_m \mathbf{H}. \quad (3.36)$$

For the dual nanoparticle ($\alpha_e = \alpha_m = \alpha_0$), using the relationship Eq. (3.27), we obtain:

$$I_\epsilon(\mathbf{n}) \propto |\varepsilon_0 \alpha_0^* \mathbf{E}^* \cdot [\boldsymbol{\epsilon} + i\Lambda \hat{\mathbf{n}} \times \boldsymbol{\epsilon}]|^2. \quad (3.37)$$

For any scattering direction $\hat{\mathbf{n}}$, it can be shown from the definition Eq. (3.18) that $\hat{\mathbf{n}} \times \epsilon_- = -i\epsilon_-$ and $\hat{\mathbf{n}} \times \epsilon_+ = i\epsilon_+$. Thus, the squared expression in the scattering cross section (Eq. (3.37)) is proportional to

$$\begin{pmatrix} I_{LC} \\ I_{RC} \end{pmatrix} \propto \left| \begin{pmatrix} \epsilon_- \\ \epsilon_+ \end{pmatrix} + \Lambda \begin{pmatrix} \epsilon_- \\ -\epsilon_+ \end{pmatrix} \right|^2, \quad (3.38)$$

indicating that for $\Lambda = 1(-1)$ incident beams the RC (LC) polarization of the scattered light vanishes. Therefore, for the dual nanoparticle and the incident helical field, $\eta(\hat{\mathbf{n}})$ for every direction should be equal to 1, giving $\eta_{\text{tot}} = 1(-1)$ for the incident $\Lambda = -1(1)$ light.

We illustrate this scattering invariance in Fig. 3.3(b). In the panels we present the spectra of the total degree of helical polarization η_{tot} , calculated for the scatterer positioned on the axis of the beam (top panel), shifted away from it by $d = 2 \mu\text{m}$ (middle panel) or by $d = 4 \mu\text{m}$ (bottom panel), as shown schematically in the insets by the position of the blue dot. For the two wavelengths at which the two polarizabilities match ($\lambda = 1160 \text{ nm}$ and 1844 nm), η_{tot} reaches its maximum value 1, indicating an isotropic circular polarization of the scattered light.

Interestingly, the scattering of a dual nanoparticle preserves the helicity everywhere, and is not only limited to the far-field, as we have shown above. Since the scattered near-field, composed primarily of evanescent waves, is essential for the understanding of systems comprised of many scatterers, below we will investigate in detail the helicity of all the components of the field scattered on a dual particle.

Let us consider the relationship between the electric \mathbf{p} and magnetic \mathbf{m} dipoles induced in a dual nanoparticle by a helical light. Inserting Eq. (3.27) into definitions given in Eq. (3.36), we arrive at

$$\mathbf{m} = -ic\Lambda\mathbf{p}. \quad (3.39)$$

The scattered electric field from such a pair of dipoles can be expressed through the Green's functions as

$$\mathbf{E}_{\text{scatt}} = \frac{k^2}{\epsilon_0} \overset{\leftrightarrow}{\mathbf{G}}_E \mathbf{p} + iZk^2 \overset{\leftrightarrow}{\mathbf{G}}_M \mathbf{m} = \frac{k^2}{\epsilon_0} (\overset{\leftrightarrow}{\mathbf{G}}_E + \Lambda \overset{\leftrightarrow}{\mathbf{G}}_M) \mathbf{p}. \quad (3.40)$$

To calculate the action of the helicity operator on $\mathbf{E}_{\text{scatt}}$, we use the following property of the Green's function:

$$\Lambda \overset{\leftrightarrow}{\mathbf{G}}_E = \overset{\leftrightarrow}{\mathbf{G}}_M, \quad \Lambda \overset{\leftrightarrow}{\mathbf{G}}_M = \overset{\leftrightarrow}{\mathbf{G}}_E, \quad (3.41)$$

which can be derived by taking the definition of the helicity operator for monochromatic fields (Eq. (3.13)). We then have

$$\Lambda \mathbf{E}_{\text{scatt}} = \frac{k^2}{\varepsilon_0} (\mathbf{G}_M + \Lambda \mathbf{G}_E) \mathbf{p}. \quad (3.42)$$

Since the eigenvalues of the helicity operator follow $\Lambda^2 = 1$, we can further rewrite the above equation as

$$\Lambda \mathbf{E}_{\text{scatt}} = \Lambda \frac{k^2}{\varepsilon_0} (\Lambda \mathbf{G}_M + \mathbf{G}_E) \mathbf{p} = \Lambda \mathbf{E}_{\text{scatt}}. \quad (3.43)$$

Therefore, the scattered field inherits the helicity of the incident field.

3.2.2.4 Scattering on a dimer of particles

Since the helicity of the electromagnetic field is conserved in the process of scattering on a single dual scatterer, it should also be conserved in the subsequent scattering events on other dual scatterers. To illustrate this helicity invariance, we consider the scattering of the helical beam on a dimer of silicon spheres, recalling the system analyzed in the previous chapter and in Ref. [7]. We arbitrarily place one of the particles is positioned at the origin of the coordinate system, while the other is centered at $(x, y, z) = (1 \mu\text{m}, 0 \mu\text{m}, 0.5 \mu\text{m})$ (see schematics in Fig. 3.4). As previously, we address the problem by using the *coupled electric and magnetic dipole method*, that is, by solving a set of self-consistent equations for the set of four dipoles $\{\mathbf{p}_i, \mathbf{m}_i\}_{i=1,2}$ illuminated by the Bessel beam. The central panels in Fig. 3.4 show the distribution of two scalar fields defined as

$$\Lambda_{\pm} = |\mathbf{E}_{\text{scatt}} \pm ic\mu_0 \mathbf{H}_{\text{scatt}}|^2, \quad (3.44)$$

calculated in the transverse plane defined by $z = 3 \mu\text{m}$. This function differs slightly from the previously introduced $\tilde{\Lambda}_{\pm}$, which we have defined to study the field in Fig. 3.1, and which included both incident and scattered field (Eq. (3.31)), but carries identical information. Two wavelengths of the incident light are considered: (a) $\lambda = 1844 \text{ nm}$, for which the scatterers are dual, and (b) $\lambda = 1679 \text{ nm}$, at which the scatterers have a dominating magnetic dipolar response. For a helical beam with $\Lambda = -1$ interacting with a dual dimer, the scattered intensity into modes with Λ_+ will be zero as shown in Fig. 3.4(a). In contrast, for the non-dual scatterers (Fig. 3.4(b)), neither one of the two fields Λ_{\pm} vanishes, indicating the mixing of the two helicities in the scattering process. For both wavelengths, we also investigate the far-field properties of the scattered light, plotting its differential scattering cross section $I(\varphi, \theta)$ in the top plots of the right

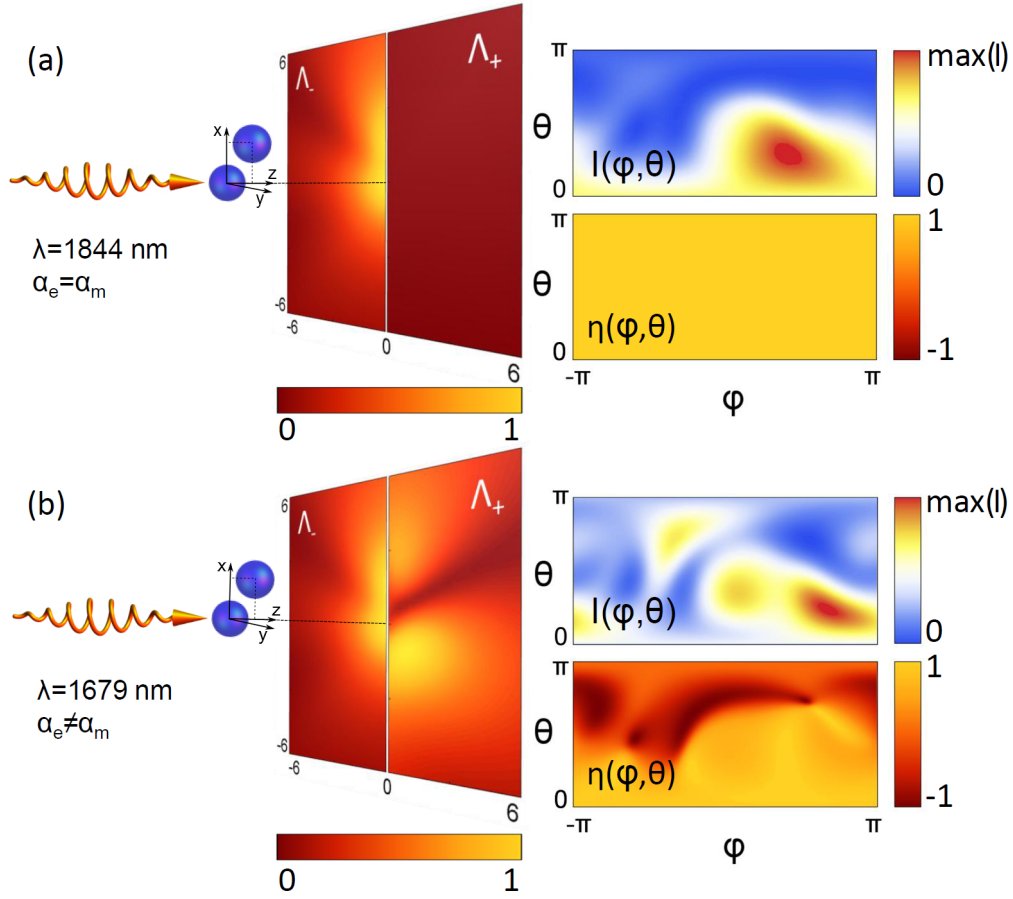


FIGURE 3.4: Light scattering by a dimer of spheres. The incident helical ($\Lambda = -1$) light of (a) 1844 nm or (b) 1679 nm wavelength is scattered on a dimer of two (a) dual and (b) non-dual silicon spheres. One of the spheres is positioned at the origin of the coordinates system and the other is shifted from it $0.5 \mu\text{m}$ along the axis \hat{z} and $1 \mu\text{m}$ in the transverse direction \hat{x} . In the near field (calculated at $z = 3 \mu\text{m}$) the helicities of the scattered light can be measured by calculating distributions Λ_{\pm} (central panels). Vanishing distribution of Λ_+ in (a) indicates that the scattered light retains the negative helicity of the incident light, while the non-vanishing distributions in (b) indicate mixing of the $\Lambda = -1$ and $\Lambda = 1$ components of light. Right panels represent the differential scattering cross sections of the scattered light $I(\varphi, \theta)$ (upper plots) and of the polarization degree $\eta(\varphi, \theta)$ (lower panel). For the dual spheres (a) $\eta(\varphi, \theta) = 1$ is a constant function, indicating that the scattered light is fully circularly polarized ($\eta_{\text{tot}} = 1$).

panels of Fig. 3.4. For neither of the wavelengths the intensity distribution exhibit a clear scattering pattern, although in the case of dual spheres (Fig. 3.4(a)) we observe a predominant scattering in the forward direction. This effect is related to the complete suppression of the backward scattering we expect from a single dual scatterer [119].

On the other hand, the maps of the degree of helical polarization $\eta(\varphi, \theta)$ shown in the bottom plots of right panels in Fig. 3.4 corroborate our analytical modeling, demonstrating that the scattered light is fully circularly polarized for the dual sphere (Fig. 3.4(a)). In the case of non-dual scatterers (Fig. 3.4(b)), no such property is observed.

3.2.2.5 Scattering in a random medium

We can also extend our considerations to the random medium, modeled as a distribution of dual scatterers, where each one preserves the helicity in every single scattering event. By using again the coupled electric and magnetic dipole method [103–105], we illustrate this conservation principle in Fig. 3.5, where we investigate the scattering of incident helical light on a distribution of 80 nanoparticles positioned randomly in a cubic volume of 60 μm edge length. Similarly as in Fig. 3.4, we consider two wavelengths of incident light: (a) 1844 nm, at which the scatterers are dual, and (b) 1679 nm where they are not. In the former case, the circular polarization degree η is constant and equal to 1 for any scattering direction (right bottom panel in (a)), indicating the conservation of helicity in the multiscattering process. For the non-dual scatterers, the polarization degree shown in the bottom right panel in (b) does not exhibit preservation of helicity, and function $\eta(\varphi, \theta)$ reveals a speckle pattern similar to that found in the intensity distribution $I(\varphi, \theta)$ (top right panels).

It is worth noting that the intensity distribution for dual particles (top right panel in Fig. 3.5(a)) presents a clear asymmetry between forward and backward scattering. Due to the conservation of angular momentum and helicity, a complete suppression of backscattering (at $\theta = 0$) is expected [119] for dual and axially symmetric samples. The partial (statistically averaged) axial symmetry of the particle distribution explains the observed results. Such an asymmetry is not observed for the non-dual medium (top right panel in Fig. 3.5(b)).

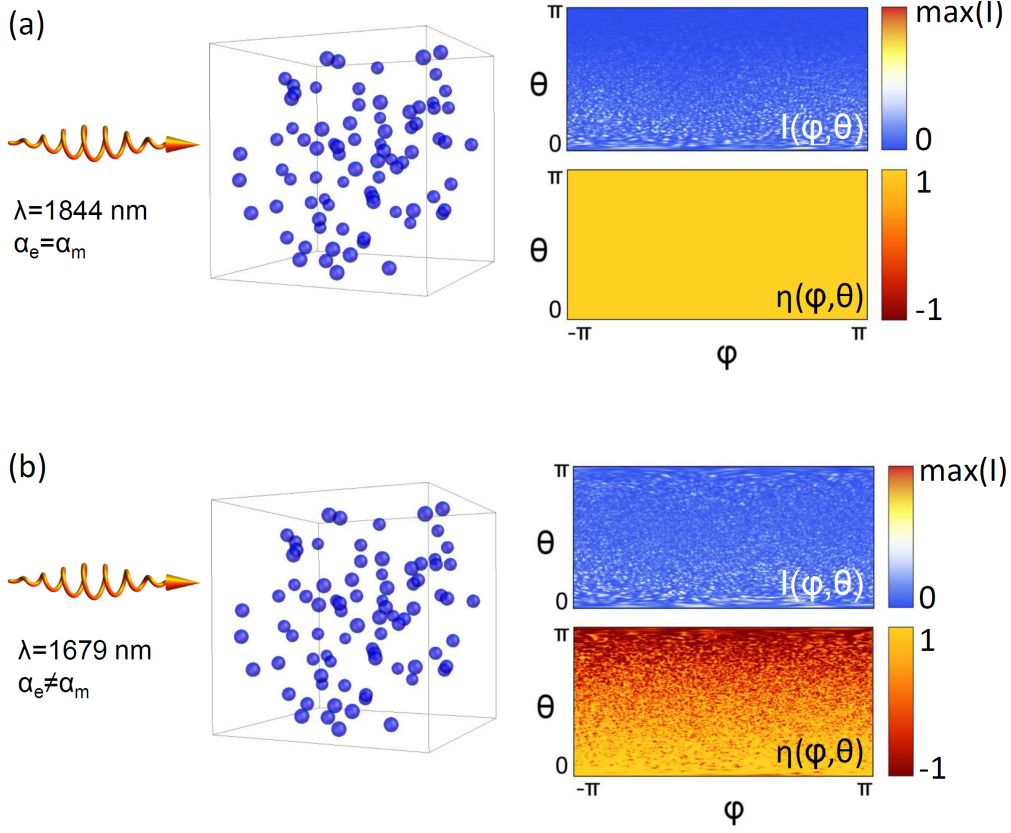


FIGURE 3.5: Light scattering by a random medium. The incident helical ($\Lambda = -1$) light of (a) 1844 nm or (b) 1679 nm wavelength scatters on an ensemble of 80 randomly distributed (a) dual and (b) non-dual silicon spheres. The scatterers were randomly distributed in a cubic box with edges of $60 \mu\text{m}$ length, centered on the axis of the beam as shown to the left of the figure. Panels on the right represent the differential scattering cross-section $I(\varphi, \theta)$ (upper plots) and of the polarization degree $\eta(\varphi, \theta)$ for each case.

3.2.2.6 Kerker conditions

As a side note, we would like to point out that studies of the relationship between the Mie coefficients, or material properties of the scatterers and the emergence of asymmetric scattering can be traced back to the seminal paper by M. Kerker *et al.* [141], to whom we owe two critical observations:

1. *The first Kerker condition* states that the backscattering from a spherical particle can be completely suppressed if the permittivity and permeability of the particle's material are equal ($\varepsilon = \mu$).

2. *The second Kerker condition* states that the forward scattering from a small (dipolar) spherical particle can be completely suppressed if the dipolar Mie coefficients describing the particle are opposite ($a_1 = -b_1$).

Recently these conditions have been related to the discussion of the helicity and generalized to describe the scattering of helical light on objects with cylindrical symmetry [142, 143].

3.2.2.7 Inhomogeneous solution

Finally, we briefly discuss the effect of a non-homogeneous distribution of scatterers in a random medium on the conservation of helicity. We calculate the effect that a fixed dispersion of sizes centered around the dual condition has on the duality of the random medium.

Let us first consider a single scattering event. For convenience, we will define the *Kerker wavelength*, λ_K , through the duality condition

$$\alpha_e(\lambda_K) = \alpha_m(\lambda_K). \quad (3.45)$$

This magnitude exhibits a parametric dependence on the radius of a silicon nanoparticle a , as illustrated in Fig. 3.6(a). We thus observe that by changing the radius of the nanoparticle by around 13% ($0.23 \mu\text{m} \pm 0.03 \mu\text{m}$), we shift the Kerker wavelength from $1.844 \mu\text{m}$ by around $0.2 \mu\text{m}$. Note that the exact magnitude of this detuning depends on the actual material of the scatterer through the refractive index.

Another measure of how rapidly the detuning from the Kerker wavelength λ_K renders a *non-dual* medium is the deviation from the duality condition, quantified as the relative difference between electric and magnetic polarizabilities

$$\kappa = \left| \frac{\alpha_m(\lambda_K) - \alpha_e(\lambda_K)}{\alpha_m(\lambda_K) + \alpha_e(\lambda_K)} \right|, \quad (3.46)$$

shown in Fig. 3.6(b) as a function of the radius of the scatterer at $\lambda_K = 1.844 \mu\text{m}$.

To place the above results in the proper context of experimentally feasible systems, in Fig. 3.6(c) we plot Gaussian functions which represent normal distributions of nanoparticle radii around $a_0 = 0.23 \mu\text{m}$. The standard deviation of these distributions is fixed as 1% (blue area), 2% (red area) and 5% (green area) of the mean radius a_0 .

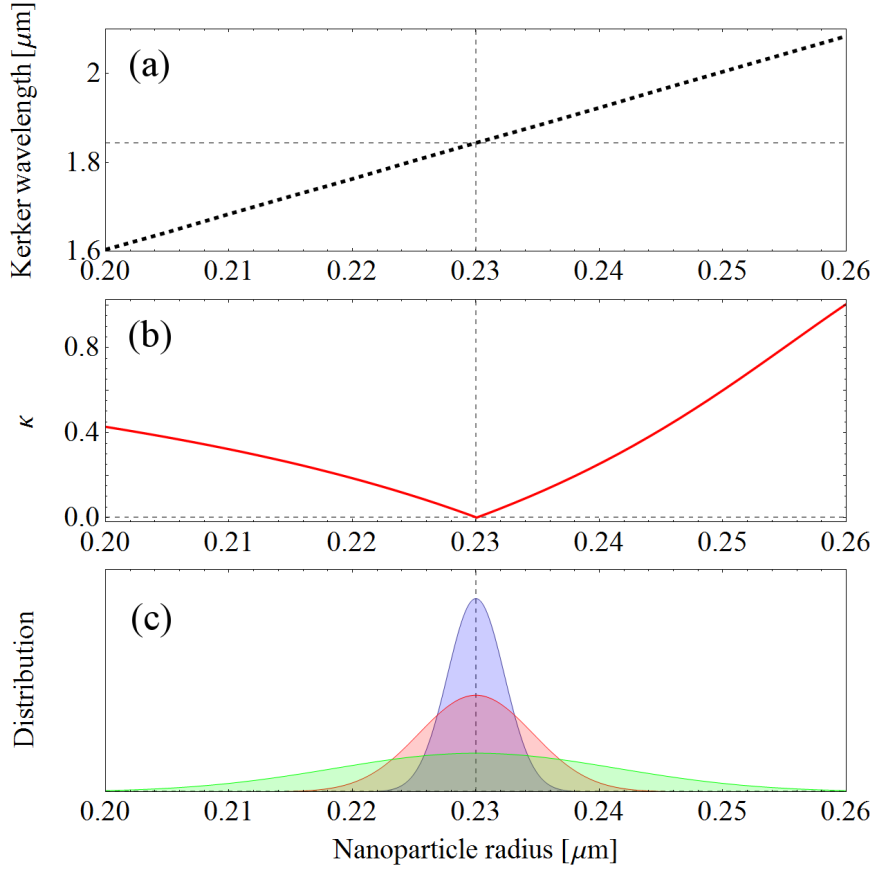


FIGURE 3.6: Effect of size distribution of scatterers on the duality of a random medium. (a) Kerker wavelength defined by equal electric and magnetic dipolar polarizabilities, as a function of the radius of the Si nanoparticle. (b) Deviation from the duality of a single scatterer defined through the parameter κ , as in Eq. (3.46), calculated at the incident light wavelength of $1.844 \mu\text{m}$, which corresponds to the Kerker wavelength of a $a_0 = 0.23 \mu\text{m}$ radius Si sphere. (c) Normal distributions used in the simulations, centered at a_0 with standard deviations of 1% (blue area), 2% (red area) and 5% (green area) of a_0 . In all the plots horizontal and vertical thin dashed lines correspond to the Kerker conditions analyzed in the manuscript.

How does this deviation from the *duality* of scatterers deteriorate the helicity conservation in the scattering by a realistic random medium? To analyze this effect we performed a series of simulations of such scattering on random distributions of scatterers, assuming that the radii of scatterers are normally distributed around $0.23 \mu\text{m}$, with the distribution as shown in Fig. 3.6(c). The spectra of the integrated polarization degree η_{tot} for each simulation are given in Fig. 3.7. Note that, as previously, the calculations are done in the dipolar approximation, and thus they do not account for higher order modes, which dominate the optical response below $\lambda = 1.2 \mu\text{m}$, and quench the effect of helicity conservation in this region. Nevertheless, the simulations reveal that for an increasing deviation of sizes, the integrated polarization degrees drop to 0.95, 0.85 and 0.60, for

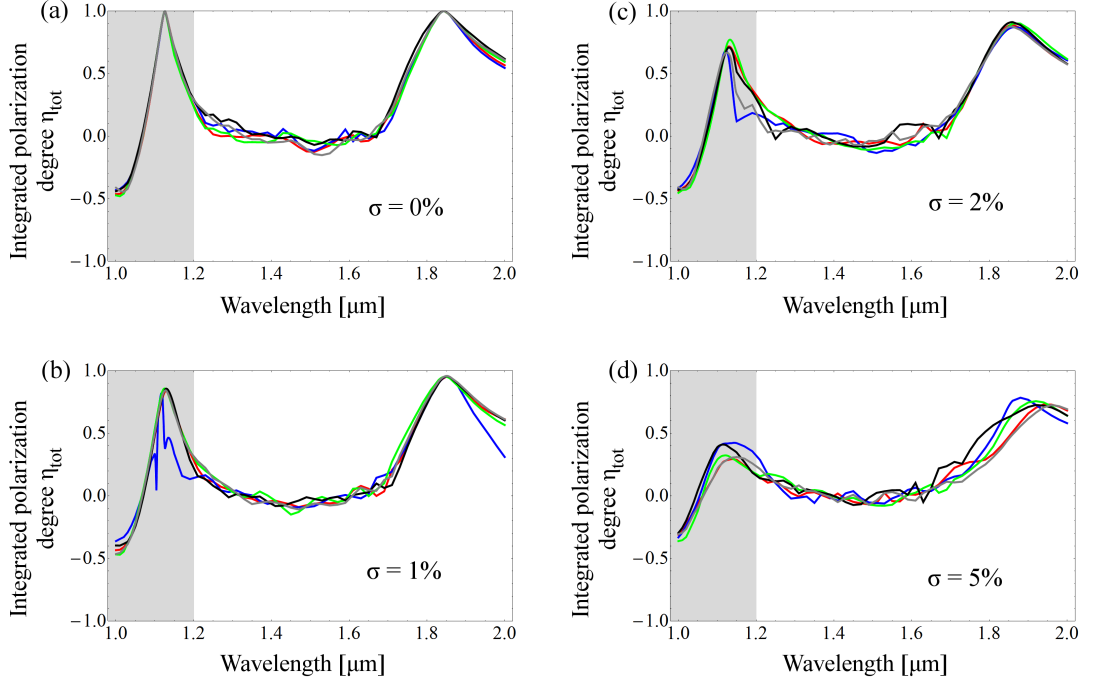


FIGURE 3.7: Spectra of integrated polarization degrees η_{tot} calculated for random solutions nanoparticles with radii given by normal distributions centered at $0.23 \mu\text{m}$, with standard deviations of (a) 0, (b) $0.01a_0$, (c) $0.02a_0$ and (d) $0.05a_0$. For each distribution of sizes, we performed simulations of light scattering in 5 random media comprising 80 nanoparticles. In the calculations the nanoparticles are considered as point scatterers with dipolar polarizabilities, accurately describing their optical response for wavelengths above $\lambda = 1.2 \mu\text{m}$. The shaded regions correspond to the spectral range ($\lambda < 1.2 \mu\text{m}$) where higher order modes dominate the optical response of medium, effectively quenching the helicity conservation.

the dispersions of 1%, 2% and 5%, respectively, around $\lambda_K = 1.844 \mu\text{m}$.

The largest assumed standard deviation of radii (5%) is close to the inhomogeneities found in realistic solutions of dielectric nanoparticles generated nowadays [144]. While weakening of helicity conservation appears to be considerable for these widths, we stress that the polarization degree of 0.6 signifies that only about 20% of the scattered light exhibits polarization opposite to that of the incident illumination.

For each of the distributions shown above, we plot in Fig. 3.8 the polarization degree η (upper panel) and intensity patterns I of the helical light scattered on representative random samples. The wavelength of incident light is $1.844 \mu\text{m}$. The increasing distribution of widths triggers an increasingly inhomogeneous and asymmetric polarization degree and intensity patterns, with higher intensity and more significant helicity conservation in the forward scattering ($\theta = 0$).

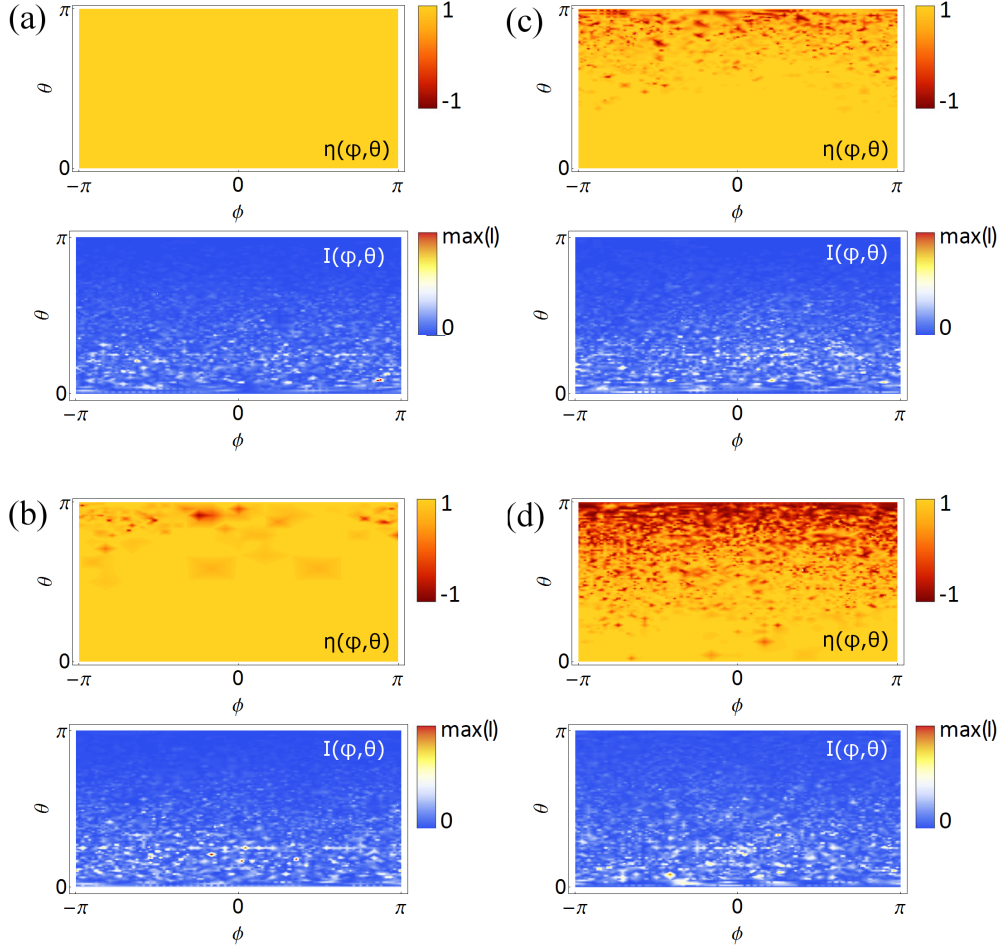


FIGURE 3.8: Patterns of polarization degree η (upper panels) and scattering intensity I (lower panels) for representative random samples of 80 scatterers with the standard deviations of radii ((a) 0, (b) $0.01a_0$, (b) $0.02a_0$, (d) $0.05r_0$) as discussed in Fig. 3.7.

3.3 Summary

In conclusion, we have investigated the problem of scattering of helical light in a piecewise-homogeneous medium and in a solution of dipolar scatterers, and formulated simple conditions for the preservation of the helicity in such systems. Specifically, in the latter case, we showed that if both electric and magnetic dipolar polarizabilities of scatterers are equal, then the electromagnetic field in the system is symmetric with respect to the duality transformations. We further discussed in details an implication of this phenomenon - an anomalous conservation of the circular polarization of light in the scattering on a single nanoparticle, a dimer and in a random solution of dielectric nanoparticles. Our results open a pathway to exploit novel properties in random scattering media, including

intriguing applications in random lasing [145, 146], as well as provide new possibilities to characterize magnetic optical properties of nanoscatterers [147].

Chapter 4

Quantum plasmonics

“ ‘You were about to run into a tree, and I stopped you.’ ‘No I wasn’t.’ She looks off after the squirrel, now safely up a bigger tree on the other side of the yard, ‘Because of quantum.’ ”

– Chad Orzel, *How to Teach Quantum Physics to Your Dog*

Previous chapters of this thesis were devoted entirely to the description of physical phenomena which, at the surface, appear to be purely *classical* effects. By *classical* we should understand that they have been successfully described and understood within models based on the description of electromagnetism offered by the Maxwell’s equations and the macroscopic formulation of dielectric functions, rather than the Quantum Physics. To arrive at such models, we have had to sacrifice the more fundamental, quantum-mechanical description of the contribution from the *d* electrons to the dielectric properties of gold, the band structure of silicon, or the coherent dynamics of molecules serving as dipolar emitters. We have made sure to only apply those approximations when their fragile quantum-mechanical nature did not play a role in the investigated phenomena. In this way, we have been carefully following the path that plasmonic and nanophotonics have been trudging on until approximately a decade ago. Around that date, which we have arbitrarily identified with the publication of the seminal contribution

by Akimov *et al.* [148], the methods for manufacturing elements of nanosystems capable of generating, transferring and emitting single photons, have reached the qualities which would allow us to foresee the feasibility and realizations of quantum-mechanical nanosystems.

In this chapter we describe a contribution to this effort, a quantum-mechanical description of Raman scattering from a molecule placed in a plasmonic cavity. The phenomenon itself has been demonstrated and studied in great detail, as illustrated in a long list of reports [5, 40, 42, 149, 150] and alternative models [151–154] that would follow every major experimental contribution. Interestingly, most of the theoretical formalisms suffer from a clear dichotomy, as they describe the plasmonic systems through the classical electromagnetism, and apply the quantum-mechanical framework to handle the dynamics of the molecule. This way, one effectively simplifies the role of the cavity to a mere concentrator of the incident light. Our model lifts this limitation, and allows us to study the coherent interaction between *quantized plasmons* populating the *plasmonic cavity* and the quantized vibrations of the molecule.

Before we introduce the model and present its predictions, we provide a brief introduction into the formalism used to describe the interactions of the molecule and the plasmon with the environment - the theory of *open quantum systems*.

4.1 Brief introduction to open quantum systems

4.1.1 Von Neumann equation

The elementary approach to addressing the coherent dynamics of a *closed quantum system*, defined as a quantum-mechanical system which does not interact in any way with elements external to the system, or environment, is through the Schrödinger equation

$$i\hbar \frac{d}{dt} |\phi(t)\rangle = \hat{H} |\phi(t)\rangle, \quad (4.1)$$

where \hat{H} is the Hamiltonian of the system and $|\phi(t)\rangle$ describes its quantum state, which corresponds to a vector in the Hilbert space \mathcal{H} .

For a so-called *pure quantum state* of a system, which can be described by a single state vector $|\phi\rangle$, we can construct a projection operator

$$\rho_\phi = |\phi\rangle \langle\phi|, \quad (4.2)$$

to which we will be referring to as the *density matrix of the pure state* $|\phi\rangle$. We can also consider a state defined as a statistical mixture of pure states:

$$\rho = \sum_i p_i |\phi_i\rangle \langle \phi_i|, \quad (4.3)$$

where p_i ($0 \leq p_i \leq 1$, $\sum_i p_i = 1$) is the probability of finding the system in the pure quantum state $|\phi_i\rangle$. Such statistical ensembles can be viewed as mixtures of the elements from the Hilbert space. The *von Neumann equation* governing the evolution of the density matrix can be derived from Eq. (4.1) as

$$\frac{d}{dt}\rho(t) = -\frac{i}{\hbar}[\hat{H}, \rho], \quad (4.4)$$

and the information about any subsystem A can be extracted from the *reduced density matrix* ρ_A defined as

$$\rho_A = \text{Tr}_{S/A} \rho, \quad (4.5)$$

where $\text{Tr}_{S/A}$ denotes the partial trace over the elements of the system S not included in A (S/A).

4.1.2 Open quantum system

One might wonder why we would sacrifice the exact description of the system provided by Eq. (4.1) and complicate the formalism by introducing density matrices. The answer is twofold:

- Often we do not have sufficient knowledge about the initial state of the whole system to formulate its description in terms of a vector state, but instead we know that the system is in a particular vector state $|\phi_i\rangle$ with given probability p_i .
- We are only interested in the observables related to some part of the system, and the remaining elements are not relevant.

An elementary example of a setup which can be effectively described through the density matrix formalism, is a two-level system (TLS) coupled to a thermal photon bath. While we are interested in the exact dynamics of populations and coherences of the TLS, we are not concerned with the exact state and dynamics of the continuous, large bath.

Let us be a bit more general and consider an abstract quantum system S coupled to a bath of modes, which we will denote as a *reservoir* R . The dynamics of these two

elements is given by the Hamiltonian of the system \hat{H}_S , reservoir \hat{H}_R and a term which describes their interaction \hat{H}_{SR} :

$$\hat{H} = \hat{H}_S + \hat{H}_R + \hat{H}_{SR}. \quad (4.6)$$

Since the system and reservoir together form a closed quantum system, its dynamics will be given by the von Neumann equation for the evolution of the density operator ρ (Eq. (4.4)). In the interaction picture, the density matrix of the system and its Hamiltonian are defined as

$$\rho_I(t) = e^{i(\hat{H}_S + \hat{H}_R)t} \rho(t) e^{-i(\hat{H}_S + \hat{H}_R)t}, \quad (4.7a)$$

and

$$\hat{H}'_{SR}(t) = e^{i(\hat{H}_S + \hat{H}_R)t} \hat{H}_{SR} e^{-i(\hat{H}_S + \hat{H}_R)t}, \quad (4.7b)$$

respectively, and we can rewrite the von Neumann equation (Eq. (vonNeumann)) as

$$\frac{d}{dt} \rho_I(t) = -\frac{i}{\hbar} [\hat{H}'_{SR}(t), \rho_I(t)]. \quad (4.8)$$

A formal solution of Eq. (4.8) is given as

$$\rho_I(t) = \rho_I(0) - \frac{i}{\hbar} \int_0^t [\hat{H}'_{SR}(\tau), \rho_I(\tau)] d\tau. \quad (4.9)$$

Inserting this solution back into the right-hand side of Eq. (4.8) and taking the partial trace over the reservoir Tr_R on both sides, we arrive at

$$\frac{d}{dt} \rho_{S,I}(t) = -\frac{i}{\hbar} \text{Tr}_R[\hat{H}'_{SR}(t), \rho_I(0)] - \frac{1}{\hbar^2} \int_0^t \text{Tr}_R[\hat{H}'_{SR}(t), [\hat{H}'_{SR}(\tau), \rho_I(\tau)]] d\tau, \quad (4.10)$$

where $\rho_{S,I} = \text{Tr}_R(\rho_I)$ is the reduced density matrix of the system in the interaction picture. We will now make a number of approximations that will lead to a simpler form of the above equation:

1. The system and the reservoir are not correlated at $t = 0$, and thus $\rho(0) = \rho_S(0) \otimes \rho_R(0)$, where \otimes denotes the tensor product.
2. Within the *Born approximation*, the once-uncorrelated setup of the system and reservoir (at $t = 0$) does not build up correlations over time, meaning that its complete density matrix can be still factorized $\rho(t) \approx \rho_S(t) \otimes \rho_R(t) \approx \rho_S(t) \otimes \rho_R$.

This approximation holds if the interaction between the system and the reservoir is weak and the influence of the former on the latter is small.

3. We apply the *Markov approximation* by replacing the integrand $\rho_I(\tau)$ by $\rho_I(t)$, and thus stating that the evolution of the system depends solely on its current state and not on its *history*. This approximation relies on the short *memory* of the reservoir, which will dissipate any information about the system in a time much shorter than the characteristic time scale of the evolution of the system.
4. To remove the term $\text{Tr}_R[\hat{H}'_{SR}(t), \rho_I(0)]$, we redefine the Hamiltonian of the system by including the term $\text{Tr}_R[\hat{H}_{SR}(t), \rho_R(0)]$ into the system's Hamiltonian \hat{H}_S and removing it from the interaction Hamiltonian \hat{H}_{SR} .

Having applied these approximations, we arrive at the *Redfield equation*

$$\frac{d}{dt}\rho_{S,I}(t) = -\frac{1}{\hbar^2} \int_0^t \text{Tr}_R[\hat{H}'_{SR}(t), [\hat{H}'_{SR}(\tau), \rho_I(\tau)]] d\tau. \quad (4.11)$$

Note that this is not yet a Markovian equation, as it exhibits an explicit dependence on the arbitrary initial time parameter $t = 0$ through the lower limit of the integral. We can correct that problem by introducing a new parameter s , substituting τ in Eq. (4.11) by $t - s$ and, recalling our argument about the short reservoir memory, extending the integration limit to ∞ .

Finally, going back to the Schrödinger picture, we obtain a general form of the *master equation* for the density matrix of the system ρ_S

$$\frac{d}{dt}\rho_S(t) = -\frac{i}{\hbar}[\hat{H}_S(t), \rho_S(t)] - \frac{1}{\hbar^2} \int_0^\infty \text{Tr}_R[\hat{H}_{SR}(t), [\hat{H}_{SR}(t-s), \rho_S(t) \otimes \rho_R]] ds. \quad (4.12)$$

The approximations listed above deserve a more careful analysis, and such has been given to them in the extensive literature on the subject (see Refs. [155, 156] for the discussion and Refs. [157–160] for examples and applications). Of particular interest is the Markov approximation, which holds if the *memory* time of the reservoir is much shorter than the time-scales of the evolution of the system. The deviation from this condition could lead to some very interesting dynamics [157–160]. However, usually the division of the setup of interest into the system and reservoir is done in such a way that these conditions are fulfilled. We briefly discuss this problem, and provide canonical examples, in the following subsection.

However, before we do that, let us rewrite Eq. (4.12) in its final, elegant form

$$\frac{d}{dt}\rho_S(t) = -\frac{i}{\hbar}[\hat{H}_S(t), \rho_S(t)] + \mathcal{L}[\rho_S]. \quad (4.13)$$

The first term on the right-hand side describes the coherent evolution of the system, while the second one, $\mathcal{L}[\rho_S]$, called the *Lindblad-Kossakowski super-operator* describes the influence of the time-independent reservoir on the dynamics of the system. Its exact form will depend on the interaction we describe in \hat{H}_{SR} , so that it can represent the decay of the excitation from the system into the reservoir, the incoherent excitation of the system by a thermal bath, or the dephasing of the system. Either way, we will be referring to the system S , its coherent dynamics and the interaction with the reservoir as the *open quantum system*.

4.1.3 Designing the open quantum system - case study

Let us consider a physical setup in which an atom, modeled as a 2-, 3- or 4-level system, is placed in an unstructured (non-resonant) large environment (the energy transferred from the atom to the environment does not significantly affect the reservoir's state) modeled as a continuous bath of free-space photons. In this case, the choice of the system and reservoir is rather natural, therefore we will consider the atom as the sole element of the open quantum system, and the bath as the reservoir (see Fig. 4.1).

In the simplest case of a 2-level atom with the resonant frequency of the atomic transition ω_{at} , the relevant Hamiltonian of the system is defined as

$$\hat{H}_S = \hat{H}_{\text{atom}} = \hbar\omega_{\text{at}}\hat{\sigma}_z, \quad (4.14a)$$

where $\hat{\sigma}_z$ is the Pauli matrix. The reservoir is modeled as a collection of free-space photons with momenta \mathbf{k} , the corresponding frequencies $\omega_{\mathbf{k}}$ and governed by the bosonic creation $\hat{a}_{\mathbf{k}}^\dagger$ and annihilation $\hat{a}_{\mathbf{k}}$ operators.

$$\hat{H}_R = \hbar \int_{\mathbf{k}} \omega_{\mathbf{k}} \hat{a}_{\mathbf{k}}^\dagger \hat{a}_{\mathbf{k}} \quad (4.14b)$$

Furthermore, the system-environment interaction is described through a familiar Jaynes-Cummings Hamiltonian

$$\hat{H}_{SR} = \hbar \int_{\mathbf{k}} g_{\mathbf{k}} \hat{a}_{\mathbf{k}} \hat{\sigma}_+ + \text{h.c.}, \quad (4.14c)$$

where h.c. denotes the *hermitian conjugate* of the respective terms, $g_{\mathbf{k}}$'s are the coupling coefficients and the spin raising and lowering operators are defined by the Pauli matrices $\hat{\sigma}_{\pm} = \hat{\sigma}_x \pm i\hat{\sigma}_y$.

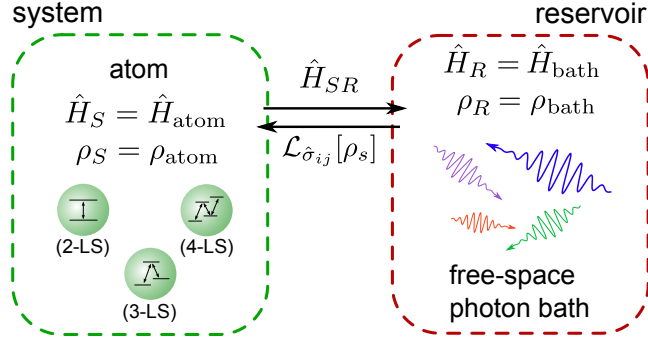


FIGURE 4.1: Division of the elements of the setup into the system and reservoir. The former contains the atom described by the density matrix ρ_{atom} , while the latter is a free-space photon bath.

We can now plug this explicit form of the interaction Hamiltonian into Eq. (4.12). If we assume that the photon bath is in a thermal equilibrium state at temperature T , we can use the following properties of the averages of the bath operators

$$\langle \hat{a}_{\mathbf{k}} \hat{a}_{\mathbf{q}} \rangle = \langle \hat{a}_{\mathbf{k}}^{\dagger} \hat{a}_{\mathbf{q}}^{\dagger} \rangle = 0, \quad (4.15a)$$

$$\langle \hat{a}_{\mathbf{k}}^{\dagger} \hat{a}_{\mathbf{q}} \rangle = N(\omega_{\mathbf{k}}) \delta_{\mathbf{k}, \mathbf{q}}, \quad (4.15b)$$

$$\langle \hat{a}_{\mathbf{k}} \hat{a}_{\mathbf{q}}^{\dagger} \rangle = (N(\omega_{\mathbf{k}}) + 1) \delta_{\mathbf{k}, \mathbf{q}}, \quad (4.15c)$$

where $N(\omega) = (e^{\hbar\omega/k_B T} - 1)^{-1}$, defined through the Boltzmann constant k_B , is the Bose-Einstein distribution that governs the thermal population of the photon bath modes. After some algebra we arrive at the following form of the master equation:

$$\frac{d}{dt} \rho_S(t) = -\frac{i}{\hbar} [\hat{H}_S(t), \rho_S(t)] + i\Delta_{\text{at}}[\rho_S, \hat{\sigma}_z] + \frac{\gamma}{2} [N(\omega_{\text{at}}) + 1] \mathcal{L}_{\hat{\sigma}_-}[\rho_S] + \frac{\gamma}{2} N(\omega_{\text{at}}) \mathcal{L}_{\hat{\sigma}_+}[\rho_S], \quad (4.16)$$

where the Lindblad-Kossakowski operator [161, 162] $\mathcal{L}_{\hat{O}}[\rho_S]$ for an arbitrary operator \hat{O} is defined as

$$\mathcal{L}_{\hat{O}}[\rho] = 2\hat{O}\rho\hat{O}^{\dagger} - \hat{O}^{\dagger}\hat{O}\rho - \rho\hat{O}^{\dagger}\hat{O}. \quad (4.17)$$

The terms on the right-hand side of Eq. (4.16) describe, in the order of appearance:

- The coherent evolution of the atom.

- The *Lamb shift* arising due to the interaction with the modes of the bath, renormalizing the energy of the atom by

$$\Delta_{\text{at}} = \mathcal{P} \int_{-\infty}^{\infty} d\omega \frac{J(\omega)N(\omega)}{\omega_{\text{at}} - \omega} + \mathcal{P} \int_{-\infty}^{\infty} d\omega \frac{J(\omega)(N(\omega) + 1)}{\omega_{\text{at}} - \omega}, \quad (4.18)$$

where $J(\omega)$ is the *spectral density* of the bath defined as $J(\omega) = \sum_{\mathbf{k}} |g_{\mathbf{k}}|^2 \delta(\omega - \omega_{\mathbf{k}})$ and \mathcal{P} denotes the principal value.

- The decay of the atom from the excited state to the ground state at a rate $\gamma[N(\omega_{\text{at}}) + 1]$, where $\gamma = 2\pi J(\omega_{\text{at}})$. The two terms in the sum $N(\omega_{\text{at}}) + 1$ describe the *stimulated* emission dependent on the thermal population of the bath and the *spontaneous* emission, respectively.
- The excitation of the atom by the energy from the bath. Note that this term, similarly to stimulated emission, will vanish if the thermal population of the bath, $N(\omega_{\text{at}})$, is equal to 0.

Having presented the description of this elementary model in the formalism of open quantum systems, we can complicate it slightly by including a cavity into the *system*, thus bringing it closer to the actual setup that we will consider in this chapter. A schematic of such expanded system and reservoir is shown in Fig. 4.2. Independently

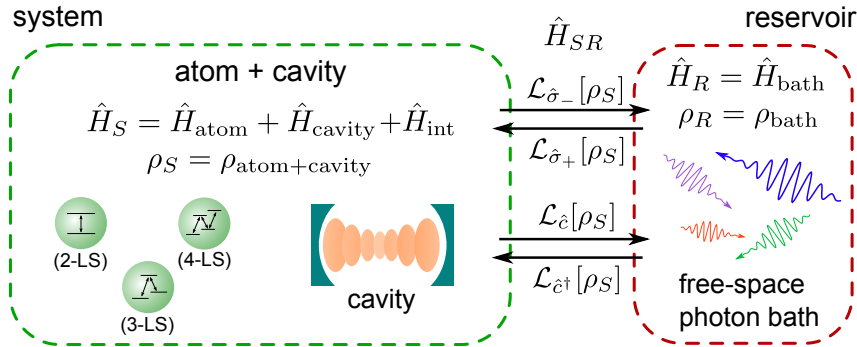


FIGURE 4.2: Division of the elements of the setup into the system and reservoir. The former contains the atom and the cavity, described together by the density matrix $\rho_{\text{atom+cavity}}$, while the latter contains all the free-space photon bath modes.

of the form of the cavity-atom interaction that is chosen, this framework will yield the coherent dynamics of the system, encapsulated by the $[\hat{H}_S, \rho_S]$ term in the master equation (Eq. (4.16)). We can thus focus on the interaction of the cavity (described by the creation \hat{c}^\dagger and annihilation \hat{c} operators) with the reservoir, which defines the

Lindblad-Kossakowski operators (denoted by $\mathcal{L}_{\hat{c}}[\rho_S]$, $\mathcal{L}_{\hat{c}^\dagger}[\rho_S]$, $\mathcal{L}_{\hat{\sigma}_-}[\rho_S]$ and $\mathcal{L}_{\hat{\sigma}_+}[\rho_S]$ in the schematic in Fig. 4.2) added to account for the interaction of the cavity and the atom with the reservoir. If we choose to describe the state of the cavity, resonant at frequency ω_c with bosonic operators, the Hamiltonian of the cavity should be given as

$$\hat{H}_{\text{cavity}} = \hbar\omega_c \hat{c}^\dagger \hat{c}, \quad (4.19)$$

and its coupling to the reservoir should be described by a proper term in the Hamiltonian

$$\hat{H}_{SR,\text{cavity}} = \hbar \int_{\mathbf{k}} g_{\mathbf{k}}^c \hat{a}_{\mathbf{k}} \hat{c}^\dagger + \text{h.c.}, \quad (4.20)$$

with the coupling coefficients $g_{\mathbf{k}}^c$. Therefore, we will finally arrive at the master equation

$$\begin{aligned} \frac{d}{dt}\rho_S(t) = & -\frac{i}{\hbar}[\hat{H}_S(t), \rho_S(t)] \\ & + i\Delta_{\text{at}}[\rho_S, \hat{\sigma}_z] + i\Delta_c[\rho_S, \hat{a}^\dagger \hat{a}] \\ & + \frac{\gamma}{2}(N(\omega_{\text{at}}) + 1)\mathcal{L}_{\hat{\sigma}_-}[\rho_S] + \frac{\gamma}{2}N(\omega_{\text{at}})\mathcal{L}_{\hat{\sigma}_+}[\rho_S] \\ & + \frac{\kappa}{2}(N(\omega_c) + 1)\mathcal{L}_{\hat{a}}[\rho_S] + \frac{\kappa}{2}N(\omega_c)\mathcal{L}_{\hat{a}^\dagger}[\rho_S]. \end{aligned} \quad (4.21)$$

The new quantities related to the cavity-reservoir interaction: Δ_c (Lamb shift arising from the interaction of the cavity with the bath)

$$\Delta_c = \mathcal{P} \int_{-\infty}^{\infty} d\omega \frac{J(\omega)_c N(\omega)}{\omega_c - \omega} + \mathcal{P} \int_{-\infty}^{\infty} d\omega \frac{J(\omega)_c}{\omega_c - \omega} (N(\omega) + 1), \quad (4.22)$$

where $J_c(\omega) = \int_{\mathbf{k}} |g_{\mathbf{k}}^c|^2$, as well as $\kappa = 2\pi J_c(\omega_c)$, and κ (decay of the cavity), are defined in a similar way as Δ_{at} and γ , respectively.

4.2 Raman scattering from molecules in plasmonic cavities

In this section, we apply the framework of open quantum systems to describe the coherent interaction between plasmons and molecular vibrations in typical configurations of *Surface Enhanced Raman Scattering* (SERS). SERS is a spectroscopic technique in which the inelastic scattering from a molecule is increased by placing it in a *hotspot* of a plasmonic cavity, where the electric fields associated with the incident and the scattered photons are strongly enhanced (see the schematic in Fig. 4.3) [17]. The difference

between the energy of those two photons provides a *fingerprint* of the molecule, i.e., detailed chemical information about its vibrational structure. Over the last decades, considerable advances in designing efficient SERS configurations [163] have resulted in the observation of Raman scattering from single molecules [149], and recently, even reaching sub-nanometer resolution image of the vibrational modes of a molecule [42]. These results suggest that some experimental realizations of SERS have reached a regime where the quantum-mechanical nature of both the molecular vibrations and the plasmonic cavity emerges [41], calling for an adequate theoretical description that goes beyond the classical treatment of the electric fields inside plasmonic cavities [17, 22, 164].

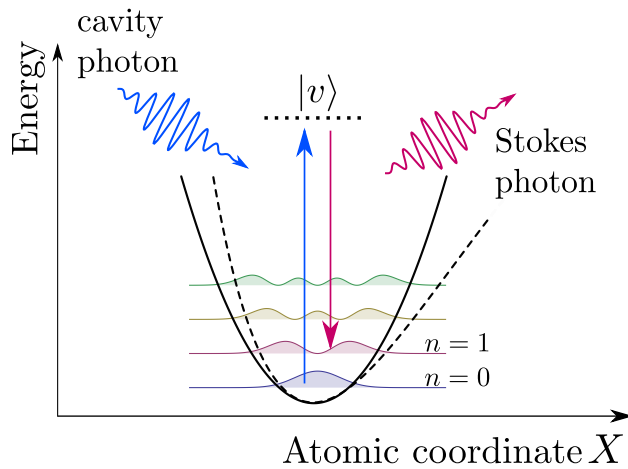


FIGURE 4.3: Schematic of the two-photon non-resonant Stokes scattering between two vibrational states of a molecule ($n = 0 \rightarrow 1$) mediated by a virtual state $|v\rangle$ (dotted line). A harmonic potential (solid line) approximates the energy landscape of the ground electronic level (dashed line).

4.2.1 Quantization of excitations

The model presented in this section addresses the underlying quantum-mechanical nature of Raman scattering processes by describing both the vibrations of the molecule and the electromagnetic field of a plasmonic cavity through *quantized bosonic modes*. In the following subsection we discuss this framework in details.

4.2.1.1 Quantized vibrations of a molecule

Let us consider a simplified one-dimensional model of the energy landscape of the ground electronic state of a molecule as a function of the generalized atomic coordinate (e.g.,

the length of a molecular C=O bond [41, 164]). Such potential, described with a dashed line in Fig. 4.3, can be approximated as a displaced harmonic potential depicted with a solid line. Therefore, the vibrations characterized by the vibrational frequency ω_m [165], can be quantized following the usual prescription for the quantization of a harmonic oscillator [166]. We thus introduce the creation and annihilation operators \hat{b} and \hat{b}^\dagger which describe the creation and annihilation of a quantum of vibrations, which we will be referring to as *phonons*. We next define a linear polarizability of the molecule along this coordinate $\hat{\alpha}_\nu$ as [17]

$$\hat{\alpha}_\nu = R_\nu Q_\nu^0 (\hat{b} + \hat{b}^\dagger), \quad (4.23)$$

where R_ν is the element of the Raman tensor and $Q_\nu^0 = \sqrt{\hbar/(2\omega_m)}$ is the zero-point amplitude of the vibrations. For the sake of simplicity, we neglect the component of the linear optical polarizability of the molecule independent of Q_ν , which describes the elastic scattering. Furthermore, we should note that by using the free-space Raman tensor R_ν , which describes interaction of a molecule with an incident planewave in free space, we will focus our attention on the *electromagnetic enhancement* mechanism, and neglect any contribution from the *chemical enhancement*. Finally, we stress that this approach is limited to the *off-resonant Raman scattering*, for which the virtual state mediating the Raman transition (dotted line in Fig. 4.3) is strongly detuned from any excited electronic state.

A detailed description of the quantization protocol of vibrations of a molecule can be found in Ref. [17].

4.2.1.2 Quantization of a plasmonic cavity

Due to the lossy and dispersive character of the metal forming the plasmonic cavity, the canonical prescription for the quantization of the electromagnetic fields cannot be applied to the quantization of plasmons [167]. An alternative path is described in the contributions listed as Refs. [168–170], where the formalism of *macroscopic QED* was presented. Within this framework, the fields inside the metal are quantized as local operators $\hat{\mathbf{f}}_\lambda(\omega, \mathbf{r})$, dependent on the position \mathbf{r} and frequency ω , describing modes with polarization $\lambda = 1, 2$, obeying the canonical commutation relations

$$\left[\hat{\mathbf{f}}_{\lambda_1}(\omega_1, \mathbf{r}_1), \hat{\mathbf{f}}_{\lambda_2}^\dagger(\omega_2, \mathbf{r}_2) \right] = \delta(\omega_1 - \omega_2) \delta(\mathbf{r}_1 - \mathbf{r}_2) \delta_{\lambda_1, \lambda_2}, \quad (4.24)$$

and yielding the following Hamiltonian of the cavity:

$$\hat{H}_{\text{macr. QED}} = \sum_{\lambda} \int d^3\mathbf{r} \int_0^{\infty} d\omega \hbar\omega \hat{\mathbf{f}}_{\lambda}^{\dagger}(\omega, \mathbf{r}) \cdot \hat{\mathbf{f}}_{\lambda}(\omega, \mathbf{r}) \quad (4.25)$$

This description is derived by diagonalizing the Hamiltonian of the more elementary system comprising radiation modes coupled to a reservoir of localized harmonic oscillators which represent the Ohmic losses of the material. For a detailed summary of this formalism and its numerous implications, we direct the reader to Ref. [170].

The electric field inside the cavity, with which our molecule will be interacting, can be then expressed through the classical electric Green's function $\overset{\leftrightarrow}{\mathbf{G}}_E(\mathbf{r}, \mathbf{r}', \omega)$

$$\hat{\mathbf{E}}(\omega, \mathbf{r}') = i\sqrt{\frac{\hbar}{\pi\epsilon_0}} \frac{\omega^2}{c^2} \sum_{\lambda} \int d^3\mathbf{r} \sqrt{\text{Im}[\epsilon_m(\omega)]} \overset{\leftrightarrow}{\mathbf{G}}_E(\mathbf{r}, \mathbf{r}', \omega) \hat{\mathbf{f}}_{\lambda}(\omega, \mathbf{r}), \quad (4.26)$$

where $\epsilon_m(\omega)$ is the dielectric function of the metal and the integration is carried out over the volume of the metal.

Pseudomodes of the cavity

While the quantization procedure sketched above might be exact, in practice it proves very difficult to apply in realistic setups, and provides little information about the physical phenomena governing the dynamics of the system. We therefore choose to consider the more familiar problem of the spontaneous decay of a two-level system (TLS) in a structured environment. The TLS is characterized by the transition frequency ω_0 and the transition dipole \mathbf{d} , and is placed in the medium described by $\overset{\leftrightarrow}{\mathbf{G}}_E$, at position \mathbf{r}' . It can be easily shown [167, 171, 172] that the amplitude $c_e(t)$ of the excited state of the molecule is given by an oscillating function $c_e(t) = \tilde{c}_e(t)e^{i\omega_0 t}$, where $\tilde{c}_e(t)$ is governed by the integro-differential equation

$$\dot{\tilde{c}}_e(t) = - \int_0^t d\tau K(t - \tau) \tilde{c}_e(\tau). \quad (4.27)$$

Memory kernel K is defined as

$$K(t) = \int_0^{\infty} d\omega J(\omega) e^{i(\omega - \omega_0)t}. \quad (4.28)$$

$J(\omega)$ is the spectral density, which we have defined earlier as the sum of the squared coupling coefficients between the elements of the open quantum system and the bath.

In the formalism of Green's functions, the spectral density is defined as

$$J(\omega) = \frac{\omega^2}{\pi\epsilon_0\hbar c^2} \mathbf{d} \cdot \text{Im} \left[\overset{\leftrightarrow}{\mathbf{G}}_E(\mathbf{r}', \mathbf{r}', \omega) \right] \cdot \mathbf{d}^*. \quad (4.29)$$

Note that, following this approach, we effectively remove the cavity from the system, and formulate the dynamics of the TLS solely in terms of the spectral density J , or the memory kernel K of the environment. This formalism can be adopted to describe numerous interesting effects, such as the non-Markovian dynamics of the excitons in structured environments [157, 160]. In Fig. 4.4 we plot an exemplary normalized spectral

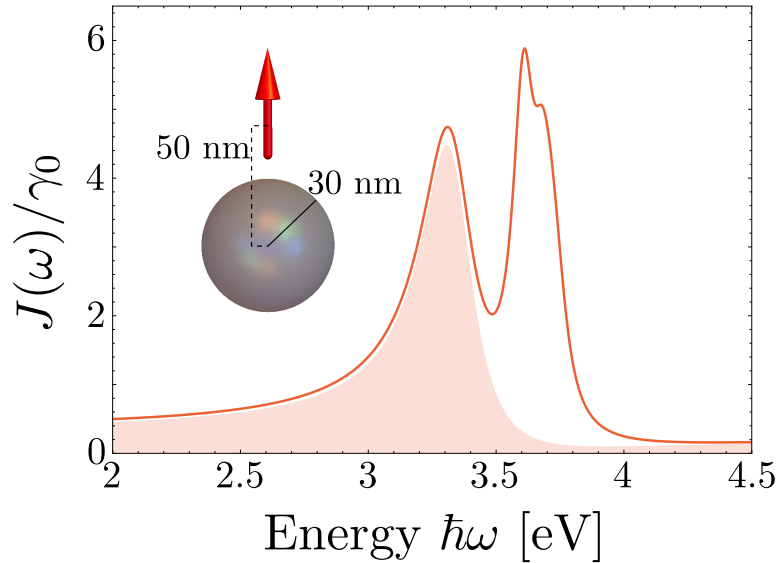


FIGURE 4.4: Spectral density $J(\omega)$ normalized by the decay rate of free-space decay rate of a dipolar quantum emitter, calculated for an emitter (red arrow in the inset) placed 50 nm from the center of a 30 nm radius silver nanoparticle. The dashed red area corresponds to the contribution from the dipolar mode of the sphere, which we identify with the cavity mode resonant at $\hbar\omega_c$, with decay rate $\hbar\kappa$ defined by the FWHM of the profile.

density $J(\omega)/\gamma_0$ calculated for a dipolar emitter characterized by a free-space decay rate γ_0 , positioned over a silver nanoparticle (described by the Drude model with $\epsilon_\infty = 4.6$, $\hbar\omega_p = 9$ eV and $\hbar\gamma_p = 0.1$ meV) as shown schematically in the inset. The spectral density was calculated by noting that, in the so-called *weak-coupling limit* (when the decay of the emitter is an *irreversible* process [166, 167, 172, 173]), $J(\omega)/\gamma_0$ is related to the enhancement factors which we have discussed in Chapter 2 ($\Gamma_{\text{tot}}^{\perp,e}/\gamma_0$):

$$\frac{J(\omega)}{\gamma_0} = \frac{1}{2\pi} \frac{\Gamma_{\text{tot}}^{\perp,e}}{\Gamma_0}. \quad (4.30)$$

We make use of the additive nature of the contribution to $J(\omega)$ from the Mie modes and separate the contribution from the radiative, dipolar mode and mark it with a red-shaded area. We now take an informal step and identify this quasi-lorentzian profile with the dominant cavity mode, characterized by the resonant frequency ω_c and the decay rate κ given by the peak frequency and the FWHM of the plasmonic profile, respectively. Similar approach has been implemented in other studies, where authors have been analyzing the coupling of quantum emitters with a *pseudomode* of a metallic interface [171] or with a *pseudomode* formed by the set of higher-order modes (peaking around 3.7 eV in Fig. 4.4) of a silver particle [174, 175].

We should admit that by following this prescription we ignore the limitations which we have been discussing in Chapter 1 of this thesis, regarding the approximation of the dipolar polarizability profiles by Lorentzian functions. Most notably, the quasi-lorentzian profile of the dipolar polarizability of the sphere, calculated with Mie theory, can have a non-vanishing real component at resonance frequency, which could lead to a significant Lamb shift. Nevertheless, our approach is a good first step to the characterization of the plasmonic system to further explore its interaction with the vibrations.

4.2.2 Cavity-vibrations interaction Hamiltonian

Having addressed the problem of quantization of the plasmonic cavity, and the vibrations of the molecules, let us consider the coupling between these elements. The electric field, \hat{E} , of the cavity mode characterized by the resonant frequency ω_c , decay rate κ and the effective volume V_{eff} [176, 177], can be expressed by the plasmon annihilation (\hat{a}) and creation (\hat{a}^\dagger) operators as

$$\hat{E} = i\sqrt{\frac{\hbar\omega_c}{2\varepsilon_0 V_{\text{eff}}}}(\hat{a} - \hat{a}^\dagger). \quad (4.31)$$

The induced *Raman dipole* [17]

$$\hat{p}_R = \hat{\alpha}_\nu \hat{E} \quad (4.32)$$

will be therefore interacting with the cavity field \hat{E} , yielding the interaction Hamiltonian

$$\hat{H}_I = -\hat{p}_R \hat{E} = R_\nu Q_\nu^0 \frac{\hbar\omega_c}{2\varepsilon_0 V_{\text{eff}}} (\hat{a} - \hat{a}^\dagger)^2 (\hat{b} + \hat{b}^\dagger) = \frac{\hbar g}{2} [\hat{a}^2 + (\hat{a}^\dagger)^2 - \hat{a}\hat{a}^\dagger - \hat{a}^\dagger\hat{a}] (\hat{b} + \hat{b}^\dagger), \quad (4.33)$$

where we have introduced the *bare* or *single-photon coupling*

$$g = R_\nu Q_\nu^0 \frac{\omega_c}{\varepsilon_0 V_{\text{eff}}}. \quad (4.34)$$

Within the so-called *rotating wave approximation* (RWA) [166, 178] the counter-propagating terms proportional to $(\hat{a}^\dagger)^2$ and $(\hat{a})^2$, which yield rapid oscillations at frequencies of $2\omega_c \gg \omega_m$, are removed. Furthermore, using the commutation relation

$$[\hat{a}, \hat{a}^\dagger] = 1, \quad (4.35)$$

we can rewrite the remaining part of the interaction Hamiltonian as

$$\hat{H}_I = -\hbar g \left(\hat{a}^\dagger \hat{a} + \frac{1}{2} \right) (\hat{b} + \hat{b}^\dagger). \quad (4.36)$$

The second term in the first parentheses describes the interaction between vibrations and the vacuum field of the cavity $g/2(\hat{b} + \hat{b}^\dagger)$. We can remove it by properly displacing the equilibrium position of the vibrations, arriving at the final form of the interaction Hamiltonian

$$\hat{H}_I = -\hbar g \hat{a}^\dagger \hat{a} (\hat{b} + \hat{b}^\dagger). \quad (4.37)$$

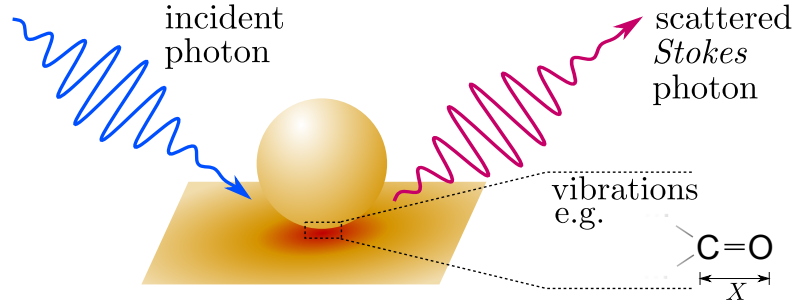


FIGURE 4.5: Schematic description of Raman scattering from a molecule placed in a plasmonic cavity.

In a direct analogy to the description of optomechanical systems, Roelli *et al.* [179] considered a plasmonic cavity coupled to a Raman-active molecule characterized with the amplitude of vibrations $\hat{Q}_\nu = Q_\nu^0(\hat{b} + \hat{b}^\dagger)$. In this picture, a Hamiltonian identical to that derived above can be found by noting that the frequency of the cavity ω_c coupled to a Raman-active molecule is a function of \hat{Q}_ν . Expanding it around the equilibrium position defined as $\hat{Q}_\nu = 0$:

$$\omega_c(\hat{Q}_\nu) \approx \omega_c(0) + \hat{Q}_\nu \left[\frac{\partial \omega_c}{\partial \hat{Q}_\nu} \right]_{\hat{Q}_\nu=0} = \omega_c(0) - g(\hat{b} + \hat{b}^\dagger). \quad (4.38)$$

4.2.2.1 Estimation of the coupling parameter

To estimate the coupling parameter g , we can compare it to the coupling parameter g_{JC} , which governs the interaction in a resonant emitter-plasmon system. Such setup, described by the Jaynes-Cummings Hamiltonian, has been thoroughly analyzed in the literature in different variations (with the emitter described through bosonic [180] or spin [181] operators) and parameter regimes [182, 183]. In its simplest form, g_{JC} is defined as [183]:

$$|g_{JC}| = d\sqrt{\frac{\omega_c}{2\varepsilon_0 V_{\text{eff}}}}, \quad (4.39)$$

where d is the dipolar moment of the emitter. As we have mentioned earlier, in the weak coupling regime, the interaction of the emitter with the single-mode lossy cavity modifies the rate of the spontaneous decay of the emitter by the *Purcell factor* F_P determined as

$$F_P = 1 + 4\frac{|g_{JC}|^2}{\kappa\gamma_0}, \quad (4.40)$$

where γ_0 is the decay rate of the uncoupled emitter. Therefore, by comparing the definitions of the two coupling parameters: g (Eq. (4.34)) and g_{JC} (Eq. (4.39)), we arrive at a simple relationship

$$g = \frac{R_\nu Q_\nu^0}{d^2} 2|g_{JC}|^2. \quad (4.41)$$

Expressing now the right-hand side of the above equations with Eq. (4.40) in the limit of large Purcell factors ($F_P \gg 1$) and plugging in the explicit definition $\gamma_0 = \omega_c^3 d^2 / (3\pi\varepsilon_0 c^3)$ [56], we get

$$g = R_\nu Q_\nu^0 F_P \frac{\kappa}{6\pi\varepsilon_0} \left(\frac{\omega_c}{c}\right)^3. \quad (4.42)$$

We can therefore find an estimate of the absolute values of the coupling coefficient g for illustration, by recalling some of the reported Purcell factors F_P [184, 184–186], and an exemplary value of the Raman tensor R_ν .

The values of the elements of the Raman tensor R_ν and the zero-point amplitude Q_ν^0 vary significantly for different molecules and each vibrational degree of freedom. The estimates of these values have been provided from theoretical and experimental studies for numerous molecules, including rhodamine 6g (R6G) [188] or various peptides [189], as well as cluster structures of e.g., silicon [190]. To provide conservative estimates of the values of g we consider the specific values of Raman activity of rhodamine 6g. The non-resonant Raman spectra of the R6G molecules exhibit vibrational energies in the

Type of cavity	F_P	$\hbar\omega_c$ [eV]	$\hbar\kappa$ [eV]	$\hbar g$ (R6G) [eV]
plasmonic patch antenna [184]	5×10^2	0.45	0.45	3×10^{-11}
plasmonic particle [185] on a dielectric substrate	8×10^3	1.5	0.1	4×10^{-8}
plasmon mode in nanorod [186]	5×10^3	2.2	0.07	10^{-7}
plasmonic dimer [187]	3×10^3	3.5	0.2	6×10^{-7}

TABLE 4.1: Values of the Purcell factors F_P for various types of cavities with resonant energies $\hbar\omega_c$ and widths $\hbar\kappa$. In the last column we provide the estimates of the coupling coefficient g calculated for the coupling with the specific transition of a rhodamine 6G molecule (see text below for details).

range of hundreds of meV and, in the strong-vibrations end of the parameters spectrum, a Raman activity (which, in the one-dimensional model of vibrations used throughout this chapter, is equal to R_ν^2) close to $5 \times 10^2 \varepsilon_0^2 \text{\AA}^4 \text{amu}^{-1}$. Including this parameter into Eq. (4.42), we arrive at the upper estimate of the coupling parameter of around $\hbar g \approx 6 \times 10^{-7}$ eV for a molecule placed in a plasmonic dimer nanoantenna [187].

We should note that, except for the dark plasmon mode in a nanorod, the structures listed above are designed to provide large Purcell factors while retaining high quantum efficiency and avoiding quenching of emission from the resonant two-level systems. This limitation can be removed when designing systems for SERS or TERS, since the Raman scattering does not suffer from quenching, and we can consider other setups, e.g. metallic dimers with subnanometer gaps and significantly reduced mode volumes. A lower limit for such structures was recently obtained by Barbry *et al.* [191] from TDDFT calculations of the dimer of sodium clusters as $V_{\min} \approx 10^{-28} \text{ m}^3$ for the mode energy of $\hbar\omega_c = 3.3$ eV.

To estimate the coupling parameter observed in such systems, we can apply the definition of the coupling given in Eq. (4.34). Taking a more conservative value of the mode volume of $V_{\text{eff}} = 10^{-26} \text{ m}^3$, and considering the Raman activity of rhodamine 6g, obtain $\hbar g \approx 1$ meV, which we will be using throughout the rest of this chapter.

4.2.2.2 Coherent pumping

The Hamiltonian of the system can be formulated as

$$\hat{H}/\hbar = \omega_m \hat{b}^\dagger \hat{b} + \omega_c \hat{a}^\dagger \hat{a} - g \hat{a}^\dagger \hat{a} (\hat{b}^\dagger + \hat{b}) + \hat{H}_{\text{pump}}/\hbar, \quad (4.43)$$

with \hat{H}_{pump} describing the coherent illumination, or *pumping* of the cavity

$$\hat{H}_{\text{pump}} = i\hbar\Omega(\hat{a}^\dagger e^{-i\omega t} - \hat{a}e^{i\omega t}). \quad (4.44)$$

Throughout this chapter Ω^2 will be referred to as a *pumping power* proportional to the power density of the input laser and the intrinsic parameters of the cavity mode. Ω itself is defined as [183]

$$\Omega = \frac{\kappa}{2} \sqrt{\frac{\varepsilon_0 V_{\text{eff}}}{2\hbar\omega_c}} |E_m^s|, \quad (4.45)$$

where $|E_m^s|$ is the maximum of the scattered fields. We can define the *field enhancement* of the plasmonic system as $K = |E_m^s|/|E_0|$, where $|E_0|$ is the amplitude of the incident coherent illumination. Since K is an intrinsic physical property of the cavity and the geometric setup of the illumination, the driving parameter Ω can be re-written as a product of a term depending solely on the cavity properties and the amplitude $|E_0|$

$$\Omega = \frac{\kappa}{2} \sqrt{\frac{\varepsilon_0 V_{\text{eff}}}{2\hbar\omega_c}} K |E_0|. \quad (4.46)$$

To provide some exemplary values of the parameter Ω , we consider an optical plasmonic cavity with plasmon resonance energy $\hbar\omega_c = 2.5$ eV, quality factor $Q = 10$ ($\hbar\kappa = 0.25$ eV), the effective volume given above $V_{\text{eff}} = 10^{-26}$ m³ and enhancement factor $K = 10^2$. Thus, for the strong laser intensity $I = 10^9$ W/cm², which yields $|E_0| \approx 6 \times 10^7$ V/m, we obtain $\hbar\Omega = 0.25$ eV.

For the strongest laser intensities used throughout this chapter, we approach the regime where Ω and ω_c become comparable. Nevertheless, even for those strong pumping coefficients, the pumping Hamiltonian (Eq. (4.44)) is written in the rotating wave approximation. We expect that the inclusion of the counter-rotating terms $i\hbar\Omega(\hat{a}e^{-i\omega t} + \hat{a}^\dagger e^{i\omega t})$ will not change significantly the dynamics of the system, as they will result mainly in energy shifts that can be corrected with appropriate laser detuning.

In the following, the phonon energy is set to $\hbar\omega_m = 0.1$ eV and the phonon decay rate is set to $\hbar\gamma_m = 1$ meV, in agreement with the literature data (see Ref. [192]). The plasmonic cavity with quality factor of $Q = 10$ is chosen to be resonant at $\hbar\omega_c = 2.5$ eV and therefore decaying with rate $\hbar\kappa = \hbar\omega_c/Q = 0.25$ eV. The coupling parameter is taken as $\hbar g = 1$ meV in accordance with the reported characteristics of the resonant plasmon-emitter systems discussed above.

4.2.3 Master equation

Before we write down the master equation for the dynamics of the density matrix of the system to which, from now, we will be referring to as ρ , let us consider the populations of the thermal bath, given by the Bose-Einstein distribution function $N(\omega)$, for the energies corresponding to the cavity photon ω_c and the vibration of the molecule ω_m , at ambient temperature $T = 300$ K:

$$N(\hbar\omega_c = 2.5 \text{ eV}; T = 300 \text{ K}) \approx 10^{-42} \approx 0, \quad \bar{n}_m^{\text{th}} = N(\hbar\omega_m = 0.1 \text{ eV}; T = 300 \text{ K}) \approx 0.02. \quad (4.47)$$

Thus, in the master equation we can neglect the terms that describe the stimulated emission and excitation of the cavity by the environment (analyzed previously in Eq. (4.21)), and write

$$\partial_t \rho = \frac{i}{\hbar} [\rho, \hat{H}] + \frac{\kappa}{2} \mathcal{L}_{\hat{a}}[\rho] + \frac{(\bar{n}_m^{\text{th}} + 1)\gamma_m}{2} \mathcal{L}_{\hat{b}}[\rho] + \frac{\bar{n}_m^{\text{th}}\gamma_m}{2} \mathcal{L}_{\hat{b}^\dagger}[\rho], \quad (4.48)$$

4.2.4 Numerical solution

To analyze the dynamics of the system, we solve directly the master equation in Eq. (4.48) by representing both the state of the cavity, and of the molecule in the basis of Fock states

$$\{|n_{\text{vib}}, m_{\text{cav}}\rangle\}_{n_{\text{vib}}=0,1,\dots,N_{\text{max}}, m_{\text{cav}}=0,1,\dots,M_{\text{max}}} \quad (4.49)$$

which spans a truncated Hilbert space $\bar{\mathcal{H}}$ [193]. Such approach is usually not practical for optomechanical systems comprising high-quality cavities, as the number of states in the Fock basis representing its state would be too large. However, thanks to the weak coupling with vibrations and the low quality factor of the optical cavity, the latter remains very close to a coherent state. We can therefore displace the cavity operators by the complex number which corresponds to the amplitude of this coherent state and truncate the Fock space to a relatively small dimension (see Appendix B for details).

Spectra of emission from the cavity are calculated, following the Glauber's photodetection theory [194], as $I(\omega) = \alpha_{\text{det}} S(\omega)$, where the frequency-independent parameter α_{det} describes the properties of the detection system [164] and

$$S(\omega) = \omega^4 \int_{-\infty}^{\infty} dt e^{-i\omega t} \langle \hat{a}^\dagger(t) \hat{a}(0) \rangle_{\text{ss}}. \quad (4.50)$$

Subscript ss denotes the steady-state of the system. The two-time correlator is calculated by applying the *quantum regression theorem* (QRT, see Appendix B for details) [156]. In

Fig. 4.6(a) and (b) two of such spectra are shown, with removed elastic Rayleigh scattering contributions, calculated for the weak ($(\hbar\Omega)^2 = 10^{-2} \text{ eV}^2$) and strong illuminations ($(\hbar\Omega)^2 = 0.5 \text{ eV}^2$), respectively, and for the laser tuned to the cavity ($\Delta \equiv \omega_c - \omega_l = 0$). In the inset of Fig. 4.6(a) we zoom in on the anti-Stokes emission calculated with the environment at $T = 0 \text{ K}$ (dashed line) and $T = 300 \text{ K}$ (solid line). The difference between these plots illustrates the effect of *thermal pumping* of the vibrational levels by the environment [153, 195]. While a difference in the intensity of the anti-Stokes peak can be appreciated for different temperatures at low pumping (see the inset in Fig. 4.6(a)), it disappears for high pumping power (Fig. 4.6(b)).

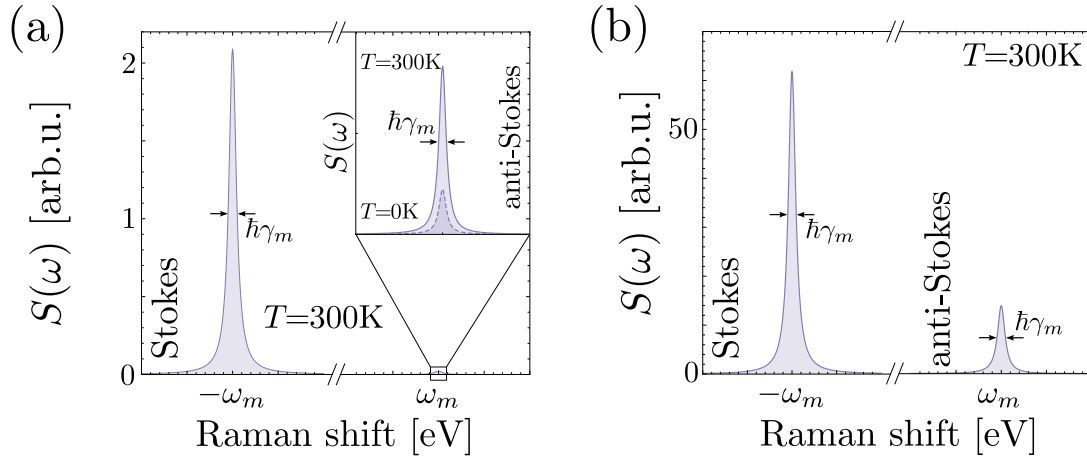


FIGURE 4.6: Spectra of Raman scattering $S(\omega)$ of a molecule in a plasmonic cavity at pumping (a) $(\hbar\Omega)^2 = 10^{-2} \text{ eV}^2$ and (b) $(\hbar\Omega)^2 = 0.5 \text{ eV}^2$ at $T = 0 \text{ K}$ (dashed lines) and $T = 300 \text{ K}$ (solid lines). All the cases assume $\Delta = 0$.

To further explore this effect and to trace the evolution of the signal with the pumping power, we plot in Fig. 4.7(a) the maxima of the Stokes emission (blue solid line) which is independent of temperature T , and of the anti-Stokes emission (orange dashed line for $T = 0 \text{ K}$ and orange solid line for $T = 300 \text{ K}$), for the increasing Ω^2 . In the weak pumping regime ($(\hbar\Omega)^2 \lesssim 10^{-2} \text{ eV}^2$), for non-zero temperature (solid lines), both the Stokes $S(\omega_S)$ and anti-Stokes $S(\omega_{aS})$ emission depend linearly on Ω^2 , indicating that the anti-Stokes transition originates from the thermally excited vibrational state. For higher driving powers ($10^{-2} \text{ eV}^2 \lesssim (\hbar\Omega)^2 \lesssim 0.5 \text{ eV}^2$) the anti-Stokes intensities become independent of the temperature, as the phonons are provided primarily by the Stokes transitions (*vibrational pumping*) [195].

The transition between the thermal and the vibrational pumping of phonons [195] is illustrated in Fig. 4.7(b), where we plot the populations of the phonons (green line) and plasmons (red line) for $T = 0 \text{ K}$ (dashed lines) and $T = 300 \text{ K}$ (solid lines).

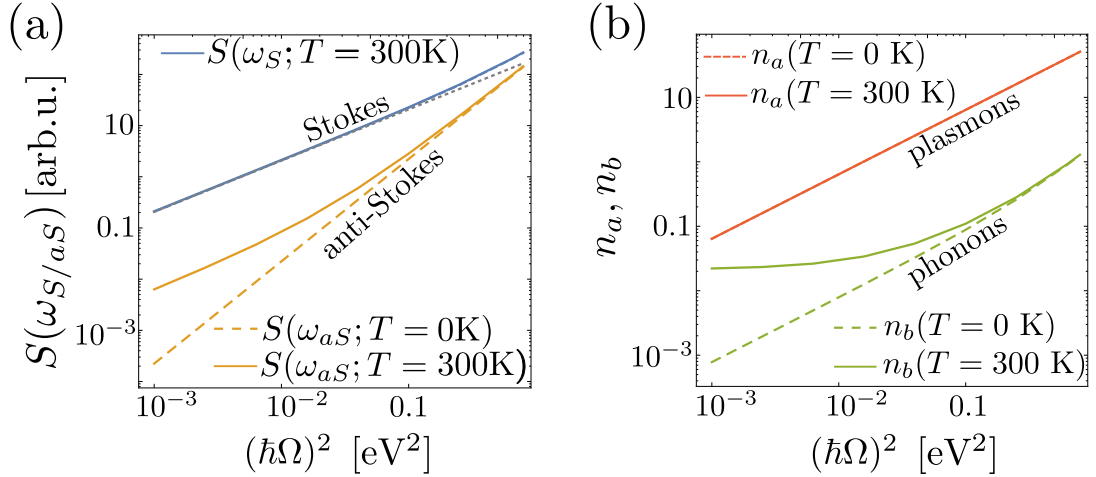


FIGURE 4.7: Dependence of the Raman scattering on the excitation power and temperature. (a) Emission intensities of the Stokes ($S(\omega_S)$, blue lines, calculated at $T = 300\text{ K}$) and anti-Stokes photons ($S(\omega_{aS})$, orange dashed and solid lines for $T = 0\text{ K}$ and $T = 300\text{ K}$, respectively) as a function of the driving intensity Ω^2 ; (b) populations of plasmons (red line) and phonons (green lines) in the steady state for $T = 0\text{ K}$ (dashed lines) or $T = 300\text{ K}$ (solid lines). All the cases assume $\Delta = 0$.

Finally, for the largest considered pumping powers ($(\hbar\Omega)^2 \gtrsim 0.5\text{ eV}^2$) the Stokes intensity $S(\omega_S)$ visibly surpasses the expected linear dependence on Ω^2 (marked with a dotted gray line in the top-right corner of Fig. 4.7(a)). To understand this effect, we have developed an analytical solution to the dynamics of the system, which we briefly present in the following subsection. The detailed derivation can be found in Appendix B.

4.2.5 Linearized Hamiltonian

To design an analytical description of the system, let us take a step back and consider the Hamiltonian of the system given in Eq. (4.43) with the coherent pumping (Eq. 4.44). If we decouple the cavity from the molecule (putting $g = 0$) the plasmonic system will be driven into a steady coherent state with amplitude $\alpha_s = \Omega / (\frac{\kappa}{2} + i\Delta)$, where $\Delta = \omega_c - \omega_l$ is the detuning between the frequency of the pumping laser and the resonant frequency of the cavity. We can therefore redefine the cavity operators, excluding the coherent amplitude:

$$\hat{a} \rightarrow \hat{a} + \alpha_s, \quad (4.51)$$

and write

$$\hat{H}/\hbar = \Delta \hat{a}^\dagger \hat{a} + \omega_m \hat{b}^\dagger \hat{b} - g|\alpha_s|^2 (\hat{b} + \hat{b}^\dagger) - g(\alpha_s \hat{a}^\dagger + \alpha_s^* \hat{a}) (\hat{b} + \hat{b}^\dagger) - g \hat{a}^\dagger \hat{a} (\hat{b} + \hat{b}^\dagger). \quad (4.52)$$

The last, nonlinear term in the above Hamiltonian is proportional to the incoherent population of the cavity, and will be small provided that the interaction with the molecule g is weak. Thus, in the regime usually discussed in optomechanics, characterized by the weak coupling g , the last non-linear term can be neglected, allowing us to write down the *linearized* Hamiltonian

$$\hat{H}'/\hbar = \Delta\hat{a}^\dagger\hat{a} + \omega_m\hat{b}^\dagger\hat{b} - g|\alpha_s|^2(\hat{b} + \hat{b}^\dagger) - g(\alpha_s\hat{a}^\dagger + \alpha_s^*\hat{a})(\hat{b} + \hat{b}^\dagger), \quad (4.53)$$

which yields a purely quadratic dynamics and linear quantum Langevin equations for operators \hat{a} and \hat{b} [180, 181].

It should be noted that, when solving the linearized Hamiltonian, we do not map the quantum Langevin equation to the classical dynamics equations, as is often done in the analysis of the optomechanical systems [196]. Consequently, our approach provides a complete characterization of the classical and quantum correlations within the system, and allows us to reproduce the proper dependence of Stokes and anti-Stokes signal on the pumping strength Ω .

As we discuss in detail in Appendix B, the linearized Hamiltonian can be solved exactly for the specific case of the laser tuned to the cavity resonance, $\Delta = 0$, by applying the *quantum regression theorem* (QRT), yielding a simple expression for the intensity of the Stokes emission:

$$S(\omega_S) = \frac{2\omega_S^4}{\gamma_m} s_2 \Omega^2 \left(1 + \bar{n}_m^{\text{th}} + s_2 \Omega^2 \frac{\kappa}{\gamma_m} \right), \quad (4.54)$$

where

$$s_2 \approx [4g/(\kappa|\kappa - 2i\omega_m|)]^2. \quad (4.55)$$

Let us analyze terms in the brackets of Eq. (4.54):

- The first term can be recognized as the conventional two-photon cavity-assisted Stokes transition, linearly dependent on Ω^2 , as demonstrated in the Appendix B. This term yields the expected $S(\omega_S) \propto K^4$ dependence on the enhancement of the incident field by the cavity K [49].
- The sum of the second and the third terms in brackets represents the incoherent population of the phonon mode

$$n_m^{\text{incoh}} = \langle \hat{b}^\dagger \hat{b} \rangle_{\text{ss}} - \langle \hat{b}^\dagger \rangle_{\text{ss}} \langle \hat{b} \rangle_{\text{ss}}, \quad (4.56)$$

arising from (i) the thermal pumping and (ii) the coupling to the plasmon cavity. Brackets $\langle \dots \rangle_{\text{ss}}$ denote the steady-state expectation values. These two terms together describe a process of *phonon-stimulated Raman scattering*, in which the population of vibrations enhances the rate of Stokes scattering. We can easily check that Eq. (4.56) represents the incoherent population of phonons by noting that the addition of a coherent contribution to \hat{b} ($\hat{b} \rightarrow \beta + \hat{b}$) does not change the covariance on the right-hand side of Eq. (4.56).

We note that phonon-stimulated Raman scattering has been reported in experiments on ensembles of Raman-active centers, for example in hydrogen gas (see Refs. [197, 198] and references therein).

Similarly, we can derive the expression for the anti-Stokes emission

$$S(\omega_{aS}) = \frac{2\omega_{aS}^4}{\gamma_m} (s_2 \bar{n}_m^{\text{th}} \Omega^2 + s_4 \Omega^4), \quad (4.57)$$

which describes the thermal pumping regime (first term in the brackets, proportional to the thermal population of phonons \bar{n}_m^{th}) and the vibrational pumping regime (proportional to Ω^4).

The intensity of Stokes and the anti-Stokes emission, given by these equations, is shown in Fig. 4.8 with solid blue and orange lines, respectively.

4.2.6 Breakdown of the linearization

As a side note, we remark that in the regime where the coupling parameter g and cavity width κ are similar [199, 200], this linearization scheme breaks down. To estimate the error induced by dropping the non-linear interaction term for our set of parameters, in Fig. 4.8 we have compared the intensities of the Raman peaks calculated numerically using Hamiltonians listed in Eqs. (4.52) (empty squares) and (4.53) (full circles), for different values of the coupling strength g : (a), $g = g_0 = \kappa/250$, (b) $g = 10g_0$ and (c) $g = 30g_0$. These results indicate that in the regime of realistic parameters discussed in this chapter ($g = g_0$, Fig. 4.8(a)) both Hamiltonians give identical strengths of the Stokes and anti-Stokes scattering. However, with increasing coupling parameter (by a factor of 10 in Fig. 4.8(b) or 30 in Fig. 4.8(c)), the linearized Hamiltonian begins to over-estimate the inelastic scattering.

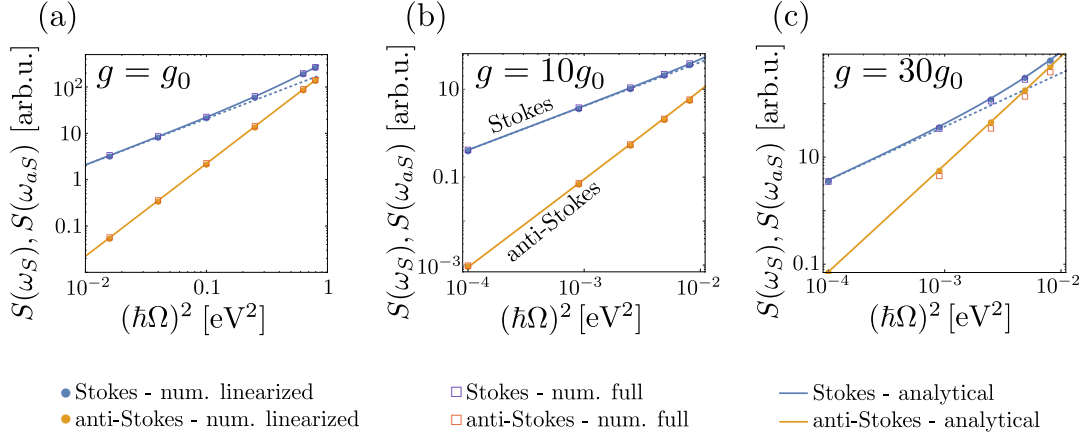


FIGURE 4.8: Dependence of the Raman scattering on the excitation power and coupling parameter g , calculated numerically using full (empty squares, Eq. (4.52)) or linearized (full circles, Eq. (4.53)) Hamiltonian or analytically (solid lines) from the quantum regression theorem (QRT) using Eqs. (4.54) and (4.57) for Stokes (solid blue lines) and anti-Stokes (solid orange lines), respectively. Coupling coefficients are given as multiples of the coefficient used throughout the manuscript $g_0 = \kappa/250$: (a) $g = g_0$, (b) $g = 10g_0$ and (c) $g = 30g_0$. Dashed lines denote the linear dependence of the Stokes signal on Ω^2 expected from the classical theories, as obtained by taking the first term of Eq. (4.54) exclusively.

4.2.7 Dependence on the laser detuning Δ

To further explore the effects of thermal and vibrational pumping of phonons on the Raman scattering, let us consider the dependence of Raman scattering on the detuning $\Delta \equiv \omega_c - \omega_l$ of the incident laser ω_l from the cavity resonance ω_c . In the typical classical models of SERS [49] the dependence of the Stokes ($S^{\text{class}}(\omega_S; \Delta)$) and the anti-Stokes ($S^{\text{class}}(\omega_{aS}; \Delta)$) emission is determined by the enhancement of the electric field of both the incoming ($|E(\omega_l)/E_0(\omega_l)|^2$, where ω_l is the frequency of the incident illumination) and outgoing ($|E(\omega_{S/aS})/E_0(\omega_{S/aS})|^2$) photons at the position of the molecule:

$$S^{\text{class}}(\omega_{S/aS}; \Delta) \propto \omega_{S/aS}^4 \left| \frac{E(\omega_l)}{E_0(\omega_l)} \frac{E(\omega_{S/aS})}{E_0(\omega_{S/aS})} \right|^2. \quad (4.58)$$

Assuming that the enhancement is given by a lorentzian profile centered on the cavity resonance ω_c with width κ (gray curves in the bottom panels of Fig. 4.9), one can expect that the calculated Raman emission spectra $S(\omega_{S/aS}; \Delta)$ will depend on the laser frequency ω_l , as depicted with the blue dashed curves in the bottom panels of Fig. 4.9. In particular, the Stokes signal should be the strongest for the incident laser blue-detuned from the cavity. This general result for the Stokes scattering is supported by

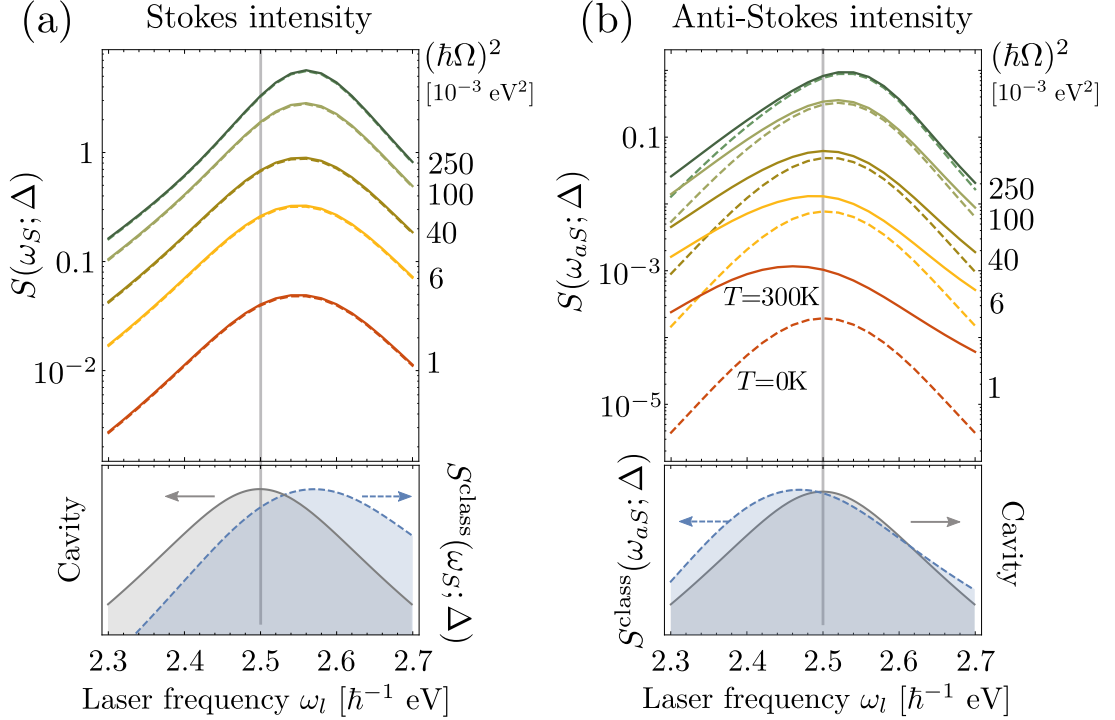


FIGURE 4.9: Dependence of the (a) Stokes and (b) anti-Stokes emission on the frequency of the incident laser ω_l . In the top panels we show the numerically calculated intensities (a) $S(\omega_S; \Delta = \omega_c - \omega_l)$ and (b) $S(\omega_{aS}; \Delta)$ for the pumping power from $(\hbar\Omega)^2 = 10^{-3}$ eV (red lines) to $(\hbar\Omega)^2 = 0.25$ eV (green lines) and environment temperature $T = 0$ K (dashed lines) and $T = 300$ K (solid lines). The bottom panels show the predictions of classical models (Eq. (4.58)) for (a) $S^{\text{class}}(\omega_S; \Delta)$ and (b) $S^{\text{class}}(\omega_{aS}; \Delta)$ (dashed blue lines) and the cavity amplitude in gray.

our calculations performed for various pumping power ($(\hbar\Omega)^2 = 10^{-3}$ eV 2 to 0.25 eV 2 , depicted in the top spectra from red to green lines) and different temperatures ($T = 0$ K and 300 K in dashed and solid lines), as shown in the upper panels of Fig. 4.9(a). We also note that, as a result of the nonlinearity in Stokes emission, the profile of $S(\omega_S; \Delta)$ narrows with increasing pumping. On the other hand, Eq. (4.58) fails to explain the dependence of the anti-Stokes scattering (Fig. 4.9(b)). For the weakest driving powers (red lines, $(\hbar\Omega)^2 = 10^{-3}$ eV 2), the $S(\omega_{aS}; \Delta)$ intensity is the largest for the laser on resonance or red-detuned from the cavity resonance both in the absence or presence of thermal pumping of phonons (at $T = 0$ K and $T = 300$ K, respectively). For stronger driving powers the intensity plots for $T = 0$ K and 300 K start to merge and peak at increasingly blue-shifted frequencies, notably crossing the cavity resonance ω_c .

This surprising property stems from the transition between the thermal and vibrational pumping of the vibrational levels. Classical Eq. (4.58) for the anti-Stokes $S^{\text{class}}(\omega_{aS}; \Delta)$

intensity does not account for the origin of the phonons in the molecule, and therefore can only be applied when these are provided by the heated reservoir (it should be noted, however, that a suitable correction to $S(\omega_{aS}; \Delta)$ introducing the vibrational pumping has been proposed by Kneipp *et al.* [153]). If the environment is cooled down, or the coherent driving dominates over the thermal phonons, the populations of the vibrations can only originate from the Stokes transition, forcing the blue-detuning of the intensity dependence, as observed in Fig. 4.9(b).

4.2.8 Correlations of the emitted light

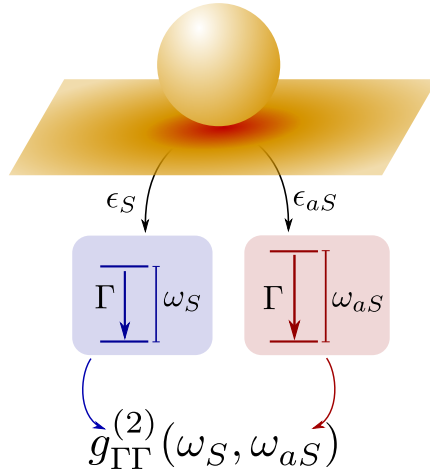


FIGURE 4.10: Two-photon frequency-resolved correlators $g_{\Gamma\Gamma}^{(2)}(\omega_S, \omega_{aS})$ are calculated by adding two lossy (Γ) weakly coupled ($\epsilon_S, \epsilon_{aS} \ll \sqrt{\gamma_m \Gamma/2}$) two-level *sensors* and calculating their intensity correlations [201].

We can further characterize the photon emission by calculating the time- and frequency-resolved photon correlations [202–204] between the Stokes and the anti-Stokes photons emitted from the cavity. This technique was proven successful in showing quantum correlations that are otherwise hidden in normal spectroscopy or standard photon correlations [205]. The correlations can be accessed experimentally either by inserting filters in a standard Hanbury-Brown-Twiss setup [204] or through a streak camera set-up [203] that allows for ps detection resolution required for the plasmonic setup.

Theoretically, these time and frequency-resolved photon correlations are computed through intensity-intensity correlations:

$$g_{\Gamma_1\Gamma_2}^{(2)}(\omega_1, \omega_2; \tau) = \lim_{t \rightarrow \infty} \frac{\langle \hat{A}_{\omega_1, \Gamma_1}^\dagger(t) \hat{A}_{\omega_2, \Gamma_2}^\dagger(t + \tau) \hat{A}_{\omega_2, \Gamma_2}(t + \tau) \hat{A}_{\omega_1, \Gamma_1}(t) \rangle}{\langle \langle \hat{A}_{\omega_1, \Gamma_1}^\dagger \hat{A}_{\omega_1, \Gamma_1} \rangle(t) \rangle \langle \langle \hat{A}_{\omega_2, \Gamma_2}^\dagger \hat{A}_{\omega_2, \Gamma_2} \rangle(t + \tau) \rangle}, \quad (4.59)$$

where

$$\hat{A}_{\omega_i, \Gamma_i}(t) = \int_{-\infty}^t dt_1 e^{(i\omega_i - \Gamma_i/2)(t-t_1)} \hat{a}(t_1) \quad (4.60)$$

is the output field after passing through a Lorentzian frequency filter with central frequency ω_i , and width Γ_i , at time t . In principle, in order to compute these correlations one must apply the quantum regression theorem three times and perform the integrals afterwards. Instead, we use the method recently proposed in Ref. [201], which avoids this complication by coupling the mode of interest, i.e., \hat{a} in our case, to two-level systems that will play the role of *sensors* (see the schematic of the concept in Fig. 4.10), with frequencies ω_i and lifetimes Γ_i , through the following Hamiltonian:

$$\hat{H}_{\text{sens}} = \sum_{i=1,2} \epsilon_i (\hat{a}^\dagger \hat{\sigma}_-^{(i)} + \hat{a} \hat{\sigma}_+^{(i)}), \quad (4.61)$$

where $\hat{\sigma}_+^{(i)}$ and $\hat{\sigma}_-^{(i)}$ are spin raising and lowering operators of the i th sensor. The coupling ϵ_i must be sufficiently weak so that the dynamics of the sensors does not perturb the system., i.e., $4\epsilon_i^2/\Gamma_i \ll \gamma_s$, where γ_s is the smallest transition rate of interest (here $\gamma_s = \gamma_m$). Notice that this condition can always be imposed as ϵ_i is a free non-zero parameter that we can choose at will in our simulation. Under this assumption it can be shown that:

$$g_{\Gamma_1 \Gamma_2}^{(2)}(\omega_1, \omega_2; \tau) = \lim_{\epsilon_i \rightarrow 0} \frac{\langle \hat{n}_1(0) \hat{n}_2(\tau) \rangle_{\text{ss}}}{\langle \hat{n}_1 \rangle_{\text{ss}} \langle \hat{n}_2 \rangle_{\text{ss}}}, \quad (4.62)$$

with $\hat{n}_i = \hat{\sigma}_+^{(i)} \hat{\sigma}_-^{(i)}$. This simplifies the calculation at the cost of a small increase in the dimension of the Hilbert space. For example, in the case of coincidences, i.e., $\tau = 0$, that we are mainly interested in, we only need to compute one-time correlators, avoiding the need of the quantum regression theorem.

For simplicity we consider $\Gamma_1 = \Gamma_2 = \Gamma$ and place the Lorentzian filters at $\omega_1 = \omega_S$ and $\omega_2 = \omega_{aS}$. The photon correlations $g_{\Gamma\Gamma}^{(2)}(\omega_S, \omega_{aS}; \tau = 0)$, are plotted in Fig. 4.11(a) as a function of the driving parameter Ω^2 for $T = 0$ K (dashed lines) and $T = 300$ K (solid lines) environment temperature. The coupling parameters g are taken as multiples of $g_0 = \kappa/250$: $g = g_0$ (blue lines), $g = 2g_0$ (orange lines), $g = 4g_0$ (green lines), and the filter linewidth $\hbar\Gamma = 0.1$ meV. As shown in Fig. 4.11(b), for these parameters the spectrum $S_\Gamma^{(1)}(\omega) = \langle \hat{A}_{\omega, \Gamma}^\dagger(0) \hat{A}_{\omega, \Gamma}(0) \rangle$ is formed by three peaks: the elastic Rayleigh scattering and the inelastic Stokes and anti-Stokes contributions.

We clearly observe that for the weak coherent pumping and in absence of thermal pumping, the system exhibits strong bunching statistics, which is a signature of strongly correlated emission [206, 207]. The physical origin of the strong correlation is that, in the

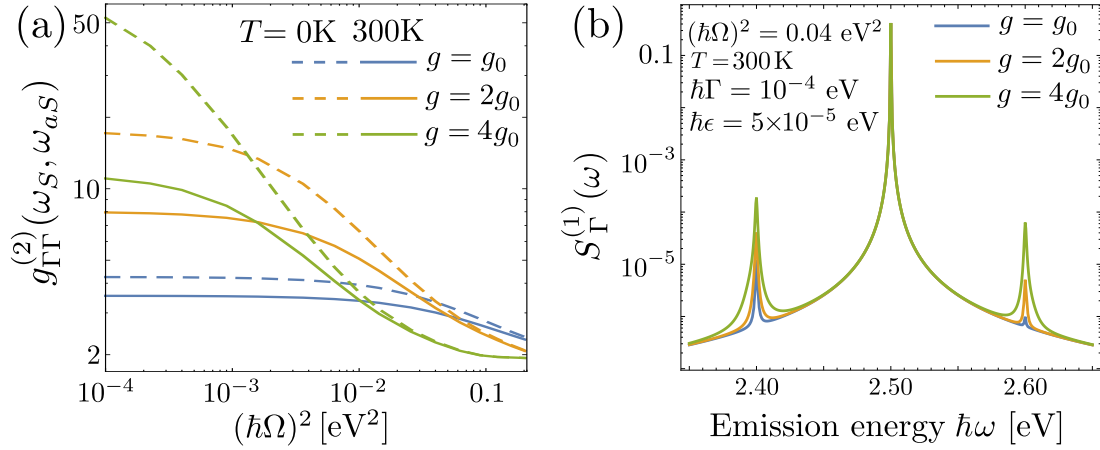


FIGURE 4.11: (a) Two-photon frequency-resolved Stokes-anti-Stokes correlators $g_{\Gamma\Gamma}^{(2)}(\omega_S, \omega_{aS})$ and (b) physical spectra of emission $S_{\Gamma}^{(1)}(\omega) = \langle \hat{A}_{\omega, \Gamma}^{\dagger}(0) \hat{A}_{\omega, \Gamma}(0) \rangle$ calculated for the temperatures $T = 0$ K (dashed lines) and $T = 300$ K (solid lines), coupling parameters chosen as multiples of $g_0 = \kappa/250$: $g = g_0$ (blue lines), $g = 2g_0$ (orange lines), $g = 4g_0$ (green lines), and laser tuned to the cavity $\Delta = 0$.

absence of other source of excitations, the Raman photons are emitted by exchanging a single phonon and therefore they are strongly correlated. Interestingly, the regions of strongly bunched frequency correlations have been linked to the violation of classical inequalities [208] and can be optimized through proper filter engineering [209], potentially providing access to producing a quantum correlated emission in this setup. The dependence of the correlations on the coupling parameter stems from the fact that for small g (and weak anti-Stokes emission), the filters detect primarily the elastically scattered photons (Fig. 4.10(b)). For larger coherent driving or increased thermal pumping, the anti-Stokes photons are increasingly created through the absorption of phonons which originate either from thermal excitation or are created by an uncorrelated, earlier Stokes transition. Thus, the correlation between the anti-Stokes and the simultaneously detected Stokes photon decreases. We note these results are consistent with those recently reported by Kasperczyk *et al.* [210] from measurements of the Stokes and anti-Stokes pairs emitted from a thin layer of diamond.

4.3 Optomechanical cavities

As we have mentioned earlier, the Hamiltonian describing the interaction between the cavity plasmons and the vibrations is reminiscent of that used to describe the dynamics of optomechanical system. In this section, we briefly comment on this resemblance and compare our system to common optomechanical setups.

In a typical optical cavity, formed by two highly reflective mirrors, the circulating photons exert a radiation pressure on the mirrors. In optomechanical cavities, this force is harnessed, by allowing one of the mirrors to move. The mechanical motion then shifts the resonance frequency of the cavity, modifying the intensity of the circulating light and, therefore, the radiation pressure force. This *backaction* [93, 196, 211] can be understood as a coherent feedback mechanism that provides paths to cool or amplify the vibrations of the mirror. For example, when the cavity is illuminated by a laser red-detuned from its resonance, the backaction cools the mechanical vibrations by transferring their energy to the optical cavity (significantly below the thermal population). Conversely, under a blue-detuned illumination, the amplification or heating of the mirror vibrations is achieved. A few realizations of optomechanical cavities, exhibiting a range of mechanical frequencies and qualities of the optical cavities, are schematically shown in panels (a)-(c) of Fig. 4.12.

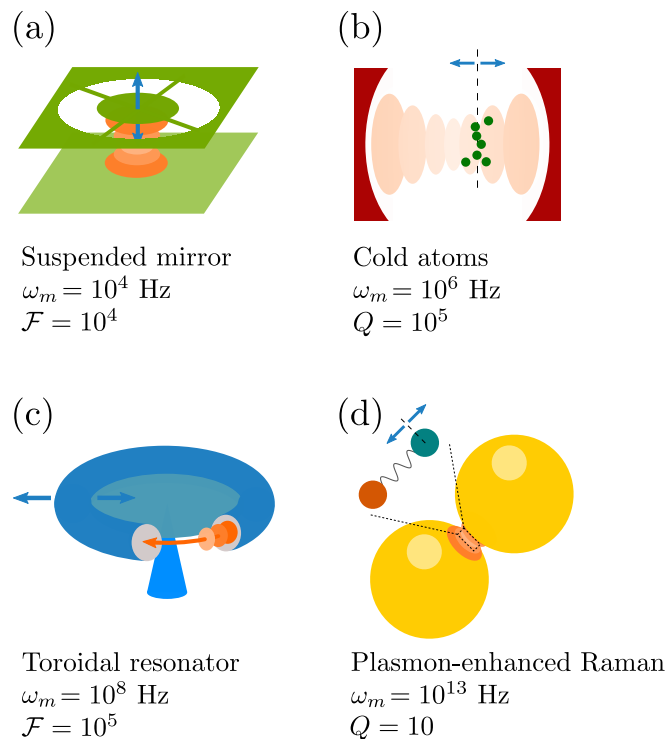


FIGURE 4.12: Schematics of typical optomechanical systems: (a) suspended trampoline mirror [212], (b) cold atoms [213] and toroidal resonator [211]. Optical and mechanical modes are marked, together with the relevant parameters for each case: the mechanical frequency (ω_m) and the quality factors (Q) or finesse (\mathcal{F}) of the optical cavities. (d) The plasmon-enhanced Raman system exhibits much larger mechanical frequencies and significantly lower quality factors of the optical plasmonic cavities.

We can therefore consider plasmon-enhanced Raman scattering as a realization of an

optomechanical system (Fig. 4.12) in a novel regime of very high mechanical frequencies, large single-photon coupling parameters ($g \sim \gamma_m$) and low- Q optical cavities. This last characteristic is usually unwelcome, since it implies very low population of the optical cavity n_a and, consequently, weakens the effective coupling coefficient

$$g_{\text{eff}} = \sqrt{n_a}g \quad (4.63)$$

(see Appendix B for details on the linearization scheme). Nevertheless, the large single-photon coupling in SERS systems can, even in the case of very small n_a , trigger the onset of interesting, non-linear effects.

Finally, the extraordinarily high mechanical frequency, significantly larger than the frequency of the thermal bath, removes any need for cooling of the vibrations, and opens avenues to implementing room-temperature quantum cavity optomechanics.

As mentioned before, this correspondence between Raman scattering and optomechanical systems was also identified and analyzed in an independent contribution from Christophe Galland and Tobias Kippenberg and colleagues at the École Polytechnique Fédérale de Lausanne [179]. Their classical model suggests that the vibrations of a molecule can be amplified by illuminating a plasmonic cavity with a blue-detuned laser, just like the heating of mirror vibrations in an optomechanical cavity can be induced by a similarly detuned laser. Under these conditions, a significant increase of the Raman signal intensity is expected. This effect appears to be reminiscent of that discussed in detail above, where the process of Stokes emission is stimulated by the incoherent population of phonons. There are however some critical differences between the results offered by the two frameworks. Most significantly, when the laser is tuned to the resonant frequency of the cavity, our formalism predicts the onset of the stimulated emission, while in the classical model, neither cooling nor amplification of vibrations occurs.

Given that in their contribution Kippenberg and his colleagues apply the usual mathematical framework to describe the dynamics of optomechanical systems (they linearize the interaction Hamiltonian and solve classical Langevin equation), the differences highlighted above need to be properly identified and understood.

4.4 Summary

In this chapter we have presented a fundamental, quantum-mechanical model of the non-linear interaction between the quantized excitations of a plasmonic cavity, and the vibrational structure of a molecule. This approach readily describes effects which are not encompassed by the classical framework: (i) the onset of stimulated Raman scattering due to the interaction with the cavity plasmons, (ii) an unexpected dependence of the anti-Stokes scattering on the frequency of the incident laser and the local temperature.

From the experimental perspective, our prediction of the stimulated Raman scattering from single molecules in plasmonic cavities should be of vital importance, as it opens a new pathway to enhancing the intrinsically weak Stokes and anti-Stokes emission. While this effect, to our best knowledge, has not been demonstrated, our results indicate that the parameters of the experimental setups, i.e., the qualities of the plasmonic cavities, could reach the regime where such observations are possible. The second major prediction (point (ii)) can serve as a guideline for optimizing the experimental setups to enhance the anti-Stokes scattering, and can contribute to the debate over the use of the Stokes/anti-Stokes intensity ratio as a local temperature probe.

On the theoretical side, our exact formalism opens avenues to studying classical and quantum correlations of the photons emitted from the cavities.

Finally, thanks to the resemblance of our interaction Hamiltonian to that used for treating optomechanical systems, the framework presented here takes the studies of such systems to a novel parameter regime characterized by relatively strong couplings, previously observed only for cold atoms, and low thermal populations.

Final remarks and outlook

In this thesis we have presented a few phenomena related to nanoscale optics, representative of the rapidly developing front of research in this field. While some of the effects discussed here, such as the shifts between different far-field optical properties of plasmonic resonances, or the magnetic response of dielectric nanoparticles, have been already verified in experiments, others are still calling for empirical verification.

One might wonder whether, should such confirmations arrive, these effects will actually lead to further work, or will be otherwise placed in a, already cluttered, repository of intriguing, but otherwise useless inventions. To try to answer this question, let us briefly look into possible directions or research that the four pillars of this thesis might contribute to.

Firstly, let us consider the results assembled in Chapter 1 and the future of research into the dynamics of plasmons using femtosecond laser pulses. On the one hand, to study the dynamics of processes occurring at the fs scale, one would ideally wish for probes that would provide a higher time resolution. However, the very fundamental wave nature of light would render such pulses as spectrally broad probes. Nevertheless, working at this limit of the trade-off between spectral- and time-resolutions, we should be able to identify the non-exponential dynamics of plasmons induced in metals and coupled to interband transitions. Furthermore, one could extend this study and consider more complex plasmonic or hybrid structures that exhibit Fano-like spectral resonances due to the coupling between bright and dark modes. Therefore, the future of this direction of research is bright, and will hopefully be aided by this contribution.

In the case of dielectric nanoparticles, which we describe in Chapter 2, the research path for the next few years appears to have been laid out by previous efforts to guide plasmonic nanosystems towards applications. Despite serious experimental challenges, high-refractive index nanoantennas of various shapes: single spheres [10, 35, 36], dimers

[7, 214, 215], trimers or oligomers [107, 109], nanorods [216, 217] or even metasurfaces [218] have been theoretically and, in some cases, also experimentally characterized, and reportedly form a rather significant competition for their plasmonic counterparts. The natural next step would be to couple those systems with quantum emitters, such as molecules, quantum dots or perhaps even ions with a complex level structure, and optimize them to match, or even outperform their conceptual ancestors, the microresonators.

The future of research into helicity conservation in scattering on random medium (Chapter 3) most likely lies in the hands of optical physicists who have been working over the last few years to boost the information capacity of optical fibers by implementing protocols based on the *angular momentum* of light. While their efforts are primarily focused on the *orbital angular momentum*, the helicity of light was also pointed out as an important and promising candidate for implementing such protocols. Therefore, research into scattering processes that could conserve this property might be crucial for the development of novel optical fibers or adapters for interaction with other devices with little loss of information.

From a more fundamental perspective, one should point out that the understanding of symmetries of Maxwell's equations, formulated over 150 years ago, and their realizations in macroscopic and microscopic inhomogeneous media seems to be a long-overdue effort.

The final chapter of this thesis is devoted to developing a quantum-mechanical description of the coupling between plasmonic cavities and molecular vibrations. As such, it is built on a concept which has been introduced in the field of plasmonics very recently (i.e. quantization of the cavity modes), and serves as an example of phenomena that can be described if one goes beyond the traditional, classical image of nanoantennas as a concentrator of energy. On the other hand, we are slowly entering into a regime of parameters of plasmonic systems which should offer the possibility to glimpse into the internal structure of molecules and ions. Soon, we will hopefully learn how to access and control their dynamics or, at the very least, exploit the intrinsically quantum nature of molecules and ions to design novel hybrid devices based on, otherwise classical, plasmonic building blocks.

In summary, we expect that the results reported in this thesis will influence a broad field of immediate research in various areas of nanophotonics and, perhaps, contribute to the development of new devices and uncovering exciting novel phenomena.

Appendix A

Mie theory

A.1 Vector spherical harmonics

In this appendix we briefly introduce the elementary theory used in the description of the scattering of light on spherical particles, the so-called *Mie theory*, named after German physicist Gustav Mie [70]. We will not make an effort to introduce to the reader the details of this framework, as those are discussed at length in many publications, but rather strip it down to the core and most interesting, in our subjective view, elements.

To begin, let us consider the simplest non-trivial three-dimensional system which comprises a linearly polarized planewave illuminating a spherical nanoparticle. Without the loss of generality, we can assume that, as illustrated in Fig. 2.1, the incident illumination wavevector \mathbf{k}_0 is parallel to the axis \hat{z} and its electric field \mathbf{E}_0 is polarized along axis \hat{x} . The scatterer, a homogeneous sphere of radius a and dispersive dielectric permittivity ε_2 , is centered at the origin of the coordinate system. The homogeneous environment in which the sphere is embedded, is characterized by a dispersive, lossless dielectric permittivity ε_1 . Thus, the wavevector \mathbf{k}_0 and the wavelength λ of the incident monochromatic planewave with frequency ω are related as

$$\mathbf{k}_0 = -\hat{z}k = -\hat{z}\frac{2\pi}{\lambda} = -\hat{z}\frac{\omega}{c}\sqrt{\varepsilon_1(\omega)}, \quad (\text{A.1})$$

where c is the velocity of light in vacuum.

In Mie theory, the incident and scattered fields, as well as the field inside the spherical scatterer, are defined in the complete and orthonormal basis of the so-called *spherical*

harmonics. We define this basis by considering the intrinsic spherical symmetry of the scatterer (note that this symmetry does not extend to the incident illumination) and following the ingenuitive prescriptions:

1. First, consider two vector fields \mathbf{M} , \mathbf{N} with vanishing divergence, defined through a scalar function Ψ as

$$\mathbf{M} = \nabla \times (\mathbf{r}\Psi), \quad \mathbf{N} = \frac{\nabla \times \mathbf{M}}{k}. \quad (\text{A.2})$$

Let Ψ be a solution of the scalar wave equation:

$$\nabla^2 \Psi + k^2 \Psi = 0. \quad (\text{A.3})$$

It can be then shown that both the \mathbf{M} and \mathbf{N} vector fields satisfy the vector wave equations

$$\nabla^2 \begin{pmatrix} \mathbf{M} \\ \mathbf{N} \end{pmatrix} + k^2 \begin{pmatrix} \mathbf{M} \\ \mathbf{N} \end{pmatrix} = 0, \quad (\text{A.4})$$

and

$$\mathbf{M} = \frac{1}{k} \nabla \times \mathbf{N}. \quad (\text{A.5})$$

Thus, if in the above equations we put $k = \omega\sqrt{\varepsilon_1}/c$, then \mathbf{M} and \mathbf{N} defined in Eq. (A.2) are the general solutions for the electric \mathbf{E} and magnetic fields \mathbf{H} . in the homogeneous medium of permittivity ε_1 .

2. To choose a specific form of a set of functions Ψ which will define the simplest set of vector spherical harmonics, we denote the spherical symmetry of the scatterer and consider Ψ as:

$$\Psi(r, \theta, \phi) = R(r)\Theta(\theta)\Phi(\phi), \quad (\text{A.6})$$

where (r, θ, ϕ) are the spherical coordinates with θ and ϕ denoting the polar and azimuthal angles, respectively. With this separation of variables, the scalar wave equation in spherical coordinates breaks into three independent equations for $R(r)$, $\Theta(\theta)$ and $\Phi(\phi)$. Solving them separately, we find two families of solutions, Ψ_{emn} and Ψ_{omn} , defined as

$$\begin{pmatrix} \Psi_{emn} \\ \Psi_{omn} \end{pmatrix} = \begin{pmatrix} \cos m\phi \\ \sin m\phi \end{pmatrix} P_n^m(\cos \theta) z_n(kr), \quad (\text{A.7})$$

where the radial function $z_n(kr)$ is any of the four spherical Bell's functions: j_n , y_n , $h_n^{(1)}$, $h_n^{(2)}$ and P_n^m are the associated Legendre polynomials. The respective

vector functions \mathbf{M}_{emn} and \mathbf{N}_{emn} (\mathbf{M}_{omn} and \mathbf{N}_{omn}) are defined by introducing the above formulations of Ψ_{emn} (Ψ_{omn}) into Eq. (A.2). An explicit representation of these harmonics in spherical coordinates can be found in Ref. [117].

This very general and mathematical definition of the *Mie modes*, \mathbf{M}_{emn} , \mathbf{M}_{omn} , \mathbf{N}_{emn} and \mathbf{N}_{omn} might appear arduous at first glance. Therefore, to familiarize the reader with its more appealing, physical interpretation, in Fig. 2.1(b) and (c) we have plotted the vector fields and intensity distributions of the two lowest-order electric (a_1 and a_2) and magnetic (b_1 and b_2) Mie modes. The dipolar modes (b) have the simplest form, as they are characterized by the electric and magnetic fields constant for a_1 and b_1 , respectively, throughout the volume of the nanoparticle, and the complementary fields circulating around these directions.

3. Expand the incident field illuminating the scatterer (\mathbf{E}_0 , \mathbf{H}_0), the field inside the particle (\mathbf{E}_i , \mathbf{H}_i) and the scattered field (\mathbf{E}_s , \mathbf{H}_s) in the basis of the Mie modes defined above:

$$\mathbf{E}_0 = \sum_n \sum_{m=n}^{\infty} \sum_{j=o,e}^{\infty} (B_0^{jmn} \mathbf{M}_{jmn} + A_0^{jmn} \mathbf{N}_{jmn}), \quad (\text{A.8a})$$

$$\mathbf{E}_s = \sum_n \sum_{m=n}^{\infty} \sum_{j=o,e}^{\infty} (B_s^{jmn} \mathbf{M}_{jmn} + A_s^{jmn} \mathbf{N}_{jmn}), \quad (\text{A.8b})$$

$$\mathbf{E}_i = \sum_n \sum_{m=n}^{\infty} \sum_{j=o,e}^{\infty} (B_i^{jmn} \mathbf{M}_{jmn} + A_i^{jmn} \mathbf{N}_{jmn}), \quad (\text{A.8c})$$

The respective magnetic fields are defined by Eqs. (A.2) and (A.5).

4. Apply the boundary conditions to find the relationship between the fields on the boundary of the scatterer

$$(\mathbf{E}_0 + \mathbf{E}_s - \mathbf{E}_i) \times \hat{\mathbf{e}}_r = (\mathbf{H}_0 + \mathbf{H}_s - \mathbf{H}_i) \times \hat{\mathbf{e}}_r = 0, \quad (\text{A.9})$$

where $\hat{\mathbf{e}}_r$ is the radial vector on the surface of the sphere defined as $|\mathbf{r}| = a$.

Thanks to the completeness of the vector spherical harmonics defined above, any electromagnetic field which satisfies the vector wave equations can be expanded in this basis. In the following section, we discuss two specific cases which are of interest to the work presented in this thesis: the illumination of the sphere by a planewave and by a radiating dipolar emitter.

A.2 Scattering of a planewave

The expansion of the fields of a planewave incident on the particle as in the schematics in Fig. 2.1(a) into a series of vector spherical harmonics is, as Bohren and Huffman phrased it "somewhat like trying to force a square peg into a round hole" [117]. Literary value aside, this picture reflects very well the dissimilar symmetries of the field and the selected basis.

Nevertheless, since the basis is complete, it allows us to expand the incident electric and magnetic fields into a slowly converging series [117],

$$\mathbf{E}_0 = E_0 \sum_{n=1}^{\infty} i^n \frac{2n+1}{n(n+1)} (\mathbf{M}_{o1n}^{(1)} - i\mathbf{N}_{e1n}^{(1)}), \quad (\text{A.10a})$$

$$\mathbf{H}_0 = -\frac{k}{\omega\mu} E_0 \sum_{n=1}^{\infty} i^n \frac{2n+1}{n(n+1)} (\mathbf{M}_{e1n}^{(1)} + i\mathbf{N}_{o1n}^{(1)}). \quad (\text{A.10b})$$

Superscripts (1) denote the choice of spherical Bessel functions, j_n , in the definition of the spherical vector harmonics \mathbf{M} and \mathbf{N} .

By plugging in the general form of the electric fields \mathbf{E}_s (Eq. (A.8b)) and \mathbf{E}_i (Eq. (A.8c)) into the boundary condition (Eq. (A.9)), the electric field scattered from and inside the sphere can be derived as

$$\mathbf{E}_s = E_0 \sum_{n=1}^{\infty} i^n \frac{2n+1}{n(n+1)} (ia_n \mathbf{N}_{e1n}^{(3)} - b_n \mathbf{M}_{o1n}^{(3)}), \quad (\text{A.11a})$$

$$\mathbf{E}_i = E_0 \sum_{n=1}^{\infty} i^n \frac{2n+1}{n(n+1)} (c_n \mathbf{M}_{o1n}^{(1)} - id_n \mathbf{N}_{e1n}^{(1)}). \quad (\text{A.11b})$$

Superscripts (3) denote the choice of spherical Hankel functions, $h_n^{(1)}$. The *Mie coefficients* a_n and b_n are defined as

$$a_n = \frac{M\psi_n(k_1a)\psi'_n(ka) - \psi_n(ka)\psi'_n(k_1a)}{M\psi_n(k_1a)\zeta'_n(ka) - \zeta_n(ka)\psi'_n(k_1a)} \quad (\text{A.12})$$

$$b_n = \frac{\psi_n(k_1a)\psi'_n(ka) - M\psi_n(ka)\psi'_n(k_1a)}{\psi_n(k_1a)\zeta'_n(ka) - M\zeta_n(ka)\psi'_n(k_1a)}, \quad (\text{A.13})$$

where $k_1 = k\sqrt{\varepsilon_2/\varepsilon_1} = kM$ is the wavenumber inside the sphere, and $M = \sqrt{\varepsilon_2/\varepsilon_1}$ is the relative refractive index of the sphere. The *Ricatti-Bessel functions* $\psi(x) = xj_n(x)$ and $\zeta(x) = xh_n^{(1)}(x)$ are introduced to simplify the notation. The coefficients for the

fields inside the particle (often referred to as the *transmitted fields*), c_n and d_n , are

$$c_n = \frac{M\psi_n(ka)\zeta'_n(ka) - M\zeta_n(ka)\psi'_n(ka)}{\psi_n(k_1a)\zeta'_n(ka) - M\zeta_n(ka)\psi'_n(k_1a)}, \quad (\text{A.14a})$$

$$d_n = \frac{M\psi_n(ka)\zeta'_n(ka) - M\zeta_n(ka)\psi'_n(ka)}{M\psi_n(ka)\zeta'_n(ka) - \zeta_n(ka)\psi'_n(k_1a)}. \quad (\text{A.14b})$$

The denominators of c_n and b_n are identical, as are those of the d_n and a_n coefficients. Therefore, any resonant behavior of the scattering coefficients a_n and b_n should be associated with a resonance observed in the intensity of the field inside the particle.

We should note that we adopt here the definitions of the Mie coefficients by Bohren and Huffman in Ref. [117], which differ from those used by Ruppin [219] and, more recently, Mertens *et al.* [220] by interchanging $a_n \leftrightarrow -b_n$ and $c_n \leftrightarrow -d_n$.

Knowing the exact expressions for both the incident and scattered fields (as well as the magnetic fields, given by Eq. (A.2)), we can now calculate the scattering and extinction cross sections of the sphere σ_{scatt} and σ_{ext} , respectively. This is done by integrating the flow of the respective time-averaged elements of the Poynting vectors formed by the scattered field, \mathbf{S}_s , and the combinations of the incident and the scattered fields, \mathbf{S}_{ext} [117]:

$$\mathbf{S}_s = \frac{1}{2}\text{Re}(\mathbf{E}_s \times \mathbf{H}_s^*), \quad \mathbf{S}_{\text{ext}} = \frac{1}{2}\text{Re}(\mathbf{E}_0 \times \mathbf{H}_s^* + \mathbf{E}_s \times \mathbf{H}_0^*) \quad (\text{A.15})$$

through a large imaginary sphere \mathcal{S} encompassing the scatterer, and normalizing it by the energy density of the incident illumination I_0 :

$$\sigma_{\text{sca}} = I_0^{-1} \int_{\mathcal{S}} \mathbf{S}_s \cdot d\mathbf{s}, \quad \sigma_{\text{ext}} = I_0^{-1} \int_{\mathcal{S}} \mathbf{S}_{\text{ext}} \cdot d\mathbf{s}. \quad (\text{A.16})$$

Plugging in the expressions for the incident (Eq. (A.10)) and scattered fields (Eq. (A.11)), centering \mathcal{S} at the origin of coordinate system for simplicity, and performing the integration, we arrive at the following expressions:

$$\sigma_{\text{sca}} = \frac{2\pi}{k^2} \sum_{n=1}^{\infty} (2n+1)(|a_n|^2 + |b_n|^2), \quad \sigma_{\text{ext}} = \frac{2\pi}{k^2} \sum_{n=1}^{\infty} (2n+1)\text{Re}(a_n + b_n), \quad (\text{A.17})$$

Where $\text{Re}(z)$ denotes the real part of z . The cross sections are often related to the geometric cross sections of the scatterer - in the case of spherical particles πa^2 - by introducing the *scattering* and *extinction efficiencies*:

$$C_{\text{sca}} = \frac{2}{(ka)^2} \sum_{n=1}^{\infty} (2n+1)(|a_n|^2 + |b_n|^2), \quad C_{\text{ext}} = \frac{2}{(ka)^2} \sum_{n=1}^{\infty} (2n+1)\text{Re}(a_n + b_n). \quad (\text{A.18})$$

A.3 Scattering of radiation of a dipolar emitter

A.3.1 Electric dipolar emitter

Following a similar path as briefly presented above, we can describe the field distribution in a system comprising a spherical scatterer illuminated by the field from a radiating dipolar emitter. This problem was analyzed in detail by Kerker *et al.* [221] to whom we owe the expansion of the field originating from an electric dipole into vector spherical harmonics.

Let us consider an electric dipole positioned at $\mathbf{r}_{\text{dip}} = (0, 0, z_{\text{dip}})$ in the Cartesian coordinate system, and, as before, a homogeneous sphere of radius $a < z_{\text{dip}}$. Without loss of generality, we can consider two orientations of the dipole: radial (along the \hat{z} axis) and polar (along the \hat{x} axis). The expansion of the incident field originated by the dipole at point \mathbf{r} depends on whether \mathbf{r} lies within an imaginary sphere of radius z_{dip} :

$$\mathbf{E}_0 = \begin{cases} \sum_{\nu} D_{\nu} \left[p_{\nu} \mathbf{M}_{\nu}^{(1)} + q_{\nu} \mathbf{N}_{\nu}^{(1)} \right], & r > z_{\text{dip}} \\ \sum_{\nu} D_{\nu} \left[s_{\nu} \mathbf{M}_{\nu}^{(3)} + t_{\nu} \mathbf{N}_{\nu}^{(3)} \right], & r < z_{\text{dip}} \end{cases}, \quad (\text{A.19})$$

where the summation is performed over indices $\sum_{\nu} \equiv \sum_{\sigma=o,e} \sum_{n=1}^{\infty} \sum_{m=0}^n$, which can be identified with subscripts identifying the vector harmonics discussed above. The amplitude coefficients are given by $D_{\nu} = \delta_m(2n+1)(n-m)!/(4n(n+1)(n+m)!)$, where

$$\delta_m = \begin{cases} 1, & m = 0 \\ 2, & m > 0. \end{cases} \quad (\text{A.20})$$

The expansion coefficients are given by

$$s_{\nu} = \frac{ik^3}{\pi} \mathbf{M}_{\nu}^{(1)}(k\mathbf{r}_{\text{dip}}) \cdot \mathbf{p}, \quad t_{\nu} = \frac{ik^3}{\pi} \mathbf{N}_{\nu}^{(1)}(k\mathbf{r}_{\text{dip}}) \cdot \mathbf{p}, \quad (\text{A.21a})$$

$$p_{\nu} = \frac{ik^3}{\pi} \mathbf{M}_{\nu}^{(3)}(k\mathbf{r}_{\text{dip}}) \cdot \mathbf{p}, \quad q_{\nu} = \frac{ik^3}{\pi} \mathbf{N}_{\nu}^{(3)}(k\mathbf{r}_{\text{dip}}) \cdot \mathbf{p}. \quad (\text{A.21b})$$

The scattered field and the field inside the sphere are expanded as

$$\mathbf{E}_s = \sum_{\nu} D_{\nu} \left[u_{\nu} \mathbf{M}_{\nu}^{(3)}(k\mathbf{r}) + v_{\nu} \mathbf{N}_{\nu}^{(3)}(k_1\mathbf{r}) \right], \quad (\text{A.22a})$$

$$\mathbf{E}_i = \sum_{\nu} D_{\nu} \left[f_{\nu} \mathbf{M}_{\nu}^{(1)}(k_1\mathbf{r}) + g_{\nu} \mathbf{N}_{\nu}^{(1)}(k_1\mathbf{r}) \right]. \quad (\text{A.22b})$$

Applying the boundary conditions, Eq. (3.28), to the expansions of the electric fields given in Eqs. (A.19) and (A.22), we obtain

$$u_\nu = -b_n p_\nu, \quad v_\nu = -a_n q_\nu, \quad (\text{A.23a})$$

$$f_\nu = -c_n p_\nu, \quad g_\nu = -d_n q_\nu \quad (\text{A.23b})$$

where a_n and b_n are the Mie coefficients given by Eqs. (A.12) and (A.13).

We can now calculate the power scattered from the system by integrating the flux of Poynting vector, \mathbf{S}_{ext} , defined in Eq. (A.15) over the sphere \mathcal{S} , which now encapsulates both the particle and the dipole. Using the orthogonality of the \mathbf{M} and \mathbf{N} basis, we can express this quantity as

$$P_{\text{sca}} = \int_{\mathcal{S}} \mathbf{S}_{\text{ext}} \cdot d\mathbf{s} = \sqrt{\frac{\varepsilon_0}{\mu_0}} \frac{\pi}{k^2} \sum_{\nu} \delta_m \frac{(2n+1)(n-m)!}{8n(n+1)(n+m)!} (|s_\nu + u_\nu|^2 + |t_\nu + v_\nu|^2). \quad (\text{A.24})$$

The power lost into the other decay channel, related to the losses inside the scatterer, can be calculated as

$$\begin{aligned} P_{\text{abs}} &= \frac{1}{2} \int \omega \text{Im}(\varepsilon_2) |\mathbf{E}_1(\mathbf{r})|^2 d\mathbf{r} = \\ &= \frac{1}{2} \int \sigma |\mathbf{E}_1(\mathbf{r})|^2 d\mathbf{r} = \\ &= \frac{\pi\sigma}{8} \sum_{\nu} \epsilon_m \frac{(2n+1)(n-m)!}{n(n+1)(n+m)!} \times \\ &\quad \times \int_0^a \left\{ |f_\nu|^2 |j_n(k_1 r)|^2 + \frac{|g_\nu|^2}{2n+1} [(n+1)|j_{n-1}(k_1 r)|^2 + n|j_{n+1}(k_1 r)|^2] \right\} r^2 dr, \end{aligned}$$

where σ is the conductivity of the material of the scatterer and $\text{Im}(z)$ denotes the imaginary part of z . The integrals of the spherical Bessel functions can be solved analytically [222].

Plugging in the explicit forms of the expansion coefficients listed in Eq. (A.23) into the above equations, and normalizing the scattered power by the radiative energy loss of the dipole in the absence of the sphere, P_0 , we arrive at explicit expressions for the normalized power scattered by an electric dipolar emitter:

$$\frac{P_{\text{sca}}^{\perp,e}}{P_0} = \frac{3}{2} \sum_{n=1}^{\infty} (2n+1)n(n+1) \left| \frac{j_n(kz) - a_n h_n^{(1)}(kz)}{kz} \right|^2, \quad (\text{A.25a})$$

$$\frac{P_{\text{sca}}^{\parallel,e}}{P_0} = \frac{3}{4} \sum_{n=1}^{\infty} (2n+1) \left[|j_n(kz) - b_n h_n^{(1)}(kz)|^2 + \left| \frac{\psi_n'(kz) - a_n \zeta_n'(kz)}{kz} \right|^2 \right]. \quad (\text{A.25b})$$

Here the superscripts \perp and \parallel denote the radial and polar orientation of the dipole, respectively, and e stresses the *electric* nature of the dipole. Similarly, we can calculate the sum of the powers emitted into radiation and lost through the absorption in the scatterer as $P_{\text{tot}} = P_{\text{sca}} + P_{\text{abs}}$ and write

$$\frac{P_{\text{tot}}^{\perp,e}}{P_0} = 1 - \frac{3}{2} \text{Re} \sum_{n=1}^{\infty} (2n+1)n(n+1)a_n \left[\frac{h_n^{(1)}(kz)}{kz} \right]^2, \quad (\text{A.26a})$$

$$\frac{P_{\text{tot}}^{\parallel,e}}{P_0} = 1 - \frac{3}{4} \sum_{n=1}^{\infty} (2n+1) \text{Re} \left[a_n \left[\frac{\zeta_n'(kz)}{kz} \right]^2 + b_n [h_n^{(1)}(kz)]^2 \right]. \quad (\text{A.26b})$$

A.3.2 Magnetic dipolar emitter

We can now derive the respective quantities for *magnetic* dipolar emitters. To achieve this goal, we make use of the invariance of Maxwell's equations in a homogeneous medium under the transformation

$$\mathbf{E} \rightarrow -Z\mathbf{H}, \quad \mathbf{H} \rightarrow \frac{1}{Z}\mathbf{E}, \quad \mathbf{p} \rightarrow \frac{\mathbf{m}}{c}, \quad (\text{A.27})$$

where Z is the impedance of the medium with dielectric permittivity ε_1 : $Z = \sqrt{\frac{\mu_0}{\varepsilon_0 \varepsilon_1}}$. We can thus rewrite the expansion of the magnetic field of the magnetic dipole by applying the above transformation to the electric field of the electric dipole (Eq. (A.19)):

$$\mathbf{H}_0^m = -Z \begin{cases} \sum_{\nu} D_{\nu} \left[p_{\nu}^m \mathbf{M}_{\nu}^{(1)} + q_{\nu}^m \mathbf{N}_{\nu}^{(1)} \right], & r > z_{\text{dip}} \\ \sum_{\nu} D_{\nu} \left[s_{\nu}^m \mathbf{M}_{\nu}^{(3)} + t_{\nu}^m \mathbf{N}_{\nu}^{(3)} \right], & r < z_{\text{dip}} \end{cases}, \quad (\text{A.28})$$

where the expansion coefficients, marked with the superscript m to denote the magnetic nature of the source, are given by

$$s_{\nu}^m = \frac{ik^3}{c\pi} \mathbf{M}_{\nu}^{(1)}(k\mathbf{r}_{\text{dip}}) \cdot \mathbf{m}, \quad t_{\nu}^m = \frac{ik^3}{c\pi} \mathbf{N}_{\nu}^{(1)}(k\mathbf{r}_{\text{dip}}) \cdot \mathbf{m} \quad (\text{A.29a})$$

$$p_{\nu}^m = \frac{ik^3}{c\pi} \mathbf{M}_{\nu}^{(3)}(k\mathbf{r}_{\text{dip}}) \cdot \mathbf{m}, \quad q_{\nu}^m = \frac{ik^3}{c\pi} \mathbf{N}_{\nu}^{(3)}(k\mathbf{r}_{\text{dip}}) \cdot \mathbf{m}. \quad (\text{A.29b})$$

The transformation defined in Eq. (A.27) cannot be extended to the problem of scattering on arbitrary objects (although it can be applied for arbitrarily-shaped objects with

specific macroscopic material properties, as we discuss in Chapter 3), and therefore we cannot readily apply it to the scattered fields.

To address this problem, let us take a slightly less direct approach and represent the electric field of the magnetic dipole as a sum of vector spherical harmonics,

$$\mathbf{E}_0^m = -\frac{iZ}{c\varepsilon_1} \sum_{\nu} D_{\nu} \left[s_{\nu}^m \mathbf{N}_{\nu}^{(3)} + t_{\nu}^m \mathbf{M}_{\nu}^{(3)} \right]. \quad (\text{A.30})$$

With the help of the Mie theory, we can now readily write the expansion coefficients of the scattered electric field by multiplying the s_{ν}^m and t_{ν}^m by the respective Mie coefficients:

$$\mathbf{E}_s^m = \frac{iZ}{c\varepsilon_1} \sum_{\nu} D_{\nu} \left[a_{\nu} s_{\nu}^m \mathbf{N}_{\nu}^{(3)} + b_{\nu} t_{\nu}^m \mathbf{M}_{\nu}^{(3)} \right]. \quad (\text{A.31})$$

The magnetic fields $\mathbf{H}_{\text{sca}}^m$ and \mathbf{H}_i^m can thus be written as

$$\mathbf{H}_s = -Z \sum_{\nu} D_{\nu} \left[u_{\nu}^m \mathbf{M}_{\nu}^{(3)}(k\mathbf{r}) + v_{\nu}^m \mathbf{N}_{\nu}^{(3)}(k_1\mathbf{r}) \right], \quad (\text{A.32a})$$

$$\mathbf{H}_i = -Z \sum_{\nu} D_{\nu} \left[f_{\nu}^m \mathbf{M}_{\nu}^{(1)}(k_1\mathbf{r}) + g_{\nu}^m \mathbf{N}_{\nu}^{(1)}(k_1\mathbf{r}) \right], \quad (\text{A.32b})$$

where

$$u_{\nu}^m = -a_{\nu} p_{\nu}^m, \quad v_{\nu}^m = -b_{\nu} q_{\nu}^m, \quad (\text{A.33a})$$

$$f_{\nu}^m = -d_{\nu} p_{\nu}^m, \quad g_{\nu}^m = -c_{\nu} q_{\nu}^m. \quad (\text{A.33b})$$

These equations reveal a remarkable symmetry similarity to those obtained for the scattering coefficients of the radiation from electric dipoles, given in Eq. (A.23). Even more importantly, they indicate that the expressions for the power scattered from the magnetic dipole into radiation and lost to absorption in the scatterer are identical as those for the electric dipole, with the exchange of the electric (a_n) and magnetic (b_n) Mie coefficients:

$$\frac{P_{\text{sca}}^{\perp,m}}{P_0} = \frac{3}{2} \sum_{n=1}^{\infty} (2n+1)n(n+1) \left| \frac{j_n(kz) - b_n h_n^{(1)}(kz)}{kz} \right|^2, \quad (\text{A.34a})$$

$$\frac{P_{\text{sca}}^{\parallel,m}}{P_0} = \frac{3}{4} \sum_{n=1}^{\infty} (2n+1) \left[|j_n(kz) - a_n h_n^{(1)}(kz)|^2 + \left| \frac{\psi'_n(kz) - b_n \zeta'_n(kz)}{kz} \right|^2 \right], \quad (\text{A.34b})$$

$$\frac{P_{\text{tot}}^{\perp,m}}{P_0} = 1 - \frac{3}{2} \text{Re} \sum_{n=1}^{\infty} (2n+1)n(n+1) b_n \left[\frac{h_n^{(1)}(kz)}{kz} \right]^2, \quad (\text{A.35a})$$

$$\frac{P_{\text{tot}}^{\parallel,m}}{P_0} = 1 - \frac{3}{4} \sum_{n=1}^{\infty} (2n+1) \text{Re} \left[b_n \left[\frac{\zeta'_n(kz)}{kz} \right]^2 + a_n [h_n^{(1)}(kz)]^2 \right]. \quad (\text{A.35b})$$

Appendix B

Linearization of the optomechanical Hamiltonian

B.1 Analytical treatment of the system

In the following section we present an analytical treatment of the dynamics of an off-resonant Raman scattering in plasmonic cavities, based on the quantum regression theorem (QRT) [156]. To readily apply this method, we first consider a linearized version of the optomechanical Hamiltonian and verify numerically that this approximation is well-suited for describing the system in the range of parameters discussed in Chapter 4. We then proceed to solve the linearized Hamiltonian analytically and present a solution for the case of incident coherent illumination with frequency tuned to that of the plasmon cavity.

Since we have already introduced all the parameters of the system with proper units in Chapter 4, to simplify the notation we will from now follow the tradition celebrated in academic books on quantum optics, and skip the reduced Planck constant \hbar in the following equations.

B.1.1 Quantum Langevin equations of the original Hamiltonian

Consider the optomechanical Hamiltonian in the frame rotating with the frequency of the laser ω_l ($\Delta = \omega_c - \omega_l$):

$$\hat{H} = \Delta \hat{a}^\dagger \hat{a} + \omega_m \hat{b}^\dagger \hat{b} + i\Omega(\hat{a}^\dagger - \hat{a}) - g\hat{a}^\dagger \hat{a}(\hat{b} + \hat{b}^\dagger), \quad (\text{B.1})$$

where all the parameters and operators are properly defined in Chapter 4. With the inclusion of a vacuum noise a_{in} and thermal noise b_{in} terms, which are taken to have zero mean value and arise from δ -correlated thermal baths [196]:

$$\langle a_{\text{in}}^\dagger(t) a_{\text{in}}(t') \rangle = 0, \quad (\text{B.2a})$$

$$\langle a_{\text{in}}(t) a_{\text{in}}^\dagger(t') \rangle = \delta(t - t'), \quad (\text{B.2b})$$

$$\langle b_{\text{in}}^\dagger(t) b_{\text{in}}(t') \rangle = \bar{n}_m^{\text{th}} \delta(t - t'), \quad (\text{B.2c})$$

$$\langle b_{\text{in}}(t) b_{\text{in}}^\dagger(t') \rangle = (\bar{n}_m^{\text{th}} + 1) \delta(t - t'), \quad (\text{B.2d})$$

The dynamics equations for operators \hat{a} and \hat{b} are:

$$\dot{\hat{a}} = -(\kappa/2 + i\Delta)\hat{a} + \Omega + ig\hat{a}(\hat{b} + \hat{b}^\dagger) + \sqrt{\kappa}a_{\text{in}}(t), \quad (\text{B.3a})$$

$$\dot{\hat{b}} = -(\gamma_m/2 + i\omega_m)\hat{b} - ig\hat{a}^\dagger \hat{a} + \sqrt{\gamma_m}b_{\text{in}}(t). \quad (\text{B.3b})$$

B.1.2 Analytical solution to the linearized Hamiltonian

The linearized form of the above Hamiltonian was derived in Section 4.2.5:

$$\hat{H}' = \Delta \hat{a}^\dagger \hat{a} + \omega_m \hat{b}^\dagger \hat{b} - g|\alpha_s|^2(\hat{b} + \hat{b}^\dagger) - g(\alpha_s \hat{a}^\dagger + \alpha_s^* \hat{a})(\hat{b} + \hat{b}^\dagger). \quad (\text{B.4})$$

For reference we remind that to derive it, we have redefined the cavity operators

$$\hat{a} \rightarrow \hat{a} + \alpha_s, \quad (\text{B.5})$$

removing the coherent amplitude of the cavity field $\alpha_s = \Omega/(\frac{\kappa}{2} + i\Delta)$. The third term in this linearized Hamiltonian can be interpreted as the effective coherent driving ($\propto g|\alpha_s|^2$) of the phonon mode.

A redefinition of the phononic operators in a similar manner (by removing the coherent amplitude of vibrations) leads (via the linear coupling term) to a new linear driving of

the cavity (and a renormalized Δ), and so on, successively. We can capture *all* orders of this feedback by defining displacements α'_s and β'_s through the condition that in the displaced basis the transformed Hamiltonian does not contain any linear (driving) terms, so that it can be written as

$$\hat{H}'' = \Delta \hat{a}^\dagger \hat{a} + \omega_m \hat{b}^\dagger \hat{b} - g[\alpha'_s \hat{a}^\dagger + (\alpha'_s)^* \hat{a}](\hat{b} + \hat{b}^\dagger), \quad (\text{B.6})$$

where displacements α'_s and β'_s are defined as

$$\alpha'_s = \frac{\Omega}{\kappa/2 + i\Delta - 2ig\text{Re}(\beta'_s)}, \quad (\text{B.7})$$

$$\beta'_s = -\frac{g|\alpha'_s|^2}{\omega_m - i\gamma_m/2}. \quad (\text{B.8})$$

Inserting Eq. (B.7) into (B.8), we arrive at a cubic equation

$$4g^2[\text{Re}(\beta'_s)]^3 - 4g\Delta[\text{Re}(\beta'_s)]^2 + \left[\left(\frac{\kappa}{2}\right)^2 + \Delta^2 \right] \text{Re}(\beta'_s) + \frac{g\omega_m\Omega^2}{\omega_m^2 + (\gamma_m/2)^2} = 0. \quad (\text{B.9})$$

The leading order of Eq. (B.9) gives the approximations to β'_s and α'_s , which can be otherwise derived as the coherent amplitudes of the undisplaced operators $\langle \hat{b} \rangle$ and $\langle \hat{a} \rangle$, respectively, as we discuss in the following section. The subsequent corrections decrease in value very quickly and are quantitatively negligible for our parameters. However, the presence of these terms, and in particular the appearance of higher powers of Ω^2 is a clear evidence of the fundamental *non-linearity* of the system.

B.1.2.1 Numerical solution

In our numerical calculations, we have implemented the non-linear Hamiltonian with the displaced cavity operators (Eq. (4.52)) and solved the corresponding master equation, describing the vibrational and photonic degrees of freedom in the basis of Fock states (Eq. (4.49)). For the strongest pumping and coupling parameters, the calculations were ensured to converge by using up to 15 and 10 Fock states for the description of the vibrational and photonic state, respectively.

B.1.3 Steady state of the linearized Hamiltonian

From here on, we will focus our attention on the dynamics of the system given by the linearized Hamiltonian \hat{H}' and the master equation given in Eq. (4.48). We can thus

rewrite the Heisenberg equations given in Eq. (B.3a, B.3b) using the displaced photonic operator \hat{a} as

$$\dot{\hat{a}} = -(\kappa/2 + i\Delta)\hat{a} + ig\alpha_s(\hat{b} + \hat{b}^\dagger) + \sqrt{\kappa}a_{\text{in}}(t), \quad (\text{B.10})$$

$$\dot{\hat{b}} = -(\gamma_m/2 + i\omega_m)\hat{b} - ig(\alpha_s^*\hat{a} + \alpha_s\hat{a}^\dagger) - ig|\alpha_s|^2 + \sqrt{\gamma_m}b_{\text{in}}(t). \quad (\text{B.11})$$

Denoting by A a column vector with expectation values of operators

$$A = \begin{pmatrix} \langle \hat{a}^\dagger \rangle \\ \langle \hat{a} \rangle \\ \langle \hat{b}^\dagger \rangle \\ \langle \hat{b} \rangle \end{pmatrix}, \quad (\text{B.12})$$

and by Γ_{ab} the correlation matrix

$$\Gamma_{ab} = \left\langle \begin{pmatrix} \hat{a}^\dagger \\ \hat{a} \\ \hat{b}^\dagger \\ \hat{b} \end{pmatrix} \begin{pmatrix} \hat{a} & \hat{a}^\dagger & \hat{b} & \hat{b}^\dagger \end{pmatrix} \right\rangle, \quad (\text{B.13})$$

we can rewrite Eqs. (B.10) and (B.11) as

$$\frac{d}{dt}A = MA + D, \quad (\text{B.14})$$

$$\frac{d}{dt}\Gamma_{ab} = M\Gamma_{ab} + \Gamma_{ab}M^\dagger + AD^\dagger + DA^\dagger + E, \quad (\text{B.15})$$

where

$$D = ig|\alpha_s|^2(0, 0, 1, -1)^T, \quad (\text{B.16})$$

$$E = \text{diag}([0, \kappa, \gamma\bar{n}_m^{\text{th}}, \gamma_m(1 + \bar{n}_m^{\text{th}})]), \quad (\text{B.17})$$

for superscript T denoting matrix transpose and diag - a diagonal matrix and M defined as the *dynamical matrix*

$$M = \begin{pmatrix} -(\kappa/2 - i\Delta) & 0 & -ig\alpha_s^* & -ig\alpha_s^* \\ 0 & -(\kappa/2 + i\Delta) & ig\alpha_s & ig\alpha_s \\ ig\alpha_s & ig\alpha_s^* & -(\gamma_m/2 - i\omega_m) & 0 \\ -ig\alpha_s & -ig\alpha_s^* & 0 & -(\gamma_m/2 + i\omega_m) \end{pmatrix}. \quad (\text{B.18})$$

Denoting by $\tilde{\Gamma}_{ab} = \Gamma_{ab} - AA^\dagger$ the *covariance matrix* we get a simple equation of motion without terms depending on A . For simplicity we neglect the thermal population of phonons $\bar{n}_m^{\text{th}} = 0$ and arrive at

$$\frac{d}{dt}\tilde{\Gamma}_{ab} = M\tilde{\Gamma}_{ab} + \tilde{\Gamma}_{ab}M^\dagger + \text{diag}([0, \kappa, 0, \gamma_m]). \quad (\text{B.19})$$

Computations can be simplified by vectorizing these equations. To this goal, we denote by $\vec{\Gamma}_{ab}$ the vector formed by stacking the columns of $\tilde{\Gamma}_{ab}$, and by \tilde{M} the 16×16 matrix $M \otimes 1 + 1 \otimes M^T$ [193]. Then Eq. (B.19) reads

$$\frac{d}{dt}\vec{\Gamma}_{ab} = \tilde{M}\vec{\Gamma}_{ab} + \vec{E}, \quad (\text{B.20})$$

where \vec{E} is a vectorized matrix E . The displacements and covariances at time t are then given by

$$A(t) = -M^{-1}D + e^{tM} (A(0) + M^{-1}D), \quad (\text{B.21})$$

$$\vec{\Gamma}_{ab}(t) = -\tilde{M}^{-1}\vec{E} + e^{t\tilde{M}} (\vec{\Gamma}_{ab}(0) + \tilde{M}^{-1}\vec{E}), \quad (\text{B.22})$$

and, consequently, the steady-state (denoted by subscript ss) displacements and covariances are

$$A_{\text{ss}} = -M^{-1}D, \quad (\text{B.23})$$

$$\vec{\Gamma}_{ab,\text{ss}} = -\tilde{M}^{-1}\vec{E}. \quad (\text{B.24})$$

B.1.4 Quantum regression theorem

Equation (B.14) is a closed form of equations of motion (Eqs. (B.10, B.11)) for the operators making up vector A : \hat{a}^\dagger , \hat{a} , \hat{b}^\dagger , \hat{b} , and allows us to calculate the expected values of these one-time operators in the steady state A_{ss} (Eq. (B.23)), where the subscript ss denotes the steady-state. The *quantum regression theorem* (QRT) allows us to calculate the two-time correlators $\langle \hat{a}^\dagger(t)a(0) \rangle_{\text{ss}}$ which determine the spectrum $S(\omega)$ of emission from the cavity

$$S(\omega) = \omega^4 \int_{-\infty}^{\infty} dt e^{-i\omega t} \langle \hat{a}^\dagger(t)\hat{a}(0) \rangle_{\text{ss}}. \quad (\text{B.25})$$

More generally, from the QRT, the equation of motion for $\langle X(t)Y(0) \rangle$ is the same as that for $\langle X(t) \rangle$. Therefore, for matrix of correlations $C(t)$ defined as

$$C(t) = \left\langle \begin{pmatrix} \hat{a}^\dagger(t) \\ \hat{a}(t) \\ \hat{b}^\dagger(t) \\ \hat{b}(t) \end{pmatrix} \begin{pmatrix} \hat{a}(0) & \hat{a}^\dagger(0) & \hat{b}(0) & \hat{b}^\dagger(0) \end{pmatrix} \right\rangle_{\text{ss}}, \quad (\text{B.26})$$

we can write an evolution equation

$$\dot{C}(t) = MC(t) + DA^\dagger, \quad (\text{B.27})$$

with formal solution

$$C(t) = -M^{-1}DA_{\text{ss}}^\dagger + e^{tM}\tilde{\Gamma}_{ab,\text{ss}}, \quad (\text{B.28})$$

for the steady-state covariance matrix $\tilde{\Gamma}_{ab,\text{ss}} = \Gamma_{ab,\text{ss}} - A_{\text{ss}}A_{\text{ss}}^\dagger$.

We then find that the two-time correlator $\langle a^\dagger(t)a(0) \rangle_{\text{ss}}$ used to calculate the spectrum $S(\omega)$ of emission from the cavity (Eq. (B.25)) is given by the first element of the vector defined by a product of $\exp(tM)$ and the first column of the steady-state covariances matrix $\tilde{\Gamma}_{ab,\text{ss}}$.

For the resonant case ($\Delta = 0$) and without thermal pumping ($T = 0$ K) the exponent of M can be found analytically, and we can rewrite the above product as a series of expressions with exponential factors given by the eigenvalues of M :

$$\{e^{-\kappa/2}, e^{-(\gamma_m/2 \pm i\omega_m)}\}. \quad (\text{B.29})$$

From those, we choose the terms oscillating at frequencies $\pm\omega_m$ and decaying at a rate $\gamma_m/2$, as they govern the strengths of Stokes and anti-Stokes scattering. After some algebra, we obtain the explicit expressions for the Stokes and anti-Stokes emission as second order polynomials of Ω^2 :

$$S(\omega_S) = \frac{2\omega_S^4}{\gamma_m}(s_2\Omega^2 + s_4\Omega^4), \quad (\text{B.30})$$

$$S(\omega_{aS}) = \frac{2\omega_{aS}^4}{\gamma_m}a_4\Omega^4, \quad (\text{B.31})$$

where ω_S and ω_{aS} are frequencies of the Stokes and anti-Stokes emission, respectively. The exact formulas for s_i and a_4 are somewhat lengthy, but take a simpler form in the

limit $\gamma_m \ll \kappa, \omega_m$:

$$s_2 \approx \left(\frac{4g}{\kappa|\kappa - 2i\omega_m|} \right)^2, \quad (\text{B.32a})$$

$$s_4 \approx \left(\frac{4g}{\kappa|\kappa - 2i\omega_m|} \right)^4 \frac{\kappa}{\gamma_m} = s_2^2 \frac{\kappa}{\gamma_m}, \quad (\text{B.32b})$$

$$a_4 = s_4. \quad (\text{B.32c})$$

The first term in expression for $S(\omega_S)$, proportional to Ω^2 , is dominant for low pumping power. For larger Ω the second term becomes dominant, and yields the non-linear dependence discussed in Chapter 4. Note that the coefficients of the terms proportional to Ω^4 are equal both for Stokes and anti-Stokes, and thus for larger pumping powers, the Stokes/anti-Stokes ratio becomes independent of Ω .

If $T > 0$, additional terms appear in the expressions for the Stokes and anti-Stokes emission, reflecting (i) the thermal pumping of the molecule, which effectively changes the strength of the anti-Stokes scattering and (ii) the enhancement of the Stokes scattering by stimulated phonon emission. Specifically, we find that Eq. (B.30) can be rewritten

$$S(\omega_S) = \frac{2\omega_S^4}{\gamma_m} [s_2(1 + \bar{n}_m^{\text{th}})\Omega^2 + s_4\Omega^4], \quad (\text{B.33})$$

and the anti-Stokes emission (Eq. (B.31)) becomes

$$S(\omega_{aS}) = \frac{2\omega_{aS}^4}{\gamma_m} (a_2\bar{n}_m^{\text{th}}\Omega^2 + a_4\Omega^4), \quad (\text{B.34})$$

with coefficient $a_2 = s_2$. Thus, in the region of thermal pumping (where we can neglect all the terms $\propto \Omega^4$ in the above equations), we recover the well-known formula for the anti-Stokes/Stokes ratio [17]

$$\frac{S(\omega_{aS})}{S(\omega_S)} \approx \left(\frac{\omega_{aS}}{\omega_S} \right)^4 \frac{\bar{n}_m^{\text{th}}}{1 + \bar{n}_m^{\text{th}}}. \quad (\text{B.35})$$

B.1.5 Phonon population

Our analytical approach allows us to write down the explicit expression for the thermal \bar{n}_m^{th} , incoherent n_m^{incoh} and coherent n_m^{coh} phonon populations in the case of the laser tuned to the cavity resonance ($\Delta = 0$):

$$n_b = \langle \hat{b}^\dagger \hat{b} \rangle_{\text{ss}} = \bar{n}_m^{\text{th}} + n_m^{\text{incoh}} + n_m^{\text{coh}}, \quad (\text{B.36})$$

where

$$n_m^{\text{incoh}} = \left(\frac{4g\Omega}{\kappa} \right)^2 \frac{\kappa + \gamma_m}{\gamma_m |\kappa + \gamma_m + 2i\omega_m|^2} \approx s_2 \Omega^2 \frac{\kappa}{\gamma_m}, \quad (\text{B.37})$$

$$n_m^{\text{coh}} \approx \left(\frac{2\Omega}{\kappa} \right)^4 \left(\frac{g}{\omega_m} \right)^2. \quad (\text{B.38})$$

B.1.6 Quartic dependence of Stokes intensity on the enhancement of the incident field

By inserting the definitions of Ω (Eq. (4.46)) and g (Eq. (4.34)) into the lowest-order expression for $S(\omega_S)$ (Eq. (B.30)), we can write $S(\omega_S) \propto K^2/V_{\text{eff}}$, where K is the enhancement of the incident field at the position of the molecule. The inverse volume factor can be shown to be proportional to K^2 , by relating the Purcell factor (Eq. (4.40)) to K^2 through the reciprocity theorem, thus allowing us to recover the expected dependence of the Stokes emission $S(\omega_S) \propto K^4$.

It should be also noted that a similar dependence of the anti-Stokes intensity on K can be retrieved only in the thermal pumping regime, where the phonons are primarily provided by the thermal bath, and the anti-Stokes intensity is proportional to $\bar{n}_m^{\text{th}}\Omega^2$. In the vibrational pumping regime, the phonons are provided by the Stokes transitions, and thus we expect to retrieve the higher-order dependence of $S(\omega_{aS})$ on K .

B.2 Threshold for the onset of the phonon-stimulated Raman scattering

From Eq. (B.33) and the relation between s_2 and s_4 (Eq. (B.32b)), we can derive an approximate criterion for the onset of the phonon-stimulated Raman scattering, defined arbitrarily by the stimulated Stokes emission becoming as strong as the spontaneous emission:

$$\bar{n}_m^{\text{th}} + s_2 \Omega^2 \frac{\kappa}{\gamma_m} > 1. \quad (\text{B.39})$$

Dropping the first term on the left-hand side, which becomes comparatively very small as the power is increased, and inserting the definitions of s_2 (Eq. (B.32)), g (Eq. (4.34)) and Ω (Eq. (4.46)), we can show that

$$s_2 \Omega^2 \frac{\kappa}{\gamma_m} \propto (R_\nu Q_\nu^0)^2 \frac{(K|E_0|)^2}{V_{\text{eff}} |\kappa - 2i\omega_m|^2} \frac{\kappa}{\gamma_m}. \quad (\text{B.40})$$

List of publications

Publications discussed in the Thesis:

1. *Dielectric antennas-a suitable platform for controlling magnetic dipolar emission.* **M.K. Schmidt**, R. Esteban, J.J. Sáenz, I. Suárez-Lacalle, S. Mackowski, and J. Aizpurua. *Optics Express*, 20(13), 13636–13650 (2012). [15]
2. *Low-loss Electric and Magnetic Field-Enhanced Spectroscopy with subwavelength silicon dimers.* P. Albella, M.A. Poyli, **M.K. Schmidt**, S.A. Maier, F. Moreno, J.J. Sáenz, and J. Aizpurua. *Journal of Physical Chemistry C*, 117(26), 13573–13584 (2013). [7]
3. *Isotropically polarized speckle patterns.* **M.K. Schmidt**, J. Aizpurua, X. Zambrana-Puyalto, X. Vidal, G. Molina-Terriza, and J.J. Sáenz. *Physical Review Letters*, 114(11), 113902 (2015). [120]
4. *Electromagnetic resonances of silicon nanoparticle dimers in the visible.* U. Zywietz, **M.K. Schmidt**, A.B. Evlyukhin, C. Reinhardt, J. Aizpurua, and B.N. Chichkov. *ACS Photonics*, 2, 913–920 (2015). [223]
5. *QED description of Raman scattering from molecules in plasmonic cavities.* **M.K. Schmidt**, R. Esteban, A. González-Tudela, G. Giedke, and J. Aizpurua. *ArXiv preprint arXiv:1509.03851* (2015). [18]
6. *Revisiting the energy and dynamics of plasmons for a generalized dielectric function.* **M.K. Schmidt**, P. Nordlander, C. Sönnichsen, and J. Aizpurua. In preparation (2015).

Other publications:

7. *Control of single emitter radiation by polarization- and position-dependent activation of dark antenna modes.* **M.K. Schmidt**, S. Mackowski, and J. Aizpurua. *Optics Letters* 37, 1017-1019 (2012). [[16](#)]
8. *Gold spiky nanodumbbells: anisotropy in gold nanostars.* S. M. Novikov, A. Sánchez-Iglesias, **M.K. Schmidt**, A. Chuvilin, J. Aizpurua, M. Grzelczak, and L.M. Liz-Marzán. *Particle & Particle Systems Characterization* 31, 77 (2014). [[6](#)]
9. *Polarization control of metal-enhanced fluorescence in hybrid assemblies of photosynthetic complexes and gold nanorods.* L. Bujak, M. Olejnik, T.H.P. Brotsudarmo, **M.K. Schmidt**, N. Czechowski, D. Piatkowski, J. Aizpurua, R.J. Cogdell, W. Heiss, and S. Mackowski. *Physical Chemistry Chemical Physics* 16, 9015 (2014). [[224](#)]
10. *Antenna resonances in low aspect ratio semiconductor nanowires.* D.J. Traviss, **M.K. Schmidt**, J. Aizpurua, and O.L. Muskens. *Optics Express* 23, 22771 (2015). [[216](#)]
11. *Nanocavities: Optomechanics goes molecular.* **M.K. Schmidt**, and J. Aizpurua, *Nature Nanotechnology: News and Views*, doi:10.1038/nnano.2015.287 (2015). [[225](#)]
12. *Rabi splitting in photoluminescence spectra of hybrid system of gold nanorods and J-aggregates.* D. Melnikau, R. Esteban, D. Savateeva, A. Sánchez-Iglesias, M. Grzelczak, **M.K. Schmidt**, L. Liz-Marzán, J. Aizpurua, and Y. Rakovich. Submitted (2015).
13. *Lattice surface modes in magnetoplasmonic crystals of anisotropic antennas.* N. Maccaferri, L. Bergamini, M. Pancaldi, **M.K. Schmidt**, M. Kataja, S. van Dijken, N. Zabala, J. Aizpurua, and P. Vavassori. In preparation (2015).
14. *Spectrally-selective plasmonic interaction between nanocrystals and gold nanoparticles.* K. Ciszak, M. Twardowska, M. Nyk, **M.K. Schmidt**, J. Aizpurua, D. Piatkowski, and S. Mackowski. In preparation (2015).

List of symbols

Chapter 1

ε_D	Drude-Sommerfeld dielectric function, Eq. (1.4)
ε_∞	background permittivity
ω_p	plasma frequency, Eq. (1.2)
γ_p	damping parameter in Drude-Sommerfeld model, Eq. (1.4)
α^{qs}	quasi-static polarizability of a sphere, Eq. (1.13)
$\Gamma_{NR}, \Gamma_R, \Gamma_A$	non-radiative (Eq. (1.18)), radiative Abraham-Lorentz (Eq. (1.24)), and absorption damping coefficients,
α^{HO}	harmonic oscillator polarizability, Eq. (1.26)
$\tilde{\alpha}, \alpha$	MWLWA microscopic and macroscopic polarizability, Eq. (1.37)
α_D	MWLWA polarizability with Drude-Sommerfeld model $\varepsilon_D(\varepsilon_\infty = 1)$, Eq. (1.41)
$\sigma_{\text{scatt}}, \sigma_{\text{abs}}$	MWLWA scattering (Eq. (1.42a)) and absorption (Eq. (1.42b)) cross sections
$\Gamma_{ \alpha ^2}, \Gamma_{\text{sca}}, \Gamma_{\text{abs}}$	full width half maximum of $ \alpha ^2$ (Eq. (1.37)), σ_{sca} (Eq. (1.42a)), σ_{abs} (Eq. (1.42b))

Chapter 2

a_n, b_n	Mie coefficients, Eqs. (A.12,A.13)
$M_{(e/o)mn}, N_{(e/o)mn}$	vector spherical harmonics, Eqs. (A.5,A.7)
$C_{\text{sca}}, C_{\text{ext}}$	scattering and extinction efficiencies, Eqs. (2.1,A.18)
$\Gamma_{\text{sca}}^{\dagger,x}/\Gamma_0$	radiative enhancement of the decay rate of electric ($x = e$) or magnetic ($x = m$) emitter oriented parallelly ($\dagger = $) or perpendicularly ($\dagger = \perp$) to the surface, Eqs. (2.4a-2.5d)

$\Gamma_{\text{tot}}^{\dagger,x}/\Gamma_0$	total enhancement of the decay rate of electric ($x = e$) or magnetic ($x = m$) emitter oriented parallelly ($\dagger = \parallel$) or perpendicularly ($\dagger = \perp$) to the surface, Eqs. (2.4a-2.5d)
$(\Gamma_{\text{tot}}^{\dagger,x}/\Gamma_0) _{\text{dip}}$	total enhancement of the decay rate of electric ($x = e$) or magnetic ($x = m$) emitter oriented parallelly ($\dagger = \parallel$) or perpendicularly ($\dagger = \perp$) to the surface, in a dipolar approximation, Eqs. (2.6a-2.6d)
α_E, α_M	electric and magnetic polarizabilities (Mie theory), Eq. (2.7)
$\overset{\leftrightarrow}{\mathbf{G}}_E, \overset{\leftrightarrow}{\mathbf{G}}_M$	electric (Eq. (2.12)) and magnetic (Eq. (2.13)) Green's function
$\tilde{\alpha}_{ey}, \tilde{\alpha}_{ez}, \tilde{\alpha}_{mx}$	dressed polarizabilities Eq. (2.29)
$\tilde{\alpha}_{e-m,TM}$	dressed polarizability Eq. (2.30)

Chapter 3

$\mathbf{P}, T_{\delta\mathbf{r}}$	linear momentum operator and spatial translation transformation, Eq. (3.7)
$H, T_{\delta t}$	Hamiltonian operator and time evolution transformation, Eq. (3.8)
$\mathbf{J}, R_{\hat{\mathbf{n}}}$	angular momentum AM (Eqs. (3.9a)) and rotation transformation
\mathbf{L}, \mathbf{S}	orbital AM (Eqs. (3.9b)), spin AM (Eqs. (3.9c)) operators
Λ, D_ϕ	helicity operator and duality transformation, Eqs. (3.11, 3.12)
$\mathbf{M}^{\text{TE}}, \mathbf{M}^{\text{TM}}$	TE and TM polarized planewaves, Eq. (3.15)
ϵ_\pm	planewaves with well-defined helicities, Eq. (3.18)
$\mathbf{B}_{m,\theta_k}^{\pm,\hat{\mathbf{z}}}$	Bessel beams, Eq. (3.22)
$\tilde{\Lambda}_\pm, \Lambda_\pm$	local measures of helicity, Eqs. (3.31,3.44)
I_{RC}, I_{LC}	intensity if right- and left-hand circularly polarized light, Eq. (3.35)
η, η_{tot}	degree of helical polarization, Eqs. (3.33,3.34)

Chapter 4

$\hat{H}_R, \hat{H}_S, \hat{H}_{SR}$	Hamiltonian of the reservoir (e.g. Eq. (4.14b)), system (e.g. Eq. (4.14a)), and reservoir-system interaction (e.g. Eq. (4.14c))
ρ_R, ρ_S	density matrix of the reservoir and the system
Tr_R	partial trace over the elements of reservoir
$\mathcal{L}_{\hat{O}}$	Lindblad-Kossakowski superoperator, Eq. (4.17)
$\hat{\alpha}_\nu$	Raman polarizability (Eq. (4.23))
R_ν, Q_ν^0	Raman tensor and zero-point amplitude of vibrations

\hat{H}_I	plasmon-vibrations interaction Hamiltonian, Eq. (4.33)
g	coupling, Eq. (4.34))
Ω	coherent pumping, Eq. (4.46))
\bar{n}_m^{th}	thermal population of phonons, Eq. (4.47)
ω_m, γ_m	vibrations frequency and decay rate of phonons
ω_c, κ	cavity resonance frequency and decay rate of the cavity
$S(\omega)$	spectrum of emission from the cavity, Eq. (4.50)
Δ	detuning of the coherent pumping
α_s	coherent amplitude of the cavity
ω_S, ω_{aS}	Stokes and anti-Stokes emission frequencies
$g_{\Gamma_1\Gamma_2}^{(2)}(\omega_1, \omega_2; \tau)$	two-photon frequency-resolved correlator, Eq. (4.59)

Bibliography

- [1] Prum, R., Quinn, T., and Torres, R. Anatomically diverse butterfly scales all produce structural colours by coherent scattering. *J. Exp. Biol.*, 209(4):748–765, 2006.
- [2] Schenk, F., Wilts, B., and Stavenga, D. The japanese jewel beetle: a painter’s challenge. *Bioinspir. Biomim.*, 8(4):045002, 2013.
- [3] Prum, R. and Torres, R. Structural colouration of mammalian skin: convergent evolution of coherently scattering dermal collagen arrays. *J. Exp. Biol.*, 207(12): 2157–2172, 2004.
- [4] Novotny, L. and Van Hulst, N. Antennas for light. *Nat. Photon.*, 5(2):83–90, 2011.
- [5] Xu, H., Aizpurua, J., Käll, M., and Apell, P. Electromagnetic contributions to single-molecule sensitivity in surface-enhanced Raman scattering. *Phys. Rev. E*, 62(3):4318, 2000.
- [6] Novikov, S. M., Sánchez-Iglesias, A., Schmidt, M. K., Chuvilin, A., Aizpurua, J., Grzelczak, M., and Liz-Marzán, L. M. Gold spiky nanodumbbells: Anisotropy in gold nanostars. *Part. Part. Syst. Char.*, 31(1):77–80, 2014.
- [7] Albella, P., Poyli, M., Schmidt, M., Maier, S., Moreno, F., Saáenz, J., and Aizpurua, J. Low-loss electric and magnetic field-enhanced spectroscopy with subwavelength silicon dimers. *J. Phys. Chem. C*, 117(26):13573–13584, 2013.
- [8] Fu, Y., Kuznetsov, A., Miroshnichenko, A., Yu, Y., and Luk’yanchuk, B. Directional visible light scattering by silicon nanoparticles. *Nat. Comm.*, 4:1527, 2013.
- [9] Curto, A. G., Volpe, G., Taminiau, T. H., Kreuzer, M. P., Quidant, R., and van Hulst, N. F. Unidirectional emission of a quantum dot coupled to a nanoantenna. *Science*, 329(5994):930–933, 2010.

- [10] Geffrin, J., García-Cámara, B., Gómez-Medina, R., Albella, P., Froufe-Pérez, L. S., Eyraud, C., Litman, A., Vaillon, R., González, F., Nieto-Vesperinas, M., Sáenz, J., and Moreno, F. Magnetic and electric coherence in forward- and back-scattered electromagnetic waves by a single dielectric subwavelength sphere. *Nat. Comm.*, 3:1171, 2012.
- [11] Gómez-Medina, R., García-Cámara, B., Suárez-Lacalle, I., González, F., Moreno, F., Nieto-Vesperinas, M., and Sáenz, J. Electric and magnetic dipolar response of germanium nanospheres: interference effects, scattering anisotropy, and optical forces. *J. Nanophotonics*, 5(1):053512, 2011.
- [12] Kerker, M., Wang, D., and Giles, C. Electromagnetic scattering by magnetic spheres. *J. Opt. Soc. Am.*, 73(6):765–767, 1983.
- [13] Rolly, B., Stout, B., and Bonod, N. Boosting the directivity of optical antennas with magnetic and electric dipolar resonant particles Abstract :. *Opt. Express*, 20(18):20376–20386, 2012.
- [14] Anger, P., Bharadwaj, P., and Novotny, L. Enhancement and Quenching of Single-Molecule Fluorescence. *Phys. Rev. Lett.*, 96(11):113002, 2006.
- [15] Schmidt, M., Esteban, R., Sáenz, J., Suárez-Lacalle, I., Mackowski, S., and Aizpurua, J. Dielectric antennas-a suitable platform for controlling magnetic dipolar emission. *Opt. Express*, 20(13):13636–13650, 2012.
- [16] Schmidt, M. K., Mackowski, S., and Aizpurua, J. Control of single emitter radiation by polarization-and position-dependent activation of dark antenna modes. *Opt. Lett.*, 37(6):1017–1019, 2012.
- [17] Ru, E. C. L. and Etchegoin, P. G. *Principles of Surface-Enhanced Raman Spectroscopy*. Elsevier, Amsterdam, 2009.
- [18] Schmidt, M., Esteban, R., Gonzalez-Tudela, A., Giedke, G., and Aizpurua, J. QED description of Raman scattering from molecules in plasmonic cavities. *arXiv preprint*, 2015. arXiv:1509.03851.
- [19] Stewart, M., Anderton, C., Thompson, L., Maria, J., Gray, S., Rogers, J., and Nuzzo, R. Nanostructured plasmonic sensors. *Chem. Rev.*, 108(2):494–521, 2008.
- [20] Antosiewicz, T., Apell, S., Claudio, V., and Käll, M. A simple model for the resonance shift of localized plasmons due to dielectric particle adhesion. *Opt. Express*, 20(1):524–533, 2012.

-
- [21] Willets, K. and Van Duyne, R. Localized surface plasmon resonance spectroscopy and sensing. *Annu. Rev. Phys. Chem.*, 58:267–297, 2007.
- [22] Xu, H., Wang, X.-H., Persson, M., Xu, H., Käll, M., and Johansson, P. Unified treatment of fluorescence and Raman scattering processes near metal surfaces. *Phys. Rev. Lett.*, 93(24):243002, 2004.
- [23] García-Etxarri, A. and Dionne, J. Surface-enhanced circular dichroism spectroscopy mediated by nonchiral nanoantennas. *Phys. Rev. B*, 87:235409, 2013.
- [24] Knight, M., Sobhani, H., Nordlander, P., and Halas, N. Photodetection with active optical antennas. *Science*, 332(6030):702–704, 2011.
- [25] Chalabi, H., Schoen, D., and Brongersma, M. Hot-electron photodetection with a plasmonic nanostripe antenna. *Nano Lett.*, 14(3):1374–1380, 2014.
- [26] Kelly, K. L., Coronado, E., Zhao, L., and Schatz, G. The optical properties of metal nanoparticles: The influence of size, shape, and dielectric environment. *J. Phys. Chem. B*, 107(3):668–677, 2003.
- [27] Grady, N., Halas, N., and Nordlander, P. Influence of dielectric function properties on the optical response of plasmon resonant metallic nanoparticles. *Chem. Phys. Lett.*, 399(1–3):167 – 171, 2004.
- [28] Bruzzone, S., Malvaldi, M., Arrighini, G., and Guidotti, C. Light scattering by gold nanoparticles: Role of simple dielectric models. *J. Phys. Chem. B*, 108(30):10853–10858, 2004.
- [29] Bryant, G., Garcia de Abajo, F., and Aizpurua, J. Mapping the plasmon resonances of metallic nanoantennas. *Nano Lett.*, 8(2):631–636, 2008.
- [30] Chen, J., Albella, P., Pirzadeh, Z., Alonso-González, P., Huth, F., Bonetti, S., Bonanni, V., Akerman, J., Nogués, J., Vavassori, P., Dmitriev, A., Aizpurua, J., and Hillenbrand, R. Plasmonic nickel nanoantennas. *Small*, 7(16):2341–2347, 2011.
- [31] Zuloaga, J. and Nordlander, P. On the energy shift between near-field and far-field peak intensities in localized plasmon systems. *Nano Lett.*, 11(3):1280–1283, 2011.
- [32] Kats, M. A., Yu, N., Genevet, P., Gaburro, Z., and Capasso, F. Effect of radiation damping on the spectral response of plasmonic components. *Opt. Express*, 19(22):21748–21753, 2011.

- [33] Alonso-González, P., Albella, P., Neubrech, F., Huck, C., Chen, J., Golmar, F., Casanova, F., Hueso, L. E., Pucci, A., Aizpurua, J., and Hillenbrand, R. Experimental verification of the spectral shift between near- and far-field peak intensities of plasmonic infrared nanoantennas. *Phys. Rev. Lett.*, 110:203902, 2013.
- [34] Ginzburg, P. and Zayats, A. V. Non-exponential decay of dark localized surface plasmons. *Opt. Express*, 20(6):6720–6727, 2012.
- [35] García-Etxarri, A., Gómez-Medina, R., Froufe-Pérez, L., López, C., Chantada, L., Scheffold, F., Aizpurua, J., Nieto-Vesperinas, M., and Sáenz, J. Strong magnetic response of submicron silicon particles in the infrared. *Opt. Express*, 19(6):4815–4826, 2011.
- [36] Evlyukhin, A. B., Reinhardt, C., Seidel, A. s., Luk'yanchuk, B. S., and Chichkov, B. N. Optical response features of si-nanoparticle arrays. *Phys. Rev. B*, 82(4):045404, 2010.
- [37] Liu, H., Genov, D., Wu, D., Liu, Y., Liu, Z., Sun, C., Zhu, S., and Zhang, X. Magnetic plasmon hybridization and optical activity at optical frequencies in metallic nanostructures. *Phys. Rev. B*, 76(7):073101, 2007.
- [38] Liu, H., Liu, Y., Li, T., Wang, S., Zhu, S., and Zhang, X. Coupled magnetic plasmons in metamaterials. *Phys. Status Solidi B*, 246(7):1397–1406, 2009.
- [39] Rotenberg, N., Krijger, T., le Feber, B., Spasenović, M., Garcia de Abajo, F., and Kuipers, L. Magnetic and electric response of single subwavelength holes. *Phys. Rev. B*, 88(24):241408, 2013.
- [40] Zhu, W. and Crozier, K. B. Quantum mechanical limit to plasmonic enhancement as observed by surface-enhanced Raman scattering. *Nat. Comm.*, 5, 2014.
- [41] Shalabney, A., George, J., Hutchison, J., Pupillo, G., Genet, C., and Ebbesen, T. W. Coherent coupling of molecular resonators with a microcavity mode. *Nat. Comm.*, 6, 2015.
- [42] Zhang, R., Zhang, Y., Dong, Z., Jiang, S., Zhang, C., Chen, L., Zhang, L., Liao, Y., Aizpurua, J., Luo, Y., Yang, J., and Hou, J. Chemical mapping of a single molecule by plasmon-enhanced Raman scattering. *Nature*, 498(7452):82–86, 2013.
- [43] Hell, S. W. Stefan W. Hell - Nobel Lecture: Nanoscopy with Focused Light, 2014. http://www.nobelprize.org/nobel_prizes/chemistry/laureates/2014/hell-lecture.pdf.

-
- [44] Betzig, E. Eric Betzig - Nobel Lecture: Single Molecules, Cells, and Super-Resolution Optics, 2014. http://www.nobelprize.org/nobel_prizes/chemistry/laureates/2014/betzig-lecture.pdf.
- [45] Bharadwaj, P., Deutsch, B., and Novotny, L. Optical antennas. *Adv. Opt. Photonics*, 1(3):438–483, 2009.
- [46] Olson, J., Dominguez-Medina, S., Hoggard, A., Wang, L., Chang, W., and Link, S. Optical characterization of single plasmonic nanoparticles. *Chem. Soc. Rev.*, 44:40–57, 2015.
- [47] Kinkhabwala, A., Yu, Z., Fan, S., Avlasevich, Y., Müllen, K., and Moerner, W. Large single-molecule fluorescence enhancements produced by a bowtie nanoantenna. *Nat. Photon.*, 3(11):654–657, 2009.
- [48] Muskens, O., Giannini, V., Sanchez-Gil, J., and Gómez Rivas, J. Strong enhancement of the radiative decay rate of emitters by single plasmonic nanoantennas. *Nano Lett.*, 7(9):2871–2875, 2007.
- [49] Alonso-González, P., Albella, P., Schnell, M., Chen, J., Huth, F., García-Etxarri, A., Casanova, F., Golmar, F., Arzubiaga, L., Hueso, L., Aizpurua, J., and Hillenbrand, R. Resolving the electromagnetic mechanism of surface-enhanced light scattering at single hot spots. *Nat. Comm.*, 3:684, 2012.
- [50] Neubrech, F., Pucci, A., Cornelius, T., Karim, S., García-Etxarri, A., and Aizpurua, J. Resonant plasmonic and vibrational coupling in a tailored nanoantenna for infrared detection. *Phys. Rev. Lett.*, 101(15):157403, 2008.
- [51] Kittel, C. *Introduction to solid state physics*. Wiley, 2005.
- [52] Blakemore, J. *Solid state physics*. Cambridge University Press, Cambridge, Great Britain, 2nd edition, 1985.
- [53] Ashcroft, N. and Mermin, N. *Solid State Physics*. Saunders College, Philadelphia, 1976.
- [54] Johnson, P. B. and Christy, R. W. Optical constants of the noble metals. *Phys. Rev. B*, 6(12):4370–4379, 1972.
- [55] Hao, F. and Nordlander, P. Efficient dielectric function for ftd simulation of the optical properties of silver and gold nanoparticles. *Chem. Phys. Lett.*, 446(1–3): 115 – 118, 2007.

- [56] Novotny, L. and Hecht, B. *Principles of nano-optics*. Cambridge university press, 2012.
- [57] Ritchie, R. H. Plasma losses by fast electrons in thin films. *Phys. Rev.*, 106: 874–881, 1957.
- [58] Powell, C. J. and Swan, J. B. Origin of the characteristic electron energy losses in magnesium. *Phys. Rev.*, 116:81–83, 1959.
- [59] Powell, C. J. and Swan, J. B. Origin of the characteristic electron energy losses in aluminum. *Phys. Rev.*, 115:869–875, 1959.
- [60] Stern, E. A. and Ferrell, R. A. Surface plasma oscillations of a degenerate electron gas. *Phys. Rev.*, 120:130–136, 1960.
- [61] Pitarke, J., Silkin, V., Chulkov, E., and Echenique, P. Theory of surface plasmons and surface-plasmon polaritons. *Rep. Prog. Phys.*, 70(1):1, 2007.
- [62] Teng, Y.-Y. and Stern, E. Plasma radiation from metal grating surfaces. *Phys. Rev. Lett.*, 19:511–514, 1967.
- [63] Barnes, W., Dereux, A., and Ebbesen, T. W. Surface plasmon subwavelength optics. *Nature*, 424(6950):824–830, 2003.
- [64] Moskovits, M. Surface-enhanced spectroscopy. *Rev. Mod. Phys.*, 57(3):783, 1985.
- [65] Raschke, G., Kowarik, S., Franzl, T., Sönnichsen, C., Klar, T., Feldmann, J., Nichtl, A., and Kürzinger, K. Biomolecular recognition based on single gold nanoparticle light scattering. *Nano Lett.*, 3(7):935–938, 2003.
- [66] Anker, J. N., Hall, W., Lyandres, O., Shah, N. C., Zhao, J., and Van Duyne, R. P. Biosensing with plasmonic nanosensors. *Nat. Mater.*, 7(6):442–453, 2008.
- [67] Van Duyne, R. P., Haes, A. J., and McFarland, A. D. Nanoparticle optics: sensing with nanoparticle arrays and single nanoparticles. In *Proceedings of SPIE*, volume 5223, pages 197–207, 2003.
- [68] Juan, M., Righini, M., and Quidant, R. Plasmon nano-optical tweezers. *Nat. Photon.*, 5(6):349–356, 2011.
- [69] Maragò, O. M., Jones, P. H., Gucciardi, P. G., Volpe, G., and Ferrari, A. C. Optical trapping and manipulation of nanostructures. *Nat. Nanotech.*, 8(11):807–819, 2013.

-
- [70] Mie, G. Beiträge zur optik trüber medien, speziell kolloidaler metallösungen. *Annalen der Physik*, 330(3):377–445, 1908.
- [71] Prodan, E., Radloff, C., Halas, N., and Nordlander, P. A hybridization model for the plasmon response of complex nanostructures. *Science*, 302(5644):419–422, 2003.
- [72] Nordlander, P., Oubre, C., Prodan, E., Li, K., and Stockman, M. Plasmon hybridization in nanoparticle dimers. *Nano Lett.*, 4(5):899–903, 2004.
- [73] Rudin, S. and Reinecke, T. Oscillator model for vacuum rabi splitting in microcavities. *Phys. Rev. B*, 59:10227–10233, 1999.
- [74] Schlather, A. E., Large, N., Urban, A. S., Nordlander, P., and Halas, N. J. Near-field mediated plexcitonic coupling and giant rabi splitting in individual metallic dimers. *Nano Lett.*, 13(7):3281–3286, 2013.
- [75] Choe, J.-H., Kang, J.-H., Kim, D.-S., and Park, Q.-H. Slot antenna as a bound charge oscillator. *Opt. Express*, 20(6):6521–6526, 2012.
- [76] Li, Y., Zhao, K., Sobhani, H., Bao, K., and Nordlander, P. Geometric dependence of the line width of localized surface plasmon resonances. *J. Phys. Chem. Lett.*, 4(8):1352–1357, 2013.
- [77] Draine, B. The discrete-dipole approximation and its application to interstellar graphite grains. *Astrophys. J.*, 333:848–872, 1988.
- [78] Jackson, J. D. *Classical electrodynamics*. Wiley, New York, 1962.
- [79] Meier, M. and Wokaun, A. Enhanced fields on large metal particles: dynamic depolarization. *Opt. Lett.*, 8(11):581–583, 1983.
- [80] Moroz, A. Depolarization field of spheroidal particles. *J. Opt. Soc. Am. B*, 26(3):517–527, 2009.
- [81] Draine, B. T. and Flatau, P. J. Discrete-dipole approximation for scattering calculations. *J. Opt. Soc. Am.*, 11(4):1491–1499, 1994.
- [82] Zorić, I., Zäch, M., Kasemo, B., and Langhammer, C. Gold, platinum, and aluminum nanodisk plasmons: Material independence, subradiance, and damping mechanisms. *ACS Nano*, 5(4):2535–2546, 2011.
- [83] Lumerical Solutions, Inc. <http://www.lumerical.com/tcad-products/fdtd/>.

- [84] Sönnichsen, C., Franzl, T., Wilk, T., von Plessen, G., Feldmann, J., Wilson, O., and Mulvaney, P. Drastic reduction of plasmon damping in gold nanorods. *Phys. Rev. Lett.*, 88:077402, 2002.
- [85] Kelkensberg, F., Koenderink, A. F., and Vrakking, M. J. J. Attosecond streaking in a nano-plasmonic field. *New J. Phys.*, 14(9):093034, 2012.
- [86] Süßmann, F. and Kling, M. Attosecond nanoplasmonic streaking of localized fields near metal nanospheres. *Phys. Rev. B*, 84:121406, 2011.
- [87] Prell, J., Borja, L., Neumark, D., and Leone, S. Simulation of attosecond-resolved imaging of the plasmon electric field in metallic nanoparticles. *Annalen der Physik*, 525(1-2):151–161, 2013.
- [88] Marsell, E., Losquin, A., Svärd, R., Miranda, M., Guo, C., Harth, A., Lorek, E., Mauritsson, J., Arnold, C., Xu, H., L’Huillier, A., and Mikkelsen, A. Nanoscale imaging of local few-femtosecond near-field dynamics within a single plasmonic nanoantenna. *Nano Lett.*, 15(10):6601–6608, 2015.
- [89] Dombi, P. and Elezzabi, A. Ultrafast, strong-field plasmonic phenomena. *Attosecond Nanophysics: From Basic Science to Applications*, pages 39–86, 2015.
- [90] Armani, D., Kippenberg, T., Spillane, S., and Vahala, K. Ultra-high-q toroid microcavity on a chip. *Nature*, 421(6926):925–928, 2003.
- [91] Vahala, K. *Optical microcavities*. World Scientific, 2004.
- [92] Aoki, T., Dayan, B., Wilcut, E., Bowen, W. P., Parkins, A. S., Kippenberg, T., Vahala, K., and Kimble, H. Observation of strong coupling between one atom and a monolithic microresonator. *Nature*, 443(7112):671–674, 2006.
- [93] Schliesser, A., Del’Haye, P., Nooshi, N., Vahala, K., and Kippenberg, T. Radiation pressure cooling of a micromechanical oscillator using dynamical backaction. *Phys. Rev. Lett.*, 97(24):243905, 2006.
- [94] Rakovich, Y. and Donegan, J. Photonic atoms and molecules. *Laser Photon. Rev.*, 4(2):179–191, 2010.
- [95] Staude, I., Miroshnichenko, A. E., Decker, M., Fofang, N. T., Liu, S., Gonzales, E., Dominguez, J., Luk, T., Neshev, D., Brener, I., and Kivshar, Y. Tailoring directional scattering through magnetic and electric resonances in subwavelength silicon nanodisks. *ACS Nano*, 7(9):7824–7832, 2013.

-
- [96] Rolly, B., Stout, B., and Bonod, N. Boosting the directivity of optical antennas with magnetic and electric dipolar resonant particles. *Opt. Express*, 20(18):20376–20386, 2012.
- [97] Caldarola, M., Albella, P., Cortés, E., Rahmani, M., Roschuk, T., Grinblat, G., Oulton, R., Bragas, A., and Maier, S. Non-plasmonic nanoantennas for surface enhanced spectroscopies with ultra-low heat conversion. *Nat. Comm.*, 6, 2015.
- [98] Karaveli, S. and Zia, R. Spectral tuning by selective enhancement of electric and magnetic dipole emission. *Phys. Rev. Lett.*, 106(19), 2011.
- [99] Drexhage, K. Interaction of light with monomolecular dye layers. volume 12 of *Progress in Optics*, pages 163 – 232. Elsevier, 1974.
- [100] Kunz, R. E. and Lukosz, W. Changes in fluorescence lifetimes induced by variable optical environments. *Phys. Rev. B*, 21:4814–4828, 1980.
- [101] Johnson, P. B. and Christy, R. W. Optical constants of the noble metals. *Phys. Rev. B*, 6:4370–4379, 1972.
- [102] Liu, N., Fu, L., Kaiser, S., Schweizer, H., and Giessen, H. Plasmonic building blocks for magnetic molecules in three-dimensional optical metamaterials. *Adv. Mater.*, 20(20):3859–3865, 2008.
- [103] Markel, V. Coupled-dipole approach to scattering of light from a one-dimensional periodic dipole structure. *J. Mod. Opt.*, 40(11):2281–2291, 1993.
- [104] Mulholland, G., Bohren, C., and Fuller, K. Light scattering by agglomerates: coupled electric and magnetic dipole method. *Langmuir*, 10(8):2533–2546, 1994.
- [105] Chaumet, P. and Nieto-Vesperinas, M. Coupled dipole method determination of the electromagnetic force on a particle over a flat dielectric substrate. *Phys. Rev. B*, 61(20):14119, 2000.
- [106] Tai, C. *Dyadic Green Functions in Electromagnetic Theory*. 2nd edition, IEEE Press, New York, 1993.
- [107] Hopkins, B., Filonov, D., Glybovski, S., and Miroshnichenko, A. Hybridization and the origin of fano resonances in symmetric nanoparticle trimers. *Phys. Rev. B*, 92:045433, 2015.

- [108] Sheikholeslami, S., García-Etxarri, A., and Dionne, J. Controlling the interplay of electric and magnetic modes via fano-like plasmon resonances. *Nano Lett.*, 11(9):3927–3934, 2011.
- [109] Hopkins, B., Filonov, D. S., Miroshnichenko, A. E., Monticone, F., Alù, A., and Kivshar, Y. S. Interplay of magnetic responses in all-dielectric oligomers to realize magnetic fano resonances. *ACS Photonics*, 2(6):724–729, 2015.
- [110] Zywietz, U., Evlyukhin, A. B., Reinhardt, C., and Chichkov, B. N. Laser printing of silicon nanoparticles with resonant optical electric and magnetic responses. *Nat. Commun.*, 5:3402, 2014.
- [111] Evlyukhin, A. B., Novikov, S. M., Zywietz, U., Eriksen, R. L., Reinhardt, C., Bozhevolnyi, S. I., and Chichkov, B. N. Demonstration of magnetic dipole resonances of dielectric nanospheres in the visible region. *Nano Lett.*, 12(7):3749–3755, 2012.
- [112] Palik, E. D. *Handbook of Optical Constants of Solids*. Academic Press, 1997.
- [113] Barnett, S. and Loudon, R. Sum Rule for Modified Spontaneous Emission Rates. *Phys. Rev. Lett.*, 77(12):2444–2446, 1996.
- [114] Carminati, R. and Sáenz, J. Density of States and Extinction Mean Free Path of Waves in Random Media: Dispersion Relations and Sum Rules. *Phys. Rev. Lett.*, 102(9):093902, 2009.
- [115] Bayer, M., Reinecke, T. L., Weidner, F., Larionov, A., McDonald, A., and Forchel, A. Inhibition and enhancement of the spontaneous emission of quantum dots in structured microresonators. *Phys. Rev. Lett.*, 86:3168–3171, 2001.
- [116] Lodahl, P., Van Driel, A., Nikolaev, I., Irman, A., Overgaag, K., Vanmaekelbergh, D., and Vos, W. Controlling the dynamics of spontaneous emission from quantum dots by photonic crystals. *Nature*, 430(7000):654–657, 2004.
- [117] Bohren, C. and Huffman, D. *Absorption and scattering of light by small particles*. John Wiley & Sons, 2008.
- [118] Zambrana-Puyalto, X. *Control and characterization of nano-structures with the symmetries of light*. PhD thesis, Macquarie University, 2014.

-
- [119] Fernandez-Corbaton, I., Zambrana-Puyalto, X., Tischler, N., Vidal, X., Juan, M., and Molina-Terriza, G. Electromagnetic duality symmetry and helicity conservation for the macroscopic Maxwell's equations. *Phys. Rev. Lett.*, 111(6):060401, 2013.
- [120] Schmidt, M., Aizpurua, J., Zambrana-Puyalto, X., Vidal, X., Molina-Terriza, G., and Sáenz, J. Isotropically polarized speckle patterns. *Phys. Rev. Lett.*, 114:113902, 2015.
- [121] Dainty, J. *Laser speckle and related phenomena*. Springer-Verlag, 1984.
- [122] Goodman, J. *Speckle Phenomena in Optics: Theory and Applications*. Roberts & Company, 2010.
- [123] Carswell, A. and Pal, S. Polarization anisotropy in lidar multiple scattering from clouds. *Appl. Opt.*, 19(24):4123–4126, 1980.
- [124] Kuga, Y. and Ishimaru, A. Retroreflectance from a dense distribution of spherical particles. *J. Opt. Soc. Am. A*, 1(8):831–835, 1984.
- [125] Van Albada, M. and Lagendijk, A. Observation of weak localization of light in a random medium. *Phys. Rev. Lett.*, 55(24):2692, 1985.
- [126] Wolf, P.-E. and Maret, G. Weak localization and coherent backscattering of photons in disordered media. *Phys. Rev. Lett.*, 55(24):2696, 1985.
- [127] Lenke, R. and Maret, G. *Multiple scattering of light: coherent backscattering and transmission*. CRC Press, 2000.
- [128] Moscoso, M., Keller, J., and Papanicolaou, G. Depolarization and blurring of optical images by biological tissue. *J. Opt. Soc. Am. A*, 18(4):948–960, 2001.
- [129] Angelsky, O., Ushenko, A., Ushenko, Y. A., and Ushenko, Y. G. Polarization singularities of the object field of skin surface. *J. Phys. D: Appl. Phys.*, 39(16):3547, 2006.
- [130] Pierangelo, A., Benali, A., Antonelli, M.-R., Novikova, T., Validire, P., Gayet, B., and De Martino, A. Ex-vivo characterization of human colon cancer by mueller polarimetric imaging. *Opt. Express*, 19(2):1582–1593, 2011.
- [131] Zerrad, M., Sorrentini, J., Soriano, G., and Amra, . Gradual loss of polarization in light scattered from rough surfaces: Electromagnetic prediction. *Opt. Express*, 18(15):15832–15843, 2010.

- [132] Schwartz, C. and Dogariu, A. Backscattered polarization patterns, optical vortices, and the angular momentum of light. *Opt. Lett.*, 31(8):1121–1123, 2006.
- [133] Flossmann, F., OHolleran, K., Dennis, M., and Padgett, M. Polarization singularities in 2d and 3d speckle fields. *Phys. Rev. Lett.*, 100(20):203902, 2008.
- [134] Bicout, D., Brosseau, C., Martinez, A., and Schmitt, J. Depolarization of multiply scattered waves by spherical diffusers: Influence of the size parameter. *Phys. Rev. E*, 49(2):1767, 1994.
- [135] Gorodnichev, E., Kuzovlev, A., and Rogozkin, D. Diffusion of circularly polarized light in a disordered medium with large-scale inhomogeneities. *J. Exp. Theor. Phys. Lett.*, 68(1):22–28, 1998.
- [136] Rojas-Ochoa, L., Lacoste, D., Lenke, R., Schurtenberger, P., and Scheffold, F. Depolarization of backscattered linearly polarized light. *J. Opt. Soc. Am. A*, 21(9):1799–1804, 2004.
- [137] Nieto-Vesperinas, M., Gomez-Medina, R., and Sáenz, J. J. Angle-suppressed scattering and optical forces on submicrometer dielectric particles. *J. Opt. Soc. Am. A*, 28(1):54–60, 2011.
- [138] Gómez-Medina, R., García-Cámara, B., Suárez-Lacalle, I., González, F., Moreno, F., Nieto-Vesperinas, M., and Sáenz, J. J. Electric and magnetic dipolar response of germanium nanospheres: interference effects, scattering anisotropy, and optical forces. *J. Nanophotonics*, 5(1):053512–053512, 2011.
- [139] Person, S., Jain, M., Lapin, Z., Sáenz, J., Wicks, G., and Novotny, L. Demonstration of zero optical backscattering from single nanoparticles. *Nano Lett.*, 13(4):1806–1809, 2013.
- [140] Zambrana-Puyalto, X., Vidal, X., Juan, M., and Molina-Terriza, G. Dual and anti-dual modes in dielectric spheres. *Opt. Express*, 21(15):17520–17530, 2013.
- [141] Kerker, M., Wang, D.-S., and Giles, C. Electromagnetic scattering by magnetic spheres. *J. Opt. Soc. Am.*, 73(6):765–767, 1983.
- [142] Zambrana-Puyalto, X., Fernandez-Corbaton, I., Juan, M., Vidal, X., and Molina-Terriza, G. Duality symmetry and Kerker conditions. *Opt. Lett.*, 38(11):1857–1859, 2013.

-
- [143] Zambrana-Puyalto, X., Vidal, X., Juan, M. L., and Molina-Terriza, G. . Dual and anti-dual modes in dielectric spheres. *Opt. Express*, 21(15):17520–17530, 2013.
- [144] Commercial offer by MKNano (division of M K Impex Corp.), (private communication).
- [145] Wiersma, D. The physics and applications of random lasers. *Nat. Phys.*, 4(5):359–367, 2008.
- [146] Gottardo, S., Sapienza, R., Garcia, P., Blanco, A., Wiersma, D., and López, C. Resonance-driven random lasing. *Nat. Photon.*, 2(7):429–432, 2008.
- [147] Karaveli, S. and Zia, R. Spectral tuning by selective enhancement of electric and magnetic dipole emission. *Phys. Rev. Lett.*, 106:193004, 2011.
- [148] Akimov, A., Mukherjee, A., Yu, C., Chang, D., Zibrov, A., Hemmer, P., Park, H., and Lukin, M. Generation of single optical plasmons in metallic nanowires coupled to quantum dots. *Nature*, 450(7168):402–406, 2007.
- [149] Kneipp, K., Wang, Y., Kneipp, H., Perelman, L., Itzkan, I., Dasari, R., and Feld, M. Single molecule detection using surface-enhanced Raman scattering (SERS). *Phys. Rev. Lett.*, 78(9):1667, 1997.
- [150] Kneipp, K., Kneipp, H., Kartha, V., Manoharan, R., Deinum, G., Itzkan, I., Dasari, R. R., and Feld, M. Detection and identification of a single dna base molecule using surface-enhanced Raman scattering (SERS). *Phys. Rev. E*, 57(6):R6281, 1998.
- [151] Kerker, M. Electromagnetic model for surface-enhanced Raman scattering (SERS) on metal colloids. *Acc. Chem. Res*, 17(8):271–277, 1984.
- [152] Moskovits, M. Surface-enhanced Raman spectroscopy: a brief retrospective. *J. Raman Spectrosc.*, 36(6-7):485–496, 2005.
- [153] Kneipp, K., Wang, Y., Kneipp, H., Itzkan, I., Dasari, R., and Feld, M. Population pumping of excited vibrational states by spontaneous surface-enhanced Raman scattering. *Phys. Rev. Lett.*, 76:2444–2447, 1996.
- [154] García-Vidal, F. J. and Pendry, J. B. Collective theory for surface enhanced Raman scattering. *Phys. Rev. Lett.*, 77:1163–1166, 1996.
- [155] Petruccione, F. and Breuer, H.-P. *The theory of open quantum systems*. Oxford university press, 2002.

- [156] Carmichael, H. J. *Statistical Methods in Quantum Optics 1: Master Equation and Fokker-Planck Equations*, volume 1. Springer Science & Business Media, 2002.
- [157] Chang, T.-M. and Skinner, J. Non-markovian population and phase relaxation and absorption lineshape for a two-level system strongly coupled to a harmonic quantum bath. *Physica A*, 193(3):483 – 539, 1993.
- [158] Lewenstein, M., Zakrzewski, J., and Mossberg, T. W. Spontaneous emission of atoms coupled to frequency-dependent reservoirs. *Phys. Rev. A*, 38:808–819, 1988.
- [159] Lewenstein, M., Zakrzewski, J., Mossberg, T. W., and Mostowski, J. Non-exponential spontaneous decay in cavities and waveguides. *J. Phys. B*, 21(2): L9, 1988.
- [160] Galland, C., Högele, A., Türeci, H. E., and Imamoglu, A. m. c. Non-markovian decoherence of localized nanotube excitons by acoustic phonons. *Phys. Rev. Lett.*, 101:067402, 2008.
- [161] Gorini, V., Kossakowski, A., and Sudarshan, E. C. G. Completely positive dynamical semigroups of n-level systems. *J. Math. Phys.*, 17(5):821–825, 1976.
- [162] Lindblad, G. On the generators of quantum dynamical semigroups. *Commun. Math. Phys.*, 48(2):119–130, 1976.
- [163] Sharma, B., Frontiera, R. R., Henry, A.-I., Ringe, E., and Van Duyne, R. P. SERS: materials, applications, and the future. *Materials Today*, 15(1):16–25, 2012.
- [164] Johansson, P., Xu, H., and Käll, M. Surface-enhanced Raman scattering and fluorescence near metal nanoparticles. *Phys. Rev. B*, 72:035427, 2005.
- [165] Bougeard, D. and Smirnov, K. S. Calculation of off-resonance Raman scattering intensities with parametric models. *J. Raman*, 40(12):1704–1719, 2009.
- [166] Fox, M. *Quantum Optics: An Introduction*, volume 6. Oxford university press, 2006.
- [167] González Tudela, A. *Dynamics of open quantum systems: excitons, cavities and surface plasmons*. PhD thesis, Universidad Autonoma de Madrid, 2013.
- [168] Huttner, B. and Barnett, S. M. Quantization of the electromagnetic field in dielectrics. *Phys. Rev. A*, 46:4306–4322, 1992.

-
- [169] Gruner, T. and Welsch, D.-G. Green-function approach to the radiation-field quantization for homogeneous and inhomogeneous kramers-kronig dielectrics. *Phys. Rev. A*, 53:1818–1829, 1996.
- [170] Scheel, S. and Buhmann, S. Y. Macroscopic quantum electrodynamics—concepts and applications. *Acta Phys. Slovaca*, 58(5):675–809, 2008.
- [171] González-Tudela, A., Huidobro, P. A., Martín-Moreno, L., Tejedor, C., and García-Vidal, F. J. Reversible dynamics of single quantum emitters near metal-dielectric interfaces. *Phys. Rev. B*, 89:041402, 2014.
- [172] Huidobro, P. *Frontiers in plasmonics: transformation optics, magnetic plasmons, brownian ratchets and quantum phenomena*. PhD thesis, Universidad Autónoma de Madrid, 2013.
- [173] Auffèves, A., Gerace, D., Gérard, J.-M., Santos, M. F. m. c., Andreani, L. C., and Poizat, J.-P. Controlling the dynamics of a coupled atom-cavity system by pure dephasing. *Phys. Rev. B*, 81:245419, 2010.
- [174] Delga, A., Feist, J., Bravo-Abad, J., and Garcia-Vidal, F. J. Quantum emitters near a metal nanoparticle: Strong coupling and quenching. *Phys. Rev. Lett.*, 112:253601, 2014.
- [175] Delga, A., Feist, J., Bravo-Abad, J., and Garcia-Vidal, F. J. Theory of strong coupling between quantum emitters and localized surface plasmons. *J. Opt.*, 16(11):114018, 2014.
- [176] Maier, S. A. Plasmonic field enhancement and sers in the effective mode volume picture. *Opt. Express*, 14(5):1957–1964, 2006.
- [177] Koenderink, A. F. On the use of purcell factors for plasmon antennas. *Opt. Lett.*, 35(24):4208–4210, 2010.
- [178] Gerry, C. and Knight, P. *Introductory quantum optics*. Cambridge university press, 2005.
- [179] Roelli, P., Galland, C., Piro, N., and Kippenberg, T. J. Molecular cavity optomechanics: a theory of plasmon-enhanced Raman scattering. *arXiv preprint arXiv:1407.1518*, 2014.
- [180] Laussy, F. P., del Valle, E., and Tejedor, C. Luminescence spectra of quantum dots in microcavities. i. bosons. *Phys. Rev. B*, 79:235325, 2009.

- [181] del Valle, E., Laussy, F., and Tejedor, C. Luminescence spectra of quantum dots in microcavities. ii. fermions. *Phys. Rev. B*, 79:235326, 2009.
- [182] Hümmer, T., García-Vidal, F. J., Martín-Moreno, L., and Zueco, D. Weak and strong coupling regimes in plasmonic QED. *Phys. Rev. B*, 87:115419, 2013.
- [183] Esteban, R., Aizpurua, J., and Bryant, G. W. Strong coupling of single emitters interacting with phononic infrared antennae. *New J. Phys.*, 16(1):013052, 2014.
- [184] Esteban, R., Teperik, T. V., and Greffet, J. J. Optical patch antennas for single photon emission using surface plasmon resonances. *Phys. Rev. Lett.*, 104:026802, 2010.
- [185] Chen, X.-W., Agio, M., and Sandoghdar, V. Metallodielectric hybrid antennas for ultrastrong enhancement of spontaneous emission. *Phys. Rev. Lett.*, 108(23):233001, 2012.
- [186] Liu, M., Lee, T.-W., Gray, S. K., Guyot-Sionnest, P., and Pelton, M. Excitation of dark plasmons in metal nanoparticles by a localized emitter. *Phys. Rev. Lett.*, 102(10):107401, 2009.
- [187] Zeng, X., Yu, W., Yao, P., Xi, Z., Lu, Y., and Wang, P. Metallo-dielectric hybrid antenna for high purcell factor and radiation efficiency. *Opt. Express*, 22(12):14517–14523, 2014.
- [188] Watanabe, H., Hayazawa, N., Inouye, Y., and Kawata, S. DFT vibrational calculations of Rhodamine 6G adsorbed on silver: Analysis of tip-enhanced Raman spectroscopy. *J. Phys. Chem. B*, 109(11):5012–5020, 2005.
- [189] Gupta, V., Smirnov, K. S., Bougeard, D., and Tandon, P. Electro-optical parameters for computation of nonresonance Raman scattering intensities of peptides. *J. Chem. Theory Comput.*, 5(5):1369–1379, 2009.
- [190] Honea, E., Ogura, A., Murray, C., Raghavachari, K., Sprenger, W. O., Jarrold, M., and Brown, W. Raman spectra of size-selected silicon clusters and comparison with calculated structures. *Nature*, 366(6450):42–44, 1993.
- [191] Barbry, M., Koval, P., Marchesin, F., Esteban, R., Borisov, A. G., Aizpurua, J., and Sánchez-Portal, D. Atomistic near-field nanoplasmonics: Reaching atomic-scale resolution in nanooptics. *Nano Lett.*, 15(5):3410–3419, 2015.

-
- [192] Yampolsky, S., Fishman, D. A., Dey, S., Hulkko, E., Banik, M., Potma, E. O., and Apkarian, V. A. Seeing a single molecule vibrate through time-resolved coherent anti-stokes Raman scattering. *Nat. Photon.*, 8(8):650–656, 2014.
- [193] Navarrete-Benlloch, C. Open systems dynamics: Simulating master equations in the computer. *arXiv preprint arXiv:1504.05266*, 2015.
- [194] Glauber, R. J. Photon correlations. *Phys. Rev. Lett.*, 10:84, 1963.
- [195] Maher, R., Etchegoin, P., Le Ru, E., and Cohen, L. A conclusive demonstration of vibrational pumping under surface enhanced Raman scattering conditions. *J. Phys. Chem. B*, 110(24):11757–11760, 2006.
- [196] Aspelmeyer, M., Kippenberg, T. J., and Marquardt, F. Cavity optomechanics. *Rev. Mod. Phys.*, 86:1391–1452, 2014.
- [197] Wang, C.-S. Theory of stimulated Raman scattering. *Phys. Rev.*, 182:482–494, 1969.
- [198] Becker, P., Bohatý, L., Rhee, H., Eichler, H., Hanuza, J., and Kaminskii, A. Observation of many-phonon stimulated Raman scattering and related cascaded nonlinear-laser effects in monoclinic LaBO₂ MoO₄ single crystals. *Laser Phys. Lett.*, 5(2):114, 2008.
- [199] Rabl, P. Photon blockade effect in optomechanical systems. *Phys. Rev. Lett.*, 107:063601, 2011.
- [200] Nunnenkamp, A., Børkje, K., and Girvin, S. M. Single-photon optomechanics. *Phys. Rev. Lett.*, 107:063602, 2011.
- [201] del Valle, E., González-Tudela, A., Laussy, F. P., Tejedor, C., and Hartmann, M. J. Theory of frequency-filtered and time-resolved n -photon correlations. *Phys. Rev. Lett.*, 109:183601, 2012.
- [202] Cohen-Tannoudji, C. and Reynaud, S. Atoms in strong light-fields: Photon antibunching in single atom fluorescence. *Phil. Trans. R. Soc. Lond. A*, 293:223, 1979.
- [203] Silva, B., González-Tudela, A., Munoz, C. S., Ballarini, D., Gigli, G., West, K. W., Pfeiffer, L., del Valle, E., Sanvitto, D., and Laussy, F. P. Measuring photon correlations simultaneously in time and frequency. *arXiv:1406.0964*, 2014.

- [204] Hanbury Brown, R. and Twiss, R. Q. A test of a new type of stellar interferometer on Sirius. *Nature*, 178:1046, 1956.
- [205] Glauber, R. J., Kleber, M., Patnaik, A. K., Scully, M. O., and Walther, H. A simple study of photon correlations from hanbury-brown and twiss to einstein, podolsky, rosen and beyond. *J. Phys. B.: At. Mol. Phys.*, 38:S521, 2005.
- [206] González-Tudela, A., Laussy, F. P., Tejedor, C., Hartmann, M. J., and del Valle, E. Two-photon spectra of quantum emitters. *New J. Phys.*, 15:033036, 2013.
- [207] del Valle, E. Distilling one, two and entangled pairs of photons from a quantum dot with cavity QED effects and spectral filtering. *New J. Phys.*, 15:025019, 2013.
- [208] Sanchez Muñoz, C., del Valle, E., Tejedor, C., and Laussy, F. Violation of classical inequalities by photon frequency filtering. *Phys. Rev. A*, 90:052111, 2014.
- [209] González-Tudela, A., del Valle, E., and Laussy, F. P. Optimization of photon correlations by frequency filtering. *Phys. Rev. A*, 91:043807, 2015.
- [210] Kasperczyk, M., Jorio, A., Neu, E., Maletinsky, P., and Novotny, L. Stokes-anti-Stokes correlations in diamond. *Opt. Lett.*, 40(10):2393–2396, 2015.
- [211] Schliesser, A., Rivière, R., Anetsberger, G., Arcizet, O., and Kippenberg, T. Resolved-sideband cooling of a micromechanical oscillator. *Nat. Phys.*, 4(5):415–419, 2008.
- [212] Kleckner, D., Pepper, B., Jeffrey, E., Sonin, P., Thon, S., and Bouwmeester, D. Optomechanical trampoline resonators. *Opt. Express*, 19(20):19708–19716, 2011.
- [213] Schleier-Smith, M., Leroux, I., Zhang, H., Van Camp, M., and Vuletić, V. Optomechanical cavity cooling of an atomic ensemble. *Phys. Rev. Lett.*, 107(14):143005, 2011.
- [214] Zywietz, U., Schmidt, M., Evlyukhin, A., Reinhardt, C., Aizpurua, J., and Chichkov, B. Electromagnetic resonances of silicon nanoparticle dimers in the visible. *ACS Photonics*, 2(7):913–920, 2015.
- [215] Bakker, R., Permyakov, D., Yu, Y. F., Markovich, D., Paniagua-Domínguez, R., Gonzaga, L., Samusev, A., Kivshar, Y., Luk’yanchuk, B., and Kuznetsov, A. Magnetic and electric hotspots with silicon nanodimers. *Nano Lett.*, 15(3):2137–2142, 2015.

-
- [216] Traviss, D., Schmidt, M., Aizpurua, J., and Muskens, O. Antenna resonances in low aspect ratio semiconductor nanowires. *Opt. Express*, 23(17):22771–22787, 2015.
- [217] Abujetas, D. R., Paniagua-Domínguez, R., and Sánchez-Gil, J. A. Unraveling the Janus role of Mie resonances and leaky/guided modes in semiconductor nanowire absorption for enhanced light harvesting. *ACS Photonics*, 2(7):921–929, 2015.
- [218] Arbabi, A., Horie, Y., Bagheri, M., and Faraon, A. Dielectric metasurfaces for complete control of phase and polarization with subwavelength spatial resolution and high transmission. *Nat. Nanotech.*, 10:937–943, 2015.
- [219] Ruppin, R. Decay of an excited molecule near a small metal sphere. *J. Chem. Phys.*, 76(4):1681, 1982.
- [220] Mertens, H., Koenderink, A., and Polman, A. Plasmon-enhanced luminescence near noble-metal nanospheres: Comparison of exact theory and an improved Gersten and Nitzan model. *Phys. Rev. B*, 76(11):115123, 2007.
- [221] Kerker, M., Wang, D.-S., and Chew, H. Surface enhanced Raman scattering (SERS) by molecules adsorbed at spherical particles: errata. *Appl. Opt.*, 19(24):4159–4174, 1980.
- [222] Chung, H. Y., Leung, P. T., and Tsai, D. P. Equivalence between the mechanical model and energy-transfer theory for the classical decay rates of molecules near a spherical particle. *J. Chem. Phys.*, 136(18):184106, 2012.
- [223] Zywiets, U., Reinhardt, C., Evlyukhin, A. B., Birr, T., and Chichkov, B. N. Generation and patterning of si nanoparticles by femtosecond laser pulses. *Appl. Phys. A: Mater. Sci. Process.*, 114(1):45–50, 2014.
- [224] Olejnik, M., Brotosudarmo, T., Schmidt, M., Czechowski, N., Piatkowski, D., Aizpurua, J., Cogdell, R., Heiss, W., Mackowski, S., et al. Polarization control of metal-enhanced fluorescence in hybrid assemblies of photosynthetic complexes and gold nanorods. *Phys. Chem. Chem. Phys.*, 16(19):9015–9022, 2014.
- [225] Schmidt, M.K. and Aizpurua, J. Nanocavities: Optomechanics goes molecular. doi:10.1038/nnano.2015.287, 2015.

